2007

Laboratory Characterization and Numerical Modeling of Geogrid Reinforced Bases in Flexible Pavements

Munir Darwish Nazzal
Louisiana State University and Agricultural and Mechanical College, mnazza1@lsu.edu

LABORATORY CHARACTERIZATION AND NUMERICAL MODELING OF GEOGRID REINFORCED BASES IN FLEXIBLE PAVEMENTS

A Dissertation

Submitted to the Graduate Faculty of the
Louisiana State University and
Agricultural and Mechanical College
in partial fulfillment of the
requirements for the degree of
Doctor of Philosophy

In

The Department of Civil and Environmental Engineering

By
Munir Darwish Nazzal
B.S., Birzeit University, Birzeit, Palestine, 2002
M.S., Louisiana State University, 2003
May 2007

Dedications

To

The memory of my father

My mother, wife and daughter

My sister and brother

Uncle Bassam and aunt Shairly

&

All the people who helped me

Acknowledgments

I would like to express my deep gratitude and appreciation to my advisors Dr. Murad Abu-Farsakh and Dr. Louay Mohammad for their thoughtful guidance, encouragement, and continued support throughout the course of my PhD work. Moreover, I would like to thank the faculty who contributed to this work by accepting to serve in my PhD committee: Dr. Mehmet Tumay, Dr. George Z. Voyiadjis, and Dr. Paul Russo.

My Wife, Inas, a woman of great patience, kindness, and understanding deserves my deepest thanks and appreciation. The daily encouragement and support she provided, makes this dissertation as much her as it is mine. I also have to acknowledge my lovely daughter, Sarah, for filling my life with joy and happy moments. I want also to thank my mother, sister and brother for their continuous support and help.

During my graduate study at LSU, I had the chance of meeting new friends and colleagues, and renewing appreciation for the old. I would like to express my gratitude for the sincere friendship of: Rashid Halal, Thaer Jallood, Abdallah Awad, Khalid Alshamsi, Farid Abed, Fuad Odeh, Bashar Alramahi, Walid Alywan, Zyadoon Abu Salem, Ameen Al-Masri, Ziad Taqydine, and other wonderful people who I might not listed. To all, I say Thank you for a friendship that made life much easier away from home.

Special thanks to my colleagues at the Louisiana Transportation Research Center: Xiong Zhang, Minjing Tao, Qiming Chen, Rohit Pant, Amar Raghavendra, and Keith Beard for their technical support and stimulating discussions which were of a great value to this research. Thanks are also extended to the rest of the LTRC staff.

This research project was funded by the Louisiana Transportation Research Center (LTRC Project No. 05-1GT) and Louisiana Department of Transportation and Development.

Table of Contents

Abstract

This dissertation documents the results of an extensive research study that was conducted to characterize the behavior of geogrid reinforced base course materials. The research was conducted through an experimental testing and numerical modeling programs. The experimental testing program included performing different laboratory tests to evaluate the effect of various factors on the performance geogrid reinforced base course materials. Finite element models were also developed to investigate the benefits of placing geogrids within the base course layer in a flexible pavement structure.

The results of the experimental testing demonstrated that the inclusion of the geogrid reinforcement layer(s) improved the compressive strength and stiffness of base course materials under static loading. This improvement was more pronounced at higher strain levels. Furthermore, the results showed that the geogrid significantly reduced the base course material permanent deformation under cyclic loading, but it did not show appreciable effect on their resilient deformation. The results also showed that for stress levels less than the plastic shakedown stress limit, the geogrid had a minimum contribution to the permanent deformation resistance during primary post-compaction stage; however, it significantly increased the permanent deformation resistance during the secondary stage. The results also showed that the change in the moisture content of the crushed limestone material altered the material state of stress; this significantly affected the geogrid improvement.

The finite modeling program showed that the geogrid reinforcement reduced the lateral, vertical, and shear strains within the base course and subgrade layers. Furthermore, the geogrid had appreciable reduction in permanent deformation for pavement sections built on top of weak subgrade soils with medium to thin base layer thickness; with the thin

base layer thickness showing greater values of improvement. However, negligible to modest reinforcement effect on permanent deformation was obtained for sections having a firm subgrade or thick base layer thickness. The geogrid reinforcement had modest to high values of improvement in fatigue life of pavement structure.

Finally, regression models that can be readily used in the design of geogrid reinforced pavements were developed. In addition, an approach for the implementation of the shakedown concept in the design of unreinforced and geogrid reinforced pavement sections was recommended.

Chapter One
Introduction

1.1 Dissertation Organization

This dissertation documents the methodology and findings of the research conducted to characterize the behavior of geogrid reinforced base course layer in flexible pavement structure, and to investigate the benefits of the geogrid reinforcement. Chapter one is an introductory chapter that presents brief background information and highlights the research motivations. It also describes the objectives and the scope of work. Chapter two presents a detailed literature review conducted on some important aspects of the research area. Chapter three describes the properties of the materials used in this study, the test procedures followed to conduct the experimental testing program, and the different features of the numerical models developed in this study. Chapter four presents and discusses the findings of the experimental testing program. Chapter five presents the calibration and verification of the material constitutive models used in the numerical analyses. Chapter six and seven discusses the findings of the numerical modeling program. Finally, chapter eight summarizes the keyfindings and provides the conclusions that can be drawn based on the results obtained from this research study.

1.2 Problem Statement

The United States of America has one of the largest highway systems in the world with over 3.9 million miles of roads as of year 2004. Its highways have reached almost 2.7 trillion vehicle-miles in 2000. This is equivalent to 7.4 billion vehicle-miles of travel every day. Truck travel (single-unit and combinations) has increased by 231% from 1970 to 2004, while the combination truck travel has increased by 285 %; to account for 4.9% of the total annual vehicle-miles of travel versus 3.2% in 1970 (NCHRP, 2004).

The inadequacy of many of the existing roads due to the rapid growth in traffic volume and the escalating costs of materials and energy provide a motivation for exploring alternatives to existing methods of building and rehabilitating roads. Stabilizing paved and unpaved roads with fabrics offers one such alternative. In recent years, polymer geogrids have been proposed and used to improve the performance of paved roadways. Many experimental and analytical studies have been conducted to validate the improvements associated with geogrid reinforcement of roadways. It was reported that the use of geogrid reinforcement of pavement structure has three main benefits: help in construction soft subgrades, improvement or extension of the pavement's projected service life, and reduction of the pavement structural cross section for a given service life.

Several design methods have been proposed for flexible pavements with geogrid reinforced unbound base aggregate layer. These design methods were either based on empirical or analytical approaches. Empirical design methods are usually based on obtaining a performance level from a laboratory model test, which is then extrapolated to the field conditions for application in the design (Berg et al., 2000). This makes these methods limited to the conditions associated with the experiments of the study. The geogrid reinforced pavement design methods based on analytical solution do not address all the variables (location of geogrid, stiffness of geogrid, base course layer thickness, and strength/stiffness of subgrade, etc) that affect the performance of these pavements, which have been validated by experimental data (e.g. Perkins and Ismeik, 1997).

Given the complex nature of a geogrid reinforced flexible pavement and the introduction of a new variables associated with the reinforcement, a mechanistic procedure is needed for providing a design procedure expressed in terms of material properties of the pavement layers (asphalt concrete, base, subgrade), and the geogrid

materials composing the pavement system. The mechanistic design procedure should include the effect of all of the different variables on the performance of geogrid reinforced flexible pavements.

In order to develop a mechanistic design procedure for reinforced pavement structures, a better understanding and characterization of the geogrid reinforced mechanisms should be established. In addition, the factors that affect the performance geogrid reinforced pavement structures should be determined and evaluated.

1.3 Objectives

The main objective of this research study is to characterize the behavior of geogrid reinforced base course aggregate layer in a flexible pavements structure, and to investigate the effects of different variables that significantly influence the performance of geogrid reinforced base course layer. The study has specific objective:

1. Assess the behavior of geogrid reinforced unbound granular base course material under monolithic and cyclic loading, and to evaluate the following factors:
    a. Geogrid stiffness,
    b. Geogrid location,
    c. Number of geogrid layers,
    d. Base course material state of stress, and
    e. Base course moisture content.
2. Assess the benefits of reinforcing the base course layer in a flexible pavement structure with geogrid reinforcement, and to evaluate the influence of the different variables on the degree of improvement in the performance of these structures. These variables includes:
    a. Strength of the subgrade soil

b. Thickness of the base course layer

c. Stiffness and location of the geogrid layer

3. To use the shakedown concept to develop a serviceability method to design reinforced pavement structures.

1.4 Scope

The stated objectives were achieved through conducting both experimental testing and numerical modeling programs. The experimental testing program included the following variables:

1. Base course Materials**:** Two types of unbound granular base course materials were used
    a. Crushed limestone I
    b. Crushed limestone II
2. Geogrid Type: Five types of geogrids were used:
    a. Tensar BX6100
    b. Tensar BX1100
    c. Tensar BX6200
    d. Tensar BX1200
    e. Tensar BX1500
3. Geogrid Layer Arrangements: Four arrangements were investigated
    a. Lower one third of samples height
    b. Upper one third of samples height
    c. Samples mid-height
    d. Two layers at upper and lower one third locations.
4. Moisture Content: Three moisture contents were studied:
    a. Optimum moisture content

b. +2.5% of the optimum moisture content

c. -2.5% of the optimum moisture content

Different laboratory tests were conducted to investigate the performance of unreinforced and reinforced base course samples, which included the following:

a. Monotonic Compression Triaxial
b. Resilient Modulus Repeated loading triaxial (RLT) tests
c. Single-stage RLT tests
d. Multi-stage RLT tests

The numerical modeling program included developing finite element models using ABAQUS software for typical pavement sections that were used to evaluate the effect of the following variables on the geogrid reinforced flexible pavements:

1. The location of the reinforcement material: Five different locations were investigated to determine the optimum location, this included:
   a. Bottom of the base course layer
   b. Middle of the base course layer
   c. Upper one third of the base course layer
   d. Lower one third of the base course layer
2. The thickness of the base course layer: five base course layer thicknesses were investigated, this included: 150 mm, 175 mm, 200 mm, 225 mm, and 250 mm.
3. The stiffness of reinforcement material: four geogrid types with different stiffness properties were evaluated.
4. The strength of the subgrade material: three subgrades with different strength properties were investigated; representing materials that are, weak, moderate, and stiff.

Chapter Two
Literature Review

This chapter presents the background information required for the forthcoming chapters. The emphasis is on unreinforced and geogrid reinforced base course materials used in flexible pavements in terms of their behavior under repeated traffic loafing.

Topics covered begin with a brief introduction of flexible pavement structures. A literature review on the behavior of granular base course materials under repeated loading is then presented. The chapter also discusses the factors that affect the resilient and permanent strains of the pavement materials.

The concept of shakedown is then introduced to explain the different permanent strain behaviors that were observed for base course materials, and were predicted by many permanent strain models. The shakedown concept will be taken further in this dissertation to characterize base course layer performance determined based on the response obtained from finite element models of the pavement structure.

This is followed by a comprehensive review of the experimental studies conducted on reinforced base course materials in flexible pavements and the results of these studies. It also discusses the geogrid reinforcement mechanisms and improvements in terms of the permanent strain behavior of granular pavement layers that has been observed to occur in large-scale pavement tests and small scale laboratory tests. Finally, a review of numerical modeling studies of geogrid reinforced pavements is presented.

2.1 Flexible Pavement Structures

Pavement structures are built to support loads induced by traffic vehicle loading and to distribute them safely to the subgrade soil. A conventional flexible pavement

structure consists of a surface layer of asphalt (AC) and a base course layer of granular materials built on top of a subgrade layer. Pavement design procedures are intended to find the most economical combination of AC and base layers' thickness and material type, taking into account the properties of the subgrade and the traffic to be carried during the service life of the roadway. The two main structural failure mechanisms considered in the design of a flexible pavement structure are permanent deformation (rutting) and fatigue cracking. These two failure modes are shown in Figure 2.1. Rutting is the result of an accumulation of irrecoverable strains in the various pavement layers. For thin to moderately thick pavements, subgrade and granular base layers contribute most to rutting of a pavement. Fatigue cracking has been defined as the phenomenon of fracture under repeated or fluctuating stress having a maximum value generally less than the tensile strength of the material (Ashby and Jones, 1980).

Although base course layer is an intermediary element of the pavement structure, its correct functioning in the road pavement layers is vitally important. The major structural function of a base layer is to provide a stable platform for the construction of the asphalt layer and reduce the compressive stresses on the subgrade and tensile stresses in the asphalt layer. The base layer should distribute the stresses applied to the pavement surface by traffic loading. These stresses must be reduced to levels that do not overstress the underlying subgrade soil.

Base course layer can be the cause of pavement failures, due to inadequate capacity of support to upper layers or to being insufficiently stiff, such that they fail to transfer the load uniformly to the subgrade, leading to localized overloading of the subgrade, and resulting in excessive pavement rutting. These pavement failures usually necessitate complete pavement reconstruction, and not only remedial treatment of the

(a) (b)

Figure 2.1 Distresses in Flexible Pavements a) Rutting b) Fatigue Cracking

pavement surface where the problem is visible. Therefore, when constructing a pavement structure on a weak subgrade soil layer, it may be required to increase the thickness of base layers, or use good quality base course material. However, the depletion of high quality aggregates is at a rapid pace as a consequence of the increasingly demands on highway systems. In addition, there are usually limitations on the thickness of the pavement structures. These problems provide a motivation for exploring alternatives to existing methods of building and rehabilitating roads. Geogrid reinforcement in base course layer offers one such alternative. Geogrids have been studied and used for the last two decades as reinforcement in the base course layer of flexible pavements; primarily since its application improves the performance of base course material layer, and consequently may extend the service life of flexible pavements (Berg et al., 2000).

2.2 Stresses in Base Course Layer

The stresses acting on a given element in a material can be defined by its normal and shear stress components. It can be proven that for any general state of stress through any point in a body, three mutually perpendicular planes exist on which no shear stresses

act. The resulting stresses on these planes are thus represented by a set of three normal stresses, called principal stresses σ_1, σ_2 and σ_3 (Figure 2.2).

Pavements materials are subjected to traffic loads, which are considered to be repetitive moving loads. These loads produce normal and shear stresses at all points throughout the pavement structure and the natural soil. Figure 2.3 illustrates the general stress regime experienced by an element in base course layer within a pavement structure as a result of a moving wheel load within the plane of the wheel track. Due to the wheel load, pulses of vertical and horizontal stress, that are accompanied by a double pulse of shear stress with a sign reversal, affect a pavement element (Brown, 1996).

2.2.1 Residual Stress

It is usually assumed that the only confining stress acting on a base course layer is due to the overburden pressure. However, compaction of the granular pavement layers during construction results in the application of large vertical stresses. These vertical stresses are reported to cause lateral stresses to develop that become locked into the granular bases and subgrades (Sowers, et al., 1957; Uzan, 1985; Selig, 1987; Duncan and Seed, 1986). It was shown by Selig (1987) that in a granular layer, large plastic lateral strain develops in the bottom of the layer during the first cycle of loading. Upon subsequent loading cycles; however, the response rapidly approaches an elastic condition. The lateral stress in the bottom of the granular layer, in both the loaded and unloaded condition, gradually increases up to about 50 load cycles. After 50 load cycles the lateral stresses in both the loaded and unloaded states were found to be in the order of 20 times greater than before the first load cycle. However, the horizontal stress in the unloaded condition was larger than the stress existing when fully loaded which was not the case when loading first started. This important finding suggests that tensile stresses at the base

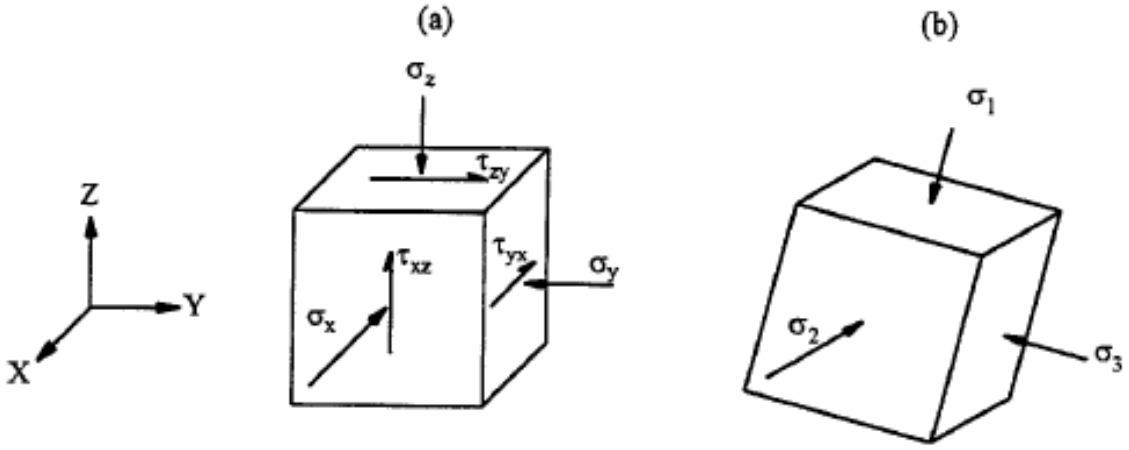

Figure 2.2 Stress components acting on an element (Lekarp, 1997)

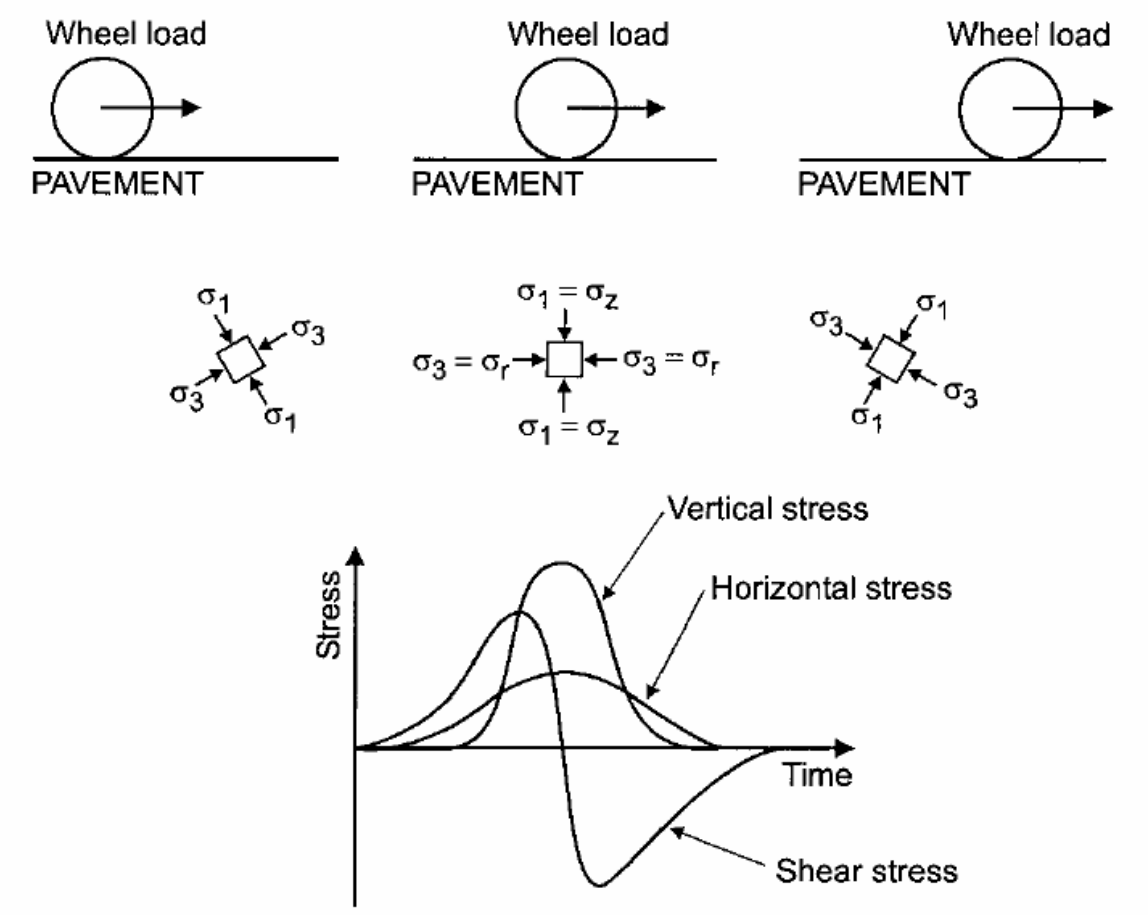

Figure 2.3 Stresses on Pavement Element Under A Moving Wheel Load (Brown, 1996)

of the granular occur in the first few cycles but are quickly cancelled out by residual lateral stresses developing. The result is a net horizontal compressive stress state at the base of the granular layer.

Selig (1987) concluded that the residual lateral stress is the most important factor limiting permanent deformation of the bottom of the granular base. Further, the work of both Selig (1987) and Uzan (1985) indicates the need to properly consider the residual stresses that exist in a granular base in the analyses used in mechanistic based pavement design procedures. Almeida et al. (1993) recognized that a pavement in its original state has residual lateral stresses which are under-estimated from the coefficient of earth pressure at rest, *Ka* (Equation 2.1). They suggested that the residual stresses are likely to be of substantial magnitude which would increase the elastic stiffness of the material and change the stress distribution and recommended that a realistic estimate of horizontal residual stresses be made. However, they indicated that the actual value of the residual stresses is difficult to measure and predictive models for the residual stresses require the stress history of the pavement during construction.

Rankine's theory of earth pressure explained that a certain lateral horizontal stress must exist to ensure stress states do not exceed the Mohr-Coulomb failure envelope (Craig 1992). These are the active and passive lateral earth stress states. The active state represents the minimum horizontal stress conditions that will be experienced by a vertical wall moving away from the surrounding soil, while the passive case represents the maximum lateral horizontal stress when the vertical wall moves towards the soil. Rankine showed that the two values of horizontal lateral stress (σ_{hr}) can be defined by following equations:

$$\sigma_{3a} = \sigma_1 K_a - 2cK_a \qquad 2.1$$

$$K_a = \left(\frac{1 - \sin\phi}{1 + \sin\phi} \right) \quad 2.2$$

$$\sigma_{3p} = \sigma_1 K_p - 2cK_p \quad 2.3$$

$$K_p = \left(\frac{1 + \sin\phi}{1 - \sin\phi} \right) \quad 2.4$$

where,

σ_{3a} is the horizontal lateral stress in the active state;

K_a is coefficient of active earth pressure;

σ_{3p} is horizontal lateral stress in the passive state;

K_p is coefficient of passive earth pressure;

σ_1 is overburden stress or major principal stress;

c is Mohr-Coulomb cohesion; and

ϕ is Mohr-Coulomb friction angle.

If the lateral strain in the soil is zero the corresponding lateral pressure is called earth pressure at rest. Since, the at rest condition does not involve failure of the soil, the Mohr-Coulomb criteria cannot be used to determine the pressure at rest. Triaxial tests are required in which the axial stress and all-round pressure are increased simultaneously such that the lateral strain in the specimen is maintained. For normally consolidated soils the lateral earth pressure at rest can be approximated by the following equations:

$$\sigma_{3r} = \sigma_1' K_o \quad 2.5$$

$$K_{o=1-\sin\phi`} \quad 2.6$$

where,

σ_{3r} : is horizontal lateral stress at rest;

σ'_1 : is overburden effective stress;

K_o : is coefficient of earth pressure at rest;

ϕ' : is Morh-Coulomb friction angle from effective stress.

The coefficient of lateral earth pressure at rest is considered an appropriate value to use for estimating the amount of residual stresses present in a granular material in a pavement structure. For granular pavement materials the cohesion may be neglected and the friction angle approximately 50 degrees. This results in the coefficient of lateral earth pressure at rest having a value of 0.23. Granular materials are located relatively near the surface, say 200mm depth, and based on a density of 2000 kg/m^3 the overburden stress would be 3.9 kPa. Thus, the horizontal residual stress at rest evaluates as approximately 1.2 kPa. However, adding, say, 550kPa vertical stress from compaction and initial traffic loading the horizontal residual stress at rest is approximately 128 kPa. The high value of 128 kPa assumes that the materials do not relax and release some locked in residual stress once the load is removed. Therefore, a value of say 21 kPa, maybe a more conservative estimate of the horizontal residual stresses. Brown (1996) considered that ratios of horizontal to vertical stress as high as 6 are quite possible in practice due to the compaction of granular layers. Although some results from test sections of railway ballast reported by Stewart et al. (1985) indicated ratios up to as high as 11. As above the overburden pressure is 3.9 kPa and therefore if the ratio of horizontal to vertical stress is taken as a value of 6 then again the horizontal stresses are estimated at 21 kPa.

2.3 Response of Base Course Material under Repeated Loads

As a vehicle passes over pavement structure a stress pulse is applied to base course layer. These stress pulses are applied repeatedly in large numbers for the duration

of the life of the pavement. Unbound granular base course material as well as other pavement materials exhibits a combination of resilient strains, which are recovered after each load cycle, and permanent strains, which accumulate with every load cycle. Even at small stresses, resilient and permanent strains can arise. The stress-strain relationship for unbound granular base course material is given by a non-linear curve, which is not retraced on the removal of stresses but forms a hysteresis loop. This is illustrated in Figure 2.4. The area of such a hysteretic loop corresponds to the deformation work per volume applied on the material or the dissipated energy into the material. The energy dissipated into the soil brings changes to the soil's properties and leads to strengthening or damaging effects to the soil depending on loading levels and the soil's initial conditions (e.g., void ratio).

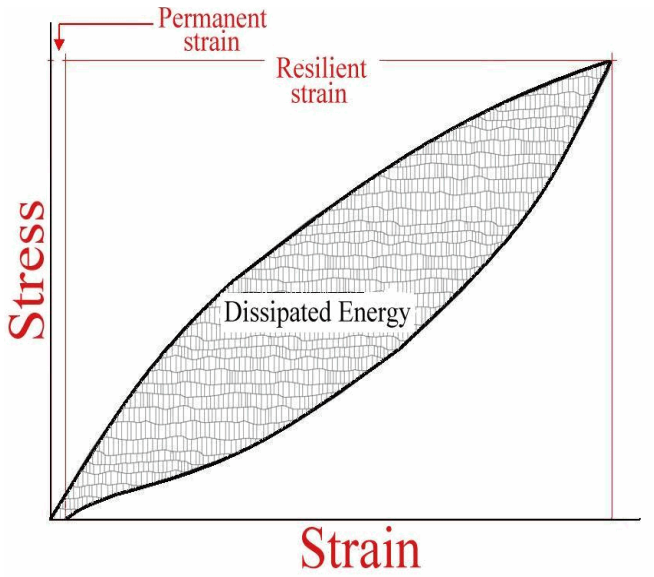

Figure 2.4 A Typical Stress-Strain Hysteretic Loop of Granular

In pavement design it is anticipated that the resilient deformation increases more than the permanent deformation as more load cycles are applied, such that after a large number of cycles the deformation under each cycle is nearly recoverable (Arnold, 2004). The resilient behavior of unbound granular base course materials is characterized by

resilient modulus. Therefore, the resilient modulus has gained recognition by the pavement community as the property that describes the base course materials. The Mechanistic Empirical Pavement Design Guide (MEPGD) has adopted the use of the resilient modulus of base layers as a material property in characterizing pavements for their structural analysis and design (NCHRP, 2004). However, recent studies showed that resilient modulus alone can not properly characterize base course materials (e.g. Mohammad et al., 2006; Khogali et al., 2004; and Puppala et al., 2005) since the base course materials depends on resilient modulus and permanent deformation properties that are affected by other factors, such as environmental and traffic conditions. These properties are typically determined in a Repeated Load Triaxial (RLT) test. The RLT test is performed by placing a specimen in a triaxial cell and applying repeated axial load. Both resilient and permanent axial deformation responses of the specimen are recorded and used to calculate the resilient modulus and the permanent strain, respectively.

2.4 Factors Affecting Resilient and Permanent Deformation Properties

Many factors simultaneously affect both the resilient modulus and permanent deformation properties of granular materials. However, their influence on resilient modulus is not the same as on permanent deformation properties. In this section an overview of the factors influencing both the resilient modulus and permanent deformation is presented.

2.4.1 Stress State

Previous studies showed that the stress level has the most significant impact on the resilient properties of granular base course materials (Mitry, 1964; Monismith et al., 1967; Hicks, 1970; Smith and Nair; 1973; Uzan, 1985; and Sweere, 1990). Many studies indicated a high degree of dependence on confining pressure and the first stress invariant

for the resilient modulus of base course materials. The resilient modulus was reported to increase considerably with the increase in the confining pressure and the sum of principal stresses. Monismith et al. (1967) reported an increase of up to 500% in resilient modulus fdue to a change in confining pressure from 20 to 200 kPa. An increase of about 50% in resilient modulus was observed by Smith and Nair (1973) when the first stress invariant increased from 70 to 140 kPa.

Compared to confining pressure, deviator or shear stress is believed to be much less influential on resilient modulus of the material (Morgan, 1966). The resilient modulus was reported to decrease slightly with increasing repeated deviator stress under constant confinement. Hicks (1970) suggested that the resilient modulus is practically unaffected by the magnitude of the deviator stress applied, provided excessive plastic deformation is not generated. Hicks and Monismith (1971), on the other hand, reported a slight softening of the material at low deviator stress levels and slight stiffening at higher stress levels. Resilient Poisson's ratio is also believed to be influenced by the state of applied stresses. Hicks (1970), Brown and Hyde (1975), and Kolisoja (1997) reported that the Poisson's ratio of granular base course materials increases with increasing deviator stress and decreasing confining pressure.

On contrary to the resilient modulus, the accumulation of axial permanent strain is directly related to deviator stress and inversely related to confining pressure. Morgan (1966) observed in RLT tests conducted at a constant confining stress that an increase in the accumulation of axial permanent strain was directly related to an increase in deviator stress (cyclic axial load). Conversely, for a constant deviator stress it was found that the accumulation of permanent strain increased with a reduction in confining stress. Pappin (1979) studied a well graded limestone using RLT tests. He suggested that the permanent

strains are function of the length of the stress path and the stress ratio (deviator stress/ confining stress). The resistance to permanent deformation decreased when the applied stress approached the failure curve, i.e. the accumulated permanent strains increased at rising deviator stress. Lashine et al. (1971) conducted RLT tests on a crushed stone under a partially saturated and drained condition. They found that the measured permanent axial strain settled down to a constant value which is directly related to the ratio of deviator stress to confining pressure. Similar results were reported by Brown and Hyde (1975), who studied the response of crushed stone under repeated triaxial loading conditions under constant confinement. They also reported that similar results are obtained in tests with variable confining pressure, if the mean value of the applied confining stress is used in the analysis. Other researchers (Raymond and Williams, 1978; Pappin,1979; Thom, 1988; and Paute et al., 1996) have attempted to explain permanent strain behavior under repeated loading using the ultimate shear strength of the material. In this approach, the static failure line is considered as a boundary for permanent strain under repeated loading. Such that, stress states close to the shear failure line will result in higher magnitudes of permanent strain and stress states exceeding the failure line are not possible or will result in early failure of the material. However, Lekarp and Dawson (1998) argued that failure in granular materials under repeated loading is a gradual process and not a sudden collapse as in static failure tests. In contrary, they related the magnitude of permanent strain obtained in RLT tests to the stress ratio of deviator stress (q) to mean normal stress (p) or confining stress, and suggested the existence of a critical stress ratio limits between stable and unstable conditions of permanent strain in a pavement, which is called “shakedown limit” according to the “shakedown” concept. The shakedown concept will be thoroughly discussed later in this chapter.

2.4.2 Number of Load Applications

Most studies that investigate the effect of number of load applications on the resilient response of granular materials indicated that the resilient modulus increases slightly during the first few load cycles (50-100 cycles); however, after that it remains constant (Hicks, 1970; Allen and Thompson,1974). Moore et al. (1970) suggested that the increase in the resilient modulus at early stages of loading can be partially explained by the loss of moisture from the specimen during testing.

However, the behavior of permanent deformation with load cycles is more complex and different than the behavior of resilient deformation, The growth of permanent deformation in granular materials under repeated loading is a gradual process during which each load application contributes a small increment to the accumulation of strain. Therefore, with increasing load cycles the accumulative permanent strain will always increase; however, this increase varies. Paute et al. (1996) found that the rate of increase in permanent strain with increasing load cycles decreased constantly to such an extent to define a limit value for the accumulation of permanent strain. On the other hand, some researchers reported continuously increasing permanent strain under repeated loading (e.g. Morgan, 1966; Barksdale, 1972; Sweere, 1990). Furthermore, Theyse (2002) also reported that for high stress, the states permanent strain increased at a constant rate but between 5,000 and 10,000 load cycles an exponential increase in permanent strain occurred resulting in failure shortly after.

Lekarp (1997) and Lekarp and Dawson (1998) suggested that the effect of the number of load repetitions on the permanent strain response has to be considered in combination with the stress condition. Such that, if the applied stresses are low, the accumulation of permanent deformations will stabilize as the number of load repetitions

increases, and the curve representing the accumulated permanent deformation approaches asymptotically a limiting value, i.e. the permanent deformation rate per load cycle tends towards zero. However, increasing stress ratios lead to a progressive rise of the accumulating permanent deformations.

2.4.3 Moisture Content

The degree of saturation or moisture content of most granular materials has been found to affect the resilient response characteristics of the material in both laboratory and in situ conditions. Researchers who studied the behavior of granular materials at high degrees of saturation, reported a notable dependence of resilient modulus on moisture content, with the modulus decreasing with growing saturation level(e.g., Haynes and Yoder, 1963; Hicks and Monismith, 1971; Barksdale and Itani, 1989; Dawson et al,1996, and Heydinger et al.,1996). Haynes and Yoder (1963), for instance, observed a 50% decrease in resilient modulus in gravel as the degree of saturation increased from 70 to 97%. Hicks and Monismith (1971) showed that the resilient modulus decreases steadily as the moisture content increases above its optimum value. Saturated granular materials develop excess pore-water pressure under repeated loading. As pore-water pressure develops the effective stress in the material decreases with a subsequent decrease in the stiffness of the material. It can be argued that it is not the degree of saturation that influences the material behavior but rather the pore pressure response controls the deformational behavior. Mitry (1964), Seed et al. (1967), and Hicks (1970) stated that a decrease in the resilient modulus due to saturation is obtained only if the analysis is based on total stresses. Similarly, Pappin (1979) observed that if the test results are analyzed on the basis of effective stresses, the resilient modulus remains approximately unchanged. Thom and Brown (1987), however, argued that the presence of moisture in an aggregate

assembly has some lubricating effect on particles. This would increase the deformation in the aggregate assembly with a consequent reduction of the resilient modulus, even without generation of any pore-water pressure. Thom and Brown confirmed this hypothesis with a series of repeated load triaxial tests on a crushed rock, where the moisture content was one of the parameters changed. Using drained tests and loading frequencies of 0.1–3 Hz, no noticeable pore pressures were developed for degrees of saturation up to 85%. Despite the lack of pore pressure, the test results showed a reduction to the resilient modulus with increasing moisture content. This phenomenon was related to the lubricating effect of water and the lower inter-particle contact forces, due to the decrease in the localized pore suctions at higher water content. A study conducted by Raad et al. (1992) demonstrated that the effect of moisture on the resilient behavior of granular base aggregates is perhaps most significant in well-graded materials with a high proportion of fines. This is because water is more readily held in the pores of such materials, whereas uniformly graded materials allow water to drain freely. Dawson et al. (1996) studied a range of well-graded granular base course material and found that below the optimum moisture content stiffness tends to increase with increasing moisture level, apparently due to development of suction. Beyond the optimum moisture content, as the material becomes more saturated and excess pore water pressure is developed, the effect changes to the opposite and stiffness starts to decline fairly rapidly. Saturation of unbound granular materials also affects the resilient Poisson's ratio. Hicks (1970) and Hicks and Monismith (1971) reported that Poisson's ratio is reduced as the degree of saturation increases. According to Hicks (1970), the reduction in Poisson's ratio was noted whether the analysis was based on total or effective stresses. This suggests that a pore suction/ pressure explanation for changing resilient Poisson's ratio is insufficient.

However, the explanation involving the lubricating effect of water must also be questioned, as a higher Poisson's ratio should be expected with greater lubrication.

The moisture content was also reported to significantly affect the permanent deformation properties. The available literature reveals that researchers who have studied the effect of water content in granular pavement layers in the laboratory and in the field believe that the combination of a high degree of saturation and low permeability, due to poor drainage, leads to high pore pressure, low effective stress, and consequently, low permanent deformation resistance (Haynes and Yoder, 1963; Barksdale, 1972; Maree et al. 1982; Thom and Brown,1987).

Haynes and Yoder (1963) found that the total permanent strain rose by more than 100% as the degree of saturation increased from 60 to 80%. An increase of 68% in permanent strain was observed by Barksdale (1972) for tests on soaked specimens compared to those partially saturated. Thom and Brown (1987) reported a small increase in water content can trigger a dramatic increase in permanent strain. The RLT tests conducted by Dodds et al. (1999) showed that the aggregate contaminated with 10% clay fines did not survive for 100,000 loading cycles when saturated, while the aggregate free from clay fines did survive.

Thom and Brown (1987) studied the impact of the moisture content on the permanent deformation behavior of Dolomite-material. The outcome of the investigation showed a serious increase of permanent deformations resulting from the rise in water content of the specimens. Furthermore, it became clear that a relatively small increment of water content had a disproportionate effect on the increase in permanent deformation. This tendency was also observed without the creation of pore water pressure. It was stated that this behavior could be attributed to the fact that the existence of water within

granular assemblies partly lubricated the particles and consequently the resilient as well as permanent deformations rose. The existence of a sufficient amount of water has been shown to lubricate the grains leading to an increase of resilient and permanent deformations. Other investigators (Dawson, 1990; Lashine 1971; Barksdale, 1972) who studied the effect of the water content on the permanent deformation behavior of base course materials drew the same conclusions as mentioned above. The growing susceptibility of granular assemblies to deformation with increasing water content was also observed in field tests (Maree et al., 1982).

2.4.4 Stress History

Studies have indicated that stress history may have some impact on the resilient behavior of granular materials. According to Dehlen (1969), the stress history effects appear as a consequence of progressive densification and particle rearrangement under repeated application of stress. Boyce et al. (1976) carried out repeated load triaxial tests on samples of a well-graded crushed limestone, all compacted to the same density in a dry state. The results showed that the material was subjected to stress history effects, but these could be reduced by preloading with a few cycles of the current loading regime and avoiding high stress ratios in tests for resilient response.

Hicks (1970), on the other hand, reported that the effect of stress history is almost eliminated, and a steady and stable resilient response is achieved after the application of approximately 100 cycles of the same stress amplitude. Similar observations were reported by Allen (1973), who suggested that a specimen should be conditioned for approximately 1,000 load repetitions prior to repeated load resilient tests. Other researchers reported that resilient characteristics of unbound granular materials are basically insensitive to stress history, provided the applied stresses are kept low enough

to prevent substantial permanent deformation in the material (Brown and Hyde 1975; Mayhew 1983). Therefore, large numbers of resilient tests can be carried out sequentially on the same specimen to determine the resilient parameters of the material.

The permanent deformation behavior of base course materials is directly linked to stress history. If these materials are initially exposed to low loads, then this stress history diminishes the effect of any subsequent higher loads. Smaller permanent strains also occur if the initially applied loads are higher than the subsequent loads (Barksdale, 1991). Brown and Hyde (1975) showed that the permanent strain resulting from a successive increase in the stress level is considerably smaller than the strain that occurs when the highest stress is applied immediately. When repetitive loads are applied, the effect of stress history appears as a result of gradual material stiffening by each load application, causing a reduction in the proportion of permanent to resilient strains during subsequent loading cycles. Even though the effect of stress history on permanent deformation behavior has been recognized, very limited research appears to have been done to study this effect. In the laboratory permanent deformation tests, the effect of stress history is normally eliminated by using a new specimen for each stress path applied. However, this is not always practical as a large number of tests are required to cover the full spectra of stress states that may occur within the pavement.

2.4.5 Density

It has been known that increasing density of a granular material significantly alters its response to static loading, causing it to become both stiffer and stronger. However, the effect on resilient stiffness has been less thoroughly studied. The literature available is somewhat ambiguous regarding the impact of density on resilient response of granular materials. Several studies suggested that the resilient modulus generally

increases with increasing density (e.g., Trollope et al., 1962; Hicks, 1970; Robinson, 1974; Rada and Witczak, 1981; and Kolisoja, 1997). Trollope et al. (1962) reported slow repeated load tests on a uniform sand and found that the resilient modulus increased up to 50% between loose and dense specimens. Similar observations were made by Robinson (1974) who also studied uniform sand. The number of particle contacts per particle increases greatly with increased density resulting from additional compaction of the particulate system. This, in turn, decreases the average contact stress corresponding to a certain external load. Hence, the deformation in particle contacts decreases and the resilient modulus increases (Kolisoja 1997). On the other hand, Thom and Brown (1988) and Brown and Selig (1991) stated that the effect of density, or the state of compaction, is relatively insignificant. Hicks and Monismith (1971) found the effect of density to be greater for partially crushed than for fully crushed aggregates.

The effect of density has also been regarded in previous studies as being also significantly important for the permanent deformation behavior of base course materials (Holubec, 1969; Barksdale, 1972, 1991; Allen, 1973; Marek, 1977; Thom and Brown, 1988; and Niekerk, 2002). The resistance to permanent deformation in granular materials under repetitive loading appears to be highly improved as a result of increased density. Barksdale (1972) studied the behavior of several granular materials and observed an average of 185% more permanent axial strain when the material was compacted at 95% instead of 100% of maximum compactive density. Allen (1973) reported an 80% reduction in total plastic strain in crushed limestone and a 22% reduction in gravel as the specimen density was increased from Proctor to modified Proctor density. Holubec (1969) suggested that the reduction of plastic strain due to increased density is particularly large for angular aggregates, providing there is no accompanying increase in

the transient pore pressure during repetitive loading. For rounded aggregates, however, this decrease in strain with increasing density is not considered to be significant, as these aggregates are initially of higher relative density than angular aggregates for the same compactive effort.

2.4.6 Fines Content, and Maximum Grain Size

Granular materials consist of a large number of particles, normally of different sizes. Previous research in this area shows that the resilient modulus of such material is, in some degree, dependent on particle size and its distribution. The literature is not quite clear regarding the impact of fines content on material resilient modulus. Nevertheless, some researchers reported that the resilient modulus generally decreases when the amount of fines increases (Thom and Brown, 1987; Kamal et al., 1993). For aggregates with the same amount of fines and similar shape of grain size distribution, the resilient modulus has shown to increase with increasing maximum particle size (Gray, 1962; Thom, 1988; Kolisoja, 1997). According to Kolisoja (1997), the particulate explanation of this response is that the major part of load acting on a granular assembly is transmitted by particle queues. When the load is transmitted via coarser particles, the smaller number of particle contacts results in less total deformation and consequently higher resilient modulus.

The effect of fines content on the permanent deformation resistance of granular materials was also investigated in different studies. Barksdale (1972, 1991) and Thom and Brown (1988), reported that permanent deformation resistance in granular materials is reduced as the amount of fines increases. Allen (1973) related the difference in plastic strains between different aggregate types of the same density to the surface characteristics of the particles. He argued that angular materials, such as crushed stone, undergo smaller

plastic deformations compared to materials such as gravel with rounded particles. This behavior was said to be the result of a higher angle of shear resistance in angular materials due to better particle interlock.

2.4.7 Particle Size Distribution

The particle size distribution, or grading, of granular materials seems to have some influence on material resilient modulus, though it is generally considered to be of minor significance. Thom and Brown (1988) studied the behavior of crushed limestone at different gradings and concluded that uniformly graded aggregates were only slightly stiffer than well-graded aggregates. Similar results were reported by Brown and Selig (1991) and Raad et al. (1992). Plaistow (1994) argued that when moisture is introduced to well-graded materials, the effect of grading can be significantly increased, because these materials can hold water in the pores. They can also achieve higher densities than uniformly graded materials because the smaller grains fill the voids between the larger particles. Plaistow, therefore, concluded that grading has an indirect effect on the resilient behavior of unbound aggregates by controlling the impact of moisture and density of the system.

Dunlap (1966) noted that if a change in grading produces an increase in the relative density at the same compactive effort, then the permanent strain will decrease. The effect of grading was also studied by Thom and Brown (1988) and was found to vary with the compaction level. When uncompacted, the specimens with uniform grading resulted in the least permanent strain. On the other hand, the resistance to plastic strain was similar for all gradings when the specimens were heavily compacted. This argument was disputed by Dawson et al. (1996), who found the effect of grading on permanent deformation to be more significant than the degree of compaction, with the highest plastic

strain resistance for the densest mix. Kamal et al. (1993) reported similar observations. This difference may be a consequence of the extremely wide range of densities and gradings adopted by Thom and Brown (1988), which far exceeded the range likely to be experienced in any pavement.

2.4.8 Load Duration and Frequency

The load duration and frequency have very little effect on the resilient behavior of granular materials. Seed et al. (1) reported a study in which the resilient modulus of sands increased from 60 MPa to 190 MPa as the duration of load decreased form 20 min to 0.3s. Hicks (1970) conducted tests at stress durations of 0.1, 0.15, and 0.25 s and found no change in the resilient modulus.

2.5 Shakedown Theory in Pavement Analysis

Limit analysis has been used in geotechnical engineering for defining the soil collapse condition under static loading. However, if the loads are applied in a cyclic manner, without ever reaching the static collapse condition, other forms of collapse may occur. The shakedown analysis was here used to identify the material response under cyclic loads. This analysis is basically an extension of limit analysis to the case of periodic loading.

Most of the theoretical approaches to model the materials deformation try to identify the internal variables of postulated constitutive equations of the material based on macro-mechanical observations of the response of samples in triaxial or biaxial tests. Shakedown theory, however, is concerned with the evolution of the plastic deformation in the material. It predicts that a structure is liable to show progressive accumulation of plastic strains under repeated loading if the magnitude of the applied loads exceeds a certain limiting value, the so-called shakedown limit or limit load. The structure is then

said to exhibit an incremental collapse. On the other hand, if the loads remain below this limit, the growth of plastic deformations will eventually level off and the structure is said to have attained a state of shakedown by means of adaptation to the applied loads.

Under the aforementioned premises, four categories of material response under repeated loading can be distinguished, as illustrated schematically in Figure 2.5. For sufficiently small loads the response is always elastic and no permanent deformations occur, in this case the material is operating within the elastic range. However, for larger loads the initial response is plastic and permanent strains are induced, along with the accompanying residual stresses. Provided the amplitude of the applied cyclic loads is not too high however, these residual stresses are frequently such that the resultant stress cycle can be accommodated within the yield surface after a finite number of load applications.

The resultant stress at a point is the residual stress remaining after the previous load application plus the elastic stress induced by the current load cycle. When this stress accommodation has occurred the structure is said to have shakedown or undergone elastic shakedown and the maximum load amplitude at which this phenomenon occurs is called the (elastic) shakedown load. Two types of ultimate response are possible at operating loads above this critical load. The structure may undergo plastic shakedown, by which is meant that the ultimate response is a repeated closed cycle, as illustrated in Figure 2.5. In this situation energy continues to be dissipated but the build up of permanent strains ceases after a finite number of load applications. This phenomenon is also termed cyclic or alternating plasticity. Structures operating in this regime frequently “fail” due to some form of low cycle fatigue. Alternatively the applied loads may be so high that the permanent deformations continue to build up indefinitely, a situation known as ratcheting or incremental collapse.

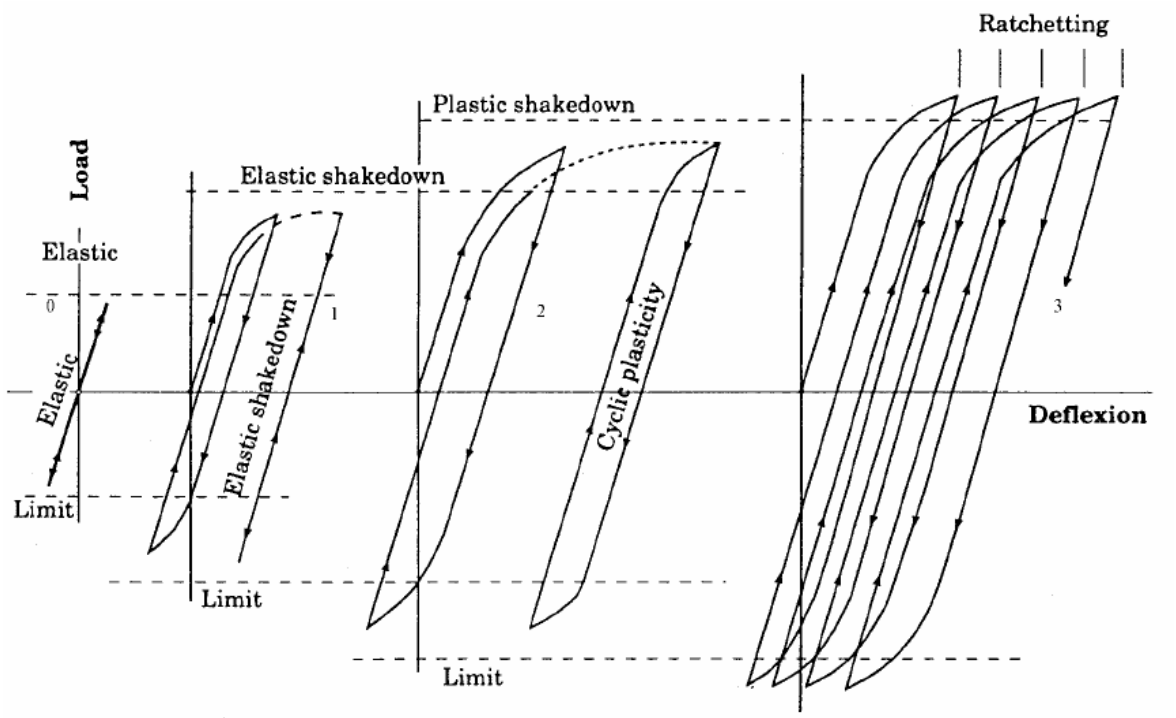

Figure 2.5 Elastic/Plastic Behavior Under Repeated Cyclic Load (Johnson, 1986)

Sharp and Booker (1984) and Sharp (1985) were probably the first researchers introducing the shakedown concept into pavement design. Sharp (1985) and Brett (1987) observed that many pavement sites in the field do shakedown rather than deteriorate continuously based on observations from the AASHTO-Road-Tests and a number of road sections in New South Wales. Their observations provide some early field confirmation to justify the application of the shakedown theory in pavement analysis. The studies on the wear of layered surface by Anderson and Collins (1995), Wong and Kapoor (1996), and Wong et al. (1997) revealed the particular relevance of shakedown theory to pavement analysis.

The attraction of applying shakedown theory to pavement structures, lies in the possibility of determining a critical stress level at each pavement sub-layer that separates stable (i.e., shakedown or resilient behavior) and unstable response (i.e., excessive

permanent deformation occurs). Such that, a durable and well-performing pavement system can be expected if none of its component layers through service life will experience stress levels exceeding their respective shakedown limits. Numerous research studies were conducted to calculate lower and upper bounds of the critical shakedown load by using finite element programs and linear programming procedures. These studies are beyond the scope of this dissertation, and the reader is referred to Sharp and Booker (1984), Raad et al. (1988, 1989a, and 1989b), Hossain and Yu (1996), Yu and Hossain (1998), and Boulbibane and Weichert (1997) for more details.

Recently, Arnold (2002), Werkmeister et al. (2001, 2005, and 2006), and Werkeister (2003) conducted extensive studies on the applications of the shakedown theory in pavement analysis on the basis of RLT tests. They proposed a criterion to discerning different responses of materials under cyclic loading in terms of vertical permanent strain rate. Specifically, by plotting vertical permanent strain rate (permanent strain per load cycle) versus vertical permanent strain, they divided the behavior of unbound granular materials into three different categories:

- Range A–plastic shakedown range: The response is plastic only for a finite number of load applications, and becomes purely resilient after completion of the post-compaction. The permanent strain rate quickly decreases to a very small level.
- Range B–intermediate response (plastic creep): The level of permanent strain rate decreases to a low and nearly constant level during the first several loading cycles.
- Range C–incremental collapse: The permanent strain rate decreases very slowly or not at all and there is no cessation of permanent strain accumulation.

For a well-designed pavement, Range A should be preferable and Range C should always be avoided while Range B can be acceptable provided that the amount of rutting for the design traffic can be calculated. Within the framework of the shakedown theory and on the basis of how the permanent strain rate changes over loading cycles, the RLT results for studied base materials are presented and discussed in the sections below.

2.6 Geogrid Reinforced Base Course Materials

The use of inclusions to improve the mechanical properties of soils dates to ancient times. However, it is only within the last quarter of century or so that the analytical and experimental studies have led to the contemporary soil reinforcement techniques (Koerner, 1998). One of these techniques is the use of geosynthetic materials. Currently, three main geosynthetic families of products are used as soil reinforcement: geogrids, geotextiles, and synthetic fibers. The most commonly used type of geosynthetics for reinforcement of base course layers in flexible pavements is geogrid.

Geogrids are extruded sheets of polyethylene or polypropylene with apertures punched in a regular pattern. The apertures are either elongated ellipses, near squares with rounded corners, squares, or rectangles (Figure 2.6). The key feature of geogrids is that the apertures are large enough to allow soil strike through from one side of the geogrid to the other. The ribs of the geogrids are often stiff compared to the fibers of geotextiles. The rib strength and junction strength are important parameters. The reason for this is that the soil strike-through within the apertures bears against the transverse ribs, which transmit the forces to the longitudinal ribs via the junctions. The junctions are where the longitudinal and transverse ribs meet and are connected. The geogrids are commercially available at different types (sizes and shapes), and tensile strengths.

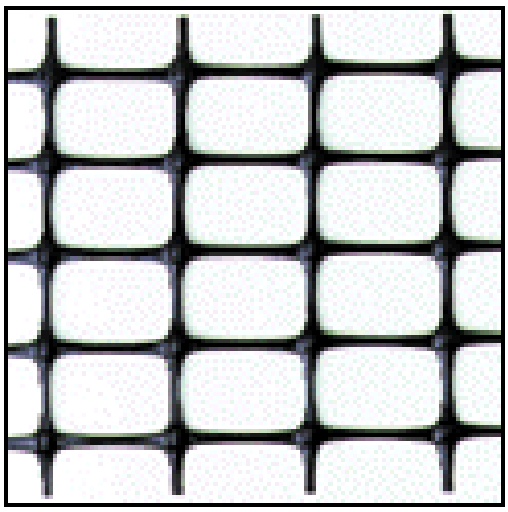

Figure 2.6 Geogrids

2.6.1 Benefits of Geogrid Reinforcement in Base Course Layer

The benefits of applying geogrid reinforcement to the base course layers of flexible reinforcement have been addressed by many researchers during the last two decades. Validating these benefits was accomplished either through indoor (reduced-scale) testing, or outdoor (large-scale) testing. Table 2.1 through 2.4 summarizes the studies reported in literature and their findings. The results of these studies showed that geogrids were able to extend the service lives for reinforced sections by reducing the amount of permanent deformation (rutting) in these sections. The increase in service life of pavement structure has been usually defined using the Traffic Benefit Ratio (TBR). The TBR is defined as the ratio of the number of load cycles to achieve a particular rut depth in reinforced section to that of an unreinforced section of identical thickness, material properties, and loading characteristics. The results of these studies also showed that the required base course thickness for a given design may be reduced when a geogrid is included in their design This reduction is usually defined by the Base Course Reduction (BCR) factor, which is defined as the reinforced base thickness divided by the unreinforced base thickness for a given traffic level.

Table 2.1 Large-Scale Experimental Studies On Geogrid Reinforced Bases

Study	Type of Facility	Facility Dimensions[1] (m)	Test Section Length (m)	Load Type	Applied Cyclic Pressure (kPa)	Applied Cyclic Load (kN)	Load Frequency or Wheel Speed
Al-Qadi (lab)	Laboratory tank	3.1 x 1.8 x 2.1	NA	Stationary circular plate, 300 mm	550	39	0.5 Hz
Al-Qadi (field)	Public roadway	135	15	Random public traffic	Random	Random	Random
Anderson	Field truck staging area	Outdoor staging area	NA	Loaded truck traffic of various types	Random	Random w/ axle loads up to 130	65-70 vehicles/ week
Barker	Outdoor test track	21 x 4.6 x 1.1	4.6	Moving single wheel	1826	120	NR
Barksdale	Indoor test track	4.9 x 2.4 x 1.5	1.6	Moving single wheel	460-500	6.6	1.3 m/s
Brown	Indoor test track	4.9 x 2.4 x 1.5	NR	Moving single wheel	530	5-11	1.3 m/s
Cancelli (lab)	Laboratory tank	0.9 x 0.9 x 0.9	NA	Stationary circular plate, 300 mm	570	40	5 or 10 Hz
Cancelli (field)	Outdoor test track	210 x 4 x 1.2	4.0	Single wheel front axle and double wheel rear axle truck	800	45 front axle, 90 rear axle, 22.5 per wheel	5.6 m/s
Collin	Indoor test track	14.6 x 4.4 x 1.2	3.4	Moving single wheel	550	20	1.2 m/s
Haas	Laboratory tank	4.5 x 1.8 x 0.9	NA	Stationary circular plate, 300 mm	550	40	8 Hz
Halliday	Outdoor test track	20 x 4.25 x 1.5	10.0	Single wheel front axle and double wheel rear axle truck	760	49 and 68 per rear wheel	1.4 -2.2 m/s
Humphrey	Public roadway	3 km road	231	Random public traffic	Random	Random	Random
Huntington	Public roadway	2.9 km road	1900 to 270	Random	Random	Random	Random

Table 2.2 Large-Scale Experimental Studies On Geogrid Reinforced Bases

Study	Type of Facility	Facility Dimensions[1] (m)	Test Section Length (m)	Load Type	Applied Cyclic Pressure (kPa)	Applied Cyclic Load (kN)	Load Frequency or Wheel Speed
Kinney	Indoor test track	19.5 x 2.4 x 1.2	6.1	Moving single wheel (& FWD)	551, 276	20	1.2 m/s
Miura (lab)	Laboratory tank	1.5 x .15 x 1.0	NA[2]	Stationary circular plate, 200 mm	200	6.3	0.18 Hz
Miura (field)	Public roadway	300 m road	50.0	Random public traffic	Random	Random	Random
Perkins	Laboratory Tank Out-door test section	2 x 2 x 1.5 6.36	NA 20	Stationary circular plate, 300 mm Heavy Vehicle Simulator	550 690	40 40	0.67 Hz 13 km/h
Small	Indoor test track	1.4 x 0.5 x 0.8	1.4	Moving single wheel	210	0.42	0.74 m/s
Tingle	Laboratory	1.83 x1.83	1.37	Stationary circular plate, 300 mm	550	40	1 Hz
Webster	Covered outdoor test track	44 x 3.8 x 1.0	11.0	Moving single wheel	470	130	NR[2]

Notes: NA = Not Applicable; NR = Not Reported.

Table 2.3 Results of Large-Scale Experimental Studies

Study	Geogrid Location[1]	AC/Base/ Subbase Thickness (mm)	Subgrade CBR	Rut Depth (mm)	Value-Added Benefits	
					Extension of Life, TBR	Base Course Reduction, BCR (%)
Al-Qadi et al. (1994)	B	70/150	2 - 4	NR	NR	NR
Al-Qadi et al. (1997)	B	90/100	7	21	1.4	NR
Al-Qadi (1997)	B	90/150	7	21	CTNC	<33
Barker (1987)	B [4]	75/150/150	27	25	1.2	CTNC
Barksdale et al. (1989)	M[3]	38/200	2.5	12.5	1.0	CTNC
Barksdale et al. (1989)	M	38/200	3.2	12.5	2.8	CTNC
Cancelli et al. (1996)	B	75/300	1	25	17	CTNC
Cancelli et al. (1996)	B	75/300	3	25	1.7	CTNC
Cancelli et al. (1996)	B	75/300	8	25	3.2	CTNC
Cancelli et al. (1996)	B	75/300	18	12.5	4.5	CTNC
Cancelli et al. (1996)	B	75/300	3	25	5.2	CTNC
Cancelli et al. (1996)	B	75/300	1	25	15	CTNC
Cancelli et al. (1996)	B-M[4]	75/300	1	25	300	CTNC
Cancelli et al. (1996)	B	75/300	3	25	CTNC	30
Cancelli et al. (1996)	B	75/300	1	25	42	CTNC
Cancelli et al. (1996)	B	75/300	3	25	7.1	CTNC
Cancelli et al. (1996)	B	75/300	1	25	70	CTNC
Cancelli et al. (1999)	B	75/300	8	7	1.2	CTNC
Cancelli et al. (1999)	B	75/500	3	13	8.4	CTNC
Cancelli et al. (1999)	B	75/300	3	20	220	CTNC
Cancelli et al. (1999)	B	75/400	3	7	340	CTNC
Cancelli et al. (1999)	B	75/400	3	5	410	CTNC
Cancelli et al. (1999)	B	75/1000	1	<15	CTNC	<50
Cancelli et al. (1999)	B	75/300	8	7	1.6	CTNC
Cancelli et al. (1999)	B	75/500	3	11	13	CTNC
Cancelli et al. (1999)	B	75/300	3	14	300	CTNC
Cancelli et al. (1999)	B	75/400	3	7	330	CTNC

Table 2.4 Results of Large-Scale Experimental Studies

Study	Geogrid Location	AC / Base / Subbase Thickness (mm)	Subgrade CBR	Rut Depth (mm)	Value-Added Benefits	
					Extension of Life, TBR	Base Course Reduction, BCR (%)
Cancelli et al. (1999)	B	75/400	3	5	410	CTNC
Cancelli et al. (1999)	B	75/1000	1	< 12	CTNC	> 50
Cancelli et al. (1999)	B	75/500	3	11	13	CTNC
Cancelli et al. (1999)	B	75/300	3	17	250	CTNC
Cancelli et al. (1999)	B	75/400	3	3	670	CTNC
Cancelli et al. (1999)	B	75/1000	1	< 12	CTNC	> 50
Collin et al. (1996)	B	50/180-300	1.9	25	2 - 3.3	CTNC
Collin et al. (1996)	B	50/180-300	1.9	25	2 - 10	CTNC
Haas et al. (1988)	B	100/200	8	20	3.3	CTNC
Haas et al. (1988)	M	100/200	8	20	3.1	CTNC
Haas et al. (1988)	T	100/200	8	20	0.8	CTNC
Haas et al. (1988)	B	75/200	3.5	20	3.0	CTNC
Haas et al. (1988)	B	75/200	1	20	1.8	CTNC
Haas et al. (1988)	B	75/300	0.5	20	0.8	CTNC
Haas et al. (1988)	B	75/200	3.5	20	CTNC	50
Huntington and Ksaibati (1999)	M	100/280	4	3	CTNC	35
Kinney et al. (1998)	B	61/240-355	2.5	20	2 - 34	CTNC
Kinney et al. (1998)	B	61/203-355	2.5	20	2 - 8.5	CTNC
Miura et al. (1990)	B	50/150/200	NR	5	8	CTNC
Miura et al. (1990)	B	50/150/200	NR	NR	NPA	NPA
Miura et al. (1990)	B	50/150/200	NR	NR	NPA	NPA

Table 2.5 Results of Large-Scale Experimental Studies

Study	Geogrid Location[1]	AC / Base / Subbase Thickness (mm)	Subgrade CBR	Rut Depth (mm)	Value-Added Benefits	
					Extension of Life, TBR	Base Course Reduction, BCR (%)
Perkins et al. (1999)	B	75/300	1.5	24	17	CTNC
Perkins et al. (1999)	U	75/300	1.5	17	56	CTNC
Perkins et al. (1999)	B	75/375	1.5	17	17	CTNC
Perkins et al. (1999)	B	75/300	1.5	16	45	CTNC
Perkins et al. (2005)	B	80/330	1	25	9-31.5	CTNC
Moghaddas-Nejad and Small (1996)	B	20/40	NR	6	4.3	CTNC
Moghaddas-Nejad and Small (1996)	M	20/40	NR	6	92	CTNC
Moghaddas-Nejad and Small (1996)	B	20/40	NR		4 - 92	CTNC
Tingle et al. (2005)	B	0/500	NR	35	1.3-5.3	CTNC
Webster (1993)	B	50/350	3	25	2.7	CTNC
Webster (1993)	B	50/450	3	25	1.3	CTNC
Webster (1993)	M	50/350	3	25	2.2	CTNC
Webster (1993)	B	50/300	3	25	3.1	CTNC
Webster (1993)	B	50/350	3	25	4.7	CTNC
Webster (1993)	B	50/250	8	25	6.7	CTNC
Webster (1993)	B	50/150	8	25	22	CTNC
Webster (1993)	B	50/250	8	25	CTNC	40
Webster (1993)	B	50/350	3	25	1.1	CTNC
Webster (1993)	B	50/350	3	25	0.9	CTNC
Webster (1993)	B	50/350	3	25	0.9	CTNC
Webster (1993)	B	50/350	3	25	1.6	CTNC

Notes :
1.Location code is B = Bottom, M = Middle, T = Top, U= 1/3 up in base.
2. NR = Not Reported, NPA = Not Possible to Analyze, NTD = None To Date, CTNC = Comparative Test Not Conducted.
3. Middle of 150 mm base with 150 mm of subbase below base.
4 . Two layers at bottom and middle of base.
5. Two layers at bottom of base and bottom of subbase.
6. Bottom of subbase.

2.6.2 Geogrid Reinforcement Mechanism

Previous studies involving geogrid reinforcement of base course layer have identified three fundamental reinforcement mechanisms: lateral confinement, increased bearing capacity, and tension membrane effect. These mechanisms are described next.

2.6.2.1 Lateral Confinement Mechanism

The lateral restraint is considered the primary function of geogrid reinforcement, and it develops mainly through shear interaction of the base course layer and geogrid layer or layers contained in or at the bottom of base aggregate as shown in Figure 2.7. By laterally restraining the soil, four components of reinforcement are potentially achieved. The first component is related to direct prevention of lateral spreading of the base course. The cohesion-less materials that make up the base has little tensile resistance and generally depends on the subgrade to provide lateral restraint. In weak subgrades, very little lateral restraint is provided. Thus, the aggregate particles at the bottom of the base tend to move apart. The placement of geogrids layer or layers in the base course allows for shear interaction to develop between the aggregate and the geogrid as the base attempts to spread laterally; this is most likely comes from particles of granular material becoming wedged in the aperture of the geogrids (Figure 2.8). Tensile load is effectively transmitted from the base course aggregate to the geogrid; since the geogrid is considerably stiffer in tension compared to aggregate; consequently this will reduce the developed lateral tensile strain.

The second component of the lateral restraint mechanism results from the increase in stiffness of the base course aggregate when adequate interaction develop between the base and the and the geogrids. The shear stress developed between the base course and the aggregate and the geogrids provides increase in lateral stress within the base (Perkins,

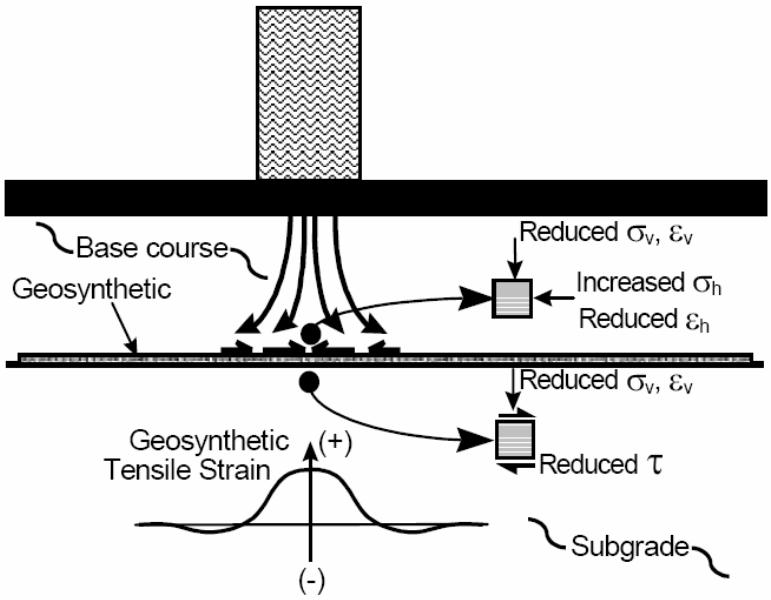

Reinforcement at base/subgrade interface.

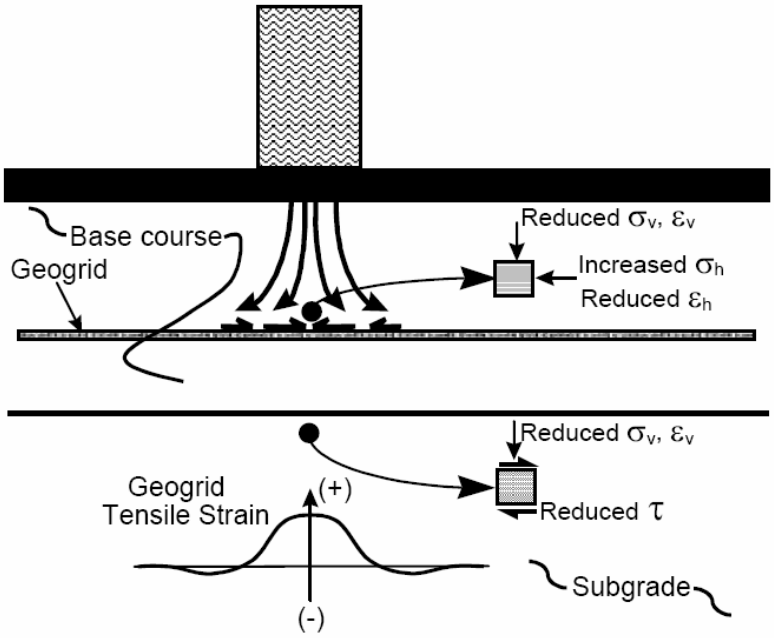

b. Reinforcement (geogrid) in base course.

Figure 2.7 Illustration of Later Restraint Reinforcement Mechanisms (Berg et al., 2000)

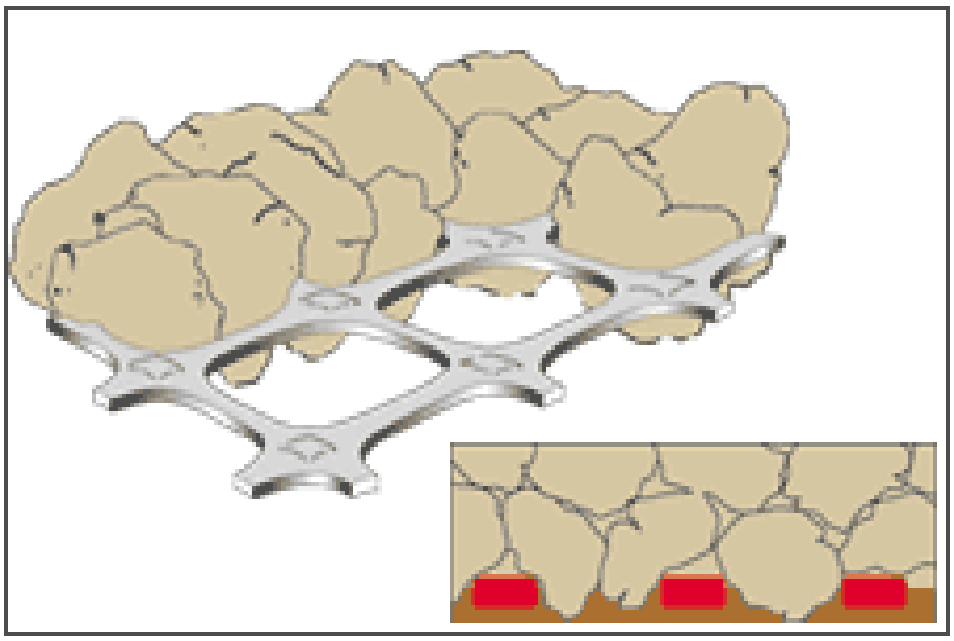

Figure 2.8 The Mechanism of Interlock (Wrigley, 1989)

1999). This tends to increase in the modulus of the base course material (Rodriguez et al., 1988). This increase in stiffness of this layer results also in lower vertical strains in the base.

The third lateral reinforcement component results from an improved vertical stress distribution on the subgrade. The presence of geogrid layer in the base can lead to a change in the state of stress and strain in the subgrade. For layered systems a weaker subgrade material lies beneath the base and an increase in the stiffness of base course layer results in an improved vertical stress distribution on the subgrade. In general, the vertical stress in the base and subgrade layer directly beneath the applied load should decrease as the base layer stiffness increases, such that the vertical stress on the subgrade will become more widely distributed (Figure 2.9). Finally, the fourth reinforcement mechanisms results from reduction of shear stress in subgrade soil. It is expected that shear stress transmitted from base course to the subgrade would decrease as shearing of the base transmits tensile load to the reinforcement.

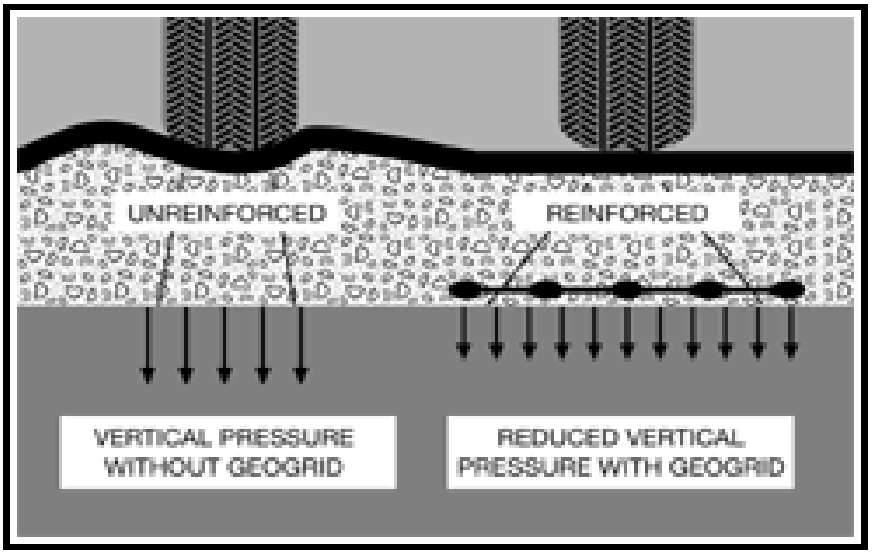

Figure 2.9 Improved Stress Distribution On Subgrade Layer

2.6.2.2 Increase of the Bearing Capacity Mechanism

The improved bearing capacity is achieved by shifting the failure envelope of the pavement system from the relatively weak subgrade to the relatively stiff base layer as illustrated in Figure 2.10. Such that, the bearing failure model of subgrade may change from punching failure without reinforcement to general failure with ideal reinforcement. Binquet and Lee (1975) initially established this finding.

2.6.2.3 Tension Membrane Mechanism

The tension membrane effect develops as a result of vertical deformation creating a concave shape in the tensioned geogrid layer; this is demonstrated in Figure 2.11. The vertical component of the tension membrane force can reduce the vertical stress acting on the subgrade. Some displacement is needed to mobilize the tension membrane effect. Generally, a higher deformation is required for the mobilization of tensile membrane resistance as the stiffness of the geosynthetic decreases. In order for this type of reinforcement mode to be significant, there is a consensus that the subgrade CBR should be less than 3 (Barksdale et al., 1989).

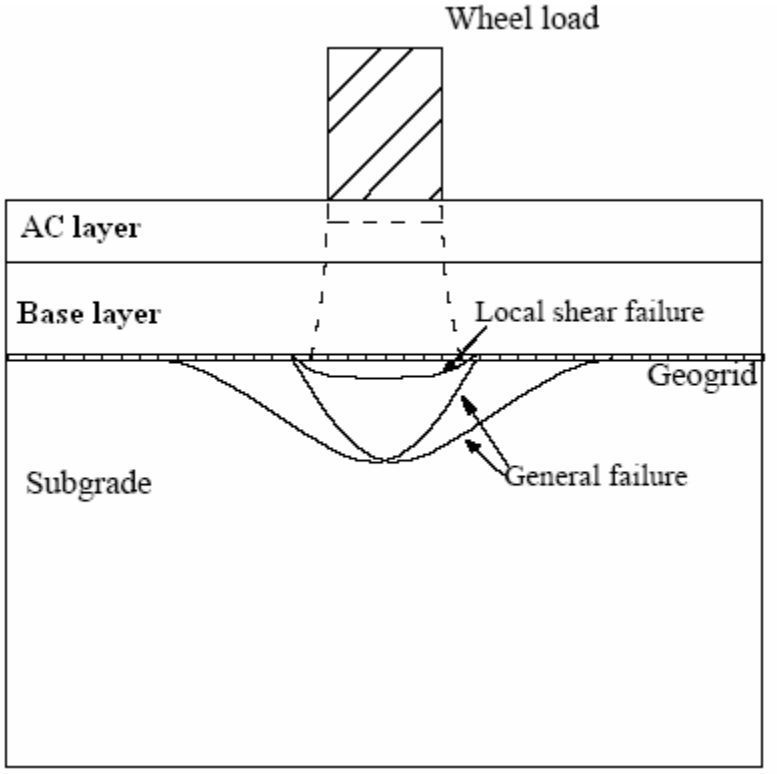

Figure 2.10 Improved Bearing Capacity

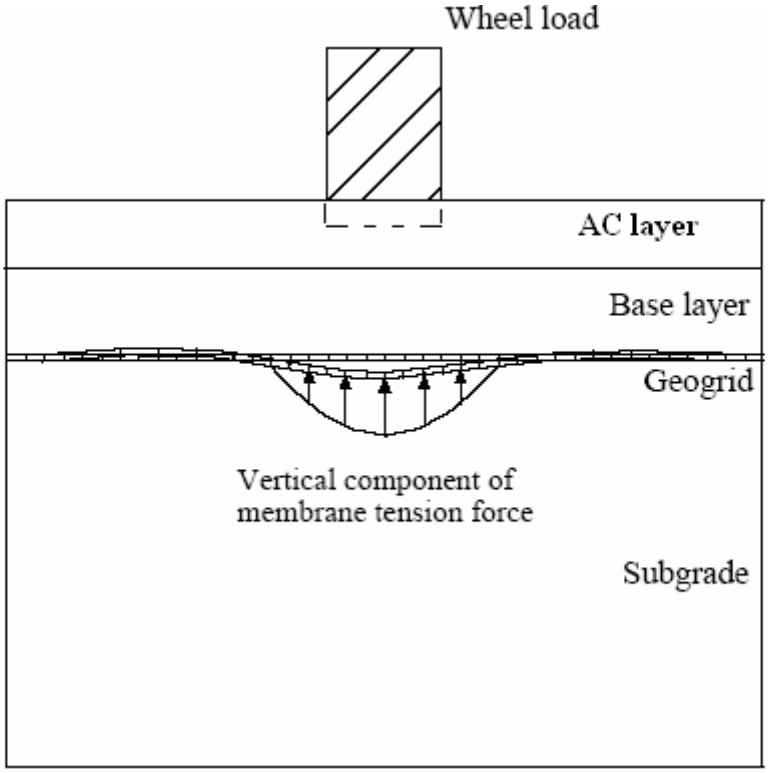

Figure 2.11 Tension Membrane Mechanism

2.6.3 Factors Affecting Geogrid Reinforcement Benefits

Results of experimental studies demonstrated that geogrid base reinforcement benefits were dependent on a number of factors. These include: location of geogrid layer within the base course layer, base course thickness, strength/stiffness of subgrade layer, and the geometric and engineering properties of the geogrids.

Generally, the location of the geogrid depends on the thickness of the base course layer, and the magnitude of applied load (Perkins and Ismeik, 1998). Moghaddas-Nejad and Small (1996) suggested that for thin base course layer (40mm) the geogrid optimal location is in the middle of that layer. For more moderate loads, studies indicated that the middle position of a 200 mm thick base layer was better than at the bottom (Perkins and Ismeik, 1998). Haas et al. (1988) suggested that for 250 mm thick base layer, the optimal location of geogrids was at the bottom of base layers. Studies; however, indicated that for heavy loads and bases thicker than 250 mm, the optimal location was at the middle of the base layer (Haas et al., 1988; Perkins, 1999). For very heavy loads, studies indicated that the bottom of a 350 mm thick base was better than the middle (Perkins and Ishmeik, 1998). For very weak subgrade layer and thick base layer, placing the geogrid slightly into subgrade provided better results in compared to placing the geogrid at the bottom of base layer. Haas et al. (1988) also suggested that for optimum geogrid reinforcement of flexible pavement, the geogrids must be placed in the zone of moderate elastic tensile strain (between 0.05-0.2 percent) beneath the load center.

Studies investigating the influence of strength of the subgrade layer indicated that geogrid reinforcement benefits were greater for weaker subgrade layers. Cancelli and Montanelli (1996) have found that the percent reduction of permanent surface deformation, between reinforced and unreinforced sections, increases with reducing the

subgrade CBR. Perkins (1999) indicated that geogrids provided better improvement when the subgrade layer beneath the reinforced section had a CBR value of 1.5.

Many studies have also been concluded to link geogrid reinforcement of pavement systems to their geometric and engineering properties. Studies investigating the influence of aperture size versus soil particle size on the frictional efficiency of a number geogrid indicated that the optimum transfer of shear stresses occurs when the minimum width of geogrid aperture is less than the average particle size of the backfill material, d_{50} (Koerner, 1998). The geogrid stiffness was also reported to have a significant influence on the achieved benefit. In general, studies demonstrated that higher modulus geogrid provided better improvement to the stress distribution transferred to the subgrade, and the plastic surface deformation compared to lower modulus geogrid (Perkins, 1999, Leng et al., 2001). In addition, some experiments studied the performance of both single layer and multi-layer geogrid reinforced sections. Cancelli and Montanelli (1999) indicated that the reinforcing capacity of the multi-layer geogrids can be mobilized at lower deformation than the typical single layer geogrid. Their tests results showed that geogrid layers were able to mobilize stresses within the reinforced sections, preventing local shear failure and deformations; this was apparently concluded from the measured geogrid strains.

2.6.4 Small-Scale Controlled Laboratory Studies

In order to better understand the reinforcement mechanisms acting in a large-scale reinforced soil structure, studies were also conducted to evaluate such mechanisms at a small-scale controlled laboratory environment. These studies have investigated the effect of geosynthetics on the deformation and strength behavior of reinforced materials using both monotonic and cyclic triaxial tests. Gray and Al-Refeai (1986) conducted triaxial

compression tests on dry reinforced sand using five different types of geotextile. Test results demonstrated that reinforcement increased peak strength, axial strain at failure, and, in most cases, reduced post-peak loss of strength. At very low strain (<1%), reinforcement resulted in a loss of compressive stiffness. Failure envelope of the reinforced sand showed a clear break with respect to the confining pressure. After the point of break, failure envelope for the reinforced sand paralleled the unreinforced sand envelope.

Ashmawy and Bourdeau (1997, 1998) conducted monotonic and cyclic triaxial tests on geotextile-reinforced silt and sand samples which was 71 mm in diameter and 170 mm in length. The results of these studies had shown that the presence of geosynthetics had significantly improved the strength of tested samples. In addition the geosynthetic layer tended to reduce the accumulated plastic strains under cyclic loading. Ashmawy and Bourdeau (1997) investigated the effects of reinforcement layers spacing and reinforcement material properties on the achieved improvement. Their results showed that the amount of improvement depends on the spacing of the geotextile layers, and to a lesser extent on the geotextile and interface properties.

Moghaddas-Nejad and Small (2003) also conducted drained repeated triaxial compression tests on two granular materials (sand and fine gravel) reinforced by geogrid. The geogrid layer was placed at the mid-height of that sample which was 200 mm in diameter and 400 mm in length. The results of this study showed that for a particular confining stress, the effect of a geogrid on the reduction in permanent deformation increases rapidly with an increase in the deviator stress, until a peak is reached, then decreases gradually. However, the geogrid did not have a considerable effect on the resilient deformation of the tested materials.

Perkins et al. (2004) have performed cyclic triaxial tests on reinforced and unreinforced aggregate specimens. The specimens were 600 mm in height and 300 mm in diameter and were compacted inside a rigid compaction mould using a vibrating plate compactor. For the reinforced specimens, a single layer of reinforcement was placed at mid-height of the sample. Four different types of reinforcements were used in the tests (two geogrids, one geotextile and one geocomposite). Their findings supported the previous work reported by Moghaddas-Nejad and Small (2003), where it showed that the reinforcement does not have an effect on the resilient modulus properties of unbound aggregates, while showed appreciable effect on the permanent deformation properties of unbound aggregate as measured in repeated load permanent deformation tests. Perkins et al. (2004) also indicted that the relatively poor repeatability seen in permanent deformation tests made it difficult to distinguish between tests with different reinforcement products. Their results also showed that the reinforcement did not have an appreciable effect on the permanent deformation until a mobilized friction angle of approximately 30 degrees is reached.

2.6.5 Numerical Modeling of Geogrid Reinforced Flexible Pavements

Several numerical studies were performed to analyze pavement sections and assess the improvements due to the geosynthetic reinforcement. Most of the numerical studies were performed using the finite element method. Different constitutive models were used to determine the model that is most capable of representing the stresses and deformations in a reinforced pavement. Table 2.6 summarizes the numerical studies that were reported in literature to investigate reinforced flexible pavement and major features associated with each study.

Table 2.6. Summary of Finite Element Studies on Geosynthetic reinforced pavements

	Author									
	Barksdale et al. (1989)	Burd and Houlsby (1986)	Burd and Brocklehurst (1990)	Burd and Brocklehurst (1992)	Dondi (1994)	Miura et al. (1990)	Wathugala et al. (1996)	Perkins (2001)	Leng and Gabr (2003)	Kwon et al. (2005)
Analysis type	Axi-symmetric	Plane strain	Plane strain	Plane strain	Three-dimensional	Axi-symmetric	Axi-symmetric	Three-dimensional	Axi-symmetric	Axi-symmetric
AC constitutive model	Isotropic, nonlinear elastic	None	None	None	Isotropic, linear elastic	Isotropic, linear elastic	Isotropic, D.P.	Transversely isotropic elastic perfectly plastic	None	Isotropic, linear elastic
AC thickness (mm)	Variable	None	None	None	120	50	89	75	None	76
Base constitutive model	Anisotropic, linear elastic	Isotropic, lastoplastic, Matusoka	Isotropic, elastoplastic, Matusoka	Isotropic, elastoplastic, Matusoka	Isotropic, D.P.	Isotropic, linear elastic	Isotropic, D.P.	Bounding Surface model	Isotropic, D.P.	Nonlinear Elastic
Base thickness (mm)	Variable	75	300	300	300	150	140	300	Variable	254
Geosynthetic constitutive model	Linear elastic	Isotropic, linear elastic	Isotropic, linear elastic	Isotropic,linear elastic	Isotropic, linear elastic	Isotropic, linear elastic	Isotropic, von Mises	orthotropic linear elastic	Isotropic linear elastic perfectly plastic	Isotropic, linear elastic
Geosynthetic element type	Membrane	Membrane	Membrane	Membrane	Membrane	Truss	Solid continuum	Membrane	Membrane	Membrane
Geosynthetic thickness (mm)	None	None	None	None	None	None	2	2	3	1.27
Interface elements and model	Linear elastic-perfectly plastic	None	None	Elastoplastic, Mohr-Coulomb	Elastoplastic, Mohr-Coulomb	Linear elastic joint element	None Isotropic, elastoplastic,	Elastoplastic, Mohr-Coulomb	Elastoplastic, Mohr-Coulomb	linear elastic spring interface element
Subbase constitutive model	None	None	None	None	None	Isotropic, linear elastic	HiSS δo	None	None	None
Subbase thickness (mm)	None	None	None	None	None	200	165	None	None	None
Subgrade constitutive model	Isotropic, non-linear elastic	Von Mises	Von Mises	Von Mises	Cam-Clay	Isotropic, linear elastic	HiSS δo	Bounding Surface model	D.P.	Isotropic, linear elastic
Load application	Monotonic	Monotonic, footing width =75mm	Monotonic, footing width = 500 mm	Monotonic, footing width = 500 mm	Monotonic, two rectangular areas, 240 mm × 180 mm	Monotonic, 200 mm diameter plate	Single cycle, peak pressure=725 kPa on 180 mm diameter plate	Montonic,304 mm plate	Montonic,304 mm plate	Monotonic, a pressure of 828 on 200 mm circular area

D.P.: Drucker Prager Model

Barksdale et al. (1989) used an existing finite element model to predict the improvement in pavement response under a monotonic load, and calculate the lateral tensile strains (fatigue) at the bottom of AC layer, and the vertical strains at the top of the subgrade. The model was calibrated using a set of data for a control (unreinforced) and a reinforced pavement. The results of Barksdale et al. (1989) showed that the BCR value increased by increasing the stiffness of the reinforcement. Increasing the thickness of the AC or base course layers reduced the magnitude of the BCR. The optimal location of the reinforcement was found to be at the bottom of the base course layer, between the bottom and up to middle of the base thickness.

Miura et al. (1990) performed a finite element analysis on reinforced and unreinforced pavements as a part of a laboratory and field test program. They compared the results of the finite element analysis with the test measurements on sections prepared at the same dimensions. The results indicated that the finite element analysis was not capable of predicting the behavior observed in the tests. The predicted reduction in surface displacements was 5% compared to an actual displacement reduction of 35% measured by the tests.

Dondi (1994) used ABAQUS software package to conduct a three dimensional finite element analysis to model the geosynthetic reinforced pavements. The results of this study indicated that the use of the reinforcement resulted in an improvement in the bearing capacity of the subgrade layer and a reduction in the shear stresses and strains on top of it.

In addition, the vertical displacements (rutting) was also reduced by 15 to 20 % due to the intrusion of geosynthetic reinforcement. Dondi (1994) also presented an empirical power function for the fatigue life of pavement which is a function of the

tensile strains developing at the bottom of the AC layer. Based on this expression, the fatigue life of the pavement was predicted to increase by a factor of 2 to 2.5 when the reinforcement was introduced.

Wathugala et al. (1996) used ABAQUS finite element software package to formulate the finite element model for pavements with geogrid reinforced bases. The results of the analysis were compared with an unreinforced pavement sections at the same geometry and material properties. The comparisons indicated that the intrusion of geogrid reinforcement reduced the permanent deformations (rutting) by 20% for a single load cycle. This level of improvement was related to the flexural rigidity of the geosynthetics caused by the model presentation used by the authors (Perkins, 2001).

Perkins and Edens (2002) also used ABAQUS software package to conduct a 3D finite element analysis to simulate the pavement layer thickness, boundary conditions, and loading presented in pavement test sections reported in Perkins (1999). In this analysis, the AC material was modeled using a transversely elastic perfectly plastic model. The base course and subgrade layers were modeled using a bounding surface model described by Dafalias and Hermann (1986). While the geogrid reinforcement was modeled as a membrane element with an anisotropic linear elastic behavior. In order to illustrate the reinforcement effects, Perkins and Edens (2002) conducted finite element analyses for three cases. These cases included: 1- perfect reinforced pavement section in which the lateral strain or displacements of base course aggregate at the interface by the subgrade were restraint. 2- Unreinforced pavement section; and 3- Geosynthetic reinforced section where a sheet of geosynthetic reinforcement was placed at the bottom of base course aggregate layer. To measure the improvement due to the reinforcement, the vertical compressive strain at the top of the subgrade directly beneath the load

centerline, and the bulk stress within the base course material, where compared for the three cases of finite element analyses. The results showed that the geosynthtic reinforcement had reduced the vertical strain on top of the subgrade and had increased the bulk stresses.

Leng and Gabr (2003) conducted a numerical analysis using ABAQUS to investigate the performance of reinforced unpaved pavement sections. Their previous experimental work was used to validate the performance of the developed finite element model of the geosynthetic-reinforced pavements Leng and Gabr (2001). The researchers reported that the performance of the reinforced section was enhanced as the modulus ratio of the aggregate layer to the subgrade decreased. The critical pavement responses were significantly reduced for higher modulus geogrid or better soil/aggregate-geogrid interface property.

Kown et al. (2005) developed a finite element model for the response of geogrid reinforced flexible pavements. The model used nonlinear isotropic and anisotropic elastic constitutive models to describe the behavior of granular base and subgrade materials, respectively. Compaction and preloading induced base course residual stresses was also considered in the mechanistic analysis. The results of this study indicated that the benefits of including geogrids in the granular base-subgrade interface could be successfully modeled by considering residual stresses concentrations assigned just above the geogrid reinforcement. These residual stresses were found to considerably increase the resilient moduli predicted in the base and subgrade of a pavement section modeled. In addition, the study indicated that low subgrade vertical strains were also predicted to demonstrate a lower subgrade rutting potential when residual stress concentrations were assigned in the vicinity of the geogrid.

2.6.6 Design Techniques of Geogrid Reinforced Flexible Pavements

Many studies suggested design approaches for geosynthetic reinforced pavements. Table 2.7 and Table 2.8 provide a summary of design approaches reported in the literature. Haas et al. (1988), Montanelli et al. (1997), and Webster (1993) presented empirical design approaches based on experimental findings from their respective studies. Davies and Bridle (1990) and Sellmeijer (1990) presented design approaches based on analytical considerations and were not necessarily verified by experimental results.

Penner et al. (1985) presented an empirical design approach based on the experimental work by Haas et al. (1988). The design approach was based on the pavement design guidelines published by the American Association of State Highway and Transportation Officials (AASHTO 1981) and was used for comparing results and developing base course equivalency charts. In this study the structural number (SN) of each control section was calculated assuming layer coefficients of 0.4 for the asphalt layer and 0.14 for the granular base layer. The subgrade soil support value (S) was determined from the subgrade California Bearing Ratio (CBR) strength and ranged from 4.3 to 5.7. The values for SN and S were then used in the AASHTO design method to determine the total equivalent 80 kN single-axle load applications, which ranged from 60,000 to 10,000,000 applications. A load correction factor was calculated for each section by dividing the number of 80 kN single-axle load applications by the actual number of load applications necessary to cause failure (failure was defined as a 20 mm rut depth). This load correction factor was intended to account for differences in loading conditions between the laboratory experiments and moving wheel loads in the field. For the control sections, the load correction factors ranged from 3.5 to 10.

Table 2.7 Design Approaches and Procedures for Base Reinforcement

Developer/ Organization	Geosynthetic Type1	Applicability	Design Method and Basis	Geosynthetic Reinforcement Modification1	Distress Mode	Design Format	Empirical Support	Maximum Range of Improvement
Mirafi, 1982	Specific geotextile	1 <CBR<6	Empirical/ modified AASHTO '72	Layer coefficient ratio equal to reinforced to un-reinforced layer coefficients	N/A	Equations and charts	Field results	7% to 18% reduction in base thickness
Penner et al., 1985	Specific geogrid	Based on 4.3<CB<5.7	Empirical/ modified AASHTO '81	SN modifier based on unreinforced to reinforced base layer thickness - reinforcement in middle for base thickness > 250 mm	20 mm rut depth	Equations and charts	Lab test (with load correction factor of 3.5 to 10)	30% to 50% reduction in base thickness
Davies and Bridle, 1990	Generic geosynthetic	Any subgrade with subgrade strain energy used in analysis	Analytical/ calculation of number of load cycles for specific rut depth	Increase in potential energy of the base layer	rut depth	Equations	Verification through comparison with single set of field results	N/A
Sellmeijer, 1990	Generic geosynthetic	N/A	Analytical/ elastic-plastic model	Membrane action and lateral restraint using simple law of friction	N/A	Equations	Not compared to experimental results	N/A

Table 2.8 Design Approaches and Procedures for Base Reinforcement

Developer/ Organization	Geosyn-thetic Type1	Applicability	Design Method and Basis	Geosynthetic Reinforcement Modification1	Distress Mode	Design Format	Empirical Support	Maximum Range of Improvement
Webster, 1993	Specific geogrid	3<CBR <8	Empirical/ mod. AASHTO (FAA, 1978)	Direct extrapolation from field test results	Rut depth (25 mm)	Design charts	Field tests	BCR = 5% to 45%
Tensar, 1996	Specific geogrid	1.9<CBR <8	Empirical/ modified AASHTO 93	Life extension and base course reduction from empirically determined TBR	20 mm to 30 mm rut depth	Equations, charts, computer program	Lab (Haas, 1985) & test tracks (Collin, et al., 1996; Webster, 1992) correlated to	TBR = 1.5 to 10
Akzo-Nobel, 1998 (now Colbond)	Specific GG-GT composite	Not stated	German road design	Increase in bearing capacity of the unsurfaced road	Bearing capacity	Equations and charts	Plate load tests (Meyer & Elias, 1999)	BCR = 32% to 56%
		1.5 <CBR <4.5	Design life extension per FEM analysis	Retards development of crack in pavement	Crack in pave-ment	Charts	None available	TBR = 1.1 to 1.3
Zhao and Foxworthy, 1999	Specific geogrid	CBR <18	Empirical/ modified AASHTO 93	Layer coefficient ratio LCR equal to reinforced to un-reinforced layer coefficients	Rut depth	Equations and spread sheet	Cyclic plate load test and test tracks	Not specifically stated
ERDC(2003)	Specific geogrid	CBR <8	Empirical/ modified Webster, 1993	Direct extrapolation from field test results	Rut depth	Charts and Tables	Field tests	Up to 56% BCR

This load correction factor was then taken to apply to the reinforced sections within a particular test series. The load correction factor for each reinforced section was then used to calculate the 80 kN single-wheel load applications by multiplying the actual number of load applications experienced in the laboratory tests by the corresponding correction factor. From the AASHTO method, a Structural Number (SN) value for that section was determined. A SN value for the reinforced granular base was then calculated by subtracting the asphalt layer SN component from the total SN value. A reinforced layer coefficient was then calculated by dividing the SN value for the reinforced base by its corresponding thickness. The ratio of the reinforced to unreinforced layer coefficients was calculated by using the layer coefficient for the unreinforced granular base. For equivalent base layer SN values, the ratio of the reinforced to unreinforced layer coefficients is equal to the ratio of unreinforced to reinforced base layer thickness. The ratio of the reinforced to unreinforced layer coefficients was plotted against the reinforced base thickness. The graph decreased as the reinforced base thickness approached 250 mm when the geogrid was placed at the bottom of the base. Additional improvement in the layer coefficient ratio was noted for a base thickness of 250 mm or more when the geogrid was placed in the middle of the base. Based on these results, Figure 2.12 was developed and shows the relationship between the thickness of a reinforced base to an unreinforced base when biaxial geogrids are used.

Montanelli el al. (1997) also used the AASHTO design method to determine a layer coefficient ratio for the granular base, which is equal to the ratio of the reinforced to

unreinforced layer coefficients. Values of this ratio ranged from 2 to 1.5 and were determined from experiments using one geogrid and subgrades with different CBR strengths. The values greater than 1.5 were calculated for subgrade CBR strengths less

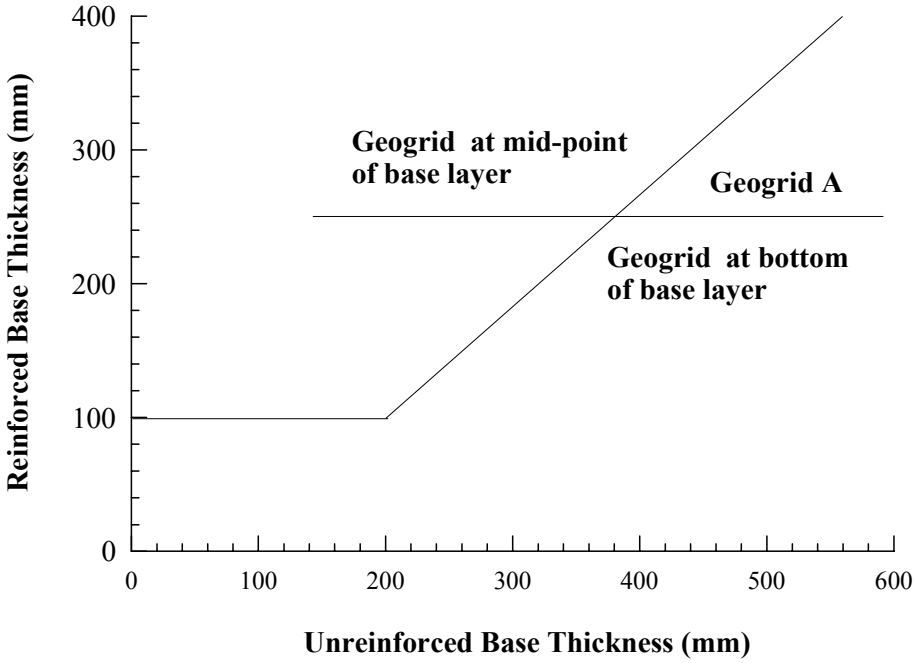

Figure 2.12 The Flexible Pavement Design Charts (After Penner et al. 1985)

than 3. The layer coefficient ratio value was used as a multiplication factor for the depth of the reinforced base in the equation used to calculate the structural number. This implies that for an equivalent structural number, the unreinforced base could be reduced by 33 to 50%.

Webster (1993) produced a design chart by directly comparing and extrapolating test results for sections of equivalent base course thickness. The original design chart included the 50 mm thick AC layer used in the experiments.

Davies and Bridle (1990) developed an analytical technique to calculate the amount of permanent deformation (rut depth) of reinforced pavements with load cycle. The displacement response of the pavement under a single monotonic load application was predicted using an energy method. An expression for the potential energy of the pavement system was developed as a function of the central displacement of the applied load. The geosynthetic layer provided an additional energy component to the system as it

deformed and was shown to increase the component of strain energy provided by the base layer of the pavement. Both the base layer and the geosynthetic were assumed to provide a component of strain energy as structural members in bending, even though both materials have little flexural rigidity. The development of permanent deformation with increasing load cycle was predicted by varying the stiffness parameters of the subgrade. Permanent deformation was assumed to be negligible in the base layer. The stiffness parameters of the subgrade during loading were assumed to be less than those during unloading. The stiffness parameters were assumed to vary with increasing load cycle, with the difference between those for loading versus unloading becoming less at a decreasing rate. The net effect of this material model was a prediction of rut depth which increased with load cycles at a decreasing rate. The values and variation of the material stiffness parameters were determined primarily from the results of repeated load experiments on reinforced pavement test sections. Calibration of material parameters from model pavement experiments limits the utility of the design approach due to the time and expense associated with model construction. Full use of this technique would be facilitated by relating the material stiffness parameters to material properties, such as resilient modulus.

Extensive research programs have also been conducted by the U.S. Army Engineer Research and Development Center (ERDC) and non-military agencies to develop design and construction guidance for the of geogrids in pavement systems. The result of this research was utilized to develop a design procedure for geogrid reinforced flexible pavement. This design procedure used the chart developed by Webster (1993). In this design procedure, the application of a geogrid reinforcing layer is typically predetermined by the subgrade soil strength. Different combinations of geosynthetics are

recommended for use in flexible pavements based upon the subgrade soil conditions. According to this design procedure geogrids should be placed at the subgrade-base interface for base thicknesses less than 14 in. and in the middle of the base layer for aggregate thicknesses greater than 14 in. The design method recommends that for subgrades with a construction platform should be designed to facilitate the construction of the flexible pavement when the subgrade CBR value is less than 0.5. While for subgrades with CBR values between 0.5 and 4 the design method recommend the use nonwoven geotextile for separation for fine-grained subgrades at strengths.

In this design method the unreinforced flexible pavement is determined using a design chart shown in Figure 2.13. This chart is based on the CBR of the supporting layer, either the subgrade strength or the subbase strength. The required pavement thickness obtained from this chart should be rounded up to the nearest 0.5 inches for surfaced flexible pavements. A minimum thickness values for the surface AC and base courses is then found using Table 2.9. This table is based on design index (DI) which combines the effect of average vehicle axle loadings and expected traffic volume as expressed by road classification. The design index ranges from 1 to 10 in order of increasing traffic loading and volumes. The difference between the total required pavement thickness above the subgrade/subbase and the minimum AC thickness (determined from Table 2.9) is the unreinforced base coursed thickness of the flexible pavement. This base thickness can be reduced using Webster's empirical reinforced pavement thickness equivalency chart for subgrade with a CBR value less than 8.0 (Figure 2.14). However the minimum base thickness to be used should be at least 6 in. It should be noted that the ERDC design procedure is based upon the development of a 1-in. (25 mm) rut after 1,000 passes of an 18-kip equivalent axle load. Base course

thickness should be increased by 10 percent for 2,000-pass designs and 20 percent for 5,000-pass designs.

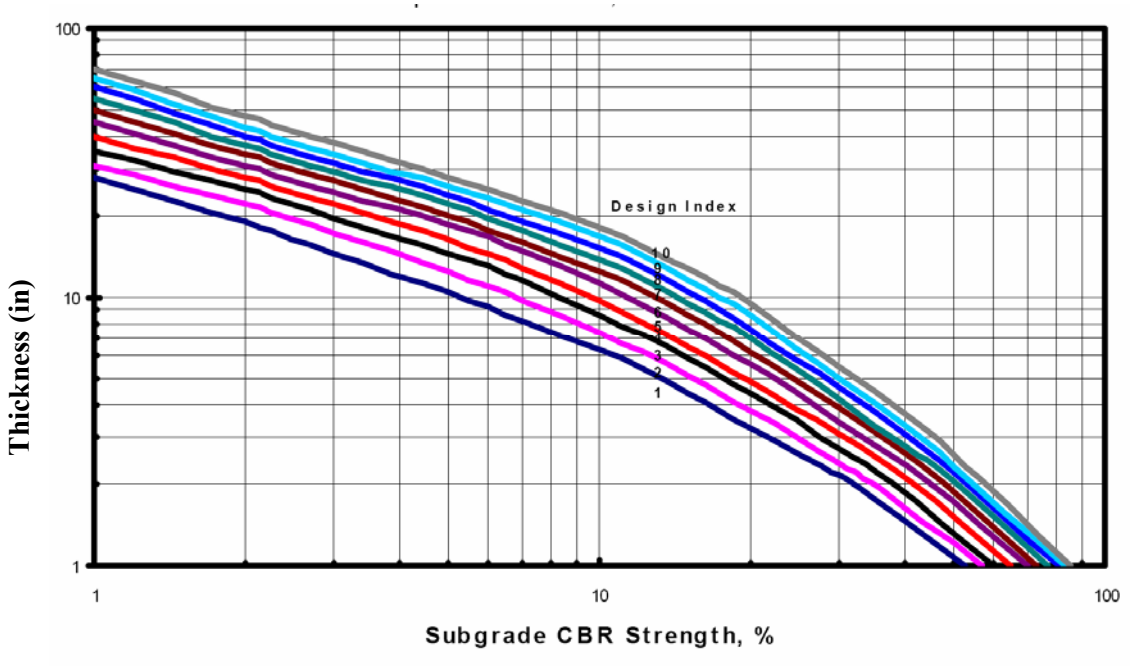

Figure 2.13 Flexible Pavement Design Curves for Roads and Streets ERDC (2003)

Table 2.9 Minimum Thickness of Pavement Layers ERDC (2003)

	Minimum Base Course CBR								
	100			80			50[2]		
Design Index	Pavement (in.)	Base (in.)	Total (in.)	Pavement (in.)	Base (in.)	Total (in.)	Pavement (in.)	Base (in.)	Total (in.)
1	ST[3]	4	4.5[5]	MST[4]	4	4.5[5]	2	4	6
2	MST[4]	4	5[5]	1.5	4	5.5[5]	2.5	4	6.5
3	1.5	4	5.5[5]	1.5	4	5.5[5]	2.5	4	6.5
4	1.5	4	5.5[5]	2	4	6	3	4	7
5	2	4	6	2.5	4	6.5	3.5	4	7.5
6	2.5	4	6.5	3	4	7	4	4	8
7	2.5	4	6.5	3	4	7	4	4	8
8	3	4	7	3.5	4	7.5	4.5	4	8.5
9	3	4	7	3.5	4	7.5	4.5	4	8.5
10	3.5	4	7.5	4	4	8	5	4	9

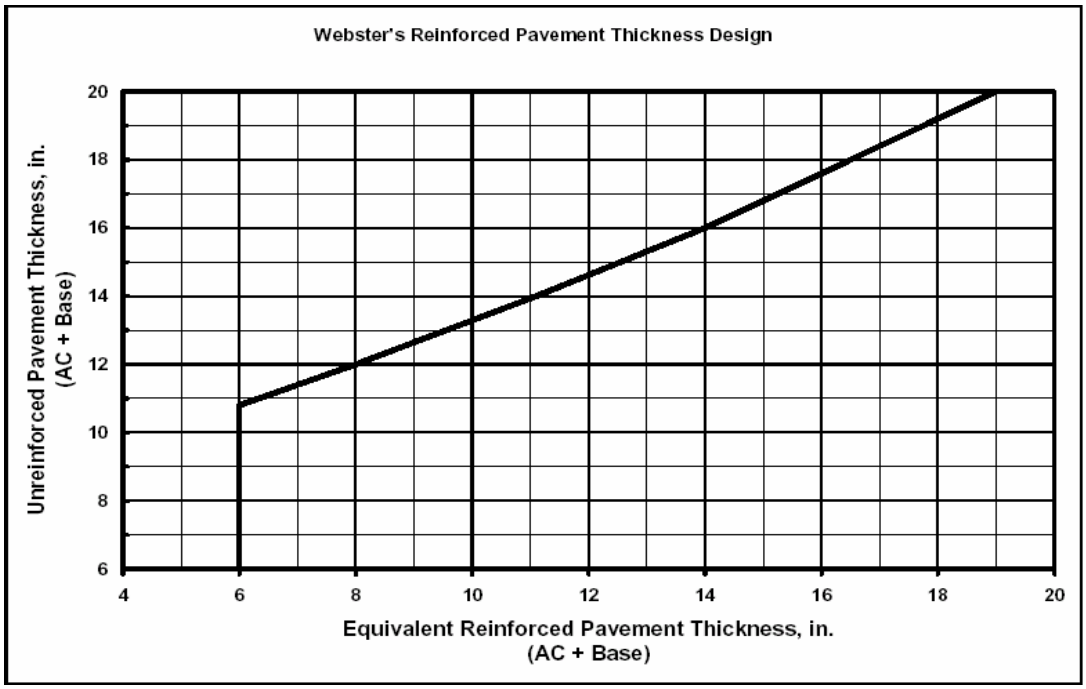

Figure 2.14 Webster's Reinforced Pavement Thickness Equivalency Chart ERDC (2003)

Chapter Three
Research Methodology

This chapter consists of a description of the research methodology pursued in this study. The chapter includes detailed information about the experimental testing and numerical modeling programs.

3.1 Experimental Testing Program

Experimental testing program was conducted to evaluate the effects of the different factors on the performance of geogrid reinforced base course granular materials. These factors include the geogrid stiffness, geogrid location, number of geogrid layers, and the effect of base course material state of stress and moisture content. Two types of triaxial tests were used for this evaluation, namely Static Triaxial Compression (STC) tests, and Repeated Loading Triaxial (RLT) tests. The following sections provide detailed information on the materials used and their properties. They also highlight the laboratory procedures for the triaxial tests performed.

3.1.1 Materials

3.1.1.1 Base Course Materials

Experimental testing was performed on two types of crushed limestone aggregate materials used in the construction of base course layers in Louisiana. The two crushed limestone materials were taken from Valkone quarries located near Baton Rouge, Louisiana. Standard compaction, specific gravity (G_s), absorption, and California Bearing Ratio (CBR) tests were performed on the base materials. The tests were performed in accordance with ASTM standards D 792, D 698, D 570, and D 1883 respectively. The

results of these tests are listed in Table 3.1, and the standard compaction curves for crushed limestone I and II are shown in Figure 3.1 and Figure 3.2, respectively.

Sieve analyses tests were also performed before and after compaction of the two base course materials at their corresponding optimum condition. The tests were conducted in accordance with ASTM-D123 standard method. Table 3.2 presents the results of these tests along with the results of the soil classification. Figure 3.3 and Figure 3.4 compare the grain size distribution before and after compaction for crushed limestone I and II, respectively. It is noted that the crushed limestone I gradation was slightly changed by compaction. On the contrary, the compaction of crushed limestone II had a significant effect on its grain size distribution, such that the whole gradation curve was shifted to the right, indicating an increase in the fine content, and demonstrating that a significant amount of crushing and abrasion of the crushed limestone II aggregates occurred during compaction. It is worth mentioning here that the after compaction gradation represent the exact gradation of the material directly before testing.

Table 3.1 Properties of Crushed Limestone Materials

Material	Bulk Specific of gravity	Apparent Specific of gravity	CBR	OMC* (%) and γ_{max} (kN/m^3)	Absorption %
Crushed lime Stone I	2.54	2.7	101	7.0, 21.9	2.14
Crushed lime Stone II	2.24	2.56	72	10.2, 19.2	5.65

*OMC: optimum moisture content obtained in Standard Proctor Test

** γ_{max} : maximum unit weight obtained in Standard Proctor Test

3.1.1.2 Geogrid Reinforcement

The reinforcement materials used in this study included five different types of biaxial geogrids, namely, BX-6100, BX-1100, BX-6200, BX-1200, and BX-1500. Where BX-

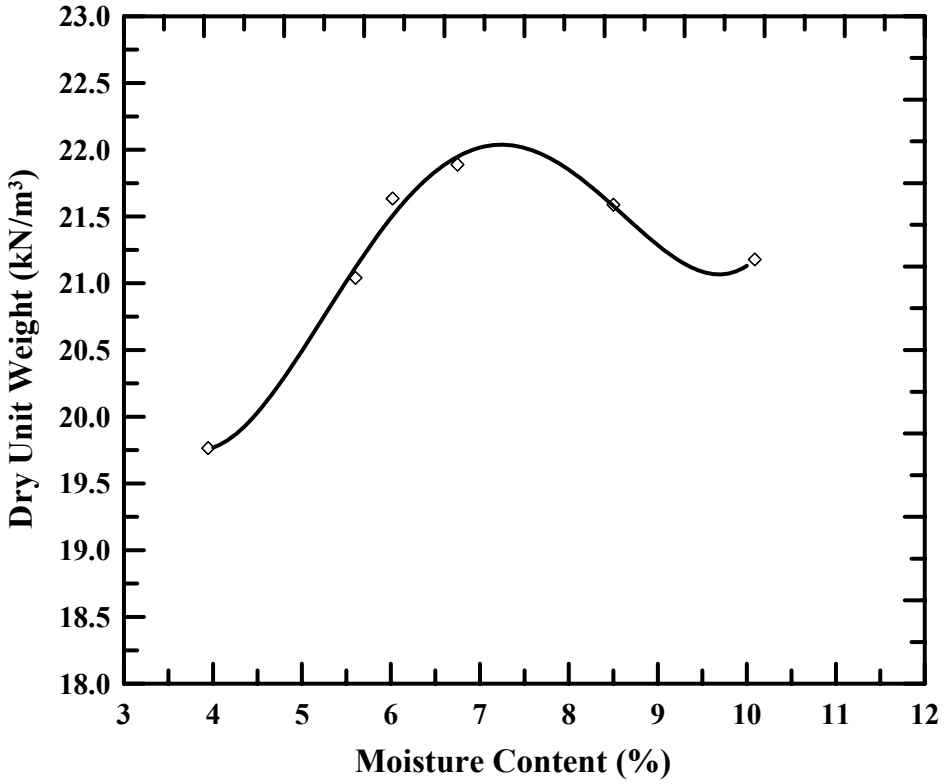

Figure 3.1 Compaction Curve of Crushed limestone I

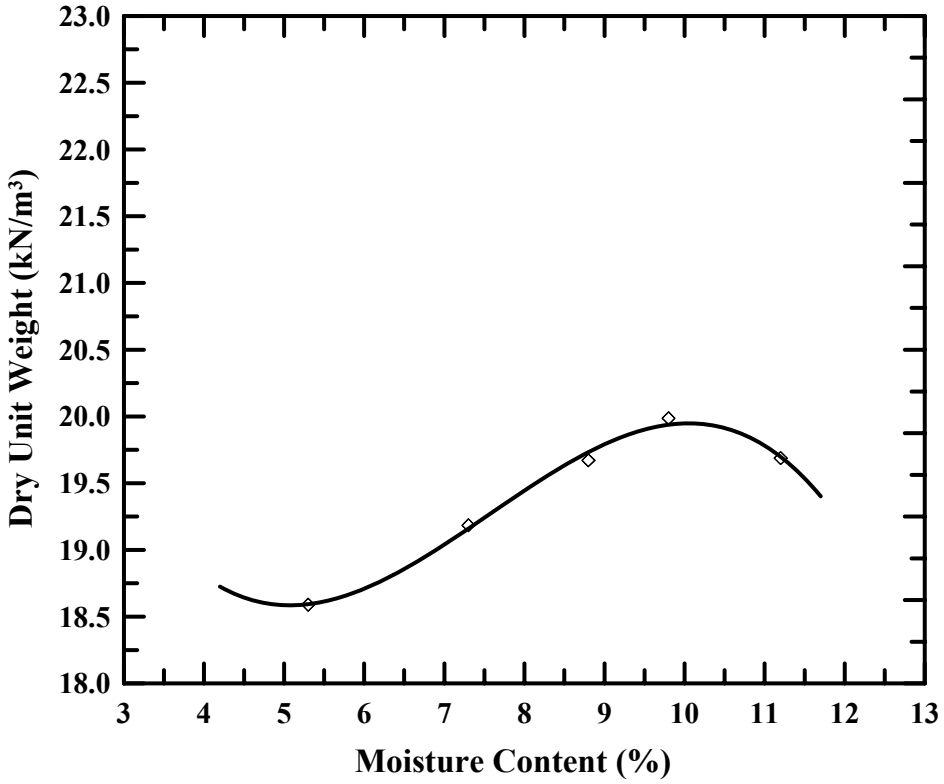

Figure 3.2 Compaction Curve of Crushed limestone I

Table 3.2 Soil Classification of Base Course Materials

Sieve Size (mm)	Finer (%)			
	Crushed Limestone I		Crushed Limestone II	
	Before compaction	After compaction	Before compaction	After compaction
31.25			100	100
25	100	100	94.63	100
19	97.98	99.34	85.56	96.41
15.6	93.92	95.52	80.36	93.74
12.5	85.96	88.49	73.75	90.18
9.5	73.09	77.99	65.36	85.1
4.75	54.5	58.56	48.12	65.89
2.36	37.9	44.68	32.93	48.44
2	35.35	41.47	29.89	45.5
1.18	27.63	33.81	22.8	35.21
0.85	23.14	24.48	17.88	24.5
0.6	19.87	19.92	14.59	19.66
0.425	16.26	16.54	11.11	15.72
0.3	13.34	13.07	8.83	11.26
0.18	9.89	10.81	5	7.83
0.15	6.3	7.12	3.6	6.62
0.075	2.18	5.49	1.56	5.45
Medium grain size,D_{50} (mm)	4	3	5	2.5
Coefficient Of Uniformity (C_u)	33	28	21	12
AASHTO (Classification)	A-1-a	A-1-a	A-1-a	A-1-a
USCS (Classification)	GW	GW- GM	GW	GW- GM

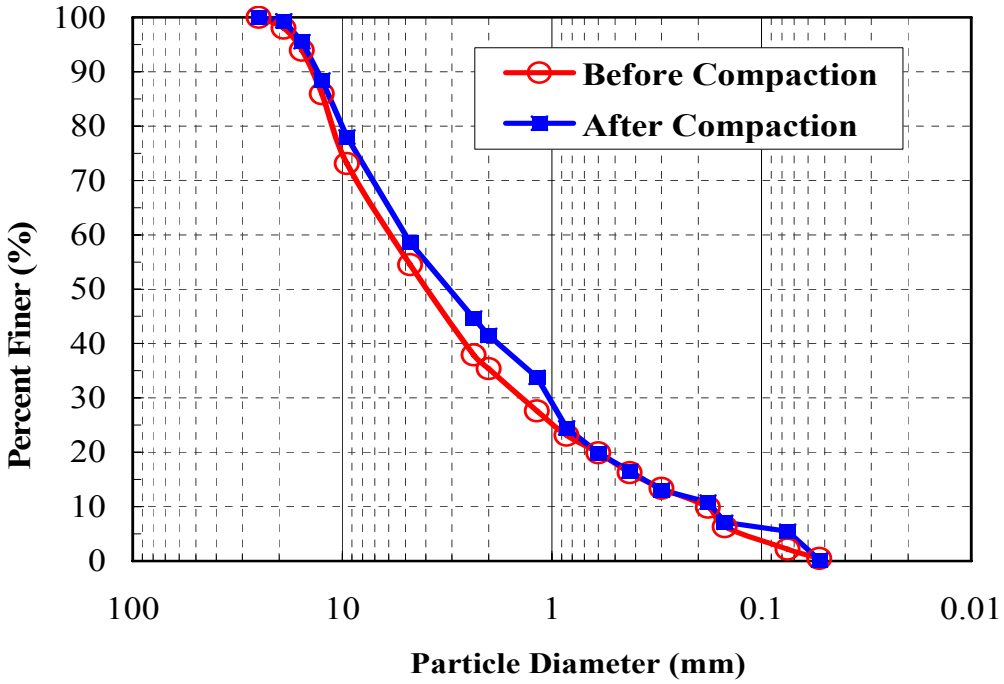

Figure 3.3 Particle Size Distribution of Crushed Limestone I

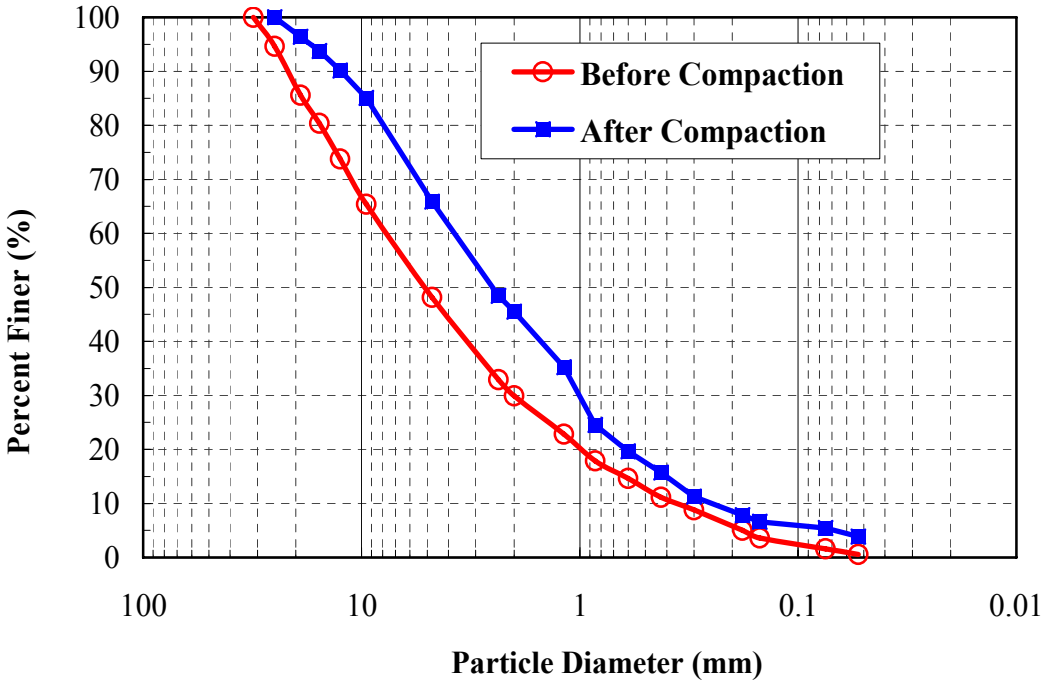

Figure 3.4 Particle Size Distribution of Crushed Limestone II

6100 represents the lowest stiffness geogrid and BX-1500 represents the stiffest geogrid. These geogrids are manufactured of a stress resistant polypropylene material, and are typically used to reinforce a base course layer in pavement structures. The physical and mechanical properties of these products as reported by the manufacturer are presented in Table 3.3 (Tensar Earth Technologies Inc., 2005). Type I, II, III, IV, and V will be used hereafter in this dissertation to refer to BX-6100, BX-1100, BX-6200, BX-1200, and BX-1500, respectively.

Table 3.3 Physical and Mechanical Properties of Geogrids

Geogrid	Tensile Stiffness @ (strain %)[a]		Aperture Dimension		Flexural Stiffness [b]
	MD (kN/m)	CMD (kN/m)	MD (mm)	CMD (mm)	(g-cm)
BX-1500	580 (2%) 1200 (5%)	690 (2%) 1370 (5%)	25	30.5	2000
BX-1200	410 (2%) 810 (5%)	650 (2%) 1340 (5%)	25	33	750
BX-6200	380 (2%) 720 (5%)	510 (2%) 1000 (5%)	33	33	250
BX-1100	280 (2%) 580 (5%)	450 (2%) 920 (5%)	25	33	750
BX-6100	250 (2%) 550 (5%)	380 (2%) 720 (5%)	33	33	250

[a] Measured in accordance with ASTM standard method for determining tensile properties of geogrids ASTM D6637 (Tensar Earth Technologies Inc., 2003).
[b] Measured in accordance with ASTM Standard Test Method for determining stiffness of non-woven fabrics using the cantilever test ASTM D-5732-95. (Tensar Earth Technologies Inc., 2003).
MX: Machine direction.
CMD: Cross- machine direction.

3.1.2 Testing Setup

All triaxial tests were performed using the Material Testing System (MTS) 810 machine with a closed loop, and a servo hydraulic loading system. The applied load was measured using a load cell installed inside the triaxial cell. Placing the load cell inside the triaxial chamber eliminate the push-rod seal friction and pressure area errors, which will results in reducing the testing equipment error. An external load cell is affected by

changes in confining pressure and by load rod friction, and the internal load cell therefore gives more accurate readings. The capacity of the load cell used was ± 22.25 kN (±5000 lbf.). The axial displacement measurements were made using two Linearly Variable Differential Transducers (LVDT) placed between the top platen and base of the cell to reduce the amount of extraneous axial deformation measured compared to external LVDTs. Air was used as the confining fluid to the specimens. Figure 3.5 depicts a picture of the testing setup used in this study.

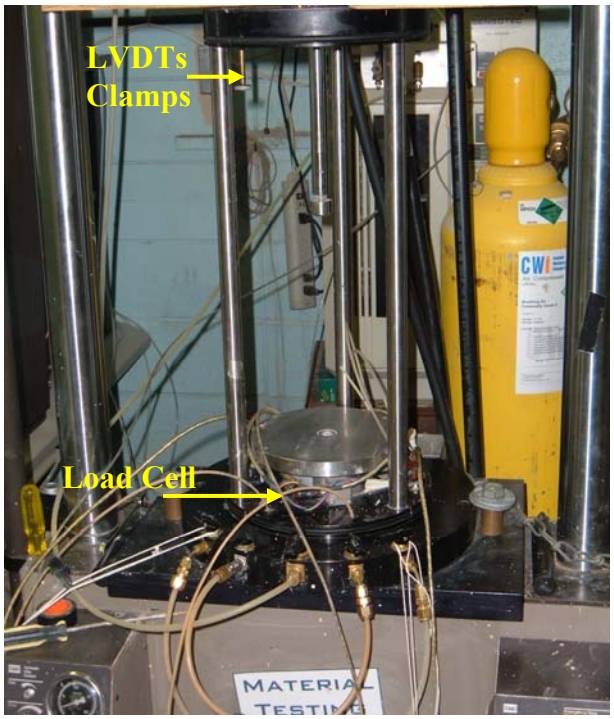

Figure 3.5 MTS Triaxial Testing Machine

3.1.2.1 Sample Size

Dimensions of the sample tested in the triaxial experiment are based on the maximum particle size of its material. The AASHTO recommends that for untreated granular base material, the tested sample should have a diameter greater than five times the maximum particle size of that material. In addition, other studies recommends the use of samples with 150 mm and diameter 300 mm height for a base material with a

maximum particle size greater than 19 mm (NCHRP, 2004). Since the base course material used in this study had a maximum particle size of 19.0 mm, all samples were prepared with 150 mm diameter and 300 mm height.

3.1.2.2 Sample Preparation

AASHTO recommends that a split mold be used for compaction of granular materials. Therefore, all samples were prepared using a split mold with an inner diameter of 150 mm and a height of 350 mm. The material was first oven dried at a pre-specified temperature and then mixed with water at the optimum moisture content. The achieved water contents were within ±0.5 percent of the target value. The material was then placed within the split mold and compacted using a vibratory compaction device to achieve the maximum dry density measured in the standard Proctor test. To achieve a uniform compaction throughout the thickness, samples were compacted in six-50 mm layers. Each layer was compacted until the required density was obtained; this was done by measuring the distance from the top of the mold to the top of the compacted layer. The smooth surface on top of the layer was lightly scratched to achieve good bonding with the next layer. The achieved dry densities of the prepared samples were within ±1 percent of the target value. Samples were enclosed in two latex membranes with a thickness of 0.3 mm. Figure 3.6 illustrates the preparation procedure of crushed limestone samples. For reinforced samples, the geogrid was placed horizontally between layers at the desired locations. Four different arrangements of reinforcement were investigated in this study; namely, single layer placed at the sample mid-height (middle arrangement), single layer placed at the upper one third of the sample height (upper one third arrangement), single layer placed at the lower one third of the sample height (lower one third arrangement), and two layers placed at one and two thirds of the sample height (double arrangement).

A sketch describing the four reinforcement arrangements investigated in this study is shown in Figure 3.7.

3.1.3 Monotonic Triaxial Compression Tests

As many pavement structures do not fail by shear, the RLT triaxial tests are considered more representative of actual performance in the road. Nevertheless, the monotonic triaxial compression tests provide valuable parameters that can be used to evaluate strength and stiffness of pavement materials. Furthermore, it is commonly thought that safe stress states for a pavement material are related to their ultimate shear strength.

The monotonic triaxial compression tests were conducted in this study with a strain rate less than 10% strain per hour. This rate was chosen to ensure that no excess pore water was developed during testing. In each test, the sample was loaded to a strain level of one percent, unloaded, and then reloaded to failure. Drained triaxial compression tests were performed under 21 kPa confinement pressures on both unreinforced and reinforced samples. The value of the confinement pressure was chosen to match the field measurement of the lateral confining pressure within the base course layer that was reported in different studies that was discussed in section 2.2.1 of this dissertation. Three replicate samples were tested for each unreinforced and reinforced case to ensure repeatability.

Four response parameters were obtained from each triaxial test to quantitatively evaluate the improvement achieved due to reinforcement inclusion under monotonic loading. The parameters are: the secant elastic moduli at one percent strain level ($E_{s1\%}$), the secant elastic moduli at two percent strain level ($E_{s2\%}$), the ultimate shear strength (USS), and residual shear strength (RSS). These response parameters were chosen to

Figure 3.6 Preparation and Testing of Crushed Limestone Sample

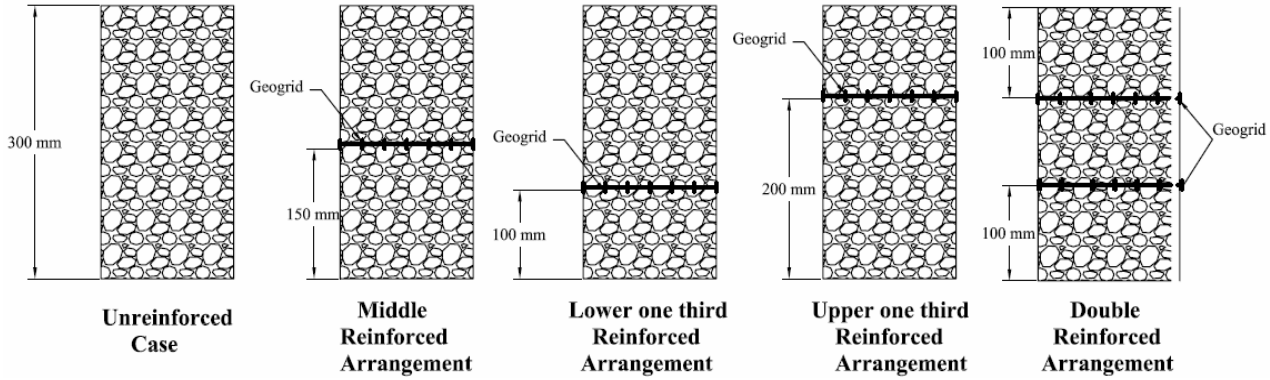

Figure 3.7 Reinforcement Arrangements Investigated in this Study

assess the reinforcement influence on the behavior of the tested material at different strain levels. Improvement factors IM-$E_{s1\%}$, IM-$E_{s2\%}$, IM-USS, and IM-RSS were then determined using the following equation:

$$\text{IM} = \frac{\text{parameter from reinforced sample}}{\text{parameter from unreinforced sample}} \qquad 3.1$$

3.1.4 Repeated Loading Triaxial Tests (RLT) Tests

RLT tests were conducted to determine the properties of granular materials under repeated loading that significantly influence the structural response and performance of base course layers under traffic loading. In these tests, a repeated axial cyclic stress with a haversine-shaped load-pulse and fixed magnitude was applied to 150mm diameter cylindrical samples. The load pulse used in this study has 0.1 sec load duration and 0.9 sec rest period as shown in Figure 3.8. The resilient and permanent deformations (Figure 3.8) of the samples were measured during this test to calculate the resilient and plastic strains, respectively. During a RLT test, cyclic deviator and confining stresses along with vertical deformations were recorded. The difference between the maximum and minimum deformation divided by the length over which this occurs gives the strain. Two types of strains are determined: resilient (elastic); and permanent (plastic). The resilient and permanent strains are defined in Equations 3.2 and 3.3 , respectively.

$$\varepsilon_{r(N)} = \frac{\delta_{res(N)}}{L_0(1-\varepsilon_{p(N-1)})} \qquad 3.2$$

$$\varepsilon_{p(N)} = \frac{\delta_{per(N)}}{L_0(1-\varepsilon_{p(N-1)})} \qquad 3.3$$

Where

L_0 is the original sample length,

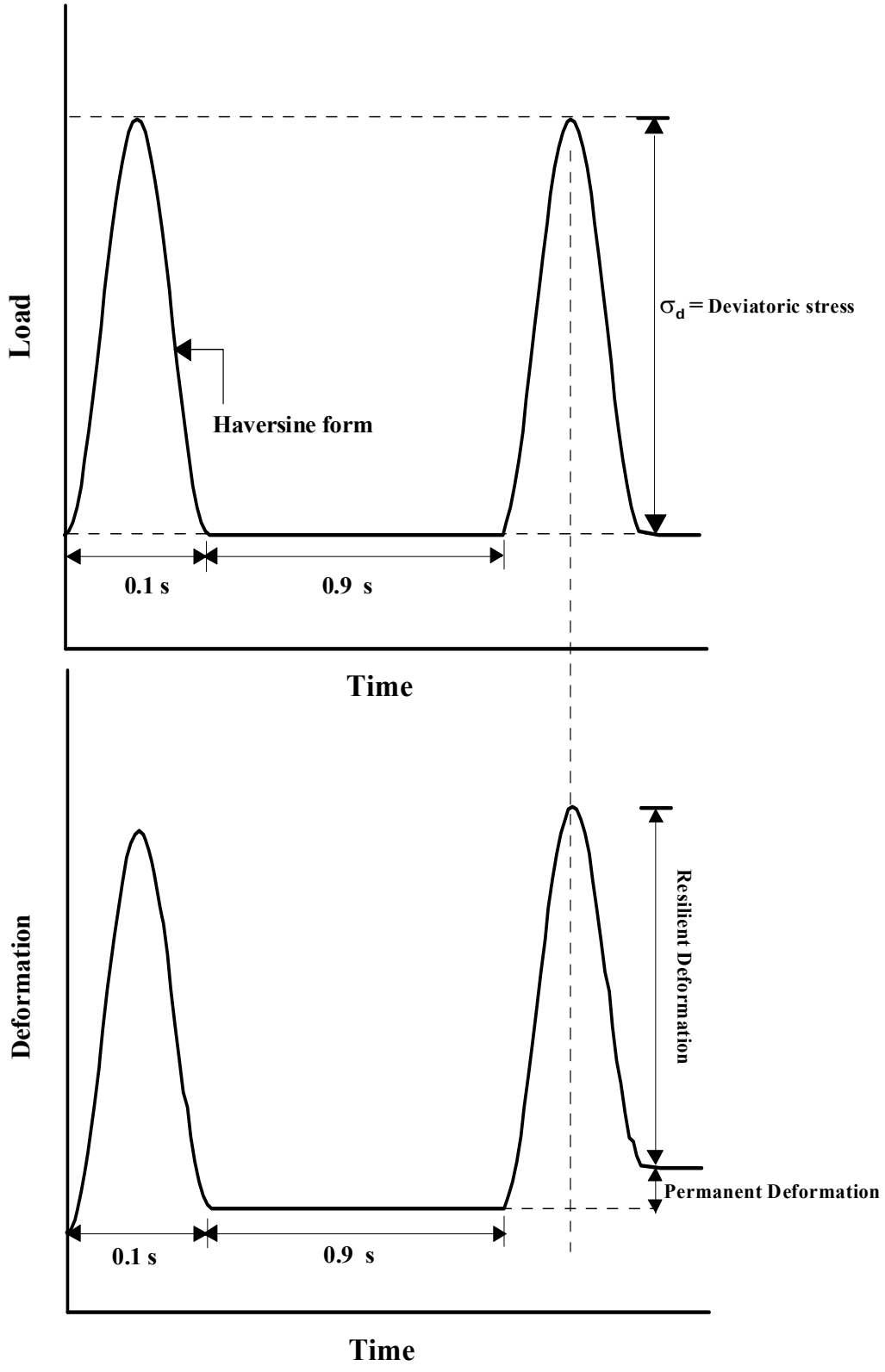

Figure 3.8 Applied Load and Response of Sample in RLT tests

$\delta_{res(N)}$ is thetotal resilient change in sample length at cycle N (mm),

$\delta_{per(N)}$ is the resilient change in specimen length at cycle N (mm/mm),

$\varepsilon_{r(N)}$ is the resilient strain at cycle N (mm/mm), and

$\varepsilon_{p(N)}$ is the permanent strain at cycle N (mm/mm).

Three different types of RLT tests were used in this study. The proceeding sections describe the procedures followed in these tests.

3.1.4.1 Resilient Modulus Tests

Resilient modulus tests were performed in accordance with AASHTO-T307 standard method for determining the resilient modulus of base course material (AASHTO, 2003). In this test method the samples are first conditioned by applying 1,000 load cycles with a deviator stress 93.0 kPa and a confining stress of 103.4 kPa. The conditioning step removes most irregularities on the top and bottom surfaces of the test sample and also suppresses most of the initial stage of permanent deformation. This step is followed by a sequence of loading with varying confining and deviator stresses. The confining pressure is set constant, and the deviator stress is increased. Subsequently, the confining pressure is increased, and the deviator stress varied. The resilient modulus values are calculated at specified deviator stress and confining pressure values as the ratio of the cyclic stress to the measured resilient strain (Equation 3.4). The stress sequences followed in this method are shown in Table 3.4.

$$M_r = \frac{\sigma_{cyc}}{\varepsilon_r} \qquad 3.4$$

Where

σ_{cyc} is the maximum cyclic stress

ε_r is the recoverable elastic strain

Table 3.4 Load Pulse Used In the Resilient Modulus Testing Procedure

Sequence No.	Confining Pressure		Deviator Stress		Number of Load Applications
	kPa	psi	kPa Psi	psi	
0	103	15	93	15	1000
1	21	3	21	3	100
2	21	3	41	6	100
3	21	3	62	9	100
4	34	5	34	5	100
5	34	5	69	10	100
6	34	5	103	15	100
7	69	10	69	10	100
8	69	10	138	20	100
9	69	10	207	30	100
10	103	15	69	10	100
11	103	15	103	15	100
12	103	15	207	30	100
13	138	20	103	15	100
14	138	20	138	20	100
15	138	20	276	40	100

In order to determine the resilient modulus parameters of unreinforced and reinforced samples, the average value of the resilient modulus for each stress sequence was first calculated. A regression analysis was then carried out to fit each test data to the generalized constitutive model given in Equation 3.5, which was adopted by the new Mechanistic-Empirical Design Guide (NCHRP, 2004).

$$M_r = p_a k_1 \left(\frac{\theta}{p_a} \right)^{k_2} \left(\frac{\tau_{oct}}{p_a} + 1 \right)^{k_3} \qquad 3.5$$

where

M_r is the resilient modulus,

p_a is the atmospheric pressure (101.3 kPa),

$\theta = (\sigma_1 + \sigma_2 + \sigma_3)$

$\sigma 1$, $\sigma 2$, $\sigma 3$ are principal stress components (Figure 2.2).

The octahedral shear stress (τ_{oct}) is a measure of the distortional (shear) stress on the material, and is defined as: $\tau_{oct} = \frac{1}{3}\sqrt{(\sigma_1 - \sigma_2)^2 + (\sigma_1 - \sigma_3)^2 + (\sigma_2 - \sigma_3)^2}$

k_1, k_2, and k_3 are the material properties.

3.1.4.2 Single-Stage RLT Tests

Single-Stage RLT tests were performed to determine the permanent and resilient deformations of unreinforced and reinforced crushed limestone samples at different number of load cycles. The tests consisted of conditioning the samples in the same procedure used in the resilient modulus tests. This is followed by applying a 10,000 load cycles at a constant confining pressure of 21 kPa and a peak cyclic stress of 230 kPa. The peak cyclic stress was selected based on finite element analysis that was conducted in this second part of this work and will be discussed later. Tests were stopped after 10,000 load cycles or when the sample reached a permanent vertical strain of 7%. Each cycle consisted of the same load pulse used in resilient modulus tests.

During Single-Stage RLT test, at pre-set regular intervals of loading, vertical deformation was recorded at a frequency of 1000 times per second during load cycle intervals of: 0-10; 50-100; 190-200; 290-300; 390-400; 490-500; 590-600; 690-700; 790-800; 890-900; 990-1000; 1490-1500; 1990-2000; 2490-2500; 2990-3000; 3990-4000; 4990-5000; 7990-8000; 9990-10000. The recorded data were processed in a FORTRAN subroutine code which was written to calculate the permanent and resilient strains.

Based on the results of the single stage tests, the reduction in the vertical permanent strain (RPS) due to geogrid reinforcement was determined at 100; 1,000; 3,000; 5,000; and 10,000 load cycles using the following equation:

$$\text{RPS}\ (\%) = \frac{\text{permanent strain without geogrid} - \text{permanent strain with geogrid}}{\text{permanent strain without geogrid}} \times 100\% \quad 3.6$$

3.1.4.3 Multi-Stage RLT Tests

Multi-stage RLT tests is commonly used to determine the permanent deformation behavior at different stress levels. In this study, these tests were conducted to determine the different shakedown ranges of crushed limestone II material, which was previously discussed in Chapter two.

For multi-stage testing it seemed sensible to simply increase the vertical cyclic stress each time, while keeping the cell pressure constant. Keeping cell pressure constant is common in many RLT standards (CEN 2000; Australia Standards 1995; and AASHTO 1994). For each cell pressure value a new specimen need to be used. However, this testing approach (keeping cell pressure constant) does not adequately cover the full spectra of stresses required to define the shakedown ranges. Furthermore, it is nearly parallel with the static failure line and will take many tests to cross through it, and therefore distinct differences between permanent strain behavior may not occur. Therefore, each multi-stage RLT test included six stages, with a gradually increasing of q/p ratio [q-deviatoric stress equal to σ_1-σ_3; and p-mean confining pressure equal to $(\sigma_1+2*\sigma_3)/3$] applied to the sample by keeping p constant while increasing q**,** such that stress level moves closer (or above) the static failure line. Each stage included applying 10,000 load cycles of the same stress level. Each cycle consisted of the same load pulse used in single-stage RLT tests. Samples were tested at four different values of p: 72, 145,

198, and 240 kPa. This covered the full spectra of stresses in *p-q* stress space for interpolation of permanent strain behavior in relation to stress level. Table 3.5 lists the stress levels at each stage for the different multi-stage RLT tests conducted in this study.

Table 3.5 Stress Level For Multi-Stage RLT Tests

	Test 1		Test 2		Test 3		Test 4	
Stage	p(kPa)	q(kPa)	p(kPa)	q(kPa)	p(kPa)	q(kPa)	p(kPa)	q(kPa)
I	72	43	145	136	198	210	246	324
II	72	91	145	183	198	276	246	381
III	72	120	145	229	198	328	246	422
IV	72	155	145	274	198	397	246	472
V	72	183	145	319	198	473	246	520
VI	72	195	145	350	198	510	246	565

3.2 Numerical Modeling

Numerical models were developed to simulate vehicular load were developed using ABAQUS finite element software package (Hibbitt, 2004) for flexible pavement sections with unreinforced and geogrid reinforced base course layers. These models were used to evaluate the benefits achieved by reinforcing pavement sections in terms of permanent deformations, stresses and strains within the pavement section. The numerical modeling program in this study aimed at investigating the effect of various variables on the design of flexible pavements with reinforced bases. The variables are:

1- The thicknesses of the base course layer

2- Interface-properties

3- The stiffness of reinforcement material

4- The location of the reinforcement material

5- The strength of the subgrade material

The following sections describe the different features of the numerical models used in this study.

3.2.1 Model Geometry

The analysis in this study were conducted using two-dimensional (2D) axisymmetric finite element numerical models. The numerical models included a conventional flexible pavement section consisting of three layers: Asphalt concrete layer (AC), base course aggregate layer, and subgrade layer. Figure 3.9 describes that section.

Eight-noded biquadratic axisymmetric quadrilateral elements were used for the subgrade, base, and asphalt concrete layers, and a three-noded quadratic axisymmetric membrane element were used to model the geogrid reinforcement. The membrane element is the most suitable element to model the geogrid as these elements are formulated to transmit in-plane forces only (no moments) and have no bending stiffness.

To determine the suitable mesh size, a series of finite element analyses were first generated with decreasing element size. Mesh sensitivity was studied to determine the level of fine mesh needed for stable finite element analysis.

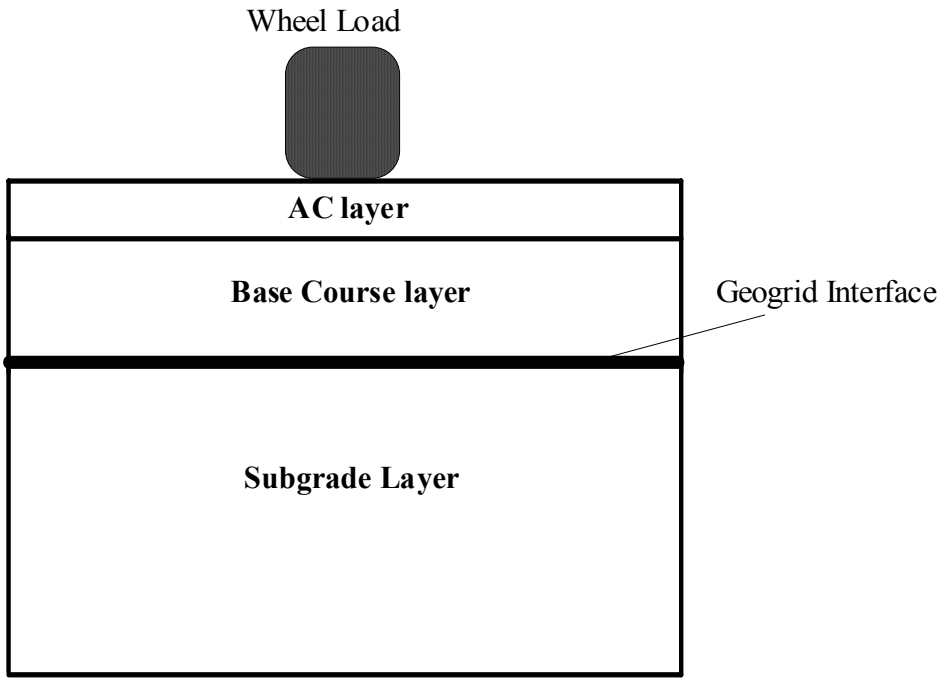

Figure 3.9 The Flexible Pavement Section

3.2.2 Loading Model

The idealized vehicle load that was used in this study consists of 80-kN single wheel axle with a total load on each wheel of 40 kN. The wheel contact pressure is taken to be 550 kPa, which is similar to the contact pressure that was adopted in the finite element analyses for the development of a MEPDG (NCHRP, 2004). Based on that contact pressure the gross contact area for each wheel was calculated to be 726 cm^2.

The wheel load was simulated by applying the contact pressure on a circular area with a radius of 152 cm at the surface. In order to better simulate traffic loads, the load in this finite element analyses was applied in a haversine-shaped form shown in Figure 3.10, such that at time t the load (F) was calculated as:

$$F = \frac{P \cdot \left[1 - \cos\left(\frac{2 \cdot \pi \cdot t}{T}\right)\right]}{2} \qquad 3.7$$

Where

P is the peak pressure (550 kPa in this study)

T is the load cycle total time.

This load simulates the approaching and departing of wheel load of specific point during moving of the wheel load. This load form is not readily available in ABAQUS software package. Therefore, load was defined through a DLOAD user subroutine.

3.2.3 Material Constitutive Models

In order to capture the behavior of different materials in a pavement structure, different constitutive models should be used. The proceeding sections provide description of the different constitutive models that were used in this study to describe the behavior of different materials.

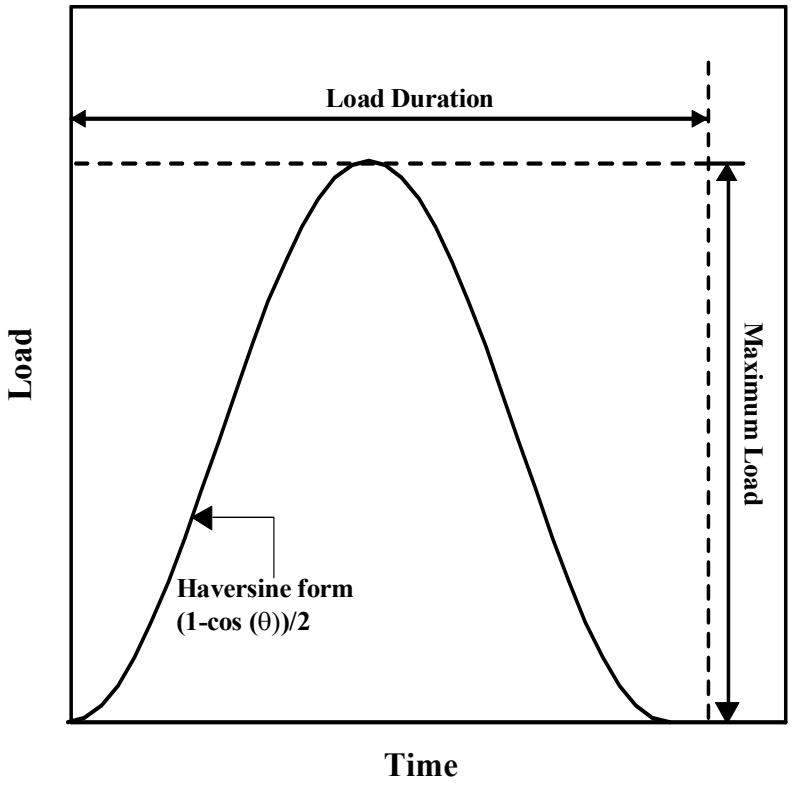

Figure 3.10 Haversine-Shaped Load Form Used In Finite Element Analysis

3.2.3.1 Drucker-Prager Model

For soils and unbound granular materials, unlike metals, there exist a number of yield criteria dependent on the hydrostatic stress component. Recognizing this, Drucker and Prager (1952) extended the well known Von Mises yield condition to include the hydrostatic component of the stress tensor.

The Drucker-Prager plasticity model is an isotropic elasto-plastic model that has been used in many studies in the literature to represent the behavior of granular base course aggregate and cohesive subgrade soils. The model is written in terms of all three stress invariants. It provides for a possibly noncircular yield surface in the deviatoric plane to match different yield values in triaxial tension and compression, associated inelastic flow in the deviatoric plane, and separate dilation and friction angles. The linear Drucker-Prager model given as follows:

$$F = J - p\tan(\beta) - d = 0 \quad 3.8$$

$$J = \frac{1}{2} q_m \left[1 + \frac{1}{K} - \left(1 - \frac{1}{K} \right) \left(\frac{r}{q_m} \right)^3 \right] \quad 3.9$$

Where:

p is mean effective stress,

q_m is the Misses equivalent stress,

β is the slope of the linear yield surface in the p-t stress plane and is commonly referred to as the friction angle of the material,

d is the cohesion of the material, and

K is the ratio of the yield stress in triaxial tension to the yield stress in triaxial compression and, thus, controls the dependence of the yield surface on the value of the intermediate principal stress.

For the linear Drucker-Prager model the ABAQUS general finite element package requires the yield surface to be defined as per the line plotted in Figure 3.11. The angle of the line, β, is inputted directly while the value of d the *q-intercept*" (Figure 3.11) is not used. Instead a value on the yield line, $\sigma_{0c,}$ is used. This value (σ_{0c}) is the yield stress where the confining stress is zero and is also shown in Figure 3.11. Data to define the yield line are conventionally obtained from a series of triaxial constant strain or stress rate failure tests (monotonic shear failure tests) at different confining stresses.

From this plot a straight line is approximated through the data to obtain d the *q intercept* and the angle of the line, β. It can be shown when confining stress is zero in triaxial test conditions, where $\sigma_2=\sigma_3$ that σ_{0c}, required by ABAQUS is calculated using Equation 3.10 .

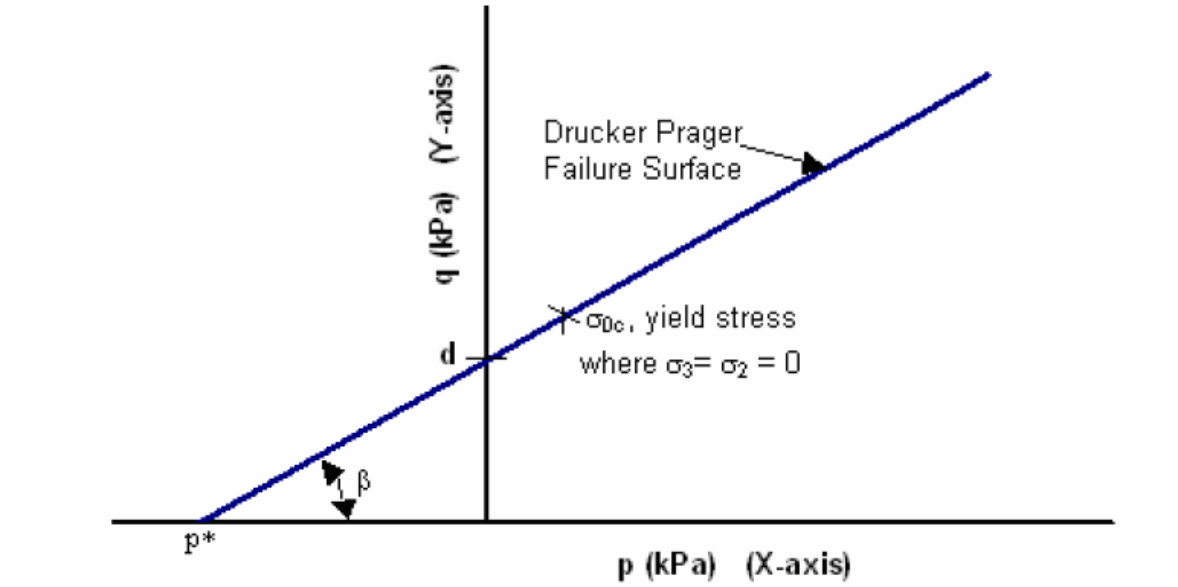

Figure 3.11 Drucker-Prager Yield Condition In p-q Stress Space

$$\sigma_{0c} = \frac{d}{(1 - 1/3\tan\beta)} \tag{3.10}$$

If the experimental data is not readily available, the yield line can be obtained from Mohr-Coulomb friction angle, ϕ, and cohesion, c. From geometry, trigonometry and the relationships between p-q stresses and principal stresses the Mohr-Coulomb failure line can be plotted in p-q space to represent a Drucker-Prager failure criterion. It can be shown that the angle of the failure line in p-q stress space, β, is defined by Equation 3.11 and the q-intercept, d is determined using Equation 3.12 for triaxial test conditions.

$$\tan\beta = \frac{6\sin\phi}{2 - \sin\phi} \tag{3.11}$$

$$d = \frac{6c\sin\phi}{3 - \sin\phi} \tag{3.12}$$

One weakness of the Drucker-Prager yield criterion is that the maximum strength in compression is the same as the maximum strength in extension (ie. for the cases when

$\sigma_1 > \sigma_2 = \sigma_3$ and when $\sigma_1 = \sigma_2 > \sigma_3$) because its yield surface is circular on the plane. That contradicts with the characteristics of granular materials. On the contrary, Mohr-Coulomb does show a difference between them by a hexagonal cross section. Thus, the Drucker-Prager criterion could overestimate the strength in extension of a granular material.

3.2.4 Critical State Two-Surface Plasticity Model

The development of the Manzari-Dafalias model was motivated by the observation that the state parameter ψ defined in the e − ln p space can be used to control the non-associative plastic flow and volumetric expansion within a critical state theoretical framework.

The model formulation proposed by Manzari and Dafalias (1997) combines the concept of bounding surface, where a plastic modulus is determined from the distance between the stress state and an image stress state on the bounding surface, and incorporates the influence of the state parameter $\psi = e - e_c$ on the volumetric response. The bounding surface formulation takes place in a deviatoric stress-ratio space and the parameter ψ is used to define the volumetric response of cohesionless soils. A distinct feature of the model is its capabilities to describe hardening and softening response based on its state and drainage condition. Moreover, using a single set of model parameters the model captures the response of granular materials with different void ratios and confining pressures. A schematic representation of the two-surface model in the n-plane is shown in Figure 3.12.

3.2.4.1 Yield Surface

The yield surface function for this model can be expressed as follows:

$$f(\sigma, \alpha, m) = [\mathbf{r} : \mathbf{r})]^{1/2} - \sqrt{3/2}mp = 0 \qquad 3.13$$

$$\mathbf{r} = (\mathbf{s} - p\boldsymbol{\alpha}) \qquad 3.14$$

s is the deviatoric stress tensor.

$\boldsymbol{\alpha}$ is the deviatoric back-stress ratio tensor describes the kinematic hardening of the yield surface, which indicates the location of the center of the yield surface.

m is the size of the yield surface, which describe the isotropic evolution of the yield surface.

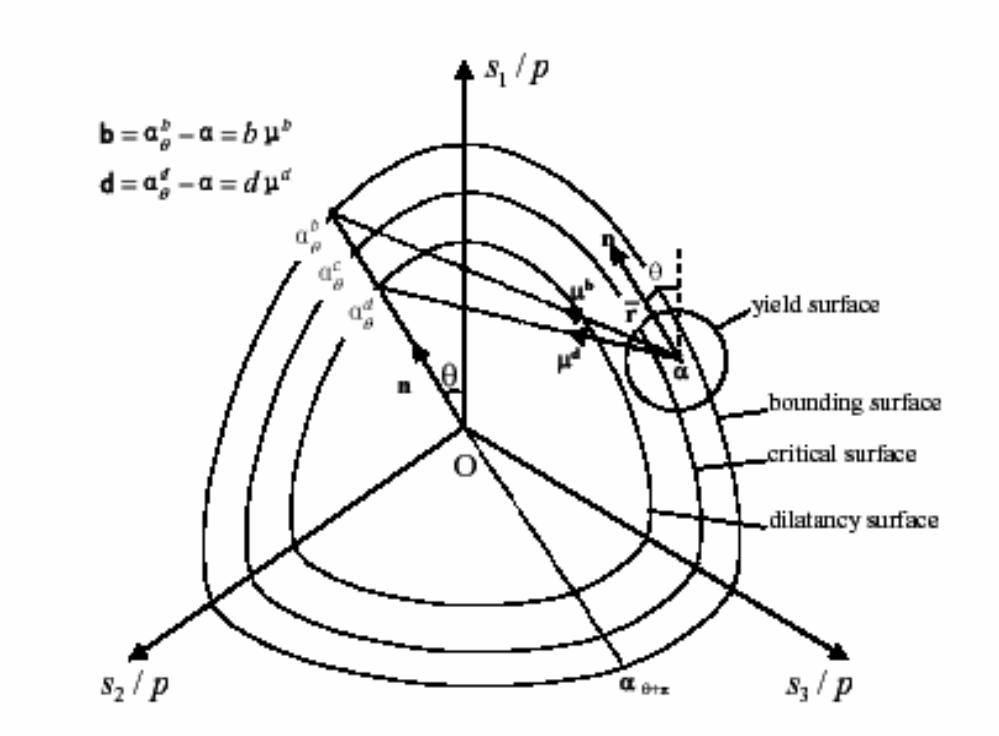

Figure 3.12 Illustration of Yield, Bounding, Critical, and Dilatancy Surfaces (Manzari and Dafalias, 1997)

The yield surface is a cone with circular cross section in the n-plane. The normal to the yield surface, defining the loading direction, is given as:

$$\mathrm{L} = \frac{\partial f}{\partial \sigma} = \mathbf{n} - \frac{1}{3} \cdot N \cdot \mathrm{I} \qquad 3.15$$

$$\mathbf{n} = \frac{\mathbf{r}}{\sqrt{\mathbf{r} : \mathbf{r}}} \qquad 3.16$$

$$N = \boldsymbol{\alpha} : \mathbf{n} + \frac{2}{3} \cdot m \tag{3.17}$$

where

I is the second rank identity tensor.

3.2.4.2 Bounding Surface and Dilatancy Surface

The third invariant of stress tensor has a significant effect on the constitutive behavior of granular soils. The critical strength of granular soil and its tendency for volume change are highly dependent on the direction of the stress path to which the soil is subjected. This can be well characterized by the Lode angle θ defined as:

$$Cos(3\theta) = \frac{3\sqrt{3}}{2}\left(\frac{J_2}{J_3}\right) \tag{3.18}$$

Where, J_2 and J_3 are the second and third invariants of the deviatoric stress tensor:

$\bar{\mathbf{r}} = \frac{\mathbf{r}}{\mathbf{p}}$, and can be defined as:

$$J_2 = \left[\frac{1}{2}\mathrm{tr}\left(\bar{\mathbf{r}}^2\right)\right]^{\frac{1}{2}} \tag{3.19}$$

$$J_3 = \left[\frac{1}{3}\mathrm{tr}\left(\bar{\mathbf{r}}^3\right)\right]^{\frac{1}{3}} \tag{3.20}$$

The bounding surface, dilatancy surface, and critical surface can then be defined in the 3-D space (Figure 3.12) in the following forms which are dependent on the Lode angle θ:

$$\boldsymbol{\alpha}_\theta^a = \sqrt{2/3} \cdot \alpha_\theta^a \cdot \mathbf{n} \qquad (a\text{=b, c, d}) \tag{3.21}$$

$$\alpha_\theta^b = g(\theta, c)M_c + g(\theta, c)k_c^d \left\langle -\psi \right\rangle - m \tag{3.22}$$

$$\alpha_{\theta}^{b} = g(\theta,c)M_c + g(\theta,c)k_c^d \langle -\psi \rangle - m \quad 3.23$$

$$\alpha_{\theta}^{d} = g(\theta,c)M_c + g(\theta,c)k_c^d \psi - m \quad 3.24$$

$$\alpha_{\theta}^{c} = g(\theta,c)M_c - m \quad 3.25$$

The superscript *a* in Equation 3.21 may take three values of b (for bounding surface), c (for critical surface), and d (for dilatancy surface). The above equations involve M_c (the critical stress ratio) and the two model parameters, k_c^b and k_c^d , that are used to define the bounding and dilatancy surfaces on the compression side. In order to complete the definition of these surfaces, it is necessary to define M_e, k_e^b and k_e^d that are the corresponding values on the extension side of these surfaces. Parameters *c*, c_b, and c_d the ratios between the values on the compression side of the above-mentioned surfaces to those on the extension side of these surfaces, that is

$$c = \frac{M_e}{M_c},\ c_b = \frac{k_e^b}{k_c^b}\ c_d = \frac{k_e^d}{k_c^d}$$

The function g(θ, c) which used to generalize the different surface equation from the triaxial space to a 3−D, is defined in the following form:

$$g(\theta,c) = \frac{2c}{(1+c)-(1-c)Cos(3\theta)} \quad 3.26$$

3.2.4.3 Flow Rule

The plastic strain increments is defined using a non-associated flow rule given by :

$$\dot{\varepsilon}^p = \Delta\gamma \frac{\partial \boldsymbol{g}}{\partial \boldsymbol{\sigma}} \quad 3.27$$

$$\frac{\partial \boldsymbol{g}}{\partial \boldsymbol{\sigma}} = \mathbf{n} - \frac{1}{3} D \cdot \mathbf{I} \quad 3.28$$

Where parameter D is known as the dilatancy coefficient and plays a major role in the modeling of the volume change response of the soil. Note that in general $D \neq N$, which leads to a non-associated flow rule. An equation presenting the explicit form of D will be given later.

3.2.4.4 Elastic Moduli

The elastic moduli, K and G, are defined through the following standard relationships:

$$\dot{\mathbf{e}}^{\mathbf{e}} = \frac{\dot{\mathbf{S}}}{2G} \tag{3.29}$$

$$\dot{\varepsilon}_v^e = \frac{\dot{p}}{K} \tag{3.30}$$

Here $\dot{e}^e$ and $\dot{\varepsilon}_v^e$ are, respectively, the elastic components of deviatoric and volumetric strain increments, $\dot{\mathbf{S}}$ and $\dot{p}$ are deviatoric and spherical parts of stress increment tensor. It is assumed that both K and G are functions of current mean effective stress, i.e.

$$G = G_o \left(\frac{p}{p_{atm}} \right)^b \tag{3.31}$$

$$K = K_o \left(\frac{p}{p_{atm}} \right)^b \tag{3.32}$$

Where, K_o and G_o are the bulk and shear modulus, respectively, corresponding to an effective stress equal to atmospheric pressure, p_{atm}. b is a model parameter, normally between 0.5 and 1 for soils.

This assumption results in a hypo-elastic response that is consistent with the stress-strain behavior of granular soils.

3.2.4.5 Hardening Rules

Both isotropic and kinematic hardening rules are used in the critical state two-surface plasticity model have.

3.2.4.5.1 Isotropic Hardening Rule

The evolution equations for the size (m), which represents the isotropic hardening rule, is given as

$$\dot{m} = C_m(1+e_o)\cdot\dot{\varepsilon}_v^p \tag{3.33}$$

$$\dot{\varepsilon}_v^p = \Delta\lambda\cdot D \tag{3.34}$$

$$\Rightarrow \dot{m} = \Delta\lambda\cdot C_m(1+e_o)\cdot D \tag{3.35}$$

Where C_m is a model parameter

3.2.4.5.2 Kinematic Hardening Rule

The kinematic hardening rule is chosen to be similar to the non-linear kinematic rule by Armstrong & Fredrick (1966) with the added advantage of function h. The function h is chosen based on the original proposition by Dafalias and Popov (1976) for two-surface models.

$$\dot{\boldsymbol{\alpha}} = \sqrt{3/2}\cdot h\left[\sqrt{\left(2/3\right)}\cdot\alpha_\theta^b\cdot\dot{\mathbf{e}}^p - \dot{\bar{e}}^p\cdot\boldsymbol{\alpha}\right] \tag{3.36}$$

$$\dot{\bar{e}}^p = \left[\left(2/3\right)\dot{\mathbf{e}}^p : \dot{\mathbf{e}}^p\right]^{1/2} \tag{3.37}$$

$$\dot{\mathbf{e}}^p = \Delta\lambda\cdot\mathbf{n} \tag{3.38}$$

Thus the evaluation of the equation for back stress, $\boldsymbol{\alpha}$, can be written as:

$$\dot{\boldsymbol{\alpha}} = \Delta\lambda\cdot h\cdot\mathbf{b} \tag{3.39}$$

$$\mathbf{b} = (\boldsymbol{\alpha}_\theta^b - \boldsymbol{\alpha}) \tag{3.40}$$

$$h = h_o\frac{|\mathbf{b}:\mathbf{n}|}{b_{ref} - |\mathbf{b}:\mathbf{n}|} \tag{3.41}$$

$$b_{bref} = 2\sqrt{\frac{2}{3}}\alpha_{\theta}^{b} \qquad 3.42$$

Where h_o is model parameter

3.2.4.6 Fabric Tensor

The fabric tensor (**F)** is a macroscopic phenomenological constitutive ingredient. Its main role is to enhance the contractive trend of a constitutive model upon stress reversal following previous dilatational response. It accounts indirectly and in a simple way, for the observed change of contact normal orientation distribution change during dilation and its subsequent effect on contractancy upon reversal. The evolution of the F tensor is given as:

$$\dot{\mathbf{F}} = \Delta\lambda \cdot C_f \langle -D \rangle \left[F_{\max}\mathbf{n} + \mathbf{F} \right] \qquad 3.43$$

Where

C_f and F_{max} are model parameter

3.2.4.7 Dilatancy Coefficient

Based on Rowe's stress-dilatancy theory, and its invariant form suggested by Nova and Wood (1979), it's assumed that the dilatancy coefficient *D* is proportional to the difference between the back-stress ratios.

$$D = A(\boldsymbol{\alpha}_{\theta}^{d} - \boldsymbol{\alpha})\mu^{d} : n = A \cdot \mathbf{d} : \mathbf{n} \qquad 3.44$$

$$A = A_o + (1 + \langle F:n \rangle) \qquad 3.45$$

Here A_0 is a positive model parameter and **F** is the fabric tensor that was defined in the previous section. The tensor $\boldsymbol{\alpha}_{\theta}^{d}$ indicates the image of the current stress state on the dilatancy surface (as defined earlier). The tensor μ^{d} is a unit tensor in the direction of **d=**

$\boldsymbol{\alpha}_{\theta}^{d} - \boldsymbol{\alpha}$ and **n** is the deviatoric part of the unit normal to the yield surface at the current stress state (Figure 3.12).

3.2.4.8 The Critical State Line

The critical state line for this model is given by a straight line in e − ln p space. That is:

$$e_c = (e_c)_{ref} \; -\lambda \cdot \ln\left(\frac{p}{p_{ref}}\right) \qquad 3.46$$

Where

λ is the slope of the critical state line in the e_c-ln (p) plane and

$(e_c)_{ref}$ is the critical void ratio corresponding to a reference mean effective stress, p_{ref} .

3.2.4.9 Normalizing the Unsaturated Behavior

The behavior of granular base materials at unsaturated condition is different and more complex than that of completely saturated or completely dry conditions, because of the difference in compressibility of the pore fluid phases, and due to the internal matric suction caused by the water surface tension. In this study the behavior of base course material is modeled at the optimum field condition, and hence at an unsaturated condition. However, the two surface critical state model is originally derived to predict the behavior of granular soils at completely saturated or completely dry conditions, In addition the model parameters are determined from triaxial tested conducted on completely saturated samples. Therefore, the model was modified based on an approach proposed by Pestana et al. (2002) to normalize the unsaturated response of the base course materials. The modified framework uses an additive approach with the pore air pressure computed using the pore fluid compressibility, and the pore water pressure computed using the matric suction and the pore air pressure. This required the use of a

modified effective stress relation similar to the one that was originally proposed by Bishop (1959), which includes the net normal stress and matric suction (u_a- u_w) as two stress state parameters as shown in Equation 3.47. The used approach has adopted by Craig (1992), Khalili and Khabbaz (1998) and Zienkiewicz et al. (1999).

$$\sigma'_{ij} = \sigma_{ij} - u_a\delta_{ij} + \chi_w(u_a - u_w)\delta_{ij} \quad 3.47$$

$$\sigma'_{ij} = \sigma_{ij} - u_a\delta_{ij} + p_{suc}\delta_{ij} \quad 3.48$$

Where

σ'_{ij} is the effective stress tensor,

σ_{ij} is the total stress tensor,

δ_{ij} is the second order identity tensor,

u_a and u_w are the pore air and pore water pressures,

χ_w is the Bishop parameter,

p_{suc} is the effective suction confinement, and is equal to . Pestana et al. (2002) proposed the following equation to determine $\boldsymbol{p_{suc}}$:

$$p_{suc} = (p_{atm})\frac{\theta}{e}\left(\frac{1}{\theta^{n1}} - \frac{1}{e^{n1}}\right)^{\frac{n3}{n2}} \quad 3.49$$

Where

n_1, n_2, and n_3 are regression parameters,

θ : is the volumetric water content,

p_{at}: is the atmospheric pressure,

e: is the void ratio.

For drained condition the pore air pressures will be zero. While for undrained conditions at constant temperature, Boyle's law can be written as:

$$u_a = \left(u_{a0} + p_{at}\right)\frac{e_0 + (h-1)\theta}{e + (h-1)\theta} - p_{at} \qquad 3.50$$

Where u_{a0} is the initial pore air pressure, e_0 is the initial void ratio, and h is the volumetric coefficient of solubility (approximately 0.02 at 20±C (Moran and Shapiro, 1996)).

Heath et al. (2004) indicated that since u_a is much smaller than p_{suc}, it is likely that the generated pore air pressures can be ignored for all practical pavement engineering purposes, provided that that degree saturation is less than 95%.

3.2.4.10 Parameters

A set of 21 parameters is required to completely define the elastoplastic two-surface critical state model. These parameters can be grouped into four categories:

1. Elastic parameters: The elastic parameters include the Bulk modulus (K_0), poison's ratio (ν), and b parameter that define the non-linear elastic behavior. These parameters are, in general, independent of the applied stress path. Since the elastic parameters must be determined from a purely elastic response, they are obtained from small strain triaxial tests.
2. Critical state parameters: Parameters in this category define the critical state of a soil. They are M_c, M_e, λ ,$e_{c,ref}$ and p_{ref} . M_c, M_e represent the slope of the critical state lines in compression and extension in q − p space, respectively. These parameters can be related to friction angle (ϕ`) using and the following equation:

$$M_c = \frac{6\sin(\phi`)}{3 - \sin(\phi`)} \qquad 3.51$$

$$M_e = \frac{6\sin(\phi`)}{3 + \sin(\phi`)} \qquad 3.52$$

The critical state in *e* versus ln (p) space is defined in terms of λ, $e_{c,ref}$ and p_{ref}. λ represents the slope of the critical state line. $e_{c,ref}$ and p_{ref} represent a reference point in

this line. These parameters are considered to be constants for a given soil regardless of initial stress state and loading condition.

3. Model specific parameters: This category includes parameters that are specific for the two-surface elastoplastic model. These are:

a. Bounding and dilatancy (phase transformation) surface parameters, $k^b_{c,}$ $k^b_{e,}$ $k^d_{c,}$ and $k^d_{e,}$

b. Initial yield surface parameter, m,

c. Hardening parameters, c_m and h_0,

d. Dilatancy parameter, $A_{0,}$

e. Fabric tensor parameters, F_{max} and C_f .

4. Suction parameters: this category include three parameters needed to normalize the unsaturated behavior of the base course material.

All of the aforementioned parameters are obtained by examining results from drained or undrained triaxial tests.

3.2.5 Modified Cam Clay Model

The Cam Clay model was first presented in the literature in 1963 (Roscoe and Schofield 1963). Later, a revised version called the Modified Cam Clay, was introduced by Roscoe and Burland (1968). Both models are elastic-plastic models based on the critical state concept. The Modified Cam Clay model has been used more widely in practice than the Cam Clay model (Wood, 1990).

The Modified Cam-clay model is expressed in terms of three variables: the mean effective pressure p, the deviator stress q, and the specific volume v. The generalized stress components p and, in three dimensions, may be expressed in terms of principal stresses, as follows:

$$p = \frac{1}{3}(\sigma_1 + \sigma_2 + \sigma_3) \qquad 3.53$$

$$q = \frac{1}{\sqrt{2}}\sqrt{(\sigma_1 - \sigma_2)^2 + (\sigma_2 - \sigma_3)^2 + (\sigma_1 - \sigma_3)^2} = \sqrt{3J_2} \qquad 3.54$$

Where J_2 is the second invariant of the effective stress deviator tensor.

The yield function of the modified Cam Clay model corresponding to a particular value p_c of the consolidation pressure has the form shown in equation, and is represented by an ellipse in the q-p plane (Figure 3.13).

$$f = q^2 - M_c{}^2 p\,(pc - p) = 0 \qquad 3.55$$

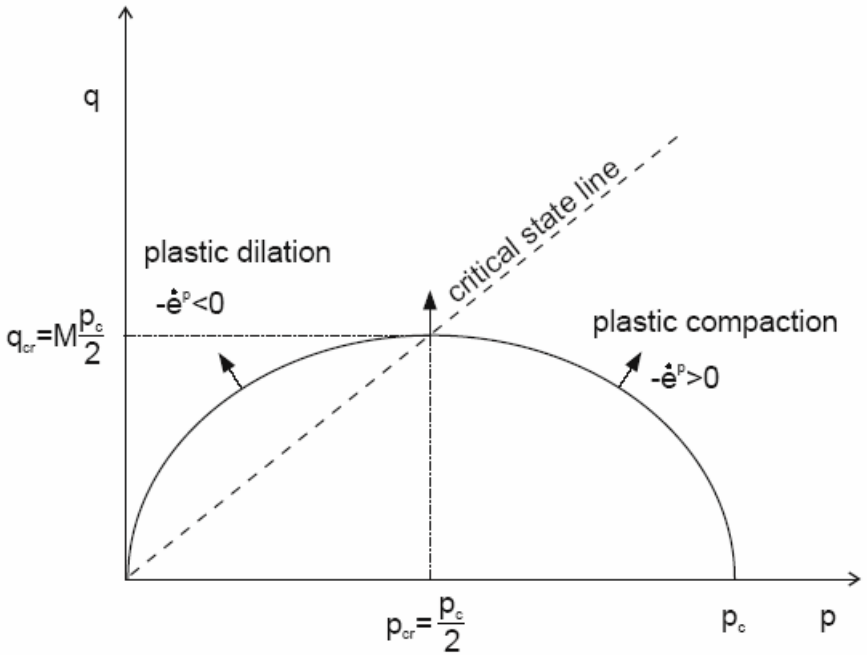

Figure 3.13 Modified Cam Clay yield Surface in p-q plane

In addition to these models, a linear elastic model was used to model the behavior of geosynthetic material. This is acceptable since the induced strain in the geosynthetic is very small (less than 2%) and is considered within the elastic range (Perkins, 2001).

3.2.6 Interface Modeling

The performance of pavement structures is affected by interface conditions between pavement layers. Therefore, finite element analyses should be able to adequately model the behavior of interfaces between pavement layers and geosynthetic material. Different approaches have been developed to study the mechanical behavior of interfaces under certain loading conditions. However, three well known approaches have been mainly used in the literature; namely the zero-thickness interface elements (Goodman et al., 1968), thin-layer interface elements (Desai et al., 1984), and the constraint approach (Katona, 1983) at the nodal level.

In this study the ABAQUS contact interaction feature was used in this study to model the geogrid-soil interface. The ABAQUS contact interaction feature uses the constraint approach to model the interaction between two deformable bodies or between a deformable body and a rigid body in two and three dimensions. With this feature one surface definition provides the "master" surface and the other surface definition provides the "slave" surface. The master surface is used for rigid body surface, while slave surface is used for deformable body surface. The nodes on the slave surface are constrained not to penetrate into the master surface; however, the nodes of the master surface can, in principle, penetrate into the slave surface. After this contact pair is defined, a family of contact elements is automatically generated. At each integration point, these elements construct series measures of clearance and relative shear sliding. These kinematic measures are then used, together with appropriate Lagrange multiplier techniques, to introduce surface interaction theories.

The interaction simulation consists of two components: one normal to the surfaces and one tangential to the surfaces. The interface in the normal direction is

assumed to be "hard contact" and no separation is allowed. While two main conditions were used to describe the interface in the tangential direction. In the first condition, full interlocking was assumed between the geogrid layer and material surrounding it. This was done by using the tie-condition in ABAQUS interaction feature, where each node of the slave surface is tied to the nearest node on the master surface. In the second case, the geogrid interface was described in terms of a Coulomb friction model. The shear stress versus shear displacement relationship for this case is shown schematically in Figure 3.14. The relationship has an elastic region whose slope, $G_{I,}$ is governed by a parameter E_{slip}.

The peak shear stress is a function of the normal stress and is governed by a friction coefficient μ. Values of E_{slip} and μ are constant for an interface, meaning that the slope of the elastic part of the $\tau - \Delta$ curve is a function of both E_{slip} and μ. The slope of the elastic portion of the $\tau - \Delta$ curve is expressed by an interface shear modulus, $G_{I,}$, which has units of kPa/m or force/distance^3. The value of G_I can be expressed by Equation , which shows the dependency on the parameters E_{slip} and μ, and the normal stress on the interface, σ_n .

$$G_I = \frac{\tau_{max}}{E_{slip}} = \frac{\mu\sigma_n}{E_{slip}} \qquad 3.56$$

3.3 Statistical Analysis Techniques

Different statistical techniques were used in this dissertation to analyze the results of experimental and numerical modeling programs. All statistical analyses were conducted using Statistical Analysis Software (SAS) package. The Different statistical methods included: analysis of variance (ANOVA) analyses, Post ANOVA Least Square Means (LSM) analysis, and simple and multiple linear regression analysis. The following sections describe the theoretical background of these methods.

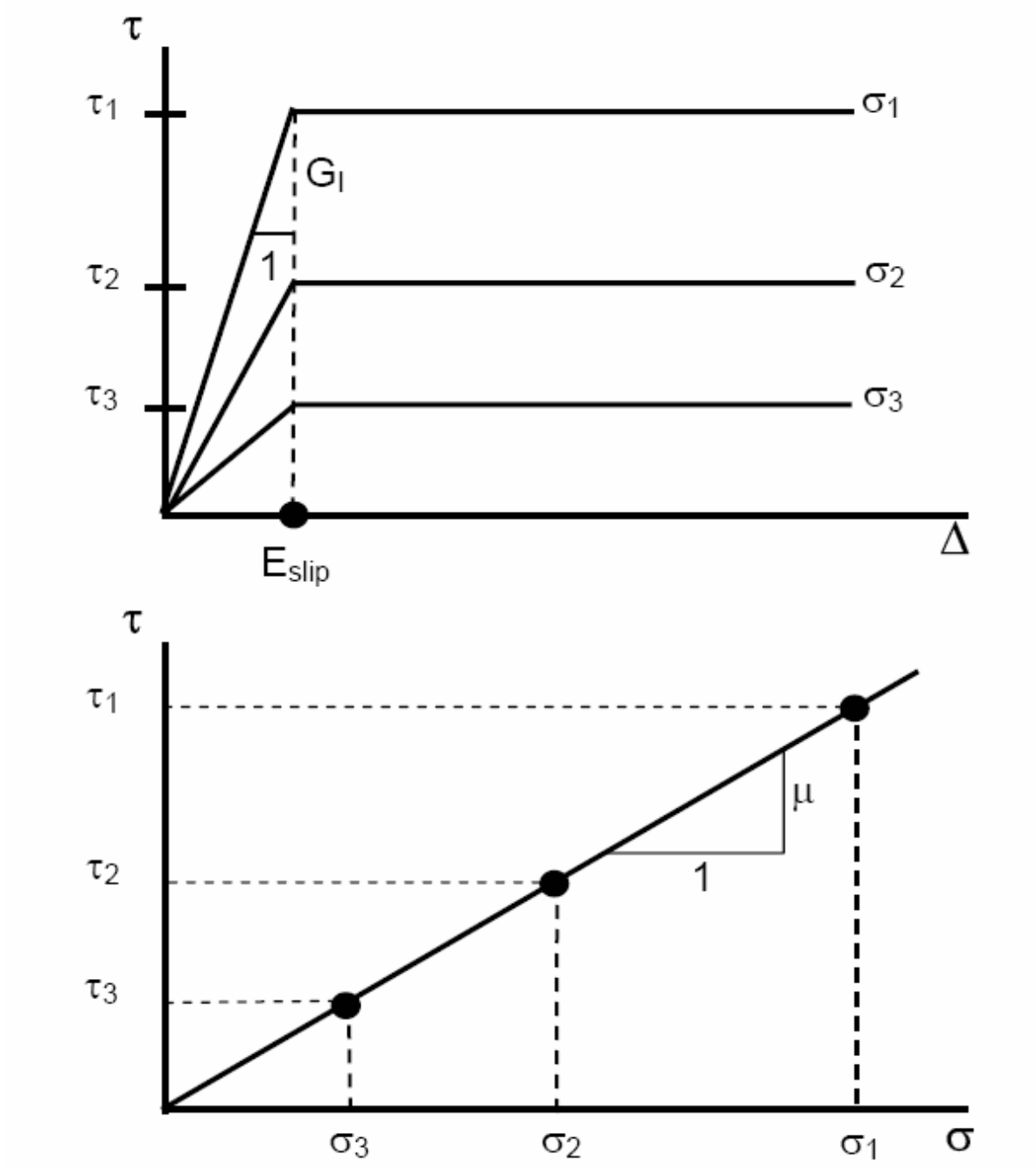

Figure 3.14 Schematic of the Coulomb interface friction

3.3.1 Analysis of Variance

Analysis of variance (ANOVA) is used to identify sources of variability from one or more potential sources, sometimes referred to as "treatments" or "factors." The ANOVA analysis performs a comparison of the means of a number of replications of experiments performed where a single or multiple input factors are varied at different settings or levels. The object of this comparison is to determine the proportion of the variability of the data that is due to the different treatment levels or factors as opposed to variability due to random error. The model deals with specific factors' levels and is involved with testing the null hypothesis $H_0 : \mu_1 = \mu_2 = \ldots \mu_\alpha$ where μ_i represents the level mean. Basically, rejection of the null hypothesis indicates that variation in the output is due to variation between the factor levels and not due to random error. In this study the rejection of the null hypothesis was based on significance level of 95% (p-value of less than 0.05)

If the null hypothesis is rejected, then there is a difference between the output of the different levels. In this case, the post ANOVA- Least Square Means (LSM) is used to determine between which factor levels the actual differences lie. The post ANOVA-LSM analyses compare the least square means of the different levels of each factor. In this study Saxton's macro was implemented in SAS software to present the results of the post ANOVA- LSM analyses in a format that is easy to read and interpret.

The ANOVA analysis can be classified in two main types based on the number of factors investigated, this include: One way and factorial ANOVA. In one way ANOVA only a single factor is investigated, while if multiple factors are used the analysis is called factorial ANOVA. Different models for ANOVA can be used depending on experimental design used. In this study, Completely Randomized Design (CRD) model was used.

3.3.2 Regression Analysis

The general purpose of simple or multiple regression is to learn more about the relationship between one or more independent or predictor variables and a dependent or criterion variable. Simple linear regression is used to examine the linear relationship between two variables. The value of the response, or dependent, variable (y) is expected to change linearly with the value of the independent variable(x). The regression equation is written as

$$Y=b_0+b_1X \tag{3.57}$$

Where b_0 is the y-intercept of the regression line and b_1 is the slope. These are generally referred to as the regression parameters.

Multiple regression allows us to make inferences and predictions about a dependent variable based on information about a number of independent variables, rather than just one. The linear model for multiple regression is

$$Y = b_0 + b_1X_1 + ... + b_pX_p \tag{3.58}$$

Where *p* is the total number of independent (predictor) variables (X's) included in the model. The assumptions are basically the same as those for simple linear regression, but the interpretations are much different.

The goodness of the regression models is usually tested through the coefficient of determination, R^2, and the square root of the mean square errors (RMSE). The R^2 represents the proportion of variation in the dependant variable that is accounted by the regression model and has values from 0 to 1. If it is equal to one, the entire observed points lie on the suggested least square line, which means a perfect correlation exists. While the RMSE represent the standard error of the regression model.

The goal of multiple regression is often to determine which independent variables are important in predicting values of the dependent variable. The ideal multiple regression model in this context provides the best possible fit while using the fewest possible parameters. Different the selection methods can be used to determine 'best' model for the data.

Backward variable selection starts with the full model and removes one variable at a time based on a user-defined selection criteria. In SAS, the default is to remove the variable with the least significant F-test for Type II sum square error. Then the model is refit and the process is repeated. When all of the statistical tests are significant (i.e. none of the parameters are zero), the reduced model has been chosen. The default level of significance for this method is 0.10, rather than the 0.05 we usually use.

Forward selection fits all possible simple linear models, and chooses the best (largest F statistic) one. Then all possible 2-variable models that include the first variable are compared, and so on. The problem with this method is that once chosen, a variable remains in the model, even if it becomes non-significant.

Stepwise selection works in much the same way as forward selection, with the exception that the significance of each variable is rechecked at each step along the way and removed if it falls below the significance threshold. In this study the stepwise selection method is used.

Finally, the R^2 selection method reports R^2 and RMSE for all possible models. Such that, the differences between the models are compared, and the best model with highest R^2 and lowest RMSE is selected.

Chapter Four
Analysis and Results of Experimental Testing Program

This chapter presents the results of the experimental testing program that was conducted to characterize the behavior of the geogrid reinforced base course materials under static as well as cyclic loading.

4.1 Triaxial Compression Test

The following sections present the results of triaxial compression tests that were conducted using the procedure described in Chapter three of this dissertation.

4.1.1 Crushed Limestone I

Drained triaxial compression tests were conducted on unreinforced crushed limestone I and samples reinforced with geogrid types I through V. For each geogrid type, the middle, lower one third, upper one third, and double arrangements were investigated. The achieved dry unit weight and moisture content of the tested samples were close to those specified in the field for construction of base course layers in Louisiana, which specifies that the materials should be mixed at the optimum moisture content and compacted to 95% of the maximum dry unit weight as determined in standard Proctor test.

Figure 4.1 through Figure 4.5 present the average stress-strain curves obtained from the drained triaxial compression tests conducted on unreinforced samples and samples reinforced with geogrid types I through V, respectively. The figures show that at the tested confining pressures and dry unit weight the samples behaves as a loose granular material, such that they exhibit an increase in shear strength with increasing strain, which is referred to as strain hardening, and eventually they stabilize at strain level of about 4%. It is clear that the inclusion of geogrid reinforcement layer(s) substantially

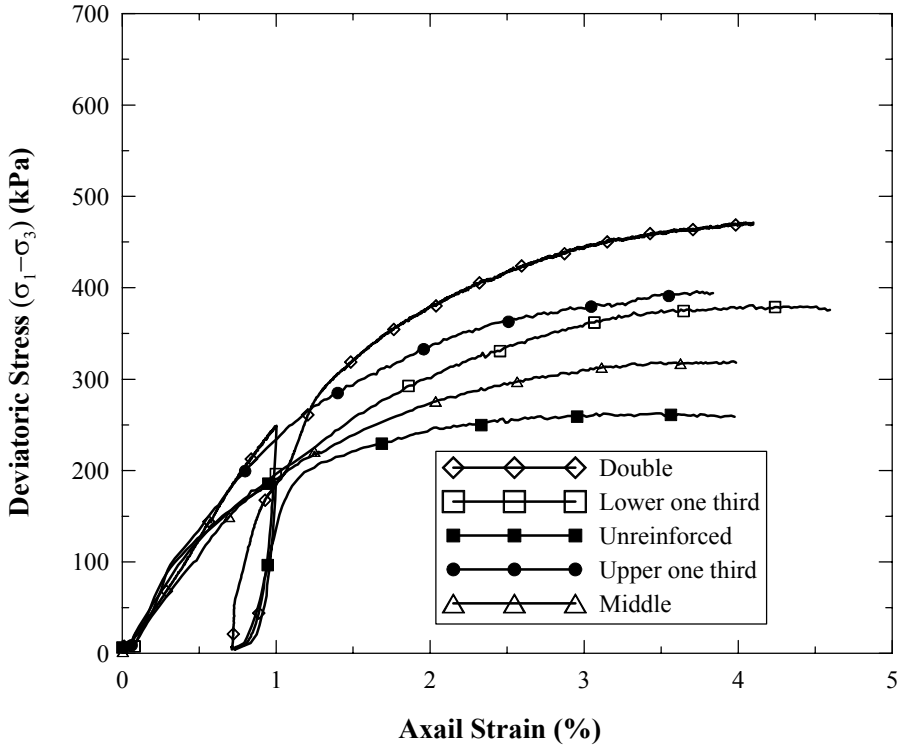

Figure 4.1 Stress-Strain Curves for Crushed Limestone I Samples Reinforced with Geogrid Type I

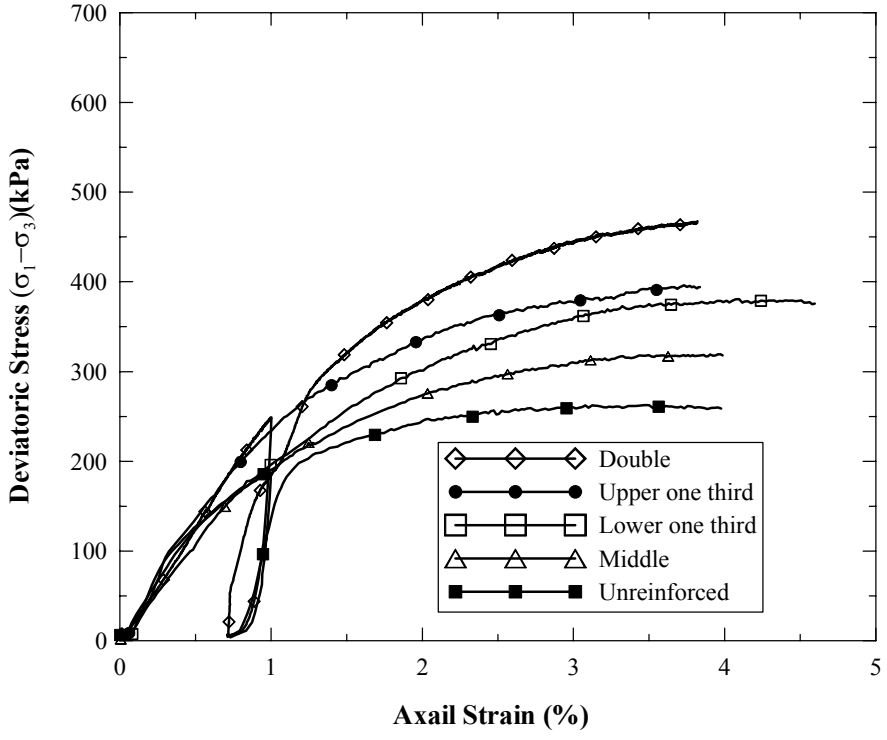

Figure 4.2 Stress-Strain Curves for Crushed Limestone I Samples Reinforced with Geogrid Type II

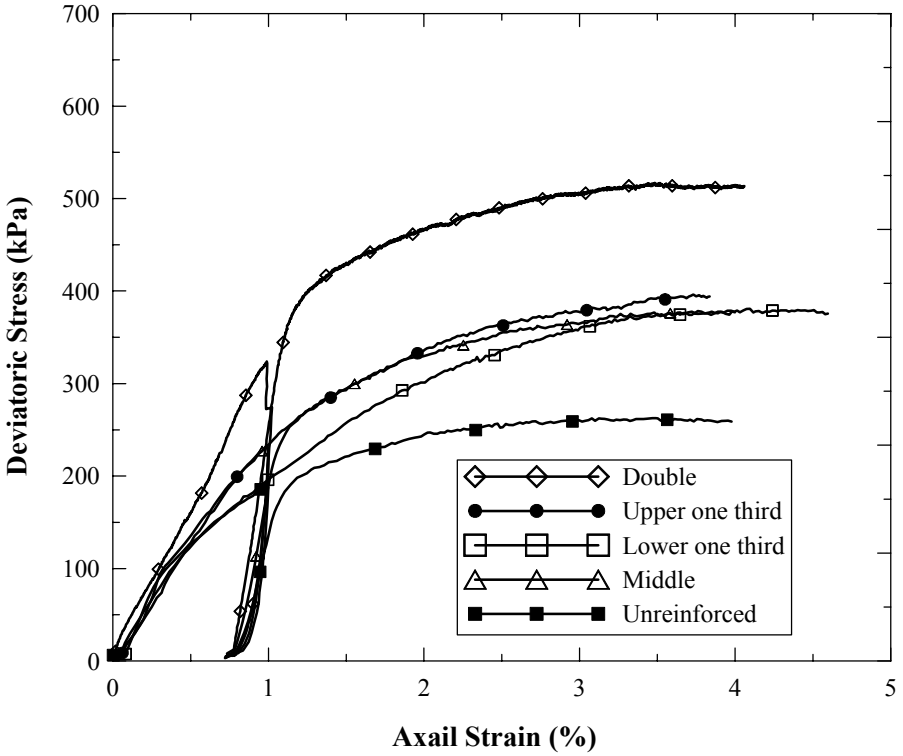

Figure 4.3 Stress-Strain Curves for Crushed Limestone I Samples Reinforced with Geogrid Type III

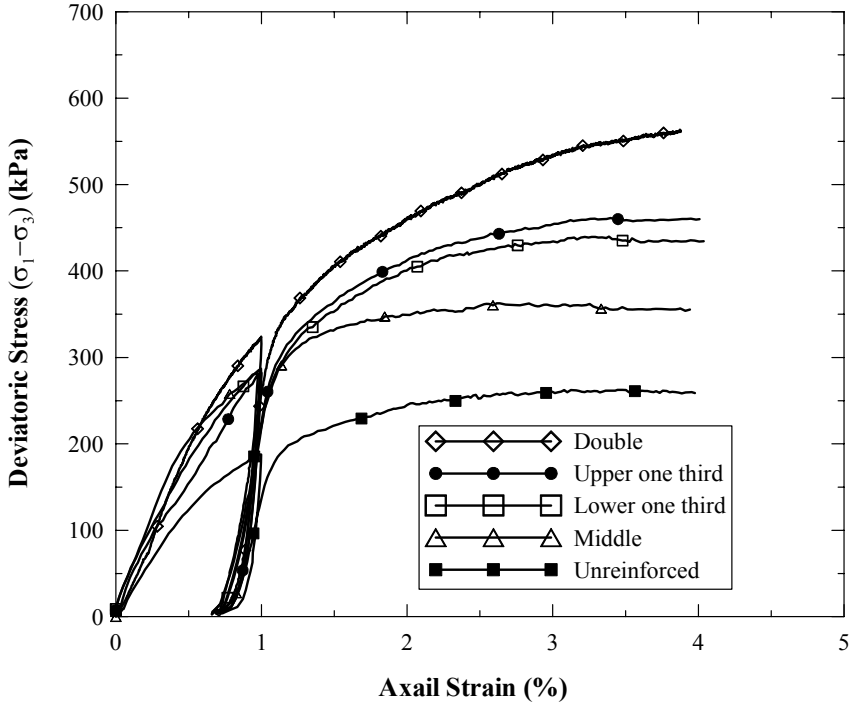

Figure 4.4 Stress-Strain Curves for Crushed Limestone I Samples Reinforced with Geogrid Type IV

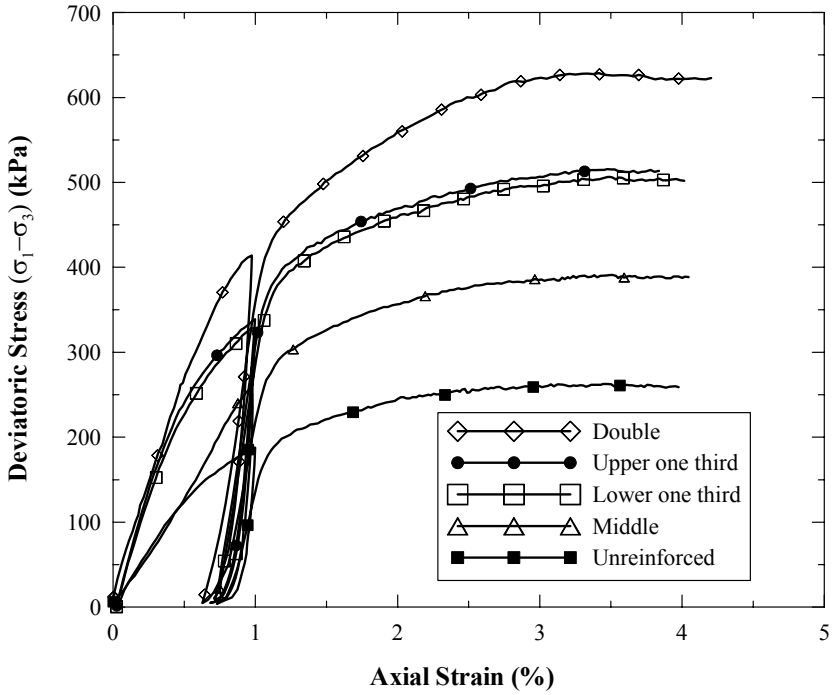

Figure 4.5 Stress-Strain Curves for Crushed Limestone I Samples Reinforced with Geogrid Type V

improved the strength and stiffness of the crushed limestone material. This improvement was more pronounced at strain levels greater than one percent.

Figure 4.6 through Figure 4.8 present the average improvement factors, described in chapter three, and the standard deviation values obtained for each reinforced case. The improvement factor for residual strength was not calculated for this material since the residual and ultimate shear strengths had similar values. The figures show that the improvement in all three parameters (IM-Es1%, IM-Es1%, and IM-USS) depends on the type, location, and number of geogrid layers. It is also noted that the improvement increases with increasing the geogrid stiffness. In addition, the double arrangement had the maximum improvement. The figures also show that the improvement was more appreciable in the Es2% and USS than those in Es1%, and the maximum improvement was detected in the USS. The IM-Es1% ranged from 0.95 to 1.82, the IM-Es2% ranged from 0.99 to 2.32, and IM-USS ranged from 1.163 to 2.42.

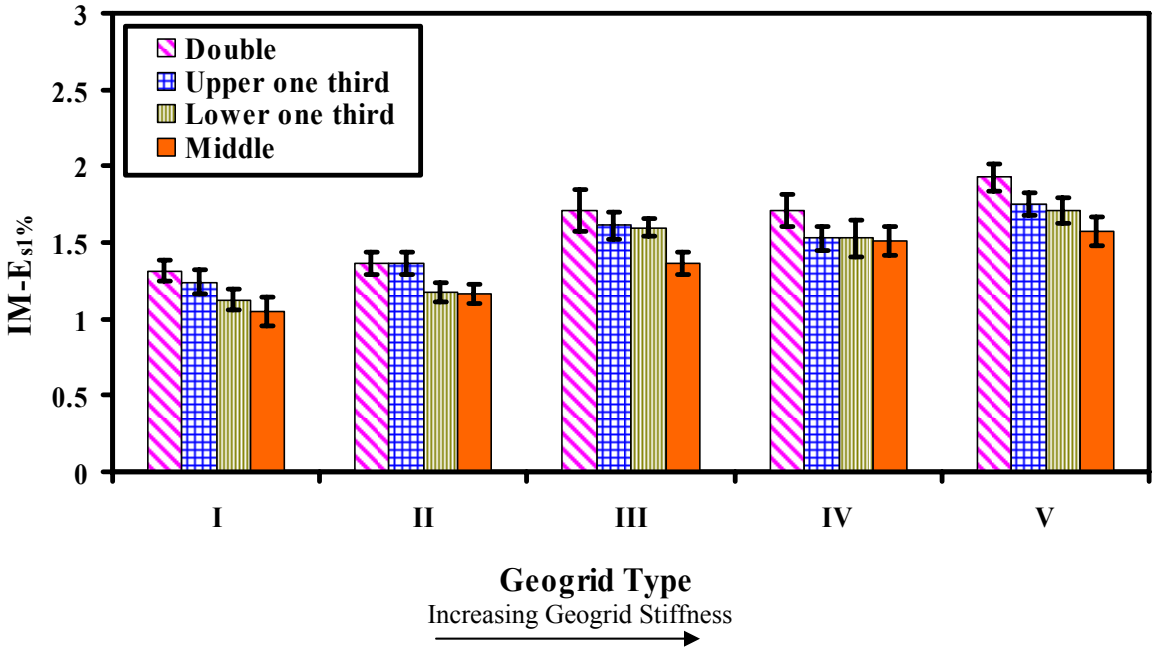

Figure 4.6 Improvement Factor IM-$E_{s1\%}$, for Reinforced Crushed Limestone I Samples

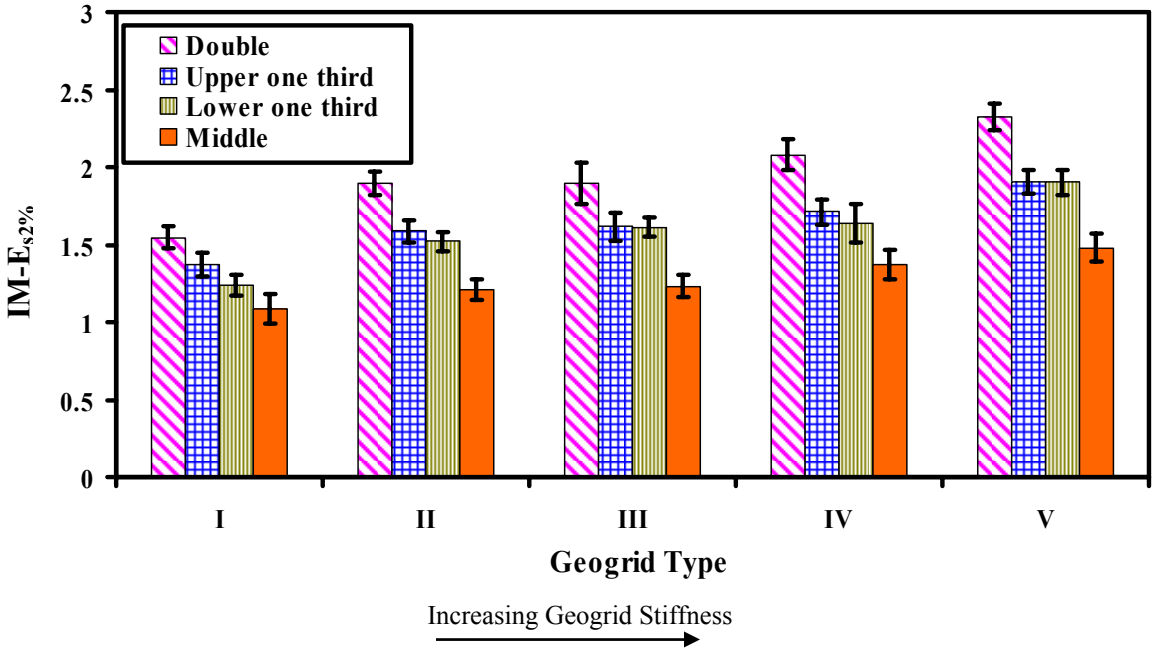

Figure 4.7 Improvement Factor IM-$E_{s2\%}$, Reinforced Crushed Limestone I Samples

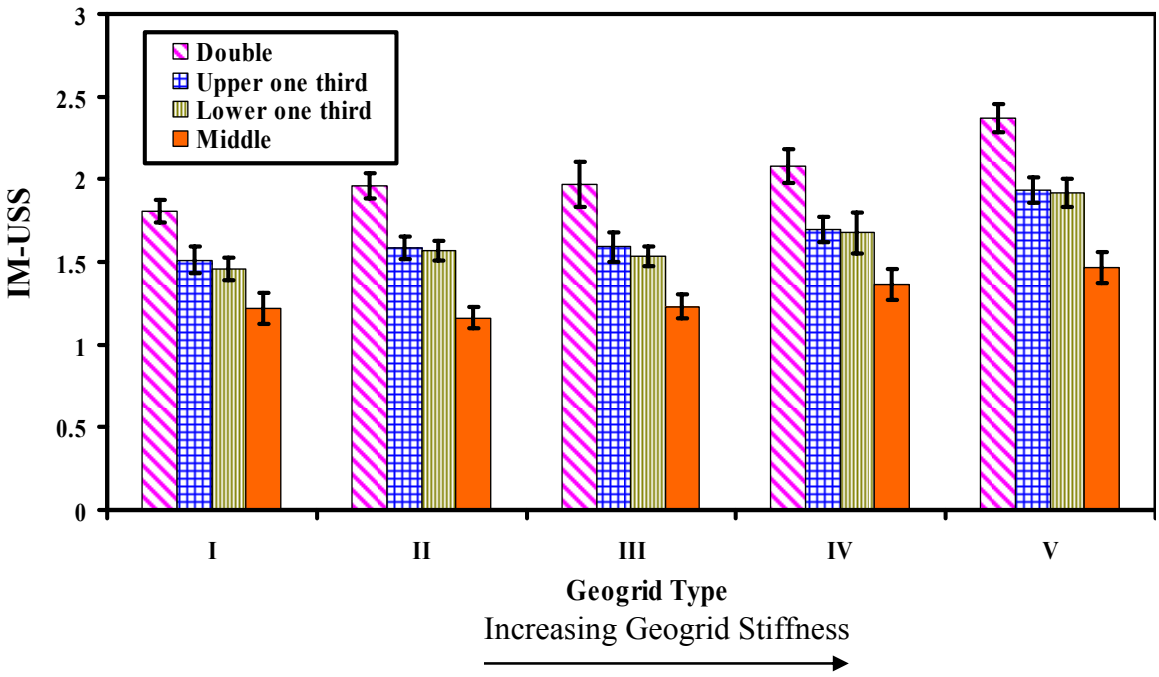

Figure 4.8 Improvement Factor IM-USS for Reinforced Crushed Limestone I Samples

Statistical analysis of variance (ANOVA) was conducted to assess the effects of geogrid type and arrangement on the IM-$E_{s1\%}$, IM-$E_{s2\%}$, and IM-USS obtained from the drained triaxial compression tests. The linear model used in these analyses was a completely randomized factorial design (geogrid arrangements × geogrid types), as shown in the following equation:

$$Y_{ijk} = \mu + \tau_{1i} + \tau_{2j}\ \tau_1\tau_{2ij} + \varepsilon_{ijk} \qquad 4.1$$

where, μ is the overall mean; τ_{1i} is the effect of geogrid arrangement; τ_{2j} is the effect of geogrid type; $\tau_1\tau_{2ij}$ is effect of the interaction between the geogrid arrangement and type; ϵ_{ijk} is the random sampling variation for observation k, at any location case and stiffness level ij; and Y_{ijk} is the dependent variable.

The results of the ANOVA analysis are presented in Table 4.1. It is noted that, at a 95% confidence level, the geogrid type and arrangement had significant effect on the IM-$Es_{1\%}$, IM-$Es_{2\%}$, and IM-USS. The geogrid type had more significant effect on IM-

$Es_{1\%}$ than the geogrid arrangement, while the geogrid arrangement affected more significantly the IM-$Es_{2\%}$, and IM-USS, as indicated by the F-value. The interaction effect of the geogrid type-geogrid arrangement ($\tau_1\tau_{2ij}$) had significant effect only on the IM-$Es_{2\%}$, and IM-USS. The significance of interaction indicates that the behaviors of the two main effects (geogrid type and arrangement) are inconsistent; which means that they do not increase and decrease by the same rate.

Table 4.1 ANOVA Results for IM-$Es_{1\%}$, IM-$Es_{2\%}$, and IM-USS

Type III Tests of Fixed Effects for IM-$Es_{1\%}$				
Effect	Num DF	Den DF	F Value	Pr > F
Geogrid Type	4	40	139.34	<.0001
Geogrid arrangement	3	40	43.19	<.0001
Interaction	12	40	1.91	0.0625
Type III Tests of Fixed Effects for IM-$Es_{2\%}$				
Effect	Num DF	Den DF	F Value	Pr > F
Geogrid Type	4	40	209.38	<.0001
Geogrid arrangement	3	40	394.00	<.0001
Interaction	12	40	3.07	0.0038
Type III Tests of Fixed Effects for IM-USS				
Effect	Num DF	Den DF	F Value	Pr > F
Geogrid Type	4	40	133.99	<.0001
Geogrid arrangement	3	40	563.00	<.0001
Interaction	12	40	3.04	0.0040

Based on the result of the ANOVA analyses, post ANOVA Least Square Means (LSM) analyses were conducted to compare the effect of all the different geogrid types and arrangements on the IM-$Es_{1\%}$, IM-$Es_{2\%}$, and IM-USS. Tukey adjustment was used in this analysis since it provides tests for all pair wise comparisons at a well balance of the type I and type II errors when compared to other adjustments available (SAS Institute Inc,

2004). The results of the post ANOVA-LSM analyses are presented in Table 4.2 through Table 4.4. In these tables the groups are listed in descending order from the best improvement to the worst, and groups with same letter next to them are not significantly different. Table 4.2 presents the grouping of the geogrid type effect on IMEs$_{1\%}$, IM-Es$_{2\%}$, IM-USS. The maximum and minimum improvements were achieved when using geogrids types V and I, respectively. These two geogrid types have the highest and the lowest stiffness, respectively. The effects of geogrid types III and IV on IM-E$_{s1\%}$ were not statistically different from each other. However, the effect of geogrid type III on IM-Es$_{2\%}$ and IM-USS was significantly different from geogrid type IV but not from geogrid type II.

Table 4.2 Grouping of Geogrid Type Effect on IM-Es$_{1\%}$, IM-Es$_{1\%}$, and IM-USS

Dependent Variable	Geogrid Type	Estimate	Standard Error	Letter Group
IM-Es$_{1\%}$	Type V	1.7413	0.01978	A
	Type III	1.5705	0.01978	B
	Type IV	1.5681	0.01978	B
	Type II	1.2658	0.01978	C
	Type I	1.1817	0.01978	D
IM-Es$_{2\%}$	Type V	1.9013	0.01532	A
	Type IV	1.6640	0.01532	B
	Type III	1.5888	0.01532	C
	Type II	1.5526	0.01532	C
	Type I	1.2847	0.01532	D
IM-USS	Type V	1.9215	0.01438	A
	Type IV	1.7038	0.01438	B
	Type III	1.5810	0.01438	C
	Type II	1.5682	0.01438	C
	Type I	1.4986	0.01438	D

Table 4.3 Grouping of Geogrid Arrangement Effect on IM-$Es_{1\%}$, IM-$Es_{1\%}$, and IM-USS

Dependent Variable	Geogrid Arrangement	Estimate	Standard Error	Letter Group
IM-$Es_{1\%}$	Double Layers	1.6049	0.01769	A
	Upper one third	1.4993	0.01769	B
	Lower one third	1.4286	0.01769	C
	Middle	1.3291	0.01769	D
IM-$Es_{2\%}$	Double Layers	1.9187	0.01371	A
	Upper one third	1.6378	0.01371	B
	Lower one third	1.5813	0.01371	C
	Middle	1.2554	0.01371	D
IM-USS	Double Layers	2.0358	0.01286	A
	Upper one third	1.6633	0.01286	B
	Lower one third	1.6302	0.01286	B
	Middle	1.2892	0.01286	C

Table 4.3 presents the grouping of the effect of geogrid arrangement on the IM-$Es_{1\%}$, IM-$Es_{2\%}$, and IM-USS. The highest benefit was achieved when the double arrangement was used; while the lowest benefit was observed for the middle arrangement. In addition, the upper and lower one third arrangement effects on IM-USS were not statistically significant from each other.

Finally, Table 4.4 and Table 4.5 present the grouping of the effect of geogrid arrangement-type interaction on IM-$Es_{2\%}$, and IM-USS factors. The tables show that the location-stiffness interactions in groups A and B are the only significantly different from all other interactions. It is interesting to notice that these two groups represent samples reinforced with two reinforcement layers of geogrid types V and IV.

Table 4.4 Grouping of the Geogrid Type-Arrangement Interaction Effect on IM-$Es_{2\%}$

Geogrid Arrangement	Geogrid Type	Estimate	Standard Error	Letter Group
Double Layers	Type V	2.3231	0.03065	A
Double Layers	Type IV	1.9361	0.03065	B
Upper one third	Type V	1.9018	0.03065	B
Lower one third	Type V	1.9010	0.03065	B
Double Layers	Type III	1.8953	0.03065	B
Double Layers	Type II	1.8915	0.03065	B
Upper one third	Type IV	1.7108	0.03065	C
Lower one third	Type IV	1.6377	0.03065	CD
Upper one third	Type III	1.6152	0.03065	CD
Lower one third	Type III	1.6117	0.03065	CD
Upper one third	Type II	1.5877	0.03065	CD
Double Layers	Type I	1.5473	0.03065	CD
Lower one third	Type II	1.5220	0.03065	DE
Middle	Type V	1.4794	0.03065	DE
Upper one third	Type I	1.3733	0.03065	EF
Middle	Type IV	1.3714	0.03065	EF
Lower one third	Type I	1.2343	0.03065	F
Middle	Type III	1.2331	0.03065	F
Middle	Type II	1.2093	0.03065	F
Middle	Type I	0.9838	0.03065	G

4.1.2 Crushed Limestone II

Drained triaxial compression tests were also conducted on unreinforced crushed limestone II samples and samples reinforced with geogrid types II, IV, and V. For each geogrid type, the middle, upper one third, and double arrangements were investigated. Samples were prepared at the optimum field conditions specified for construction of base course layers in Louisiana. Figure 4.9 through Figure 4.11 present the stress-strain curves obtained from the triaxial compression tests conducted on unreinforced and reinforced

crushed limestone II samples. A dense granular material behavior for the samples was detected. Dense granular materials exhibit an increase in the shear stress with strain increase until reaching an ultimate (peak) shear stress. Beyond the peak stress, they demonstrate strain softening behavior where the shear stress decrease with the strain

Table 4.5 Grouping of the Geogrid Type-Arrangement Interaction Effect on IM-USS

Geogrid Arrangement	Geogrid Type	Estimate	Standard Error	Letter Group
Double Layers	Type V	2.3676	0.02877	A
Double Layers	Type IV	2.0781	0.02877	B
Double Layers	Type III	1.9704	0.02877	BC
Double Layers	Type II	1.9564	0.02877	BCD
Upper one third	Type V	1.9335	0.02877	BCD
Lower one third	Type V	1.9175	0.02877	CD
Double Layers	Type I	1.8067	0.02877	DE
Upper one third	Type IV	1.6947	0.02877	EF
Lower one third	Type IV	1.6772	0.02877	EFG
Upper one third	Type III	1.5896	0.02877	FGH
Upper one third	Type II	1.5870	0.02877	FGH
Lower one third	Type II	1.5669	0.02877	FGH
Lower one third	Type III	1.5354	0.02877	GH
Upper one third	Type I	1.5117	0.02877	HI
Middle	Type V	1.4675	0.02877	HI
Lower one third	Type I	1.4540	0.02877	HI
Middle	Type IV	1.3655	0.02877	IJ
Middle	Type III	1.2285	0.02877	JK
Middle	Type I	1.2221	0.02877	JK
Middle	Type II	1.1626	0.02877	K

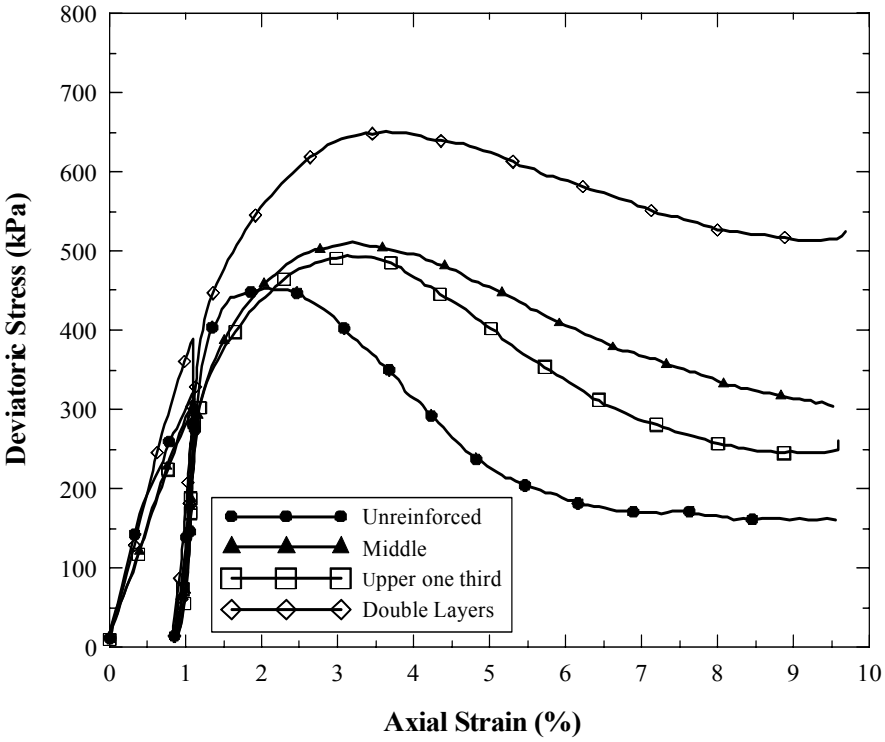

Figure 4.9 Stress-Strain Curve for Crushed Limestone II Samples Reinforced with Geogrid Type II

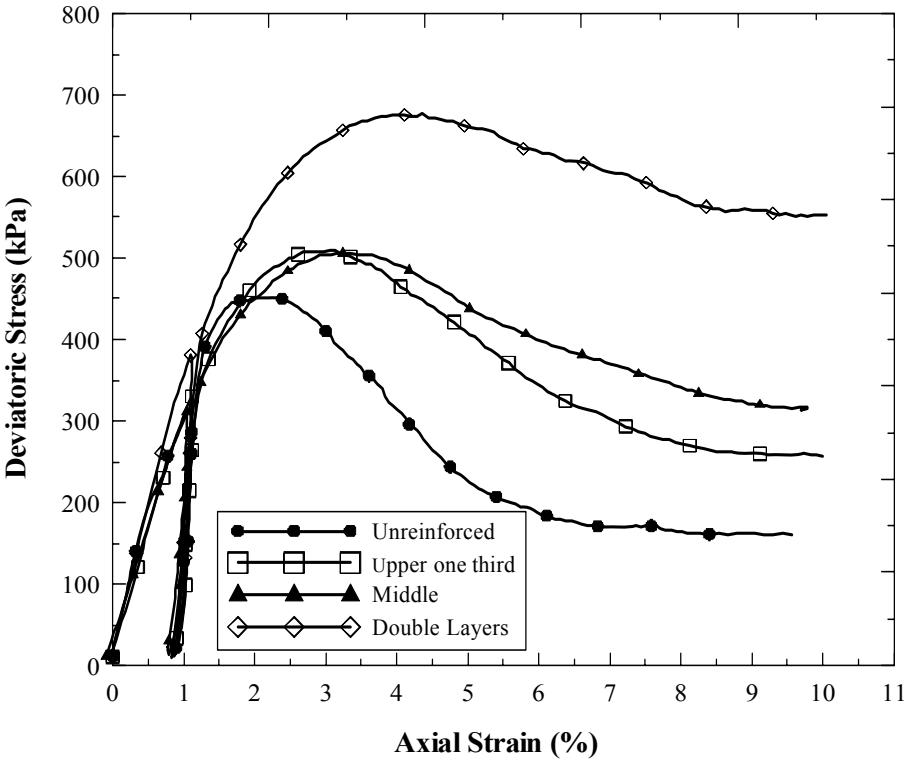

Figure 4.10 Stress-Strain Curve for Crushed Limestone II Samples Reinforced with Geogrid Type IV

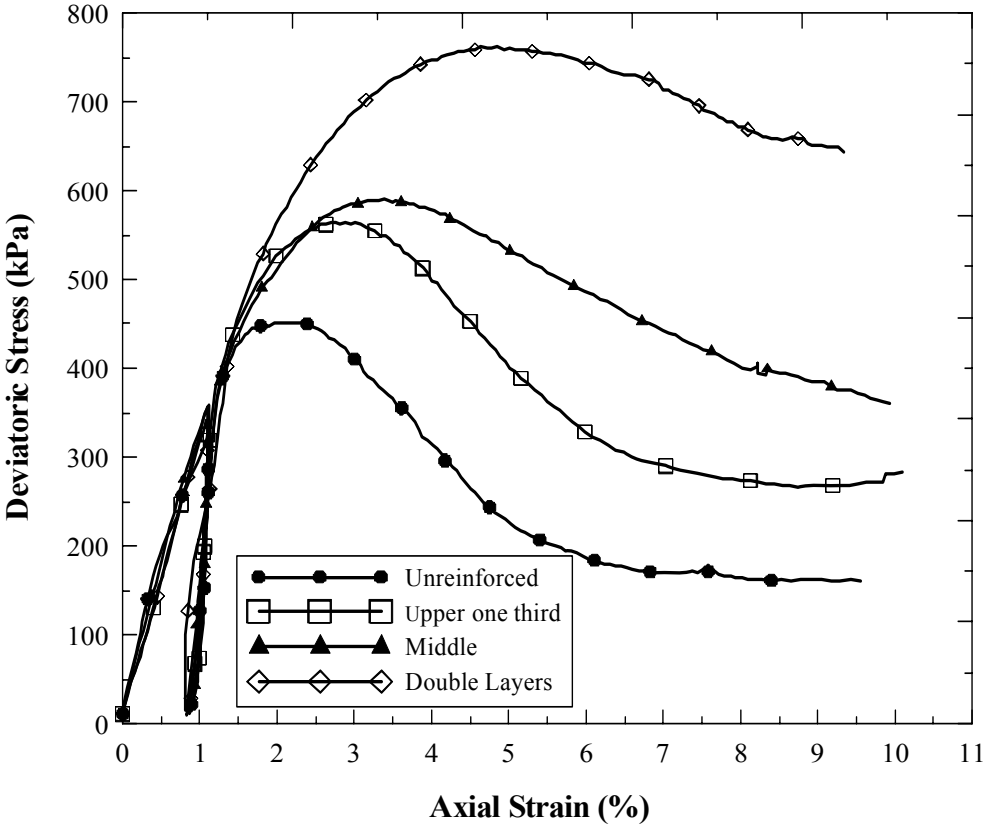

Figure 4.11 Stress-Strain Curve for Crushed Limestone II Samples Reinforced with Geogrid. Type V

increase, until eventually stabilizing and reaching a constant value, which is referred to as the residual shearing strength (RSS). In contrast to crushed limestone I samples, the RSS of the crushed limestone II samples was much smaller than the ultimate shear strength. This reduction can be attributed to the development of large shear strains localized in a narrow zone called shear band. Figure 4.12 presents a photo of tested unreinforced sample. A close examination of the photo reveals that a thick shear band was formed in the unreinofrced sample. Furthermore, the plane of failure in these samples is observed to be close to that predicted in classical soil mechanics theories, which is at $45+\frac{\phi}{2}$.

Figure 4.9 through Figure 4.11 demonstrate that in general samples reinforced with a single geogrid layer did not show a any improvement until an axial strain of 2%

Figure 4.12 Unreinforced Sample After the End of Triaxial Compression Test

was reached. It is noted that the inclusion of a geogrid layer within the samples increased the peak strength and reduced the post-peak loss of strength. However, the RSS still remains significantly less than the USS. This suggests that the geogrid layer altered the development of the shear band within the sample, but it did not stop it. Figure 4.13 and Figure 4.14 depict pictures of samples reinforced with a geogrid layer placed at middle and upper one third locations, at the end of the triaxial compression tests. The figures show that although the shear bands were developed within the tested samples; however, the orientation, location, and plane of these bands changed with the location of the geogrid layer in the sample.

The behavior of samples reinforced with two geogrid layers was a little bit different from those reinforced with single geogrid layer, such that the geogrid improved the samples' performance after reaching axial strain level of 1%. A much significant increase was detected in the peak strength, while the post-peak strain softening was very small compared to other reinforced and unreinforced samples.

Figure 4.15 depicts post testing photos of samples reinforced with two geogrid layers. It is noted that the geogrid caused the development of clogging in the shear band

Figure 4.13 Picture for Samples Reinforced at Mid Height


Figure 4.14 Picture for Samples Reinforced at Upper One Third


Figure 4.15 Picture for Samples Reinforced with Two Geogrid Layers

within the samples, such that they failed by bulging between the two adjacent layers of geogrids. This suggests that the use of the reinforcement layers changed the pattern of deformation in the collapse mechanism of reinforced samples.

Four response parameters were obtained from each triaxial test, namely, $E_{s1\%}$, $E_{s2\%}$, the USS, and RSS. An improvement factor was calculated for each parameter using Equation 3.1. Figures 6a through 6c present the average improvement factors and the standard deviation values obtained for each reinforced case. It is noted that the reinforced samples had a slight improvement in $E_{s1\%}$, and $E_{s2\%}$, such that IM-$E_{s1\%}$, and IM-$E_{s2\%}$ ranged between 0.95 and 1.15 with a maximum improvement of 15%. The improvement due to geogrid reinforcement was more appreciable in the USS than $E_{s1\%}$, and $E_{s2\%}$ especially for double arrangement cases, and it ranged between 1.1 and 1.55. However, the effect of the reinforcement on the magnitude of IM-RSS was much greater than the other factors. For example samples reinforced with two layer of geogrid Type V had four times higher RSS values than unreinforced samples. The IM-RSS ranged between 1.65 and 4, which suggests that the greatest contribution of the geogrid was in the residual strength.

ANOVA analysis, similar to the one that was conducted on the crushed limestone I triaxial test results, was performed to assess the effects of geogrid type and arrangement on the IM-$E_{s1\%}$, IM-$E_{s2\%}$, IM-USS, and IM-RSS obtained from crushed limestone II triaxial test results. The results of the ANOVA analysis are presented in Table 4.6. It is noted that, at a 95% confidence level, the geogrid type did not have a significant effect on the IM-$Es_{1\%}$, and IM-$Es_{2\%}$, while it significantly affected the IM-USS and IM-RSS. This suggests that high deformation is needed to effectively mobilize the tensile membrane resistance, which the mechanism is dominated by to the geogrid stiffness. The geogrid

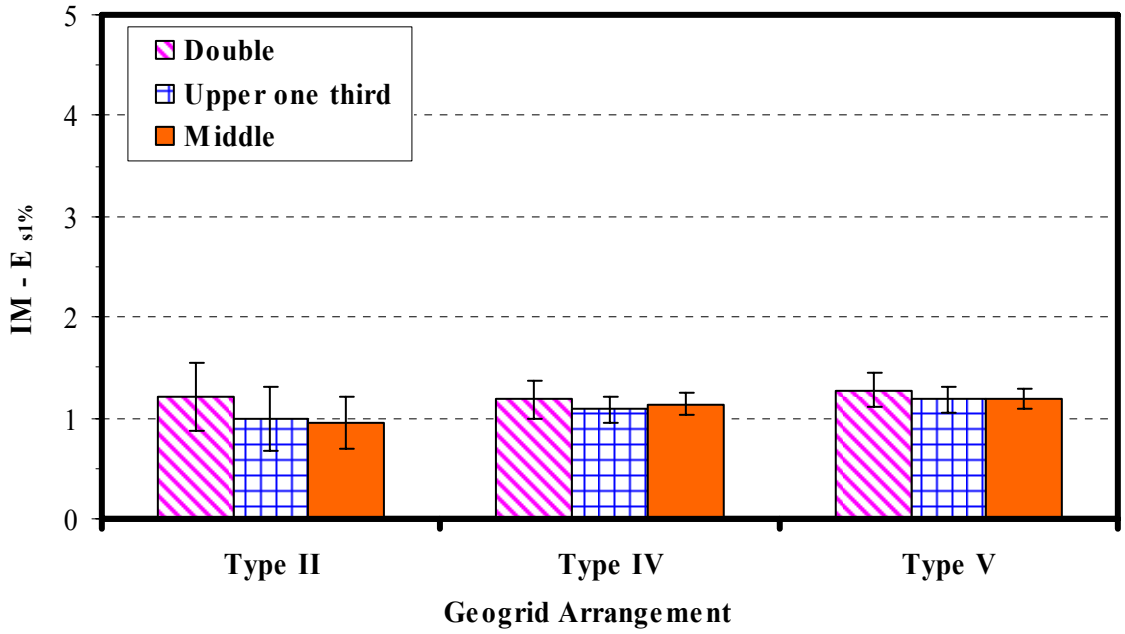

Figure 4.16 Improvement Factor IM- $E_{S1\%}$ for Reinforced Crushed Limestone II Samples

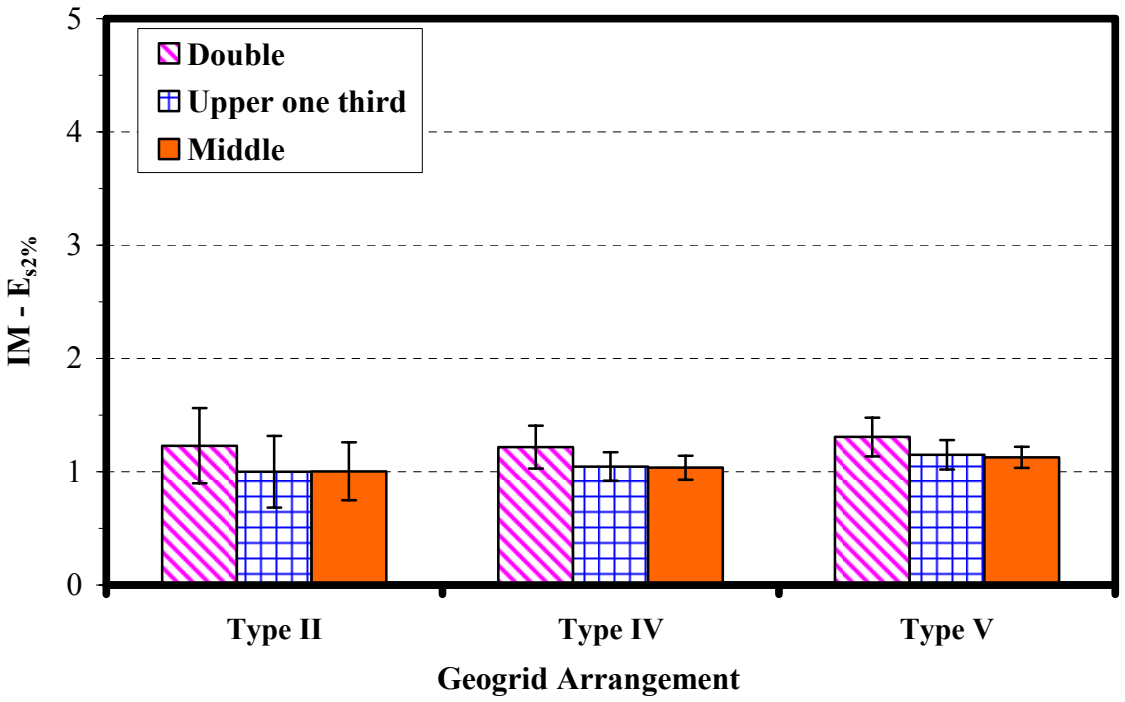

Figure 4.17 Improvement Factor IM-$E_{S2\%}$ for Reinforced Crushed Limestone II Samples

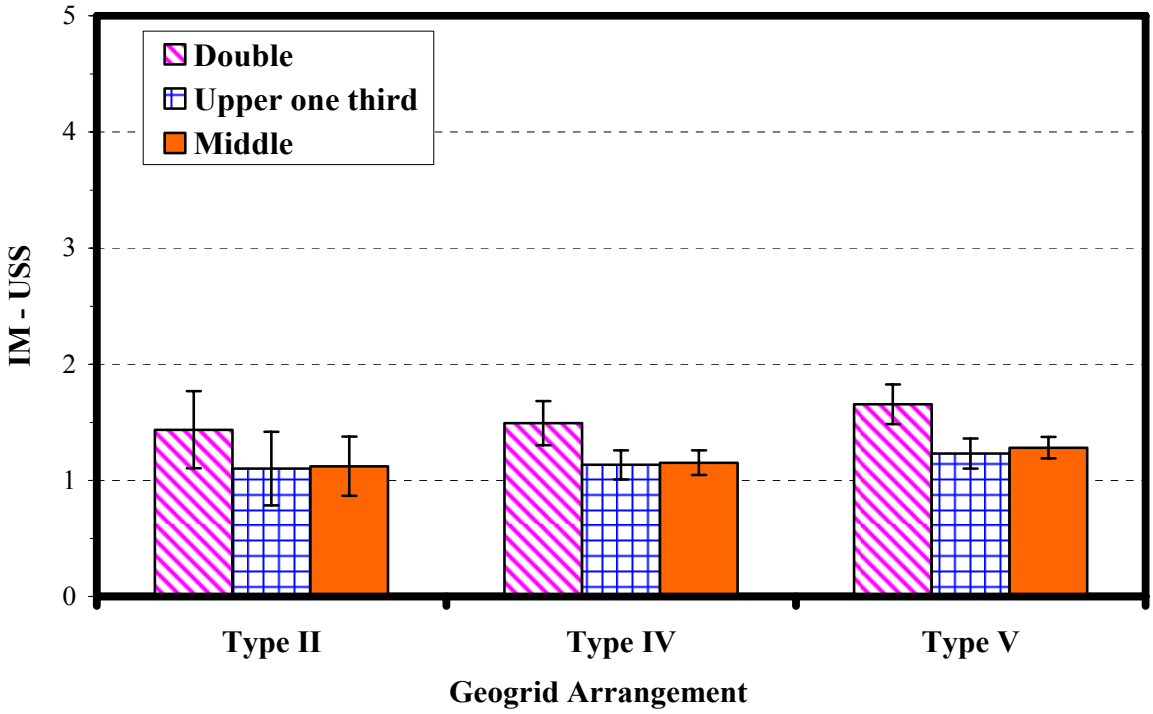

Figure 4.18 Improvement Factor IM-USS for Reinforced Crushed Limestone I Samples

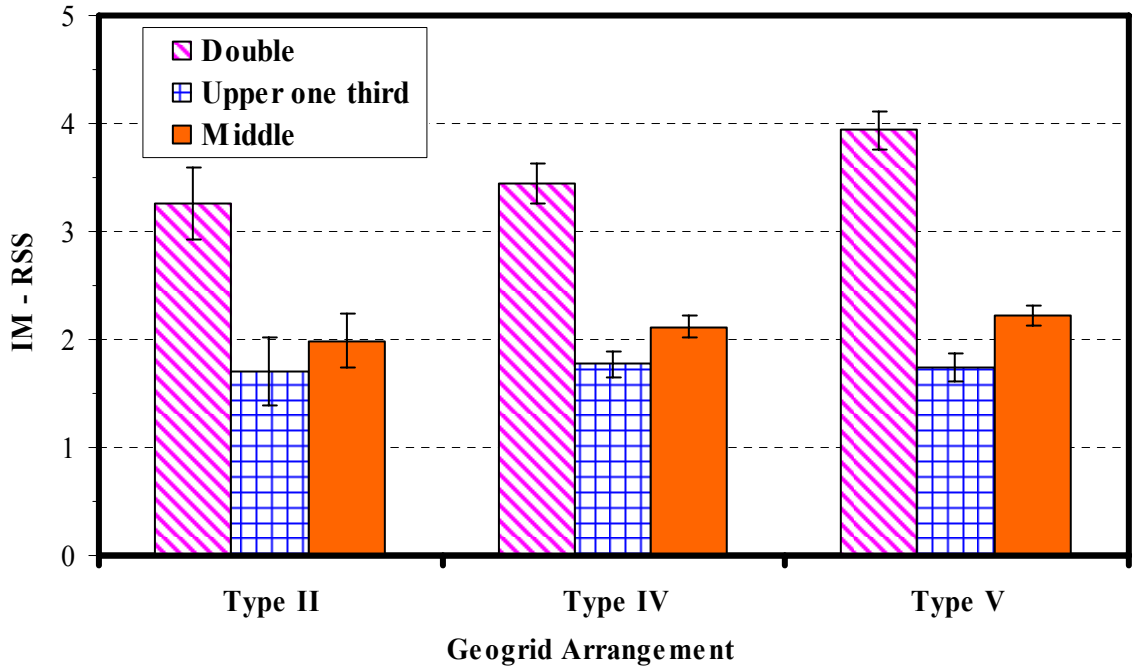

Figure 4.19 Improvement Factor IM-RSS for Reinforced Crushed Limestone I Samples

Table 4.6 ANOVA Results for IM-$Es_{1\%}$, IM$Es_{2\%}$, IM-USS, and IM-RSS

Type 3 Tests of Fixed Effects for IM-$Es_{1\%}$,

Effect	Num DF	Den DF	F Value	Pr > F
Type	2	18	2.98	0.0761
Location	2	18	19.09	<.0001
Location* Type	4	18	0.38	0.8167

Type 3 Tests of Fixed Effects for IM-$Es_{2\%}$,

Effect	Num DF	Den DF	F Value	Pr > F
Type	2	18	3.03	0.0684
Location	2	18	12.22	0.0004
Location* Type	4	18	0.71	0.5954

Type 3 Tests of Fixed Effects for IM-USS

Effect	Num DF	Den DF	F Value	Pr > F
Type	2	18	11.67	0.0006
Location	2	18	49.45	<.0001
Location* Type	4	18	0.27	0.8911

Type 3 Tests of Fixed Effects for IM-RSS

Effect	Num DF	Den DF	F Value	Pr > F
Type	2	18	13.63	0.0002
Location	2	18	200.83	<.0001
Location*S	4	18	3.13	0.0407

Table 4.7 Grouping of Geogrid Type Effect

Dependent Variable	Geogrid Type	Estimate	Standard Error	Letter Group
IM-USS	Type V	1.4125	0.03047	A
	Type IV	1.2487	0.03047	B
	Type II	1.2194	0.03047	B
IM-RSS	Type V	2.7277	0.07398	A
	Type IV	2.3406	0.07398	B
	Type II	2.2004	0.07398	B

Table 4.8 Grouping of geogrid arrangement Effect

Dependent Variable	Geogrid Arrangement	Estimate	Standard Error	Letter Group
IM-$Es_{1\%}$	Double Layers	1.1904	0.02208	A
	Upper one third	1.0254	0.02208	B
	Middle	1.0214	0.02208	B
IM-$Es_{2\%}$	Double Layers	1.2265	0.02960	A
	Upper one third	1.0556	0.02960	B
	Middle	1.0400	0.02960	B
IM-USS	Double Layers	1.5405	0.03047	A
	Upper one third	1.1829	0.03047	B
	Middle	1.1571	0.03047	B
$RPS_{10,000}$	Double Layers	3.6068	0.07398	A
	Middle	2.0502	0.07398	B
	Upper one third	1.6118	0.07398	C

Table 4.9 Grouping of the Interaction Effect on IM-RSS

Geogrid Arrangement	Geogrid Type	Estimate	Standard Error	Letter Group
Double Layers	Type V	4.1907	0.1281	A
Double Layers	Type IV	3.4422	0.1281	B
Double Layers	Type II	3.1873	0.1281	B
Middle	Type V	2.2965	0.1281	C
Middle	Type IV	1.9781	0.1281	CD
Middle	Type II	1.8758	0.1281	CD
Upper one third	Type V	1.6960	0.1281	CD
Upper one third	Type IV	1.6014	0.1281	D
Upper one third	Type II	1.5381	0.1281	D

arrangement had a significant effect on all improvement factors. Furthermore, it had a more appreciable influence than geogrid type, especially for IM-USS and IM-RSS, as indicated by the F-value. Finally, the interaction effect of the geogrid type-geogrid arrangement ($\tau_1\tau_{2ij}$) had significant effects only on the IM-RSS.

Based on the result of the ANOVA analyses, post ANOVA-LSM analyses were conducted to compare the different levels of significant effects. The results of the post ANOVA-LSM analyses are presented in Table 4.7 through 4.9. Table 4.7 shows the grouping of the geogrid types' effect on IM-USS and IM-RSS. It can be noted that Type V geogrid, the geogrid with greatest stiffness, exhibited the highest IM-USS and IM-RSS values, while the other two geogrid types had almost similar values.

Table 4.8 presents the grouping of the effect of geogrid arrangement on the IM-Es1%, IM-Es2%, IM-USS, and IM-RSS. The highest benefit was achieved when the two layers of geogrids were used to reinforce the samples. While the middle and upper one third locations had similar IM-Es1%, IM-Es2%, and IM-USS values. However, it seems that the middle location was more effective than the upper one third location in reducing the post peak strain softening, and hence, it had higher IM-RSS value.

Table 4.9 shows that the location-stiffness interactions in groups A and B are the only groups significantly different from all other interactions. These two groups represent samples reinforced with double reinforcement layers.

The preceding results of the monotonic triaxial tests is clearly showing that the geogrid improvement for the crushed limestone II was mobilized at higher strain level material, compared to crushed limestone I. The greatest benefit obtained from reinforcing the crushed limestone II material was in altering the development of shear bands, and hence minimizing the reduction in residual strength. This difference in the behavior

maybe explained by the dense state that the crushed limestone II material was tested at compared to the loose state of the crushed limestone I. The difference between the optimum moisture contents (6 and 10.5%) for each material provides another reason for the dissimilarities between the geogrid improvements. In spite of some differences between the two base course materials, the geogrid improvement had similar pattern, such that it progressively appreciated with increasing the axial deformation and strain. Furthermore, the greatest geogrid improvement was achieved when using two geogrid layers. The reason for the similarities lies in the fact that the geogrid reinforcement mechanism was the same. This mechanism can be explained as follows: the placement of a geogrid layer(s) within the sample allows the development of shear interaction and interlocking between the aggregate and the geogrid during loading. Shear stress is transmitted from the aggregate to the geogrid, which places the geogrid in tension. The relatively high stiffness of the geogrid acts to retard the development of lateral tensile strains in the material adjacent to the geogrid, and thus resulted in an increase in the confinement stresses, as the geogrid strength is mobilized. Samples reinforced with two geogrid layers had the best performance. The use of two geogrid layers makes the sample behaves as a short sample.

4.2 Resilient Modulus RLT Test Results

Resilient modulus tests were performed on unreinforced crushed lime stone I samples and samples reinforced with geogrid types I through V. Based on the results of these tests, a regression analyses was carried out to determine the parameters of resilient modulus generalized constitutive model adopted by the Mechanistic Emprical Pavement Design guide (NCHRP, 2004) (Equation 3.5). The results of this analysis are presented in Table 4.10 through Table 4.12.

The parameters presented in Table 4.10 through Table 4.12 were used to compute the resilient modulus for the different unreinforced and reinforced cases at a confining stress of 21 kPa, and three deviatoric stresses: 80 kPa, 160, and 250 kPa. Figure 4.20 through Figure 4.23 present the computed resilient modulus values. It is noticed that the resilient modulus values increased with increasing the deviatoric stress. This increase can be explained by the relation illustrated in Figure 4.24 between the aggregate particle contact force, which is directly related to the applied stresses, and the displacement between those particles.

As shown in Figure 4.22, at low stress state (low deviatoric stress) the particles touch punctually (number 0 in Figure 4.24). However, when increasing the applied stress, and hence increasing the force transmitted by the inter-particle contacts, the size of the inter-particle contact areas increase due to the compression of those contacts. This will results in increasing the resistance of the centers of individual aggregate particles approaching each other. Thus, the displacement between the particles (resilient deformation of the particles) decrease with the increase of the contact force. Figure 4.20 through Figure 4.22 also show that a slight improvement in resilient modulus was only achieved for samples reinforced with two layers of geogrid Type V at high deviatoric stresses.

The resilient modulus was also computed at the stress state applied in the single-stage RLT tests (confining pressure of 21 kPa and deviatoric stress of 230 kPa) for the different unreinforced and reinforced samples. An improvement factor (IM-M_r) was then determined using Equation 3.1. Figure 4.25 presents the average improvement factor and the standard deviation values obtained for all reinforced cases. It is noticed that only samples reinforced with two geogrid layers had a slight improvement in the resilient

Table 4.10 Resilient Modulus Model Coefficients for Unreinforced and Reinforced Samples

Material parameter	Variable	Unreinforced	Geogrid Type I		
			Middle	Upper one Third	Double
k_1	Average	1788.9	1781.1	1834.6	1813.6
	Stdv	85.7	78.2	99.0	93.6
	COV	4.8	4.4	5.4	5.2
k_2	Average	0.382	0.381	0.385	0.412
	Stdv	0.017	0.017	0.021	0.020
	COV	4.3	4.5	5.3	4.8
k_3	Average	-0.149	-0.385	-0.377	-0.290
	Stdv	0.007	0.016	0.022	0.013
	COV	4.7	4.0	5.7	4.5

Table 4.11 Resilient Modulus Model Coefficients for Samples with Geogrid Type II and III

Material parameter	Variable	Geogrid Type II			Geogrid Type III		
		Middle	Upper One Third	Double	Middle	Upper One Third	Double
k_1	Average	1790.6	1815.9	1851.9	1793.2	1811.4	1855.3
	Stdv	71.5	82.4	91.7	65.2	116.2	62.7
	COV	4.0	4.5	4.9	3.6	6.4	3.4
k_2	Average	0.408	0.401	0.393	0.384	0.392	0.424
	Stdv	0.016	0.020	0.021	0.019	0.024	0.014
	COV	4.0	4.9	5.2	5.0	6.2	3.3
k_3	Average	-0.199	-0.226	-0.192	-0.295	-0.281	-0.224
	Stdv	0.009	0.010	0.010	0.014	0.019	0.008
	COV	4.3	4.4	5.2	4.7	6.7	3.5

Table 4.12 Resilient Modulus Model Coefficients for Samples with Geogrid Type IV And V

Material parameter	Variable	Geogrid Type IV			Geogrid Type V		
		Middle	Upper One Third	Double	Middle	Upper One Third	Double
k_1	Average	1796.9	1862.9	1909.1	1815.7	1860.7	1993.8
	Stdv	116.1	103.4	99.3	58.9	70.2	104.7
	COV	6.5	5.6	5.2	3.2	3.8	5.3
k_2	Average	0.399	0.398	0.441	0.415	0.431	0.446
	Stdv	0.027	0.021	0.023	0.016	0.015	0.022
	COV	6.7	5.2	5.3	3.9	3.5	4.8
k_3	Average	-0.257	-0.248	-0.207	-0.232	-0.246	-0.339
	Stdv	0.017	0.014	0.012	0.008	0.010	0.015
	COV	6.5	5.5	5.7	3.4	4.0	4.5

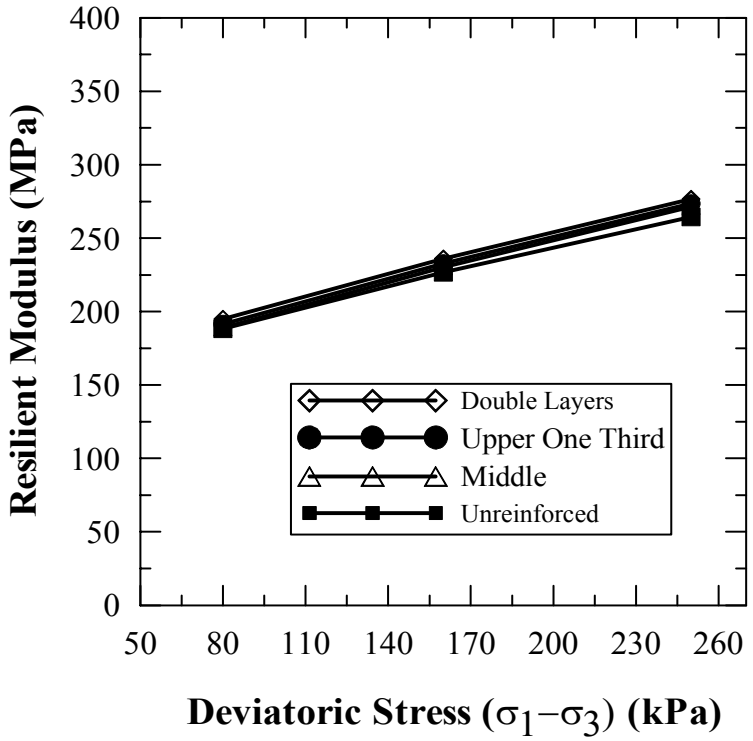

Figure 4.20 M_r at Different Deviator Stresses for Samples Reinforced with Geogrid Type I

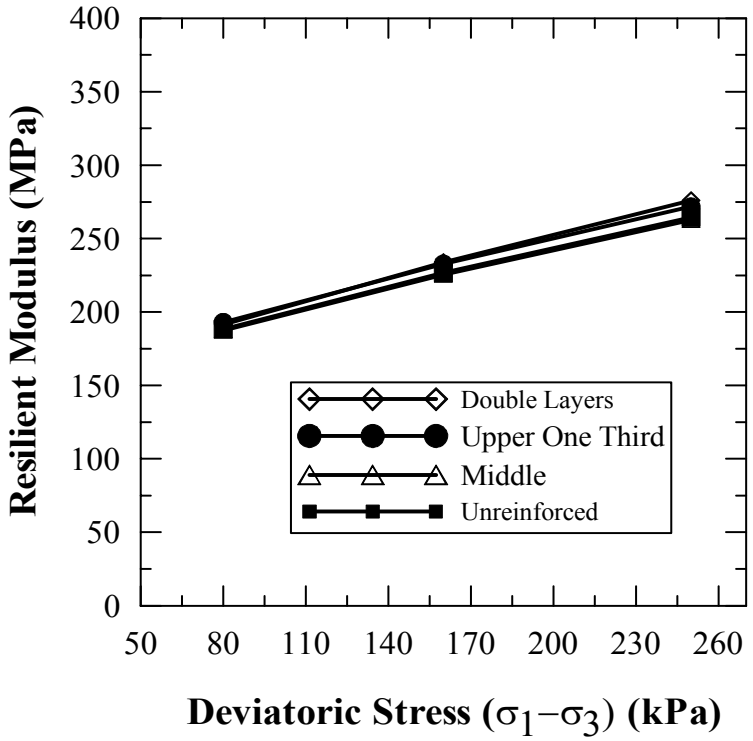

Figure 4.21 M_r at Different Deviator Stresses for Samples Reinforced with Geogrid Type II

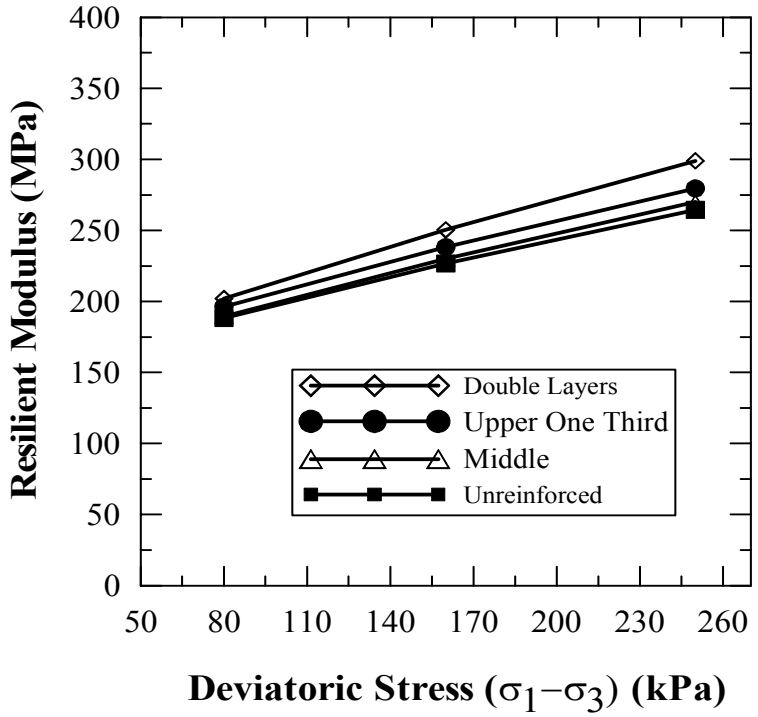

Figure 4.22 M_r at Different Deviator Stresses for Samples Reinforced with Geogrid Type III

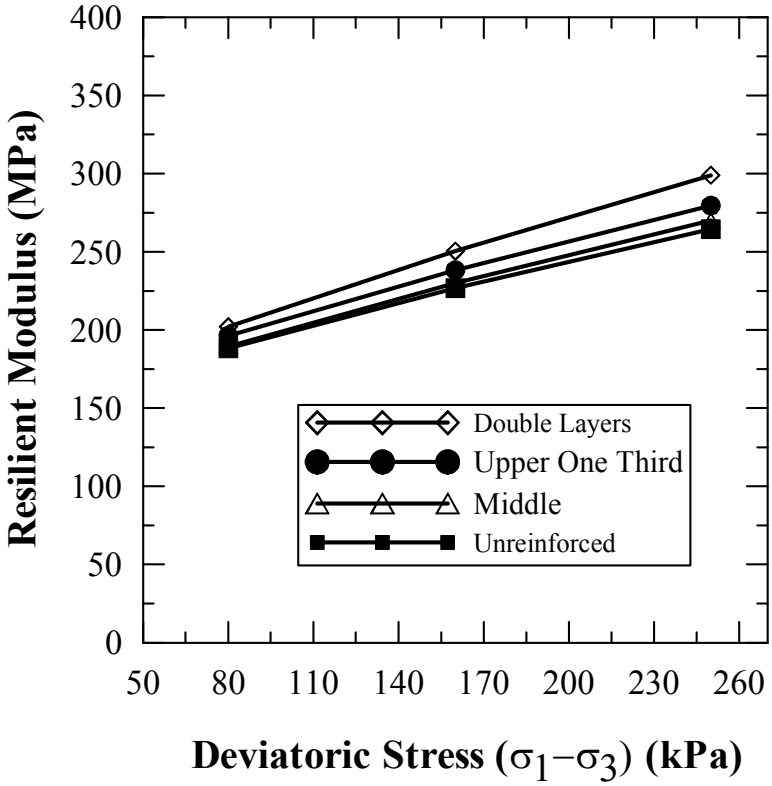

Figure 4.23 M_r at Different Deviator Stresses for Samples Reinforced with Geogrid Type IV

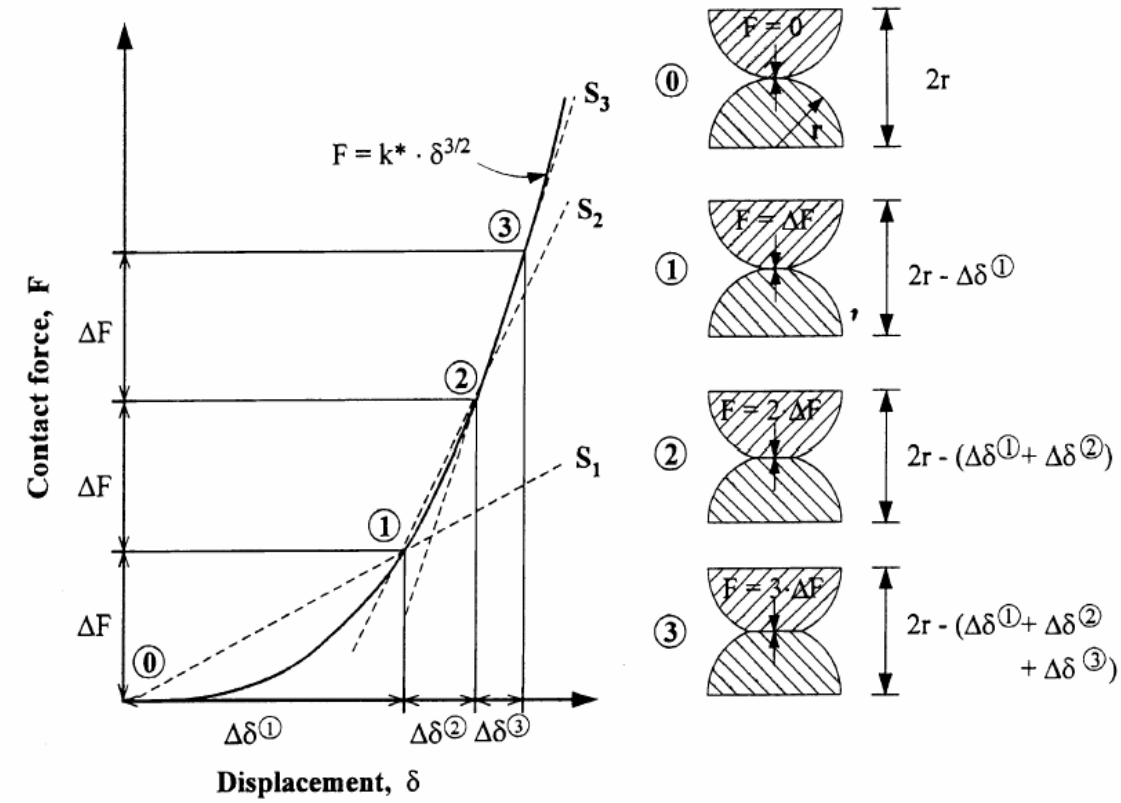

Figure 4.24 Relation between the Contact Force and Displacement between Two Particles (Kolisoja, 1997)

modulus values calculated at the selected stress state. However, no conclusion can be drawn since this improvement lies within the margin of error of the calculated values.

ANOVA and Post ANOVA-LSM analyses with a single factor CRD design and 17 levels (16 reinforced cases and one unreinforced case) was conducted to compare the resilient modulus of the reinforced samples to those of unreinforced sample. Duntte's adjustment was used in this analysis, since it is usually used to compare a control effect to all other effects (SAS Institute Inc, 2004)). Table 4.13 presents the results of this comparison. It can be observed that, at 95% confidence level, only the resilient modulus values of samples reinforced with double layers of geogrid type V were higher than those of unreinforced samples. This suggests that the reinforcement did not have much effect on the resilient modulus properties of crushed limestone.

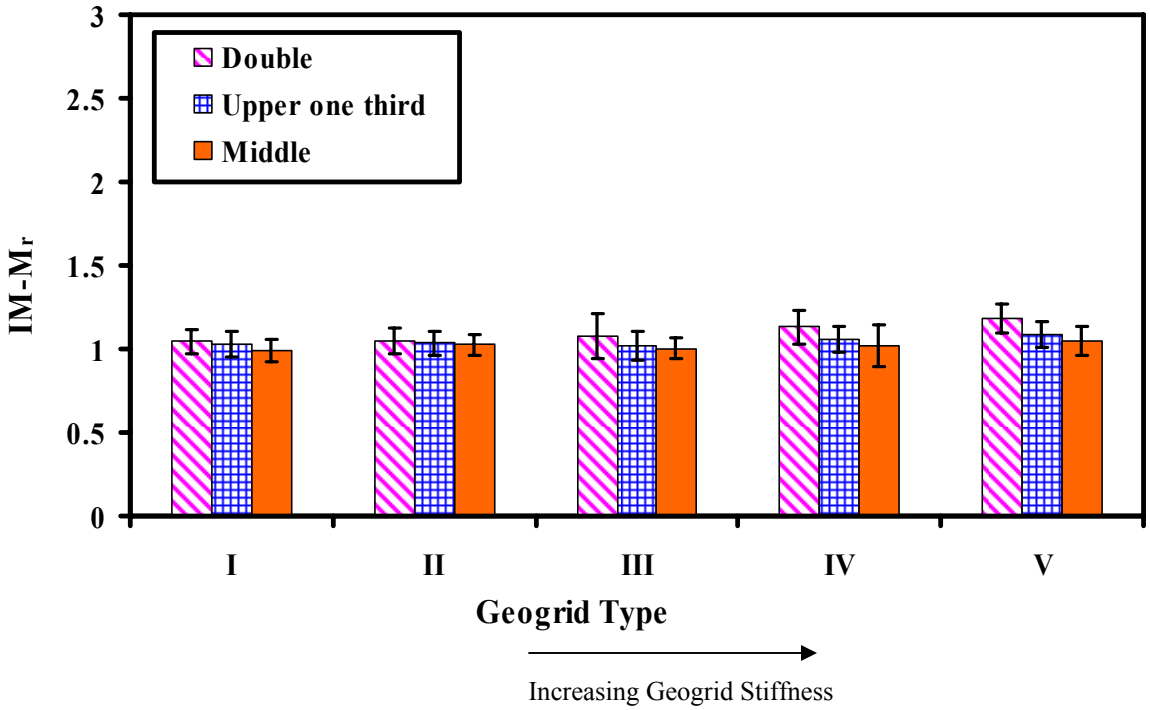

Figure 4.25 IM-M_r Values at Stress State Applied in Single Stage RLT Tests

4.3 Single-Stage RLT Tests

Single-stage RLT tests were performed on unreinforced crushed limestone I and II samples and samples reinforced with geogrid types II, IV, and V. Three reinforcement arrangements were investigated for each geogrid type, namely, middle, upper one third, and double arrangements. The following sections present the permanent and resilient deformations results obtained from the single-stage RLT tests.

4.3.1 Permanent Deformation

4.3.1.1 Crushed limestone I

The curves of the average permanent strain value versus number of load cycles for unreinforced and reinforced samples are presented in Figure 4.26 through Figure 4.28. It is noted that the permanent deformation curve can be divided into two stages. During the first stage, which will be hereafter referred to as the primary post-compaction stage, the material exhibits a high rate of permanent strain. This can be explained by the

Table 4.13 Results of Post ANOVA-LSM Analysis of Resilient modulus of Unreinforced and Reinforced Sample

Location	Geogrid Type	Estimate	t Value	Pr > |t|	Adj P
Double	Type II	5.8824	1.12	0.273	0.930
Double	Type IV	10.3785	1.97	0.058	0.383
Double	***Type V***	***18.4058***	***3.49***	***0.001***	***0.015***
Double	Type I	1.7925	0.34	0.736	1.000
Double	Type I	5.5555	1.05	0.300	0.951
Middle	Type II	-0.3372	-0.06	0.944	1.000
Middle	Type IV	0.4431	0.08	0.933	1.000
Middle	Type V	1.9367	0.37	0.715	1.000
Middle	Type I	-0.7114	-0.13	0.893	1.000
Middle	Type I	0.3821	0.07	0.947	1.000
Upper one third	Type II	2.2249	0.42	0.675	1.000
Upper one third	Type IV	6.8523	1.30	0.202	0.839
Upper one third	Type V	5.9452	1.13	0.267	0.92
Upper one third	Type I	4.3773	0.83	0.412	0.992
Upper one third	Type I	1.9997	0.38	0.706	1.000

material densification process that occurs during this stage which results in great volume change and closure of voids between the particle, and hence in the development of high permanent deformation. While the second stage of the permanent deformation, which will be hereafter referred to as the secondary stage, involved a progressive reduction of the rate of permanent deformation accumulation until the permanent strain curve almost reached an asymptote, and hence a steady state behavior was achieved. This suggests that the behavior of the material is within Range B shakedown range, defined previously in Chapter 2.

Figure 4.26 through Figure 4.28 demonstrate that there was no distinct between the behavior of unreinforced and reinforced samples during the primary post-compaction stage. However, the geogrids were able to reduce the rate of permanent deformation accumulation in the secondary stage, and hence the reinforced samples developed less permanent strain.

Figure 4.29 through Figure 4.33 present the mean and error bars of the RPS values at 100; 1,000; 3,000; 5,000; and 10,000 load cycles, respectively. It is noted that the inclusion of the geogrid reinforcement resulted in a reduction in the permanent strain of up to 65%.Furthermore, at a certain number of load cycles, the geogrid improvement in permanent deformation test depended on the geogrid type, location, and the number of reinforcement layers; such that stiffer geogrids exhibited higher reductions in permanent strains than the ones with the least stiffness, as can be seen for type V geogrids compared to type II geogrids. The figures also show that the upper one third location had better improvement than the middle location. In addition, increasing the number of geogrid layers resulted in a great reduction in the permanent strain. The reduction in permanent strain due to the geogrid reinforcement also varied with the number of load cycles. The reduction was very small at 100 load cycles, especially for samples reinforced with single geogrid layer. However, the RPS value increased with increasing the number of load cycles. A minimum RPS value of 5% was detected at 100 load cycles for samples reinforced with single layer of geogrid Type I placed at the samples' mid-height, while an RPS value of 65% was achieved at 10,000 load cycles, when reinforcing samples with two layers of geogrid Type V.

ANOVA analyses were conducted to detect the effect of geogrid stiffness and arrangement on the reduction of RPS values at 100; 1,000; 3,000; 5,000; and 10,000 load

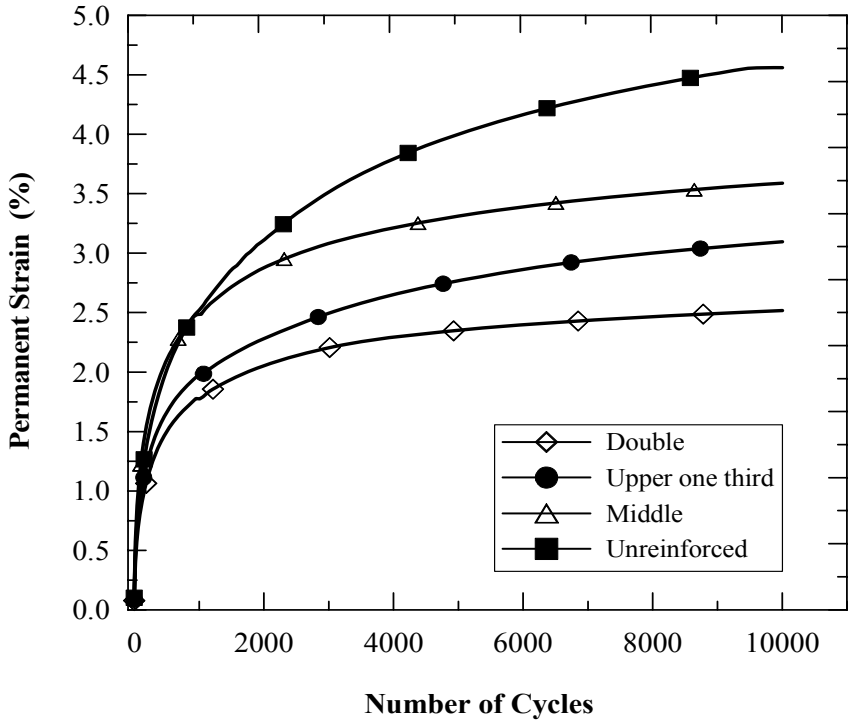

Figure 4.26 Permanent Deformation Curves for Samples Reinforced with Geogrid Type II

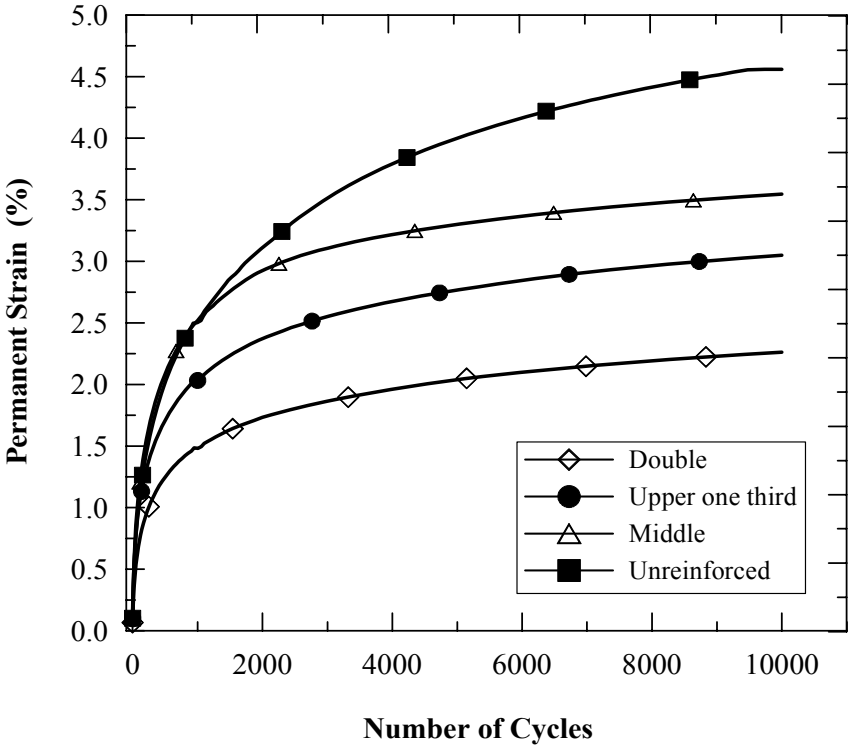

Figure 4.27 Permanent Deformation Curves for Samples Reinforced with Geogrid Type IV

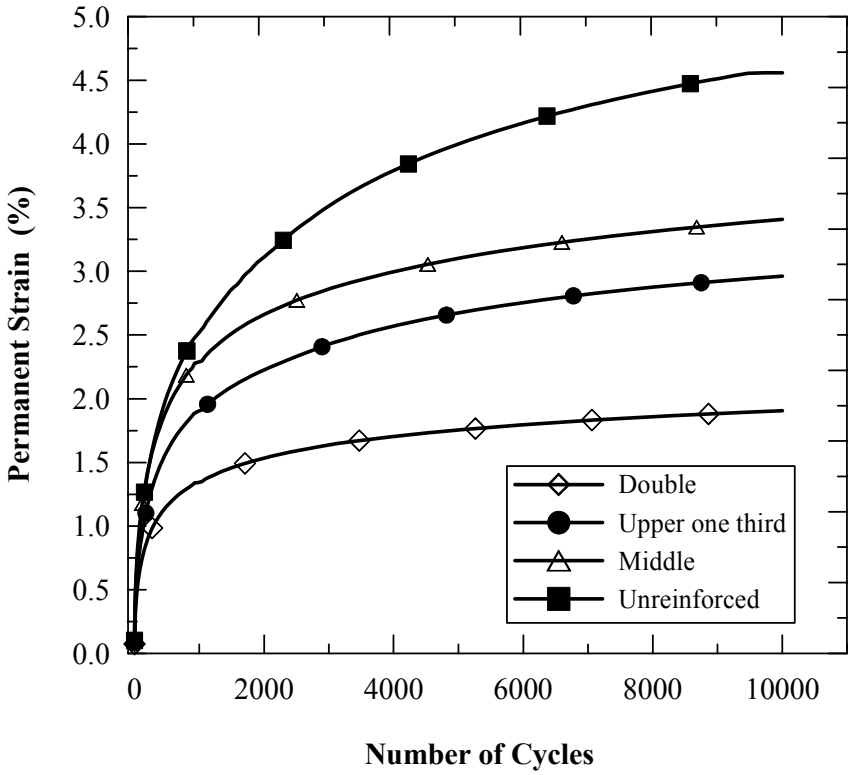

Figure 4.28 Permanent Deformation Curves for Samples Reinforced with Geogrid Type V

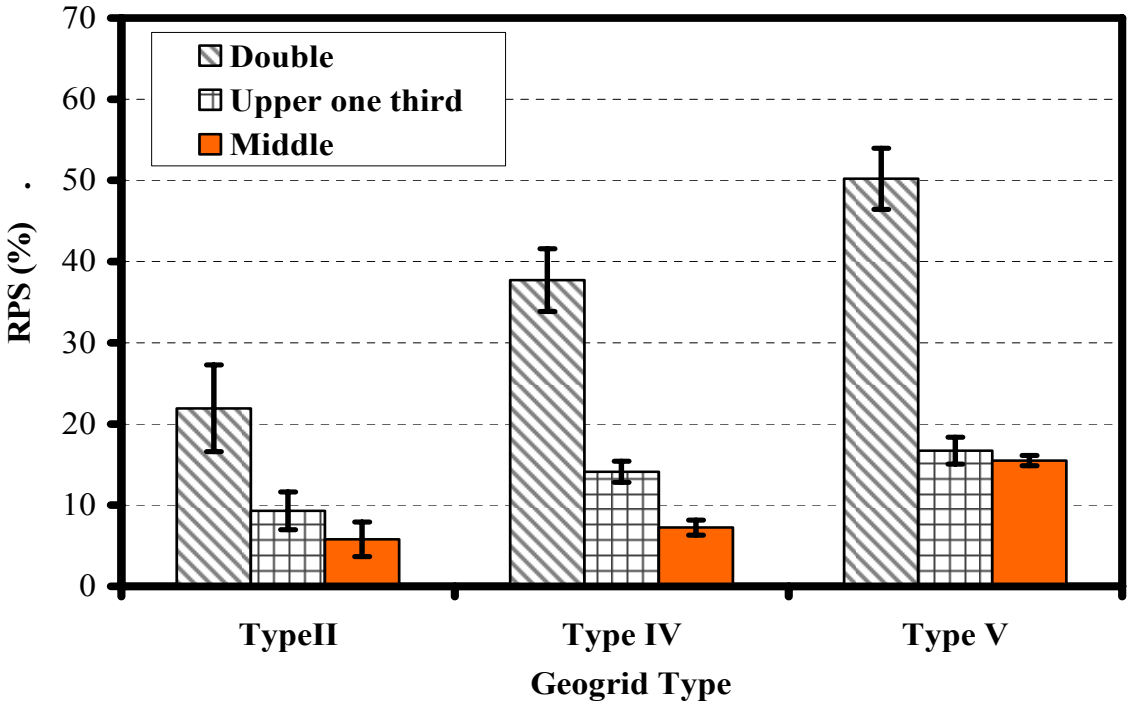

Figure 4.29 RPS at 100 Load Cycles for Crushed Limestone II

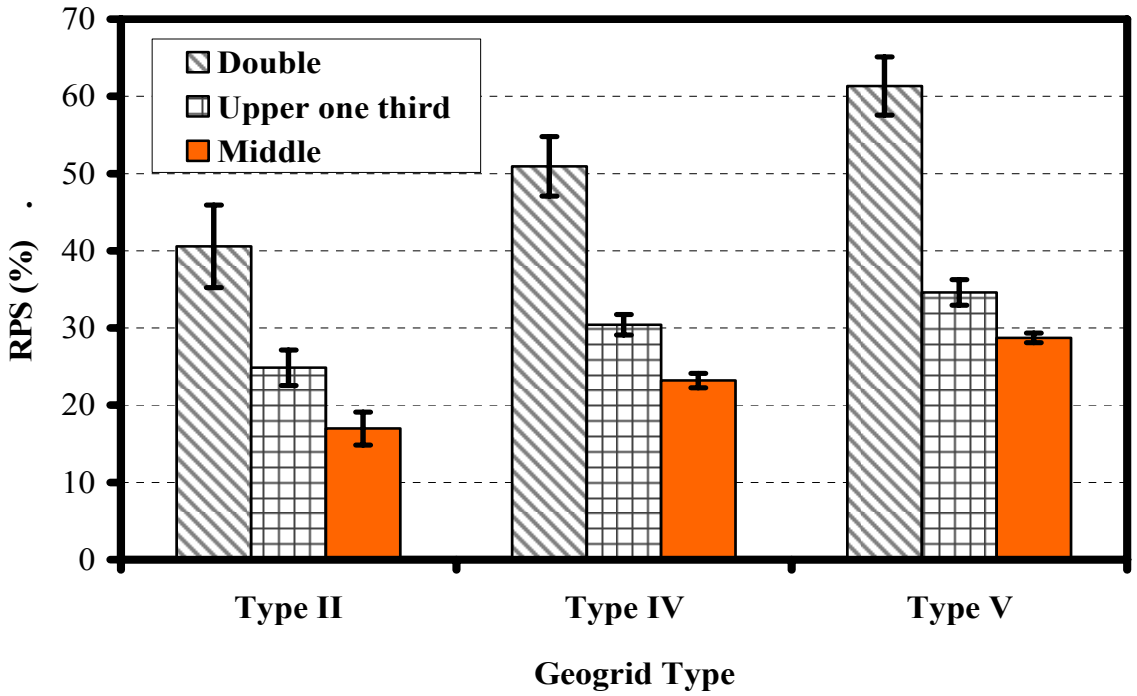

Figure 4.30 RPS at 1,000 Load Cycles for Crushed Limestone II

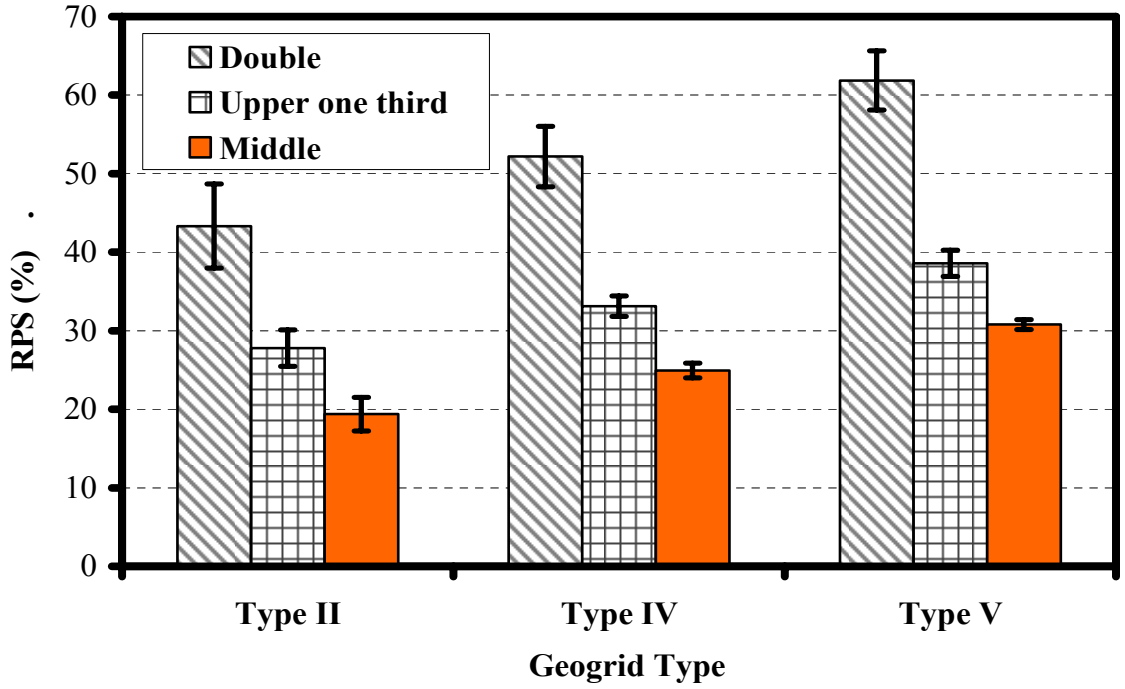

Figure 4.31 RPS at 3,000 Load Cycles for Crushed Limestone II

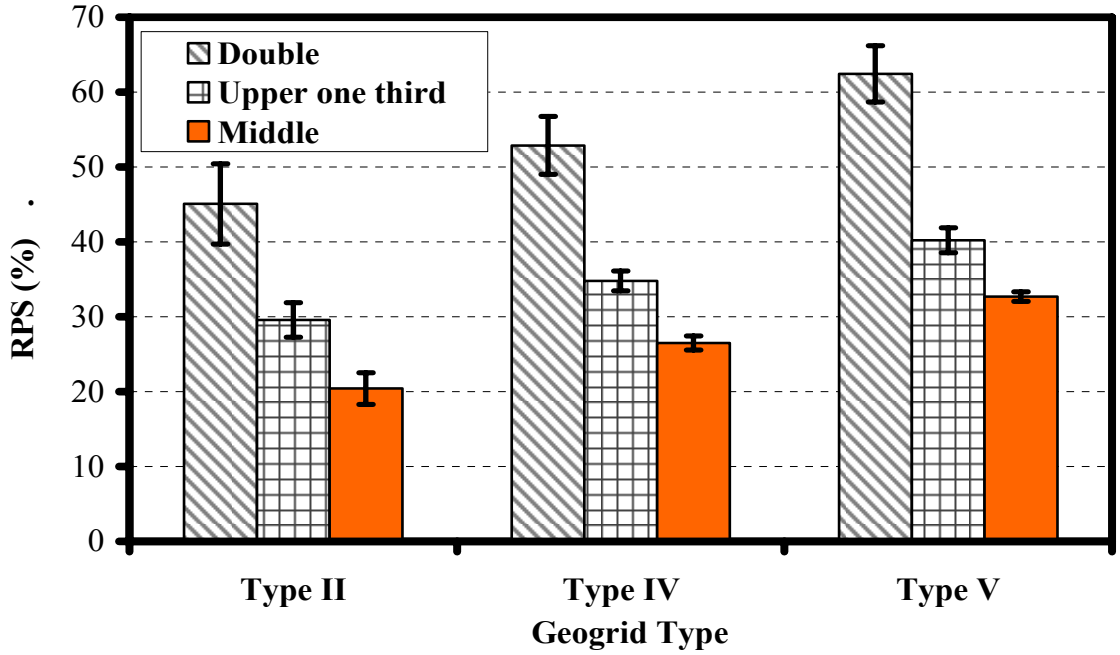

Figure 4.32 RPS at 5,000 Load Cycles for Crushed Limestone II

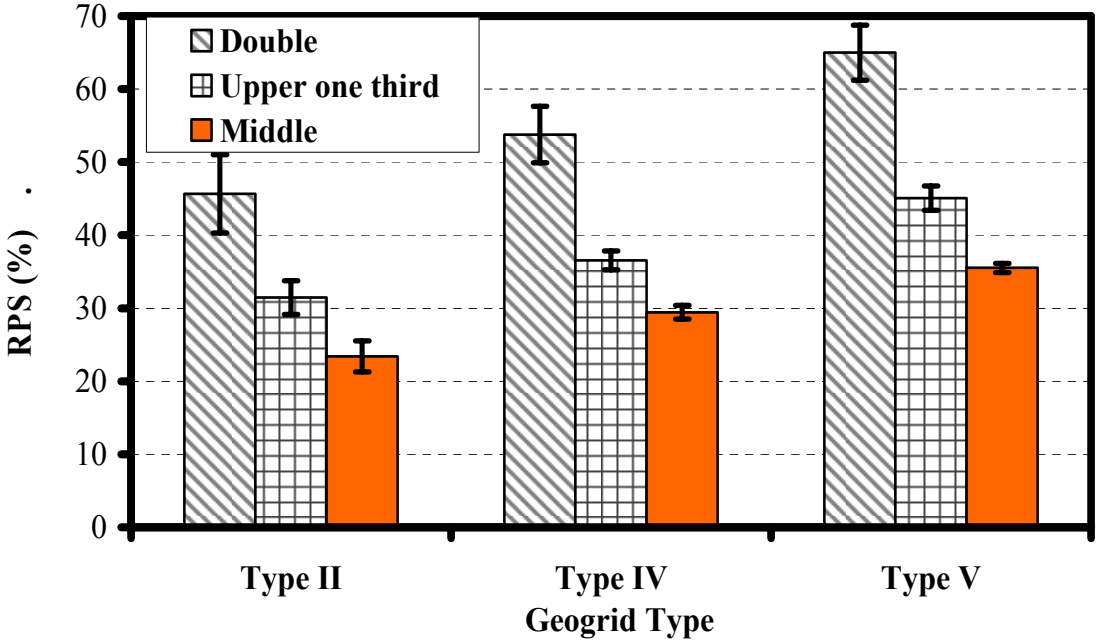

Figure 4.33 RPS at 10,000 Load Cycles for Crushed Limestone II

cycles. The linear Completely Random Design (CRD) model used in this analysis is shown in Equation 4.2. The dependent variable used in the analysis was RPS%.

$$RPS\% = \mu + \tau_{1i} + \tau_{2j} + \tau_{3k} + \tau_1\tau_{2ij} + \tau_1\tau_{3ik} + \tau_2\tau_{3jk} + \tau_1\tau_2\tau_{3ijk} + \varepsilon_{ijkl} \quad 4.2$$

In Equation 4.2, μ is the overall mean; τ_{1i} is the effect of geogrid arrangement; τ_{2j} is the effect of geogrid type/stiffness; τ_{2k} is the effect of number of load cycles, $\tau_1\tau_{2ij}$ is effect of the interaction between the geogrid arrangement and type; $\tau_1\tau_{3ik}$ is effect of the interaction between the geogrid stiffness and number of load cycles; $\tau_2\tau_{3ik}$ is effect of the interaction between the geogrid arrangement and number of load cycles; $\tau_1\tau_2\tau_{3ijk}$ is effect of the interaction between the geogrid arrangement, geogrid stiffness and number of load cycles; and ϵ_{ijkl} is the random sampling variation.

Table 4.14 presents the results of the ANOVA analysis. It is noted that, at a 95% confidence level, the geogrid stiffness, geogrid arrangement, and number of load cycles had significant effect on the reduction of permanent deformation. The geogrid arrangement was the most significant factor affecting the geogrid benefit values, as indicated by the F-value. While the geogrid type had a more significant effect than the number of load cycles. The geogrid type-geogrid arrangement interaction ($\tau_1\tau_{2ij}$) had significant effects, which indicates that the effect of geogrid type varied with the geogrid arrangement. Furthermore, the geogrid arrangement- number of load cycle interaction was also significant. This may suggest that the improvement for the different geogrid arrangements depends on the number of load cycles applied.

Based on the results of the ANOVA analyses, post ANOVA-LSM analyses were conducted to compare the different level for each effect. Table 4.15 through 4.19 present the results of this analysis. Table 4.15 presents the grouping of the geogrid type effect.

Table 4.14 Results of ANOVA Analysis for RPS of Crushed Limestone I Samples

Type 3 Tests of Fixed Effects				
Effect	Num DF	Den DF	F Value	Pr > F
Geogrid Stiffness	2	90	234.00	<.0001
Geogrid Arrangement	2	90	1073.10	<.0001
Number of Load Cycles	4	90	37.92	<.0001
Geogrid Arrangement x Type	4	90	215.35	<.0001
Geogrid Type x Number of Load Cycle	8	90	0.51	0.8429
Geogrid Location x Number of Load Cycle	8	90	2.10	0.0433
Geogrid Type x Arrangement x Number of Load Cycle	16	90	1.56	0.0952

The maximum and minimum improvements were achieved when using geogrids type V and II, respectively. These two geogrid types have the highest and the lowest stiffness, respectively.

Table 4.16 presents the grouping of the different levels in the geogrid arrangement effect. It is clear that the double arrangement has much greater LSM value of RPS compared to other arrangement; while the lowest LSM value of RPS, and hence the least improvement, is observed for the middle arrangement. Table 4.17 compares the geogrid improvement at different number of cycles. It is noted, that improvement due to the geogrid was minimal values at 100 load cycles, and it increased significantly at the 1,000 cycle, eventually stabilizing after 3,000 load cycles. Table 4.18 presents the grouping of geogrid type-arrangement interaction effect on RPS. It is noticed that the highest improvements was always achieved when using two geogrid layers, while the lowest improvement was achieved when using a single geogrid layer placed at the sample mid-height.. Finally, Table 4.19 presents of the grouping of the effect of the geogrid arrangement at different cycle numbers. It is observed that samples reinforced with single

Table 4.15 Grouping of Geogrid Type Effect on RPS of Crushed Limestone I Samples

Geogrid Type /Stiffness	Estimate of RPS%	Letter Group
Type V	41.1884	A
Type IV	32.0782	B
Type II	28.4862	C

Table 4.16 Grouping of Geogrid Arrangement Effect on RPS of crushed limestone I samples

Arrangement	Estimate of RPS%	Letter Group
Double	49.5864	A
Upper one third	29.6158	B
Middle	22.5507	C

Table 4.17 Grouping of Cycle Effect on RPS of crushed limestone I samples

Number Of Cycle	Estimate of RPS%	Letter Group
10000	40.1189	AB
5000	38.0126	B
3000	36.8681	B
1000	34.6196	C
100	19.8689	D

Table 4.18 Grouping of Geogrid Type-Arrangement Interaction Effect on RPS of Crushed Limestone I Samples

Arrangement	Number Of Cycle	Estimate	Letter Group
Double	Type V	60.1400	A
Double	Type IV	49.3747	B
Double	Type II	39.2447	C
Upper one third	Type V	34.8240	D
Upper one third	Type II	29.4260	E
Middle	Type V	28.6013	E
Upper one third	Type IV	24.5973	F
Middle	Type IV	22.2627	F
Middle	Type II	16.7880	G

Table 4.19 Grouping of Geogrid Arrangement-Number of Cycles Interaction Effect on RPS of Crushed Limestone I Samples

Arrangement	Cycle	Estimate	Letter Group
Double	10000	54.6856	A
Double	5000	53.2300	A
Double	3000	52.4267	A
Double	1000	50.9278	A
Upper one third	10000	37.1878	B
Double	100	36.6622	B
Upper one third	5000	34.7278	B
Upper one third	3000	33.1556	BC
Upper one third	1000	29.9656	CD
Middle	10000	28.7833	CDE
Middle	5000	26.0800	DEF
Middle	3000	25.0222	EF
Middle	1000	22.9656	F
Upper one third	100	13.0422	G
Middle	100	9.9022	G

layer of geogrid had different improvement trend with cycle number compared to those reinforced with two layer of geogrid.

4.3.1.2 Crushed Limestone II

Figure 4.34 through Figure 4.36 present the vertical permanent strain curves for the three types of geogrids considered. It can be noticed that similar to the crushed limestone I material, the crushed limestone II was within range B shakedown behavior under the load applied. Although the crushed limestone II demonstrated higher peak

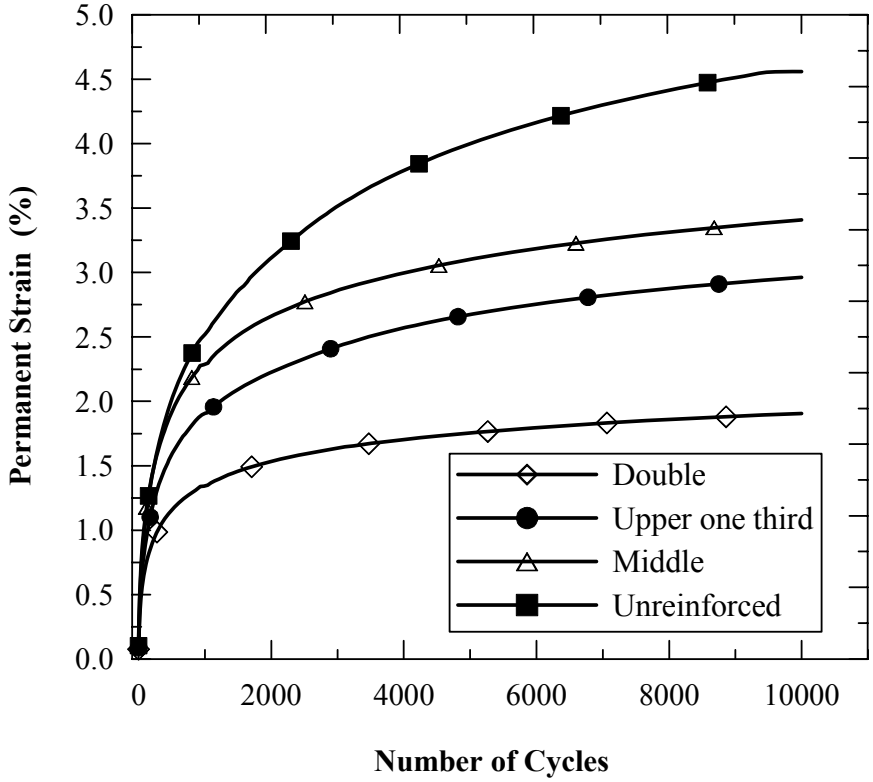

Figure 4.34 Permanent Deformation Curves for Samples Reinforced with Geogrid Type II

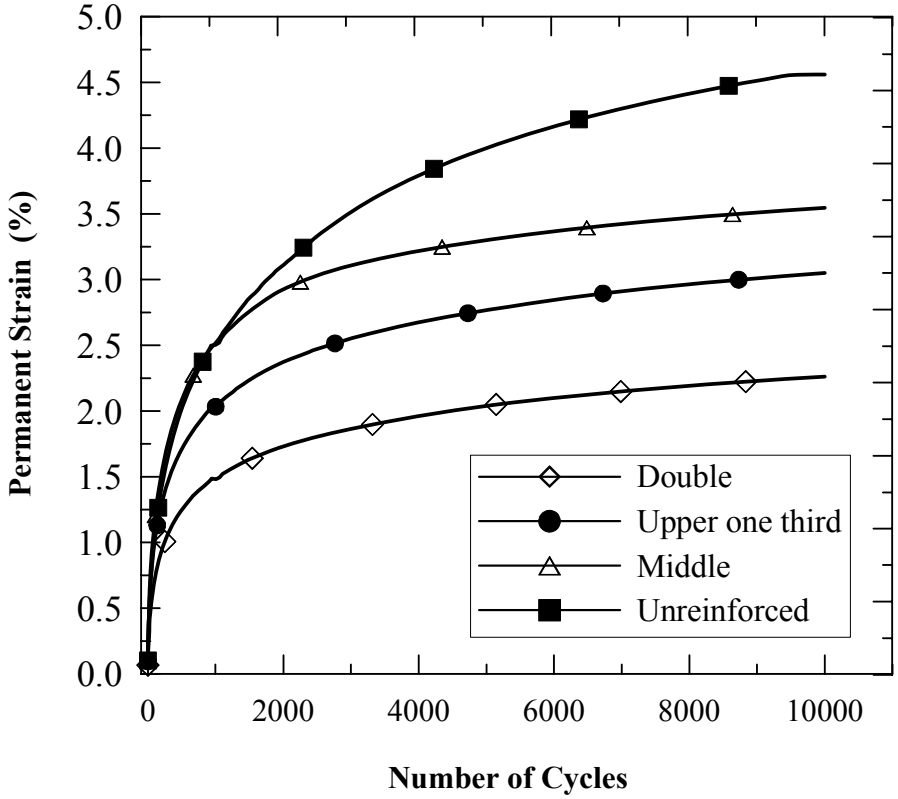

Figure 4.35 Permanent Deformation Curves for Samples Reinforced with Geogrid Type IV

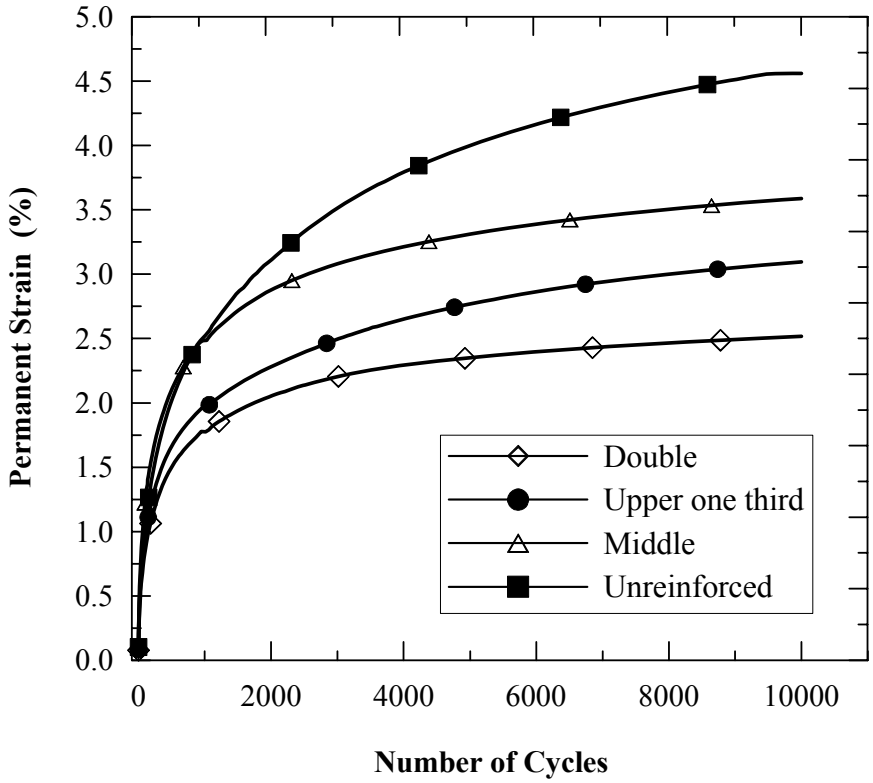

Figure 4.36 Permanent Deformation Curves for Samples Reinforced with Geogrid Type V

strength values (e.g. Figure 4.9) in monotonic triaxial tests, they developed a much higher permanent strains than the crushed limestone I samples at the same cyclic stress. This indicates that the base course peak strength can not be used alone to predict the permanent deformation response of base course materials under cyclic loading.

The reinforced crushed limestone II samples had similar behavior as those of crushed lime stone I, such that the improvement due to the geogrid reinforcement was small during the primary post-compaction stage of the permanent deformation and increased within the secondary stage till reaching its maximum value and then stabilied. Furthermore, this improvement was also affected by the geogrid type and arrangement.

Figure 4.37 through Figure 4.41 present the mean and standard deviation values of the RPS obtained at 100; 1,000; 3,000; 5,000; and 10,000 load cycles, respectively. At a certain number of load cycles, the percent reduction in vertical permanent strain was

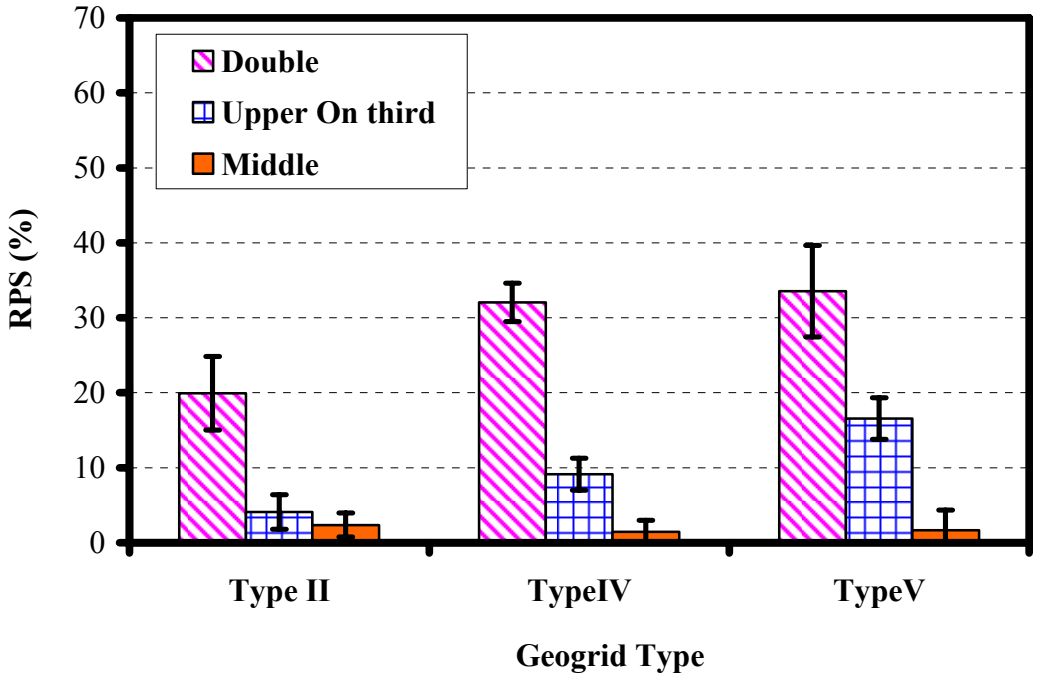

Figure 4.37 RPS at 100 of load cycles for crushed limestone II

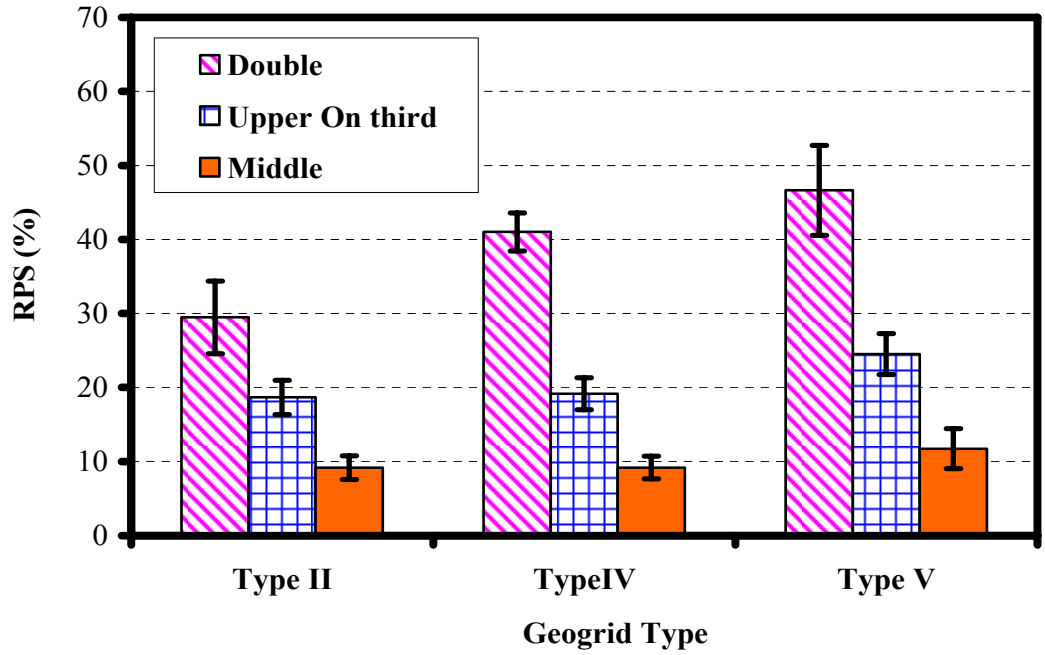

Figure 4.38 RPS at 1,000 of load cycles for crushed limestone II

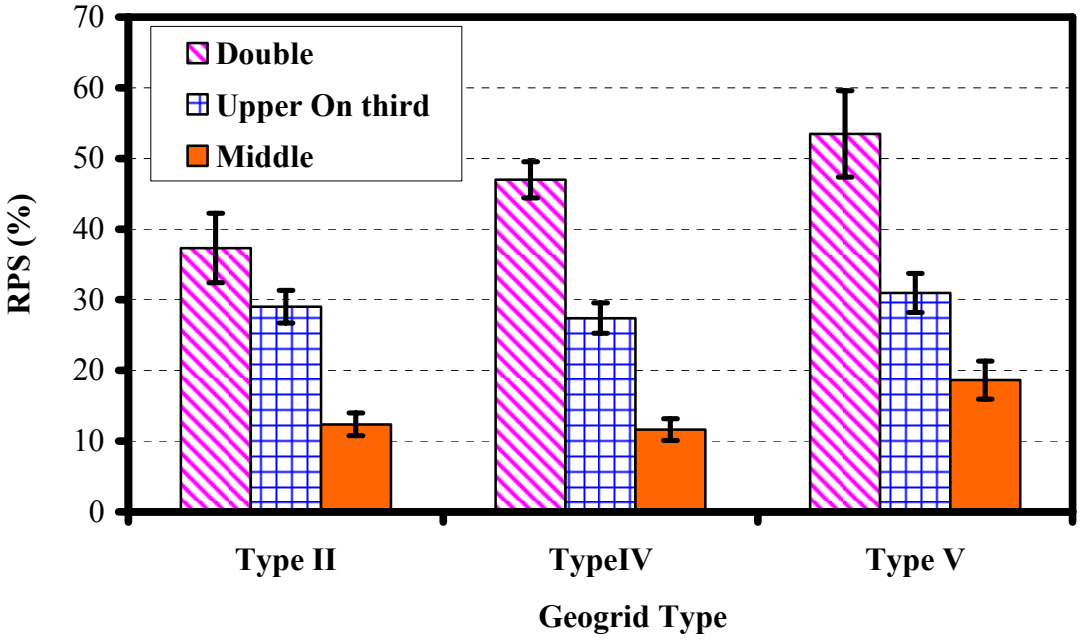

Figure 4.39 RPS at 3,000 of load cycles for crushed limestone II

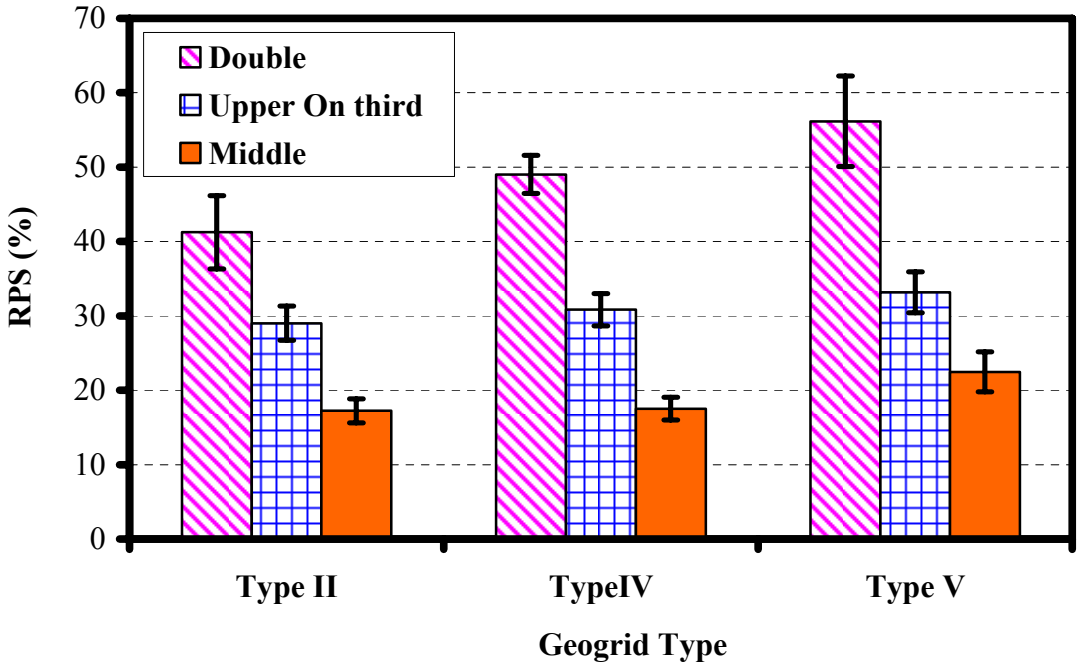

Figure 4.40 RPS at 5,000 of load cycles for crushed limestone II

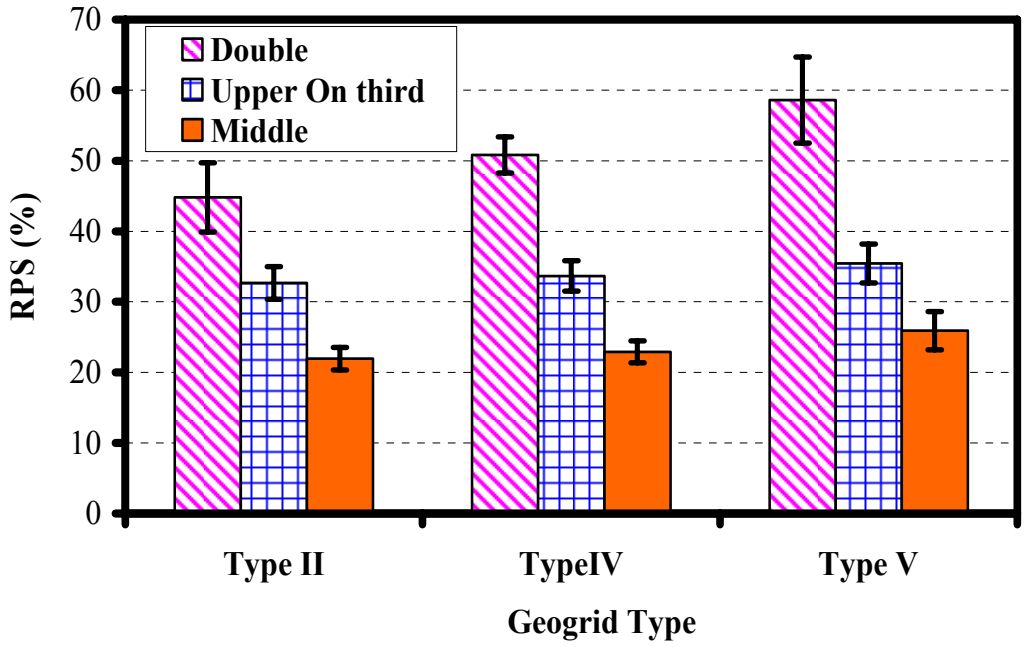

Figure 4.41 RPS at 10,000 of load cycles for crushed limestone II

affected by the geogrid type and arrangement. In general, the stiffer the geogrid used the better the achieved improvement. In addition, increasing the number of geogrid layers resulted in a great reduction in the permanent strain. Figure 4.37 through Figure 4.41 also demonstrate that the reduction in permanent strain due to the geogrid reinforcement varied with the number of load cycles. The reduction was minimal at 100 load cycles. However, it increased significantly after 1,000 load cycles and reached its maximum values at 10,000 load cycles. This indicates that the reduction in permanent strain increased as the load cycles increased. A minimum RPS value of 3% was observed at 100 load cycles for samples reinforced with single layer of geogrid Type I placed at the samples' mid-height, while a maximum RPS value of 59% was detected at 10,000 load cycles, for samples reinforced with two layers of geogrid Type III.

Table 4.20 presents the results of the ANOVA analysis conducted to evaluate the effect of geogrid stiffness and geogrid arrangement on RPS% at different number of load

cycles. At 95% confidence level (Pr<0.05), the geogrid stiffness, geogrid arrangement, and number of load cycles had significant effect on the reduction of permanent deformation. Table 4.20 also shows that the geogrid arrangement was the most significant factor affecting the geogrid benefit values, as indicated by the F-value. While the least significant factor was the geogrid stiffness, which is consistent with results of single-stage RLT tests conducted on the reinforced crushed limestone I samples. This suggests that the determination of the geogrid's optimum location and number of layers should be included as a primary step in the design of geogrid reinforced pavements.

Table 4.21

Table 4.23 presents the results of the post ANOVA-LSM analyses conducted on reinforced crushed limestone II test data. Table 4.21 shows the grouping of the geogrid types/stiffness. It is noticed that Type V geogrid, the geogrid with highest stiffness, exhibited better improvement than the other two geogrid types. This finding agrees with the results of previous single stage tests conducted on the crushed limestone I material considered in this study, as well as

Table 4.20 Results of ANOVA Analysis on RPS

ANOVA Test Results-Type 3 Tests of Fixed Effects				
Effect	Num DF	Den DF	F Value	Pr
Geogrid Stiffness	2	90	34.21	<.0001
Geogrid Arrangement	2	90	441.87	<.0001
Number of Load Cycles	4	90	115.55	<.0001
Geogrid Arrangement x Type	4	90	5.74	0.0004
Geogrid Type x Number of Load Cycles	8	90	0.39	0.9249
Geogrid Location x Number of Load Cycles	8	90	1.62	0.1292
Geogrid Type x Arrangement x Number of Load Cycles	16	90	0.52	0.9281

Table 4.21 Grouping of Geogrid Stiffness

Geogrid Type /Stiffness	Estimate of RPS%	Letter Group
Type V	30.89	A
Type IV	25.20	AB
Type II	21.95	C

Table 4.22 Grouping of Geogrid Arrangement

Arrangement	Estimate of RPS%	Letter Group
Double	42.73	A
Upper one third	25.04	B
Middle	10.26	C

Table 4.23 RPS at Different Number of Cycles

Number Of Cycles	Estimate of RPS%	Letter Group
10000	36.30	A
5000	33.16	AB
3000	29.76	B
1000	21.16	C
100	9.70	D

the results from large-scale reinforced pavement test sections reported in different studies (e.g. Perkins 1999, Leng et al. 2001), which showed that high modulus geogrids can provide better improvement to the stress distribution transferred to the subgrade and the surface permanent deformation compared to low modulus geogrids. The grouping of the effect of geogrid arrangement on the reduction in permanent deformation is presented in Table 4.22. It is noted that the highest benefit was achieved when the double arrangement was used; while the lowest benefit was observed for the middle arrangement. Finally, Table 4.23 compares the geogrid benefits at different number of load cycles. The table shows that the geogrid benefit had its minimum values at 100 load cycles, and it increased significantly after that, eventually stabilizing after 5,000 load cycles.

One interesting observation in the results of the post ANOVA-LSM analyses for both base course materials, was that the double arrangement had a much higher reduction in permanent deformation at 100 cycles compared to the other arrangement. This observation agrees with the results of field tests sections reported by Cancelli and Montanelli (1999), which demonstrated that the reinforcing capacity of the multilayer geogrids was mobilized at much lower load cycles than the typical single layer geogrid reinforcement.

The single stage RLT test results clearly demonstrated that the inclusion of geogrid reinforcement within base course material samples resulted in a reduction in the permanent deformation accumulating under cyclic loading. This improvement can be attributed to the increase in the lateral confinement due to the presence of geogrid reinforcement. The stiffness of the geogrid is a key factor in doing this. However, looking at the results of the statistical analysis reveals that the geogrid stiffness was the least significant factor affecting the reduction in permanent deformation. Thus, the reduction in the permanent deformation cannot only be explained by the apparent confining pressure caused by the stiffness of the geogrid. This agrees with the findings of Konietzky et al. (2005), who indicated that only 10% of the permanent deformation reduction can be attributed to the geogrid stiffness.

Many studies indicated that the dominant geogrid reinforcement mechanism in a pavement structure is the interlocking (McGown et al. 1990; Perkins and Ismeik, 1999; Koniazty et al., 2004; Sprague, 2004; etc.). The interlocking is caused by the interaction between the aggregates and the geogrid (e.g., traverse ribs of geogrid). McGown et al. (1990, and 1998) also recognized the existence of a dynamic geogrid–aggregate interlock mechanism under cyclic loading. Recently, a discrete element analyses (DEM) of the

geogrid reinforced samples demonstrated that the greatest effect of geogrid interlocking occurs in the immediate vicinity of the geogrid, such that the interlocking occurs across the entire cross-section (MecDowell, 2005). Beyond that, the interlocking effect is restricted only to the central part of the cross-section. The DEM results showed that the influence of the geogrid appears to extend to approximately at 10 cm on either side of the geogrid. This may explain why the highest improvement in this study was achieved when reinforcing the crushed limestone samples with two geogrid layers placed 10 cm apart.

Recalling that the imposed stress level was within range B shakedown stress limit for both base course materials considered in this study, the results of the statistical analyses demonstrated that the improvement due to the geogrid reinforcement was small during the primary post-compaction stage of range B stresses; however, it significantly increased after that. This can be explained by the fact that the geogrid improvement mainly results from the confinement effect caused by the geogrid-aggregate interlocking, and hence is expected to mainly contribute to the rotation and sliding mechanisms of the aggregate particles, which are mostly dominant in the secondary stage of range B. Based on this result, it is concluded that when the imposed stresses was within range B stress limit the geogrid had a minimum contribution to the permanent deformation resistance during the primary stage; however, its contribution significantly increased within the secondary stage.

4.3.2 Resilient Deformation

Figure 4.42 through Figure 4.47 present the average resilient strain curves for unreinforced crushed limestone I and II samples and samples reinforced with geogrid types II, IV, and V. The resilient strain had similar trend in both reinforced and unreinforced samples, such that it decreased with increasing the number of load cycles till

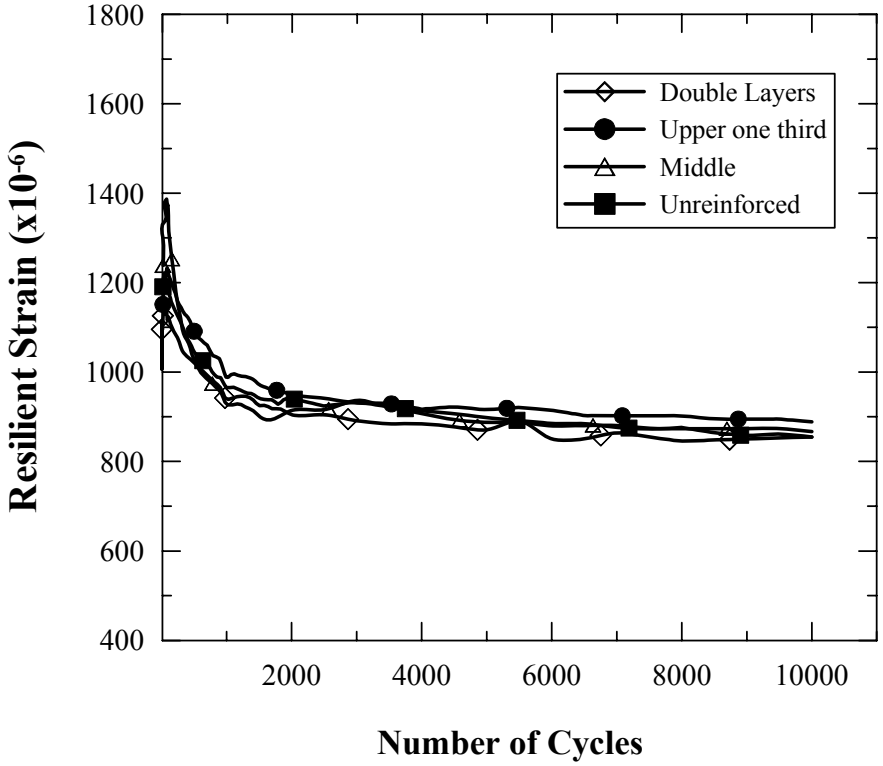

Figure 4.42 Resilient Deformation Curves of Crushed Limestone I Samples Reinfroced with Geogrid Type II

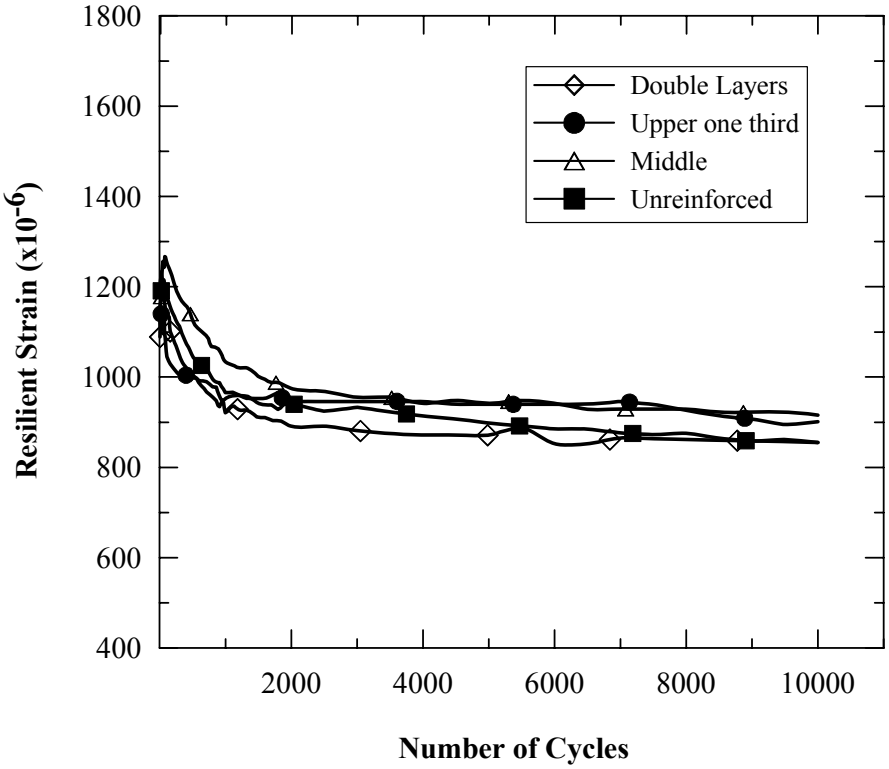

Figure 4.43 Resilient Deformation Curves of Crushed Limestone I Samples Reinfroced with Geogrid Type IV

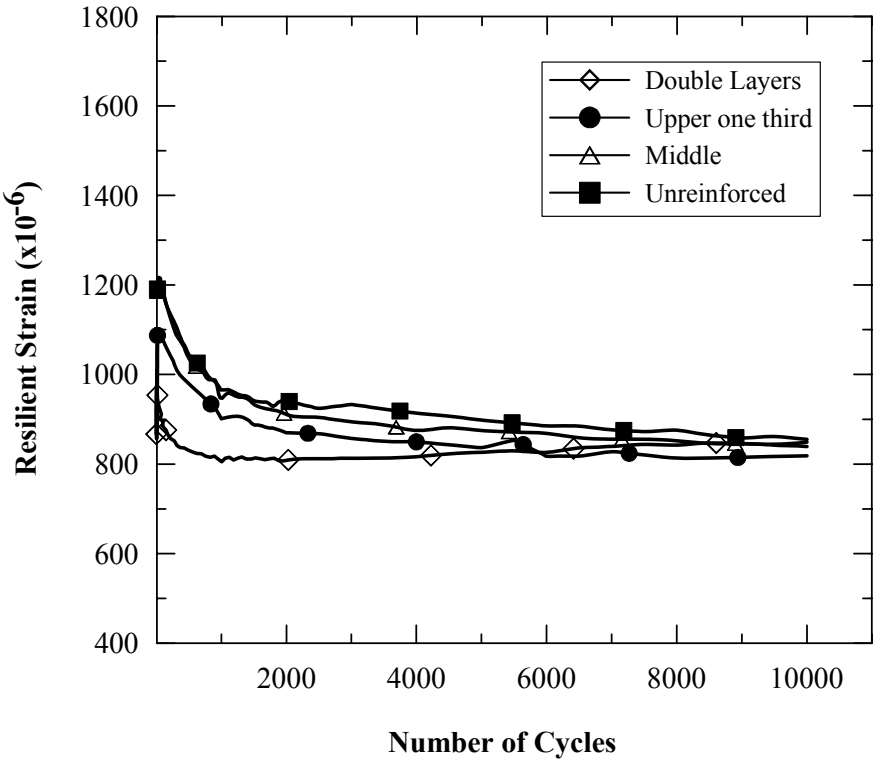

Figure 4.44 Resilient Deformation Curves of Crushed Limestone I Samples Reinfroced with Geogrid Type V

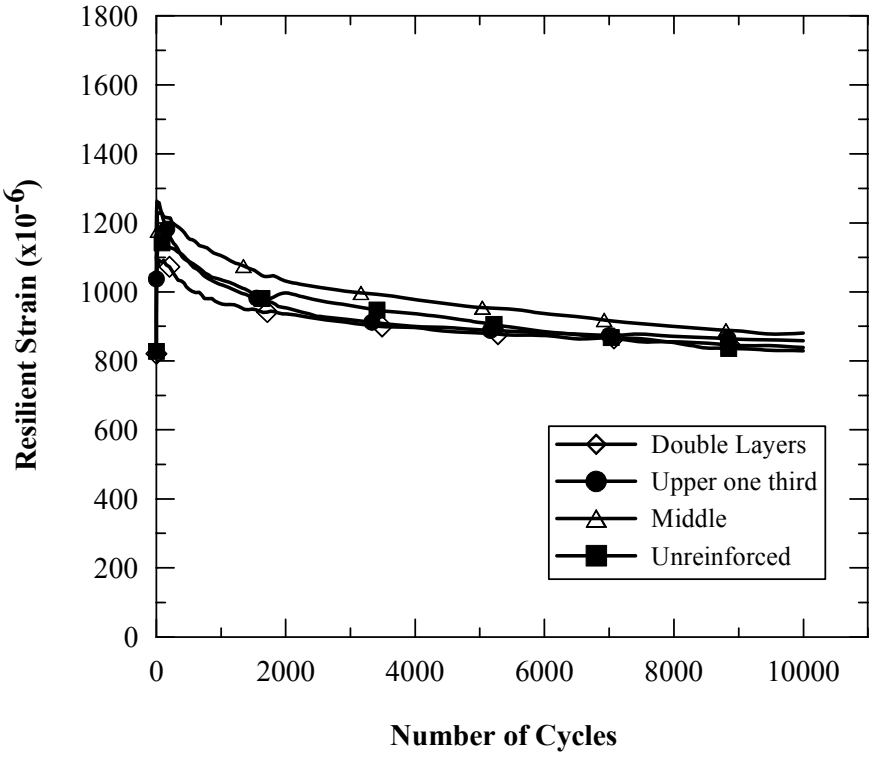

Figure 4.45 Resilient Deformation Curves of Crushed Limestone II Samples Reinfroced with Geogrid Type II

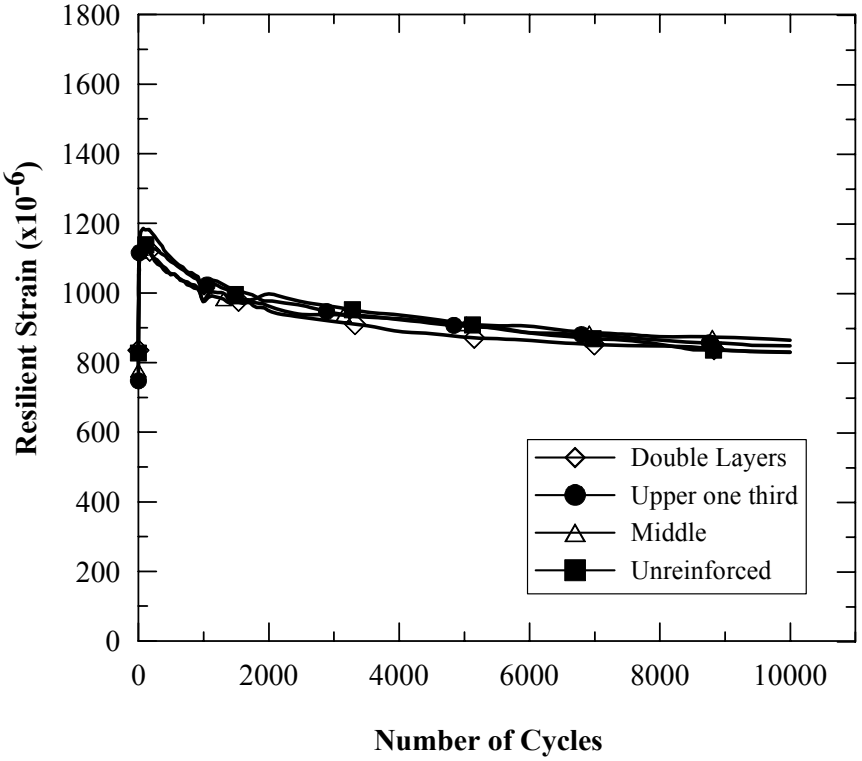

Figure 4.46 Resilient Deformation Curves of Crushed Limestone II Samples Reinfroced with Geogrid Type IV

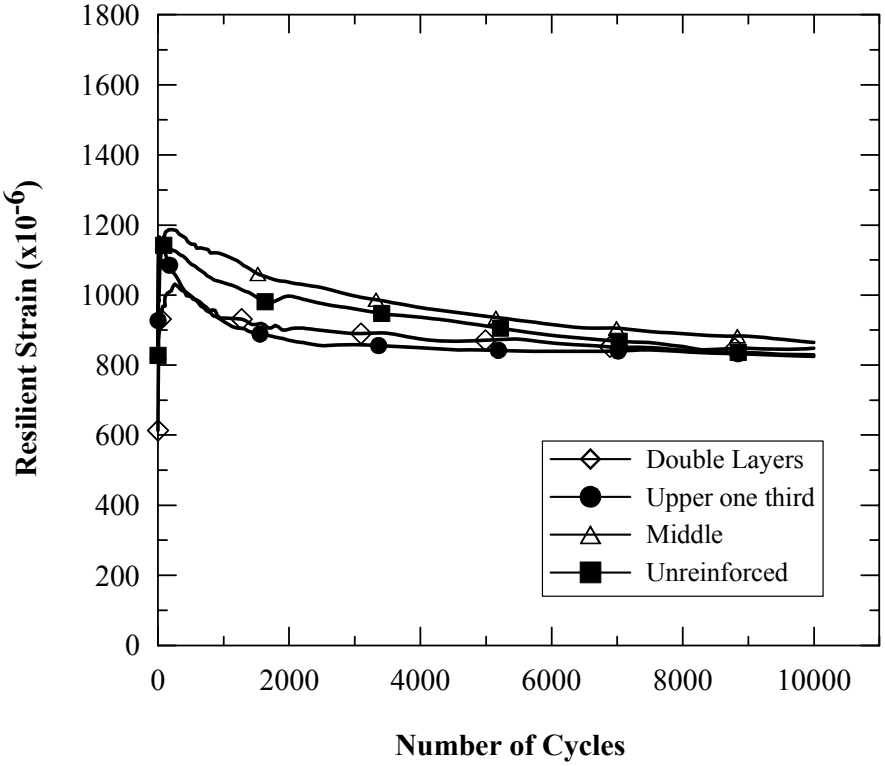

Figure 4.47 Resilient Deformation Curves of Crushed Limestone II Samples Reinfroced with Geogrid Type V

reaching an asymptote and then maintaining the same magnitude for the rest of the test, and hence reaching a steady resilient response. Similar observation was reported by Mohammad et al. (2006). The reason for this behavior is that in the primary post-compaction stage, the sample accumulates more deviatoric strain in the horizontal direction (perpendicular to the direction on which the cyclic load is applied), causing the Poisson ratio to decrease slightly. This will cause in an increase in the samples' stiffness, and hence a decrease in the resilient strain. It should be noted that the number of cycles needed for the sample to reach a steady resilient response increases as the imposed deviatoric stress is increased.

It can be noticed the crushed limestone I samples reached the steady resilient state at a lower number of load cycles (1000 cycles) compared to crushed limestone II samples (5000 cycles). This may indicates that the applied stress was closer to range A limit for crushed limestone I material than that of crushed limestone II. This can also be inferred from the permanent strain, where the crushed lime stone II accumulated higher permanent strain.

Figure 4.42 through Figure 4.47 demonstrate that the geogrids did not have a significant effect on the resilient behavior of the crushed limestone samples. This result is consistent with the recent work reported by Moghaddas-Nejad and Small (2003), and Perkins et al. (2004) where similar test results were reported on different granular materials (silica sand and aggregates) reinforced with geogrid layers. The reason for this behavior is that the resilient deformation of a granular material is primarily due to the deformation of individual grains (Werkmeister et al., 2002). However, the presence of geogrids did not alter the deformation of individual grains significantly, thus they do not have a great contribution to the resilient deformation behavior of reinforced samples.

4.4 Effect of Moisture Content

The effect of moisture content on the benefits achieved due to geogrid reinforcement was also evaluated by conducting single-stage RLT tests on unreinforced and geogrid reinforced crushed limestone II samples prepared at two moisture contents as well as the optimum moisture content. These moisture contents are: -2.5% of the optimum moisture content (dry side of optimum), and +2.5% of the optimum moisture (wet side of optimum). Based on the test results obtained at the optimum moisture content, two reinforced cases were selected to investigate the effect of moisture content; namely, the reinforced cases that had the highest and lowest geogrid reinforcement improvement (Type V–double layers case and Type II–middle location case, respectively). The following sections present the results of these tests.

4.4.1 Permanent Deformation

Figure 4.48 and Figure 4.49 compare the reduction in vertical permanent strain obtained for the two reinforced cases at the three different moisture contents considered in this study. It is observed that the geogrid benefit was more appreciable at the optimum moisture content than at dry side of optimum. In addition, for samples prepared at the dry side of optimum, the geogrid reinforcement has almost no effect on the permanent strain for the first 100 load cycles. Samples prepared wet of the optimum moisture content collapsed before reaching 10,000 cycles. This suggests that the stresses imposed on these samples exceeded the plastic shakedown stress limit, and thus were within the incremental collapse range (range C). As discussed in Chapter two of this dissertation , the main process dominating the development of the permanent deformation in range C is breakage and abrasion of particles. Alonso (2003) indicated that the increase in the

moisture content results in an acceleration of the particle contact breakage and therefore of the global deformation of the granular material.

Figure 4.48 and Figure 4.49 demonstrate that the improvement due to the geogrid reinforcement at the wet side of optimum, and hence, range C in this case, was less appreciable than that at the optimum moisture content, and hence in range B. This may indicate that the geogrid reinforcement does not have an appreciable effect on the processes causing the permanent deformation of the material within range C. To validate this statement, another set of RLT tests were conducted on unreinforced and geogrid reinforced samples prepared at +2.5% of optimum moisture content using a peak cyclic deviotoric stress of 185 kPa, which was found to be less than the plastic shakedown stress limit. Figures 6c and 6d compare the reduction in permanent strain for two reinforced cases prepared at +2.5% wet of optimum moisture content, but tested using different peak cyclic deviotoric stress. Although the samples were prepared at the same moisture content, the geogrid reinforcement had a greater improvement when the applied stress were less than range C stress limit.

4.4.2 Resilient Deformation

Figure 4.52 through Figure 4.54 present the vertical resilient strain curves obtained for unreinforced samples and samples prepared at the optimum moisture content, wet and dry sides of optimum moisture content, respectively. The resilient strain had similar trend in samples prepared at the optimum moisture content and at the dry side of optimum moisture content, such that it decreased as the number of load cycles increased until reaching a steady value. However, the magnitude of resilient strain encountered in samples prepared at the optimum was higher than those prepared at dry side of optimum. In addition, the number of cycles needed for samples prepared at dry side of optimum to

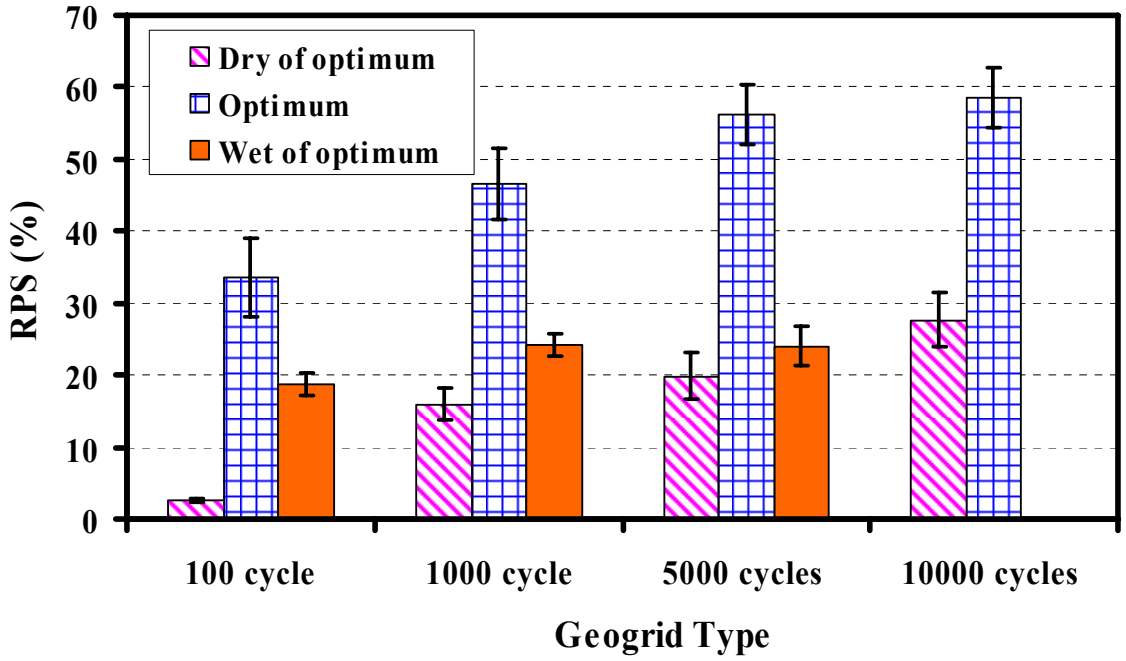

Figure 4.48 RPS for Geogrid Type IV- Double Case Prepared at Different Moisture Contents

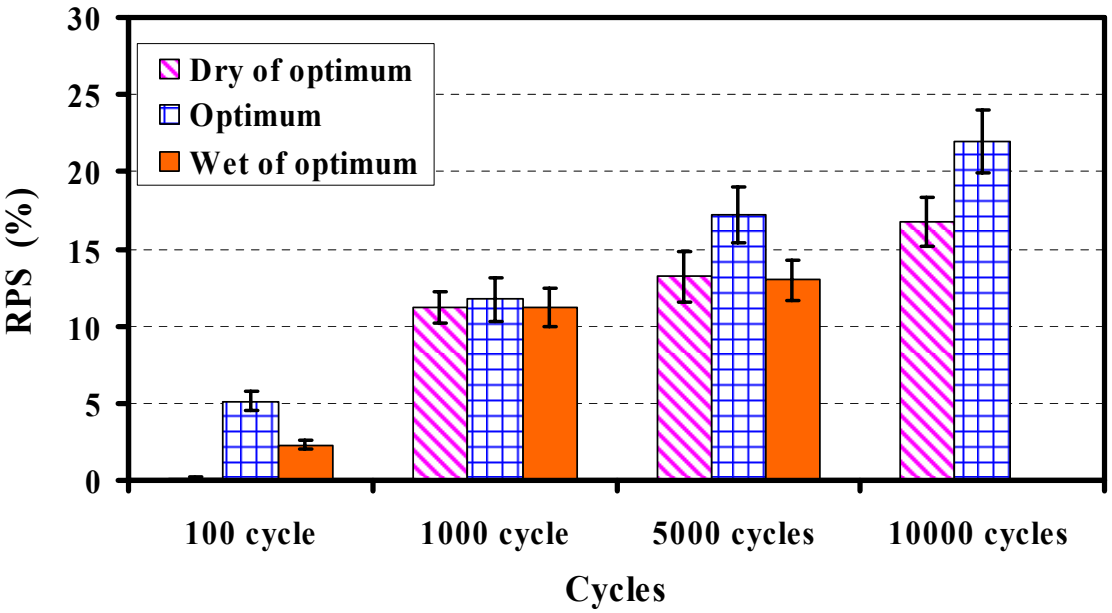

Figure 4.49 RPS for Geogrid Type II Middle Case Prepared at Different Moisture Contents

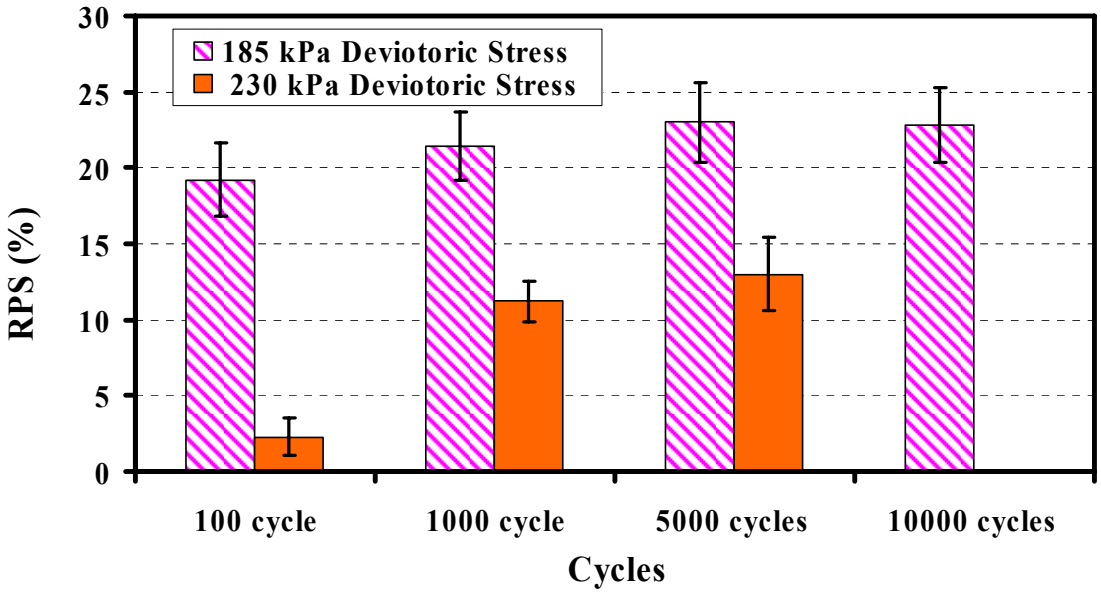

Figure 4.50 RPS for Geogrid Type V Double Case Prepared at Wet of Optimum Tested at Different Cyclic Stress

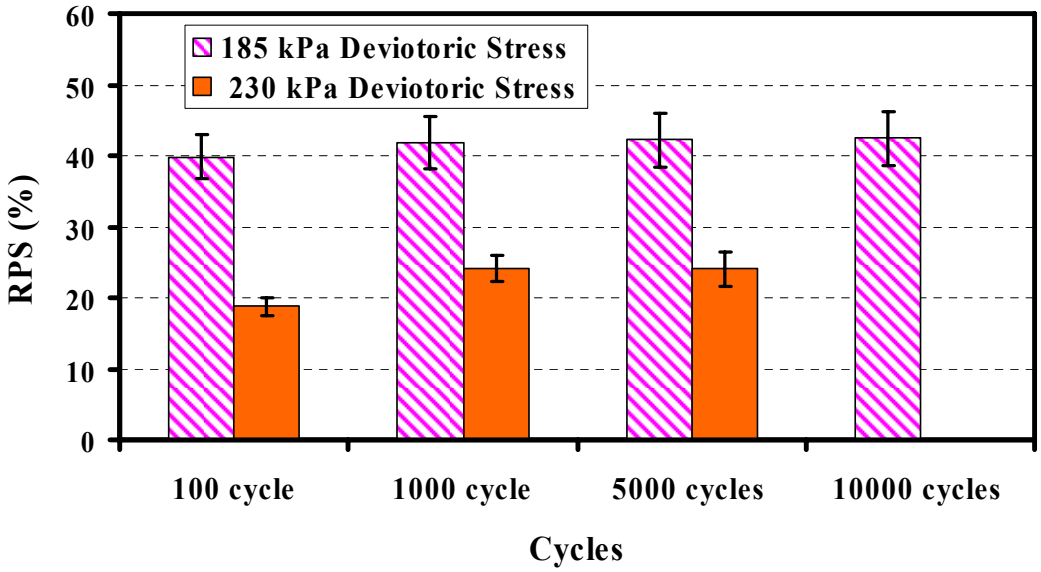

Figure 4.51 RPS for Geogrid Type II Middle Case Prepared at Wet of Optimum Tested at Different Cyclic Stress

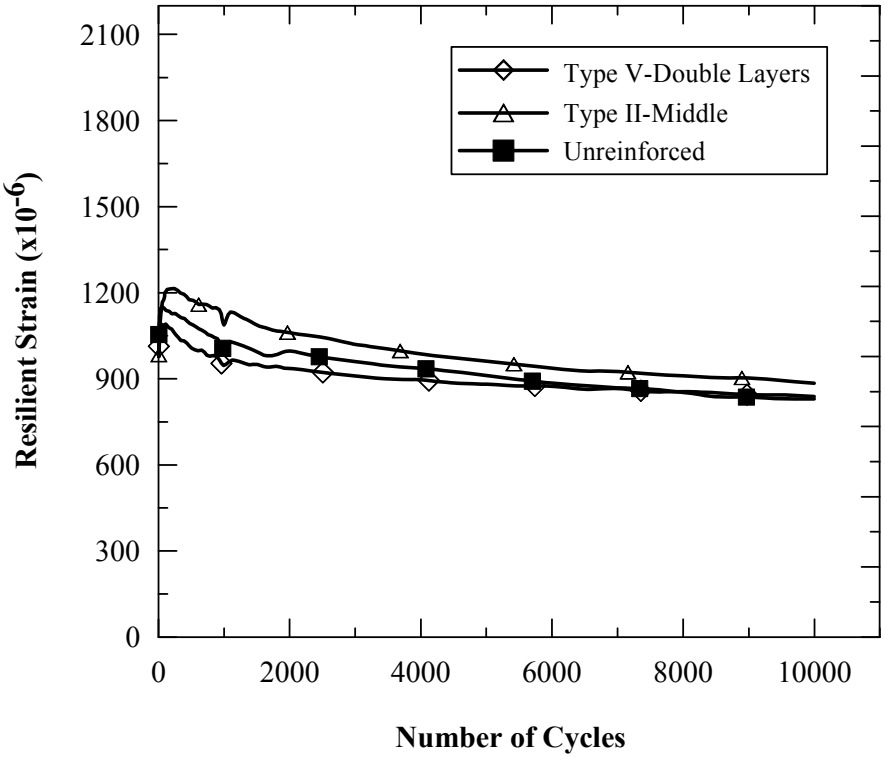

Figure 4.52 Resilient Strain Curves of Unreinforced and Reinforced Samples at Optimum of Moisture Contents

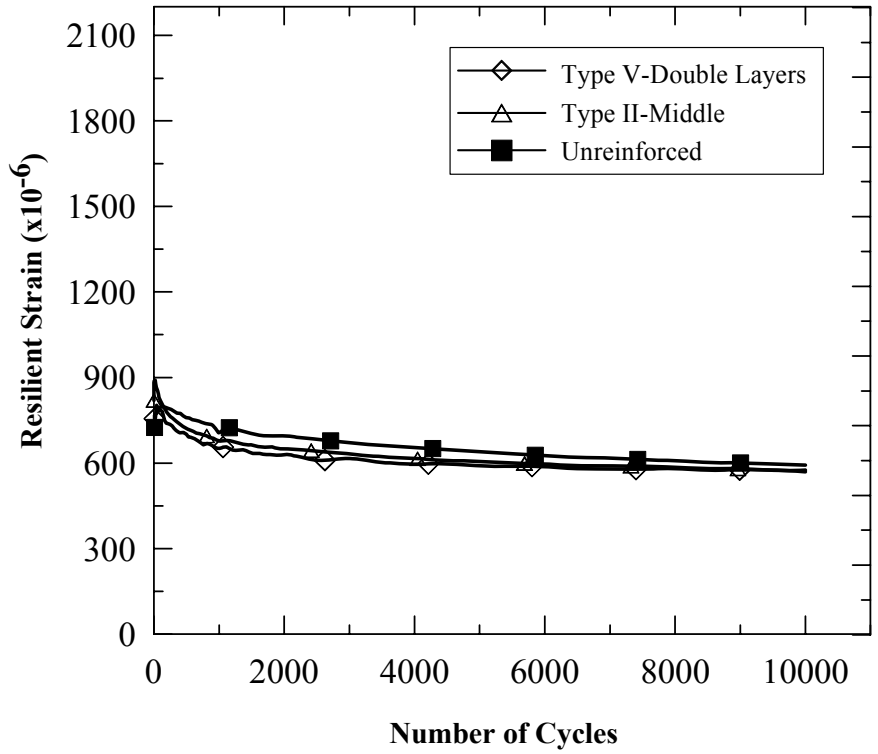

Figure 4.53 Resilient Strain Curves of Unreinforced and Reinforced Samples -2.5% Optimim of Moisture Contents

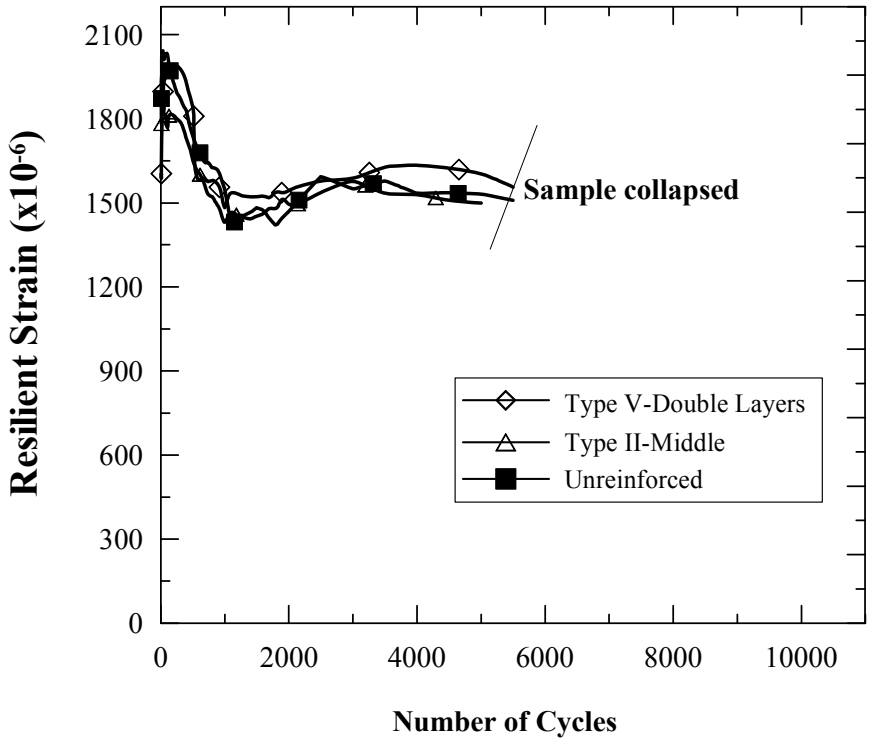

Figure 4.54 Resilient Strain Curves of Unreinforced and Reinforced Samples +2.5% Optimim of Moisture Contents

reach a steady resilient strain was less than those needed for samples prepared at the optimum moisture content. On the other hand, the resilient strain behavior for samples prepared at the wet side of optimum was different than samples prepared at the other moisture contents, such that it decreased significantly at the beginning of the test, then slightly increased, and decreased again. Werkmeister et al. (2002) reported similar behavior for base course material with applied stresses within the incremental collapse range (range C). They indicated that if the cyclic stress level exceeds the static failure line, then an initial decrease in resilient strain occurs, followed by an increase of resilient strain with a further increase in the number of load cycles. While Garc´ıa-Rojo et al. (2005) suggested that in the incremental collapse range, the resilient strain varies, reflecting the changes in the configuration of the sample.

4.5 Multi-Stage RLT Tests

Multi-stage RLT tests were conducted on crushed limestone II samples at their optimum compaction condition to characterize the permanent deformation behavior of this material at different stress levels, and to determine the shakedown ranges, which will be used later in this dissertation.

The analysis of Multi-stage RLT tests included first plotting the permanent vertical strain rate (per cycle of loading) versus the permanent vertical cumulative strain. Based on that figure, the three shakedown ranges were determined. This is illustrated in Figure 4.55 and Figure 4.56, which present the results from a multi-stage RLT tests conducted on crushed limestone II samples. Three different responses were observed at the different stages of cyclic loading. During Stage I, II, and III, the response of crushed limestone II material is within Range A; Range B response is manifested during Stage IV; and Range C response is observed during Stage V and VI as the loading approaches the failure line obtained from monotonic triaxial tests. The following sections describe the behavior of the material at each range.

It is observed that during Range A, plastic shakedown range, the material shows high permanent strain rates per load cycle during the post-compaction primary stage. This high permanent strain rate is due to the sample densification and particle rearrangement. With additional load cycles, another stage is reached, where the magnitude of permanent strain rate is progressively decreases owing to the fact that the grain assembly has already been rearranged during the initial load cycles, until it reaches a very small value, and hence, a steady state is reached, in which a nearly pure resilience behavior is observed. After reaching the steady state behavior, small amount of plastic strains still takes place but at a progressively slower rate as the number of load cycles increases. The deformation

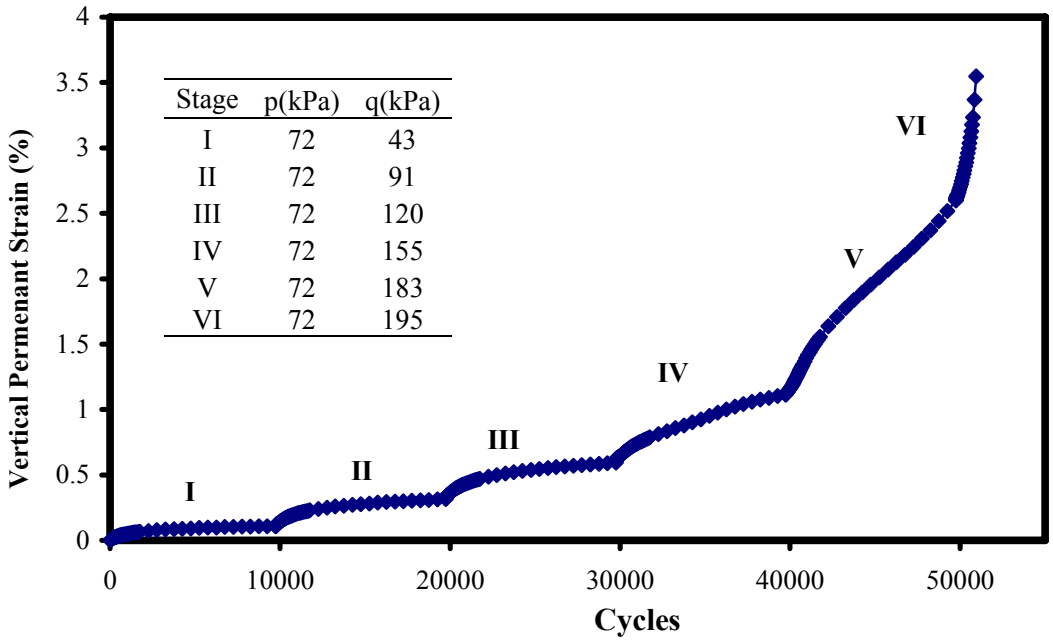

Figure 4.55 Vertical Permanent Strain Versus Number of Load Cycles Obtained from Multi-Stage RLT Tests on Crushed Limestone II

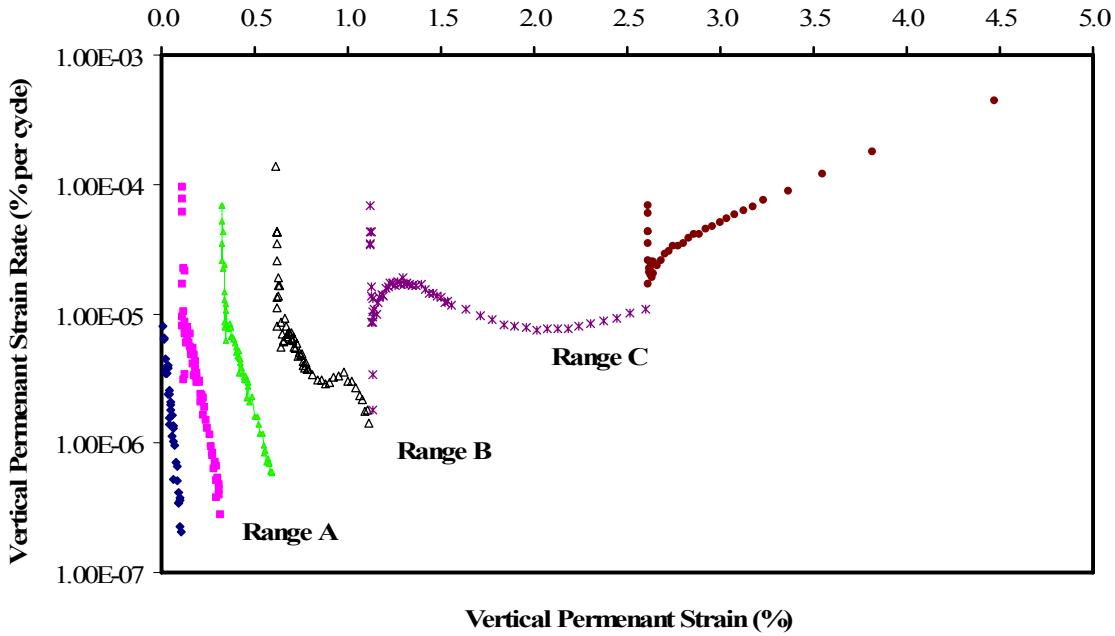

Figure 4.56 Vertical Permanent Strain Rate Versus Vertical Permanent Strain Obtained of Multi-Stage RLT Tests on Crushed Limestone II

is due only to the deformation of the single grains and to the very limited recoverable particle rotations (Werkmeister et al., 2004).

It is noted that in Figure 4.56, the range A behavior plots as a convex-downwards line because the permanent strain rate progressively decreases effectively halting any further accumulation of strain and leading to an asymptotic final (vertical) permanent strain value. For this range, Figure 4.56 shows that the level of accumulated strain depends on the load level (deviator stress). Detailed inspection of the individual test results shows that the number of cycles required, before plastic strain ceases, increases with an increase of load level.

Figure 4.56 shows that the behavior of the material during the primary stage in range B, the plastic creep shakedown range, is similar to that in Range A. However, in the secondary stage the behavior is different. Such that, it is observed that the permanent strain accumulation decreases at relatively smaller rate. The deformation in the secondary stage in this range is due to the relative inter-particle movement and the deformation of the particle themselves (Rodriguez, 1988,). The deformation at the inter-particle contact may be quite large, and consists initially of distortion and eventually local fracture and crumbling, in addition to particle re-orientation. The re-orientation mechanism is characterized by rotation and sliding of the particles. The resistance to particle sliding and rotation depends on the inter-particle friction. On the other hand, the deformation of particles includes particle breakage and crushing, which have little importance in range B stress levels. In range B the particle rearrangement, inter-particle slip and the continued frictional energy loss is associated with ongoing damage. This damage can result in reaching constant level of permanent strain rate, where permanent strain increases linearly, leading to material incremental collapse, and thus, to reaching the tertiary stage.

The number of cycles to reach incremental collapse depends on the stress level, the higher applied stresses the less the number of load cycles required to reach to the tertiary stage.

Finally, Figure 4.56 shows that in range C, the incremental collapse shakedown range, the material exhibits continuing incremental permanent strain with each additional stress cycle. Thus, the response is always plastic and each stress application results in a progressive increment in the magnitude of permanent strain. The initial behavior observed in other ranges(A, B) is probably the same as that shown in Range C, but compressed into a fewer number of stress applications as a consequence of the much higher cyclic stress level applied. In addition the tertiary stage occurs at relatively much lower number of load cycles. This suggests that the range C stresses are high enough to cause significant energy loss per cycle. Hence a great degree of damage occurs almost from the beginning of cyclic load application. It is noted in Figure 4.56 that the beginning of the collapse process is recognized by an increasing rate of permanent strain development following a period of decreasing strain-rate after which strain-rate levels remain high and there is no cessation of strain accumulation.

The non-stable material behavior and large permanent strain rates in range C results from the relatively large-scale particle re-orientation. The large-scale particle re-orientation is caused by the grain abrasion and particle crushing. This is governed by the magnitude of applied stresses, and the mineralogy and strength of the individual particles themselves.

After determining the shakedown ranges for each testing stress from the results of multi-stage RLT tests, the boundary between these ranges is interpolated assuming a linear function and plotted in *p-q* stress space. The boundary between shakedown Range

A and B was taken as the best fit straight line through the highest vertical testing stress possible for shakedown Range A for the four tests at maximum mean stresses of *p*: 72, 145, 198 and 240 kPa. A best fit straight line was fitted to the lowest vertical stresses where shakedown Range C occurred for the B/C boundary. Figure 4.57 shows the shakedown range boundaries for the material tested. For comparison the static yield line is also shown. These shakedown range plots can be used in predicting the likely performance of the material in the pavement as done in finite element modeling conducted in Chapter 6. It is assumed that if traffic induced stresses computed within the pavement material all plot below the shakedown Range A/B boundary in *p*-*q* stress space then stable Range A behavior of the material is expected.

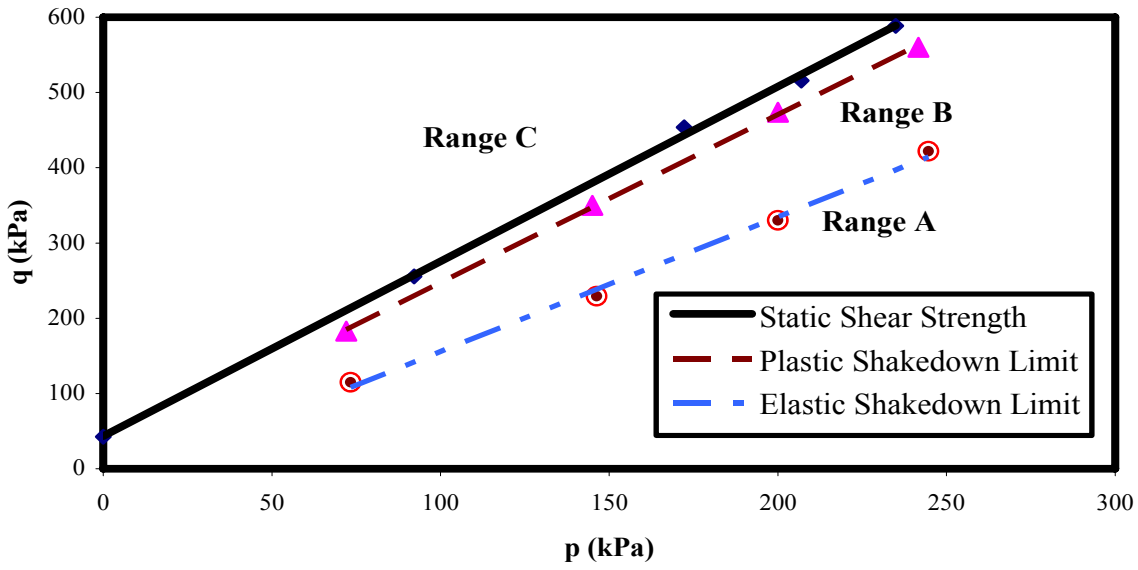

Figure 4.57 Shakedown Limits for Crushed Limestine Material II at Field Optimum Condition

Chapter Five
Calibration Implementation and Verification of Constitutive Models for Base Course Materials

This chapter discusses the calibration of the extended Drucker-Prager and the two surface critical state constitutive model parameters. Numerical implementation of the two surface model in finite element analysis is also presented. Furthermore, this chapter presents the evaluation and verification of the prediction of each of the mentioned models.

5.1 Calibration and Verification of Extended Drucker-Prager Model

The extended Drucker-Prager model used in this study requires two parameters to define its yield function, namely, the friction angle, β, and the cohesion, *d*. Both parameters can be determined using triaxial compression tests. Furthermore, the used model has isotropic hardening which can be defined using the data from triaxial tests.

A set of drained triaxial compression tests were conducted on each of the crushed limestone materials described earlier in Chapter 4, at their optimum conditions, in order to calibrate the extended Drucker-Prager model parameters. The tests were conducted using four different confining pressures. Figure 5.3 and Figure 5.4 present the static yield line in p-q plane obtained from triaxial tests conducted on crushed limestone I and II, respectively. Based on the results of the triaxial tests, the β, and *d* parameters for crushed limestone I, were 48, and 26 kPa, respectively, while for crushed limestone II material they were 50 and 45 kPa, respectively.

After the calibration of the extended Drucker-Prager model, the model was used to predict the constitutive behavior of the crushed limestone I and II materials. Measured

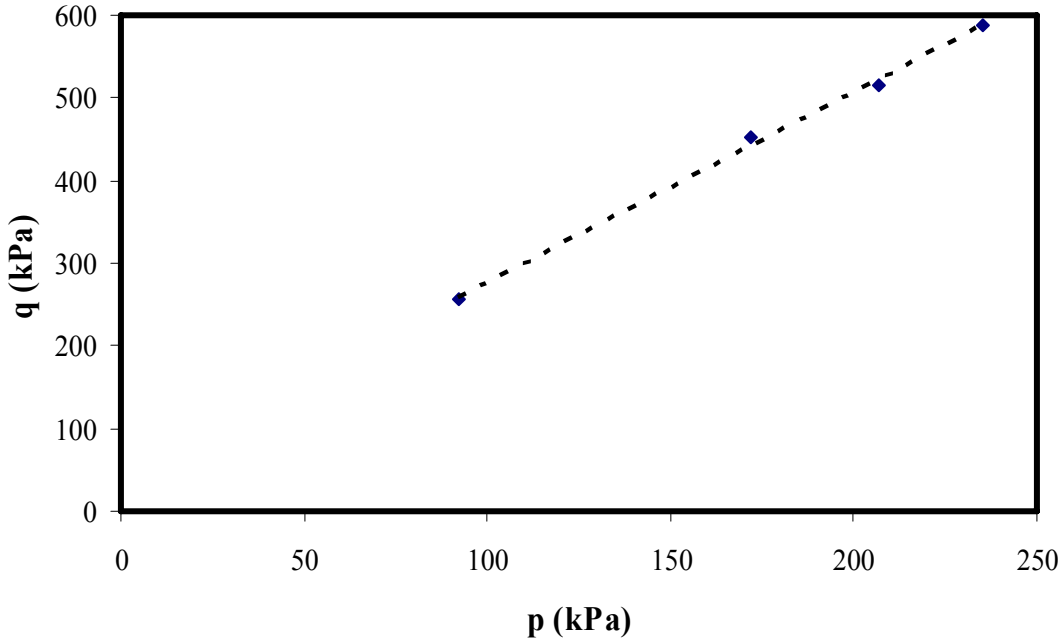

Figure 5.1 Calibration of Drucker-Prager Model Parameters for Crushed Limestone I

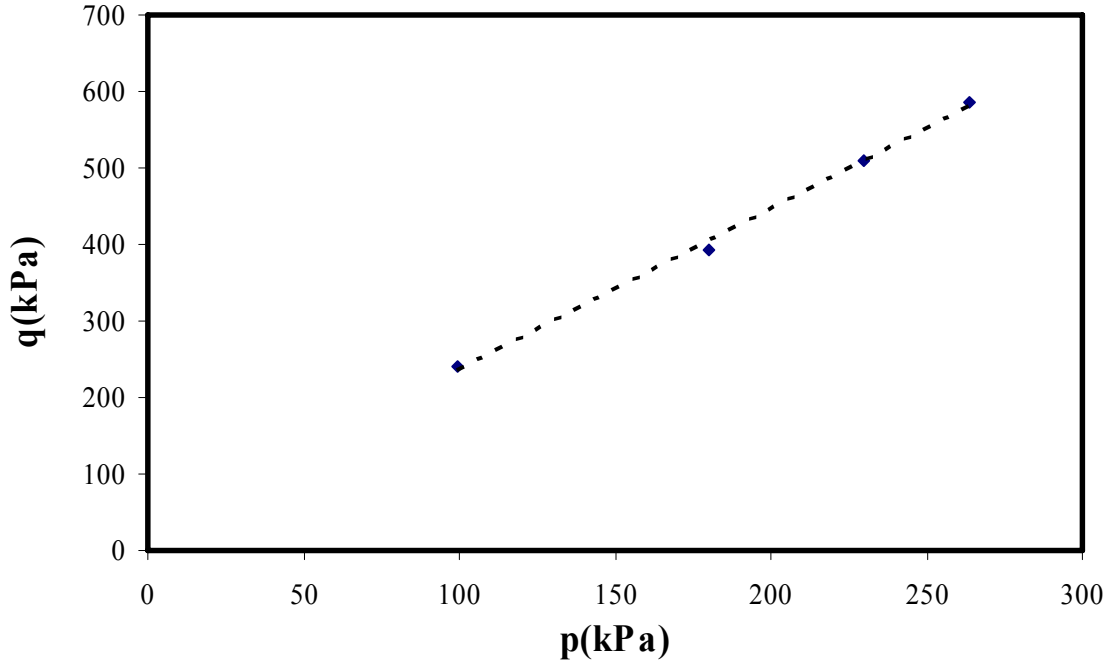

Figure 5.2 Calibration of Drucker-Prager Model Parameters for Crushed Limestone II

and predicted stress-strain results were compared for both materials. Figure 5.3 and Figure 5.4 compares the stress-strain behavior predicted using the extended Drucker-Prager model and those measured in the triaxial tests. It is noticed that for the crushed limestone I, the model prediction matched the experimental test results closely. However, extended Drucker-Prager model was not capable of predicting the peak, and post peak strain softening behavior of crushed limestone II material. Based on this result, the two surface critical state constitutive model was selected to model the behavior of the crushed limestone II material.

5.2 Calibration and Verification of the Two Surface Critical State Model

A set of 21 parameters is required to completely define the two surface elastoplastic model in a fully three-dimensional space. These parameters can be grouped into four categories:

1. Elastic parameters
2. Critical state parameters
3. Model specific parameters
4. Parameters for normalizing the unsaturated behavior.

The elastic and critical state parameters can be obtained directly from experimental test results. In contrast, model-specific parameters must be obtained using experimental test results and trial-and-error procedures. Details on the calibration procedure for all parameters are described in the following sub-sections.

5.2.1 Elastic Parameters

The two surface critical state model requires three material parameters to define the non-linear elastic behavior of the material, namely, initial bulk modulus, K_o , Poisson's ratio, υ, and a properly defined exponent yielding the variation of the elastic

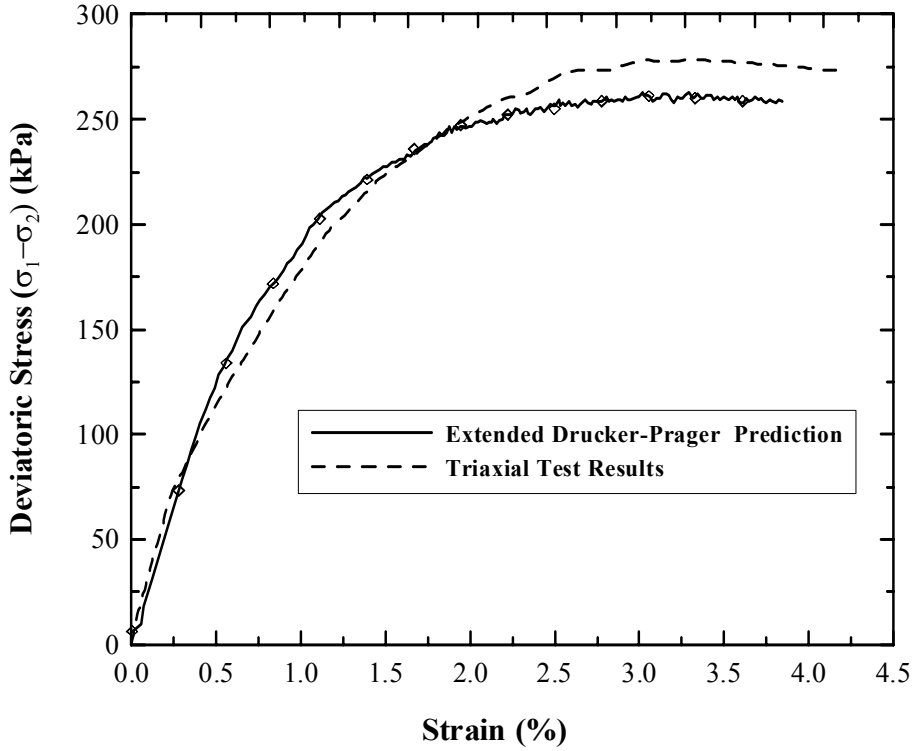

Figure 5.3 Extended Drucker-Prager Prediction of Crushed Limestone I Behavior

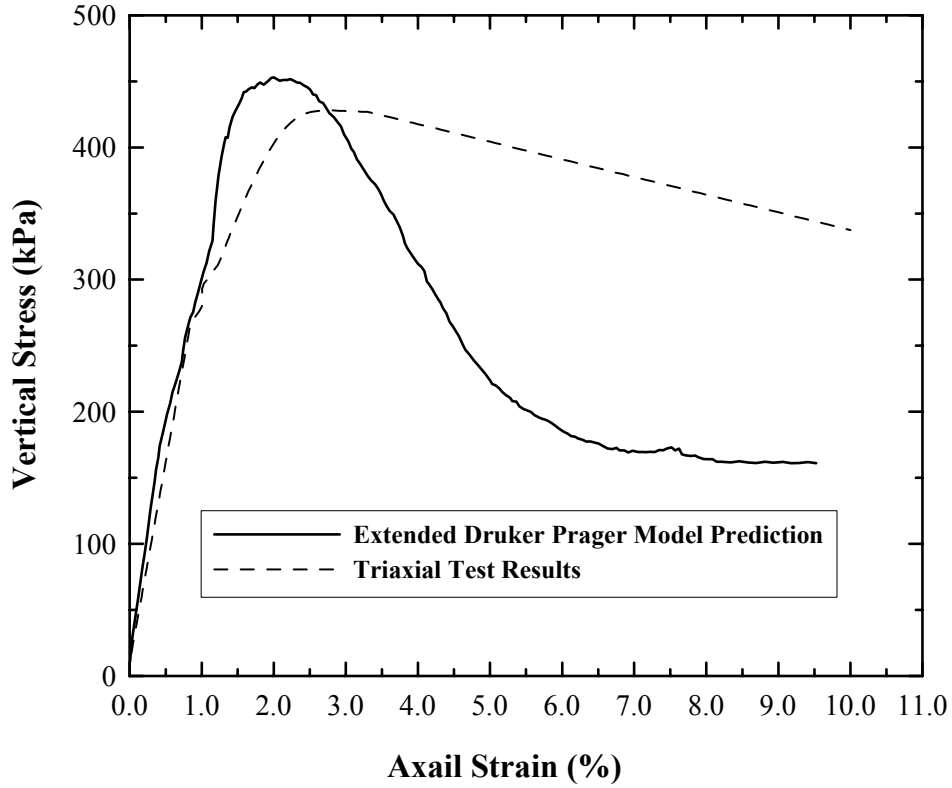

Figure 5.4 Extended Drucker-Prager Prediction of Crushed Limestone II Behavior

modulus with the mean stress (p), b. Since the non-linear elastic modulus elastic part of this model depends on the first stress invariants (mean stress p), any type of triaxial test can be used to define the three parameters. For this study, consolidated undrained triaxial tests were used.

The calibration of the three model paramters, involved first determining the elastic modulus, *E,* directly from triaxial test data. Since the initial elasticity modulus can be sometime misleading, the elastic modulus was estimated from the loading-unloading and reloading cycle. Knowing E, and υ, the bulk modulus (K) was computed using Equation 5.1. In this study, a Poisson's ratio value of about 0.3 was used, which was reported by Heath (2002) for crushed limestone materials. It should be noted that the variation of the Possion's ratio does not affect the numerical results of the present model.

$$K = \frac{E}{3(1-2\nu)} \qquad 5.1$$

Knowing the bulk modulus at different values of mean stresses, K_o and b parameters were estimated by plotting K versus the $\frac{P}{Patm}$ as shown in Figure 5.5, and fitting a non-linear regression model through the data. Based on the results of triaxial tests a K_o and b values of 103.1 MPa and 0.72 were obtained, respectively.

5.2.2 Critical State Parameters

Parameters in this category define the critical state of a soil. The critical state of a soil describe a unique relationship between mean effective stress, p, deviatoric stress, q, and void ratio, e, at which plastic shearing continues indefinitely without changes in volume or effective stresses. Because three variables (p, q, and e) are required to determine the critical state, it is defined as a 3-D line or surface. Alternatively, it can also be identified in terms of three-dimensional stress ratios, or stress invariants (q and p) and

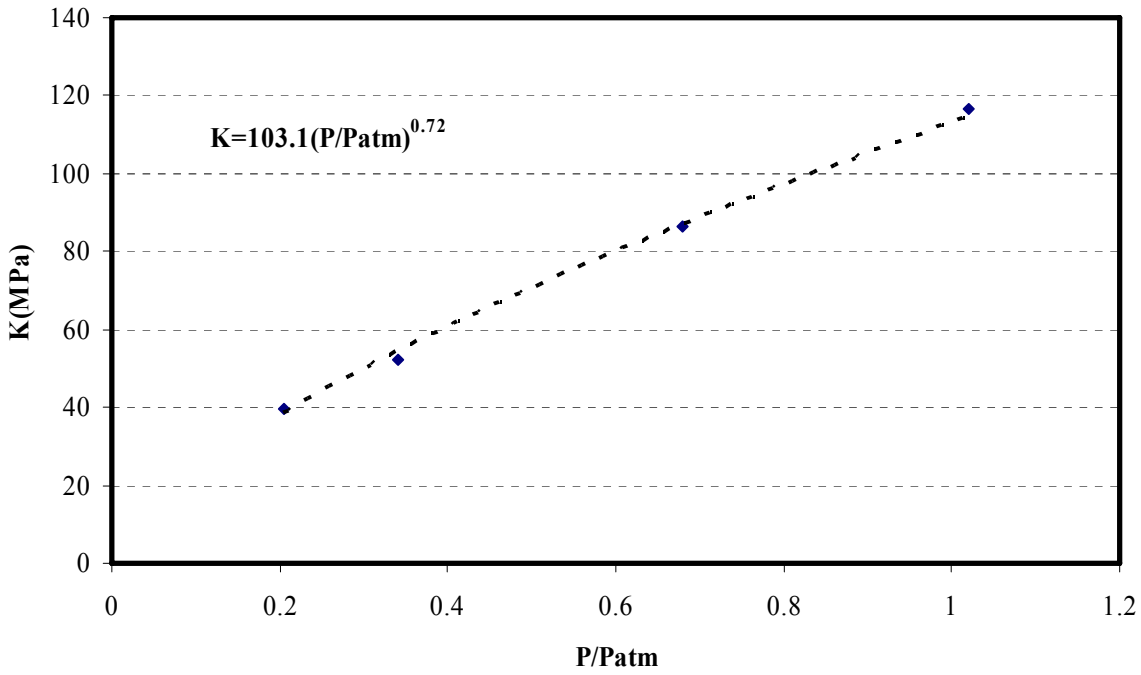

Figure 5.5 Calibration of None-Linear Model Parameters

a relationship between mean effective stress, p, and void ratio, e. In this study the second approach was used.

The critical state parameters are M_c, M_e, λ ,$e_{c,ref}$ and p_{ref} . M_c and M_e represent the slope of the critical state lines in compression and extension in q − p space, respectively. These parameters can be related using the following equations:

$$M_c = \frac{6\sin(\phi`)}{3-\sin(\phi`)} \qquad 5.2$$

$$M_e = \frac{6\sin(\phi`)}{3+\sin(\phi`)} \qquad 5.3$$

Where $\phi`$ is the critical state friction angle.

Figure 5.6 shows the critical state line in p-q space that was obtained from the results of undrained triaxial tests. Based on this result M_c and M_e values of 1.91and 1.14 were obtained. The critical state in e vs. ln p space is defined in terms of λ ,$e_{c,ref}$ and p_{ref}. λ represents the slope of the critical state line. $e_{c,ref}$ and p_{ref} represent a reference point on

this line. These parameters are considered to be constants for a given soil regardless of initial state and loading condition. Based on the results of undrained trixaial tests a relationship between void ratio, e, and mean effective stress, p, was obtained as shown in Figure 5.7 . In this figure, the critical state is given by a straight line in e −ln p space with a slope of $\lambda = 0.0165$.

5.2.3 Model Specific Parameters

This category includes parameters that are specific for the current two-surface elastoplastic model. These are:

1) Surface parameters: Bounding and dilatancy (phase transformation) surface parameters $k^b_{c,e}$ and $k^d_{c,e}$

2) Initial yield surface parameter, m,

3) Hardening parameters, c_m and h_0,

4) Dilatancy parameter, A_0,

5) Fabric tensor parameters, F_{max} and C_f .

The following sections present the description and the method for obtaining each of these parameters and their effect on the model response.

5.2.3.1 Surface Parameter

Parameters $k^b_{c,e}$ and $k^d_{c,e}$ define the rate of evolution of the bounding and dilatancy stress ratios, $M^b_{c,e}$ and $M^d_{c,e}$, which in turn are associated with the critical stress ratios, $M_{c,e}$ and state parameter, ψ. In the current model formulation, these values are related to the evolution of the back stress ratios $\alpha^b_{c,e}$, $\alpha^d_{c,e}$, and $\alpha_{c,e}$. Due to their relationship to ψ, these parameters are also referred as state parameters. Good estimates for $k^b_{c,e}$ and $k^d_{c,e}$ can be obtained from evaluating test results: the peak and dilatancy stress ratios, $M^b_{c,e}$ and $M^d_{c,e}$, and initial state parameter, ψ_0.

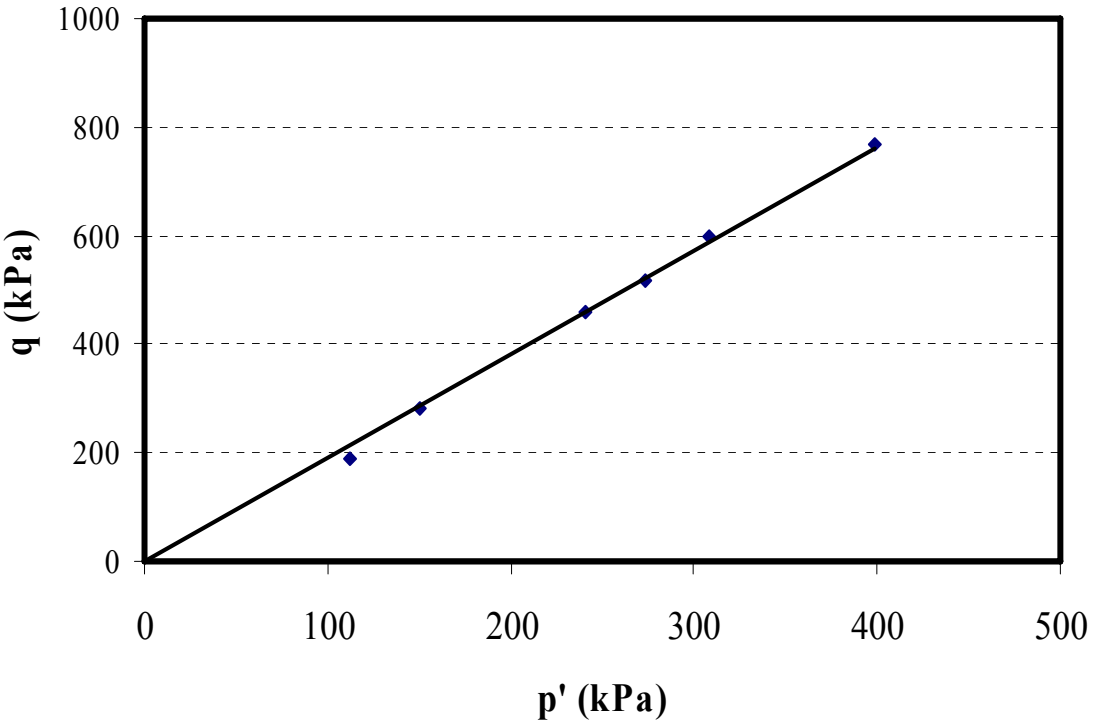

Figure 5.6 Critical state line (CSL) in p-q Space for Crushed Limestone II Material

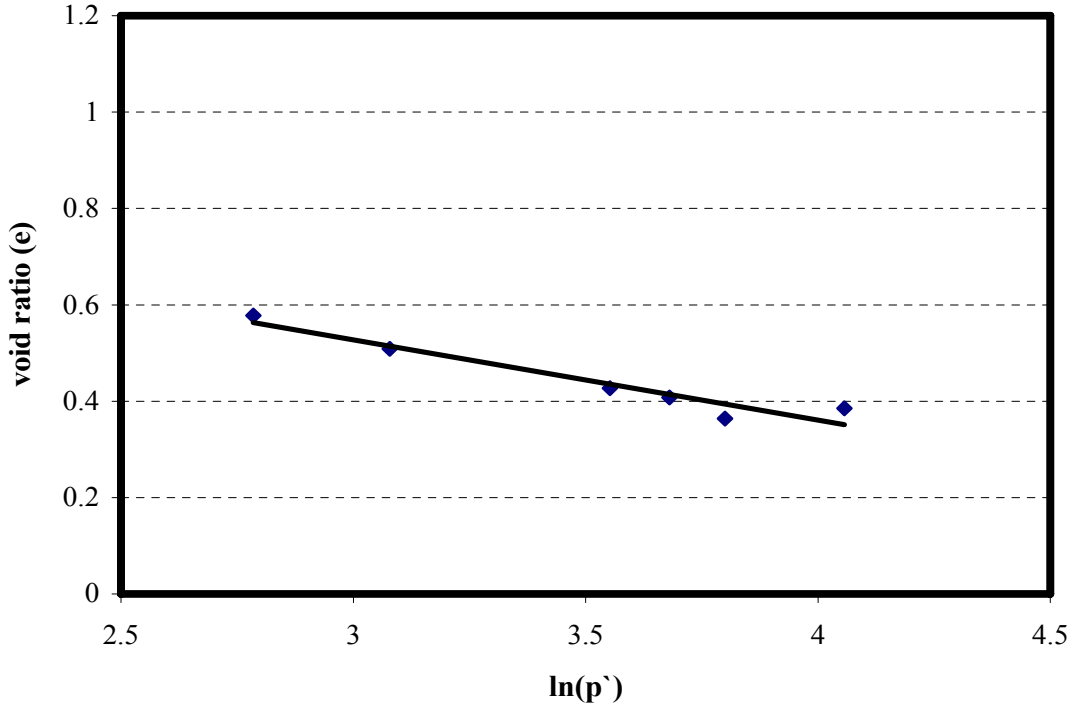

Figure 5.7 Crtical State Line (CSL) in e− ln p Spaces for Crushed Limestone II Material

Parameters $k^b_{c,e}$ play an important role in the evolution of the kinematic hardening, and, therefore, in the determination of the plastic modulus, K_p. K_p increases as $k^b_{c,e}$ increases. In turn, an increase in $k^b_{c,e}$ results in a decrease in the plastic strain. In this study values of $k^b_{c,e}$ were obtained from examining results from drained compression tests. Figure 5.8 presents the bounding stress line which connects the peak stresses obtained from the different triaxial tests. Based on the results and utilizing a procedure similar to that used for M_c/ M_e, M^b_c/ M^b_e values of 2.35/1.31 and k^b_c./ k^b_e. values of 4.5/1.74 were obtained.

Parameters $k^d_{c,e}$ control the rate of change of the dilatancy back-stress ratios, $\alpha^d_{c,e}$ which determine if a volumetric response is contractive or dilative. $k^d_{c,e}$ also affect the volumetric response and the plastic flow non-associativity. $k^d_{c,e}$ are obtained using undrained tests, since from these tests a distinct sign change in Δp can be observed when dilative behavior is triggered. Ishihara (1975) defined the point on the stress path, at

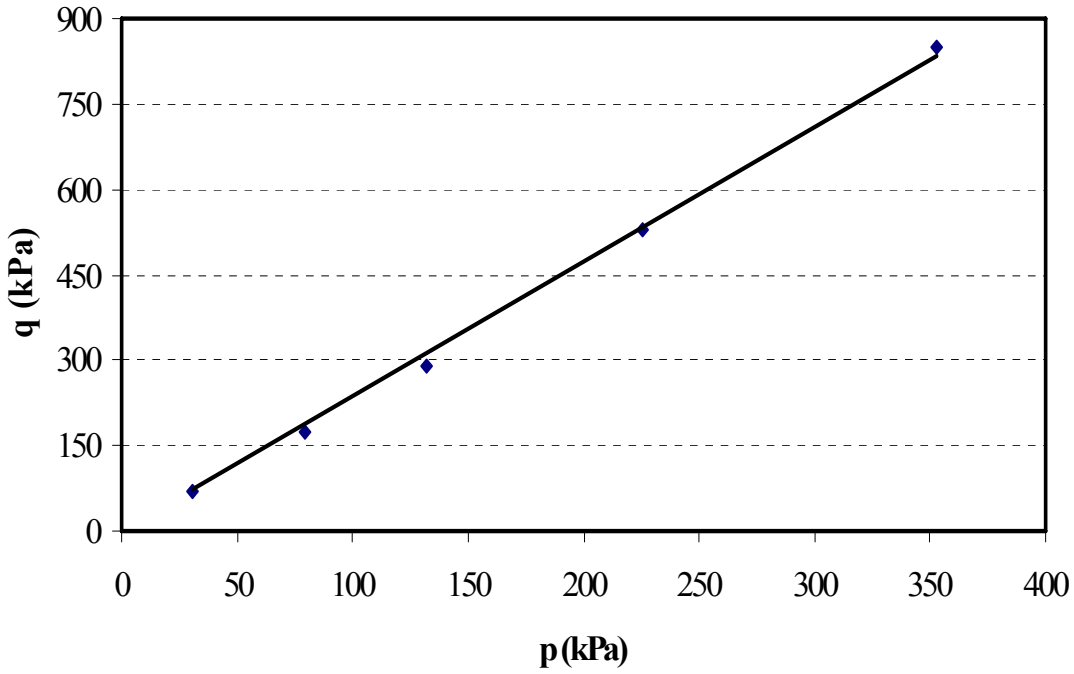

Figure 5.8 Bounding Stress Line in p-q Space for Crushed Limestone II Material

which the sign of Δp changes from negative to positive (or from contractive to dilative), as the state of phase transformation, and the line that connects these points to the origin as the phase transformation line (PTL). Phase transformation stress ratios are usually denoted by $M^d_{c,,e}$ In this study the phase transformation line was obtained from undrained triaxial test conducted on crushed limestone samples. The PTL was determined by fitting appropriate straight line from the origin to the points that satisfy the PTL definition given above. From the experimental tests, M^d_c/ M^d_e values of 1.675/1.07, and k^d_c/ k^d_e values of 2.3/0.72 were obtained.

5.2.3.2 Isotropic Hardening Parameters

The parameter *m* defines a purely elastic region in stress ratio space. The evolution *m*, referred to as an isotropic hardening law. The parameter c_m, together with the dilatancy coefficient *D* and plastic void ratio e^p, define this evolution. Manzari and Daflias (1997) suggested that small values of *m* and c_m should be used for granular soils. They suggested that a *m* value of 0.1 M_c can be used. In this study *m,* c_m values of 0.19 and 0.01 were used.

5.2.3.3 Kinematic Hardening Parameter

The parameter h_0 defines the evolution of the back-stress. Therefore, it defines the kinematic hardening. In fact the evolution law of the back-stress is a key ingredient of the model used. The h_0 works like a scaling factor for the plastic modulus which is determined by the distance between the stress state and the projected "image" state on the bounding surface. An increase in h_0 results in an increase in the plastic modulus K_p and, therefore, a decrease in plastic strains. h_0 can be obtained by matching the model prediction to the flattening slope of the deviatoric stress -vertical axial strain (q-ε_1) curve obtained in triaxial test.

Hardening parameters, h_0, was calibrated using a trial-and-error procedure evaluated using monotonic simulations (where there is no fabric effects do exist). A range of h_0 = 300-1000 was used for gravels subjected to monotonic triaxial test. Among the range used, h_0 = 800 appeared to be appropriate to reproduce the observed behavior of all monotonic tests.

5.2.3.4 Dilation Parameter A_0 and Fabric Tensor Parameters C_f and F_{max}

The volumetric response (dilation or contraction) due to shear loading is a key aspect of granular soil behavior to be predicted by any soil constitutive model. The two surface model used in this study predicts such volumetric behavior using a volumetric flow rule characterized by the dilatancy coefficient *D*. The incorporation of *D* results in an non-associative flow rule. In this study, to be consistent with the definition of kinematic hardening, it was assumed that *D* is related to back stress ratios. The evolution of the fabric tensor, **F**, is related to the dilatancy coefficient and its effect is manifested by an increase in the dilatancy parameter, A, upon loading reversals enhancing the contractive response. A change in dilatancy parameter occurs only when the directions of F and the gradient to the deviatoric yield surface, **n**, make an angle smaller than 90◦ (i.e., $\mathbf{F} : \mathbf{n} > 0$). F evolves only when dilation occurs (i.e., $D < 0$). C_f controls the rate of evolution of **F**, and F_{max} represents a maximum norm for **F**. A maximum value of F (i.e., $F = -F_{max}\mathbf{n}$) is reached at a loading reversal. It is also expected that at the critical state $\Delta\varepsilon^p_v = 0$ and D = 0, then $\dot{F} = 0$.

F_{max}, C_f and A_0 were calibrated using a trial-and-error procedure and were evaluated for the using the unload-reload curve in undrained consolidated triaxial tests. Initial values F_{max}, C_f, and A_0 were first estimated. Because these parameters affect the dilative/contractive model response, it was necessary to iterate all of them together.

Unfortunately, an unbalanced combination of these parameters can cause numerical instability particularly when the mean effective stress approaches zero, i.e., p = 0. Therefore, a certain level of care was required in this procedure. Based on the results of the trial-and-error procedure F_{max}, C_f, and A_0 values of 100, 100, and 0.35 were obtained, respectively.

5.2.3.5 Parameters for Normalizing the Unsaturated Response

Parameters for normalizing the unsaturated response of the crushed limestone material were calibrated in this study following a procedure similar to that presented by Heath (2002). In this procedure crushed lime stone II samples were prepared at three different moisture contents, namely, optimum moisture content, -2.5% of the optimum moisture content (dry side of optimum) and +2.5% of the optimum moisture (wet side of optimum). For each moisture content, drained triaxial compression test were conducted at three confining pressure. The peak strengths for each samples was then determined and used to plot the static failure line in p-q space as shown in Figure 5.9.

A nonlinear regression analysis was then conducted on the data to determine the regression parameters that yield the least square error when predicting q using Equation 5.4. The results of this analysis are shown Figure 5.10. Based on the results of this regression analysis, n_1, n_2, and n_3 were 0.0263, 1.975, and 2.363, respectively.

$$q = M_b\left(p + p_{suc}\right) = M_b\left(p + \left(p_{atm}\right)\frac{\theta}{e}\left(\frac{1}{\theta^{n_1}} - \frac{1}{e^{n1}}\right)^{\frac{n_3}{n_2}}\right) \qquad 5.4$$

5.3 Numerical Implementation of Critical State Two-Surface Elastoplastic Model

A key step in the implementation of any elasto-plastic model involves integrating the constitutive relations to obtain the unknown increment in the stresses. These relations define a set of ordinary differential equations and methods for integrating them are usually

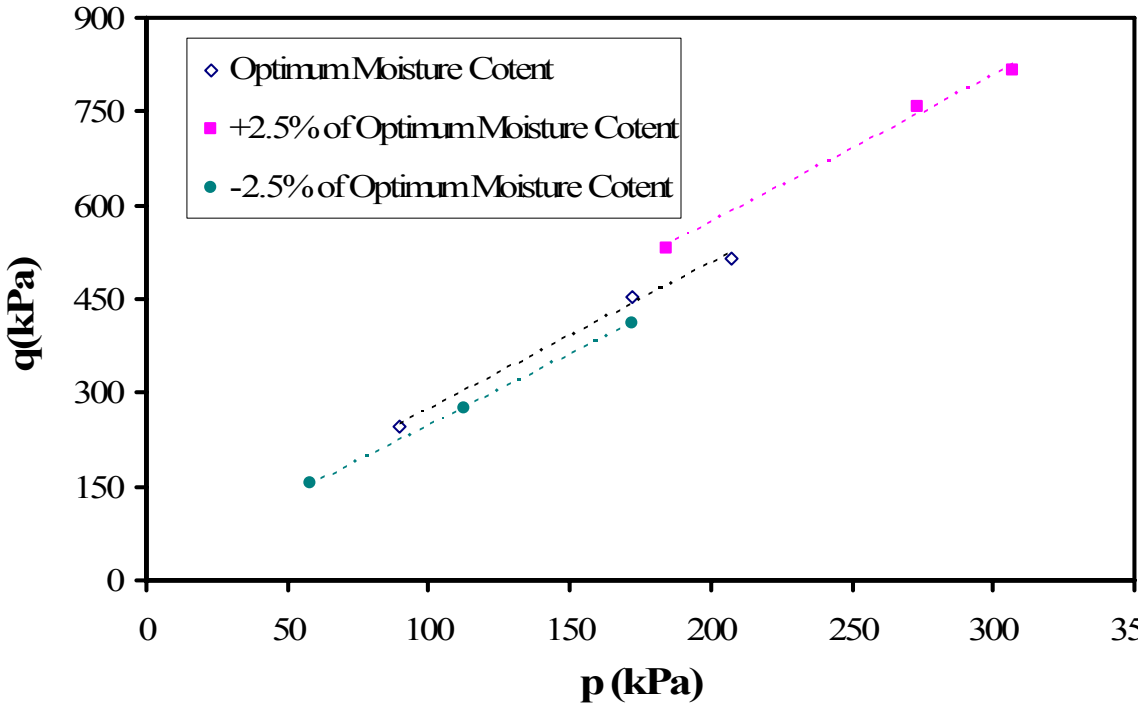

Figure 5.9 Static Failure Lines at Different Moisture Contents

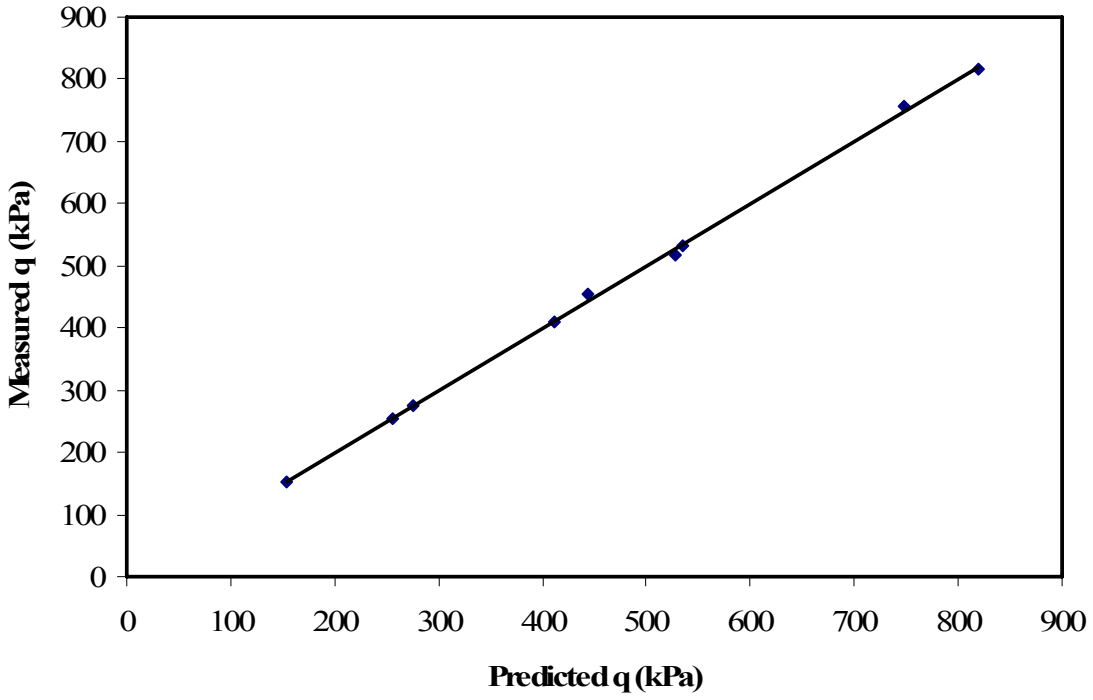

Figure 5.10 Results of the Non-Linear Regression Analysis to Obtain Parameters for Normalizing the Unsaturated Response

classified as explicit or implicit. In an explicit integration scheme, the yield surface, plastic potential gradients and hardening law are all evaluated at known stress states and no iteration is strictly necessary to predict the final stresses. However, it is prudent to introduce a simple iterative correction to restore the final stresses and hardening parameters to the yield surface, as this condition is not enforced by the integration. In a fully implicit method, the gradients and hardening law are evaluated at unknown stress states and the resulting system of non-linear equations must be solved iteratively. If a Newton scheme is used for this purpose, then second derivatives of the yield function and plastic potential are required to implement the iteration. This can lead to much tedious algebra for complex soil plasticity models such as the critical state family (Schofield and Wroth, 1968). In practice, both implicit and explicit methods have been used to integrate advanced constitutive relations in soil mechanics (Borja and Lee, 1990; Borja, 1991; Potts and Gens, 1985; Britto and Gunn, 1987), but computational details of the schemes are seldom given.

Implicit methods are attractive because the resulting stresses automatically satisfy the yield criterion to a specified tolerance. Furthermore, they do not require the intersection with the yield surface to be computed if the stress point changes from an elastic state to a plastic state. A comprehensive discussion of various implicit integration schemes for elastoplastic models can be found in Ortiz and Simo (1986) and Crisfield (1991; 1997). One of the most popular of these is the backward Euler algorithm. This computes an elastic trial stress state, using either tangent elastic moduli or secant elastic moduli, and returns it back to the yield surface by closest-point projection iteration. In its most general form, the final stresses and hardening parameters are found by solving a small system of non-linear equations at each Gauss point. When using the Newton-

Raphson algorithm for this task, care must be taken to allow for possible non-convergence of the resulting iteration scheme and some form of strain sub-incrementation may be necessary. The backward Euler return scheme has found wide application in metal plasticity studies since it provides all the information required for the formation of the consistent tangent stiffness matrix. This matrix, first identified by Simo and Taylor (1985), includes second order terms that are usually ignored in the standard form of the elastoplastic constitutive relations, and gives a quadratic rate of convergence for Newton-Raphson iteration of the global stiffness equations. Although powerful, the backward Euler return method is difficult to implement for complex constitutive relations because it requires second order derivatives of the yield function and plastic potential. Moreover, for yield surfaces with vertices or rapid changes in curvature, divergence may occur and it is advisable to use multi-vector return schemes (Crisfield, 1997). A discussion of various implicit integration methods for critical state models, including the backward Euler return scheme, can be found in Borja and Lee (1990) and Borja (1991).

Compared with implicit methods, explicit methods have the advantage of being more straightforward to implement. Since explicit schemes employ the standard elastoplastic constitutive law and require only first derivatives of the yield function and plastic potential, they can be used to design a general purpose integrator that can be used for a wide range of models. As discussed by Wissmann and Hauck (1983) and Sloan (1987), the accuracy and efficiency of explicit methods is significantly enhanced by combining them with automatic sub-stepping and error control. Such schemes limit the error in the computed stresses with no intervention from the user, and are best employed in conjunction with a correction to restore the stresses to the yield surface during the integration process. Unlike implicit methods, explicit methods do not require the solution

of a system of non-linear equations to compute the stresses at each Gauss point. They do, however, need to find the intermediate yield point if the stresses pass from an elastic state to a plastic state. This additional step only involves the solution of a single non-linear equation, but should be handled with care to avoid spurious intersections being found.

In this study an explicit sub-stepping integration scheme was used to implement the two surface model in ABAQUS finite element software. This scheme integrates the constitutive law by automatically dividing the strain increment into a number of sub-steps. An appropriate size for each sub-step is found through the use of modified Euler, which are specially constructed to provide an estimate of the local error. The method used in this study is generalized to incorporate algorithms for computing the yield intersection points, and restore the stresses to the yield surface. Each of these aspects is described in more details in the following sections.

5.3.1 Yield Surface Intersection

Given a vector of imposed strain increments $\Delta\boldsymbol{\varepsilon}$, an elastic trial stress increment $\Delta\boldsymbol{\sigma}_e$ can be found using Hooke's law according to:

$$\Delta\boldsymbol{\sigma}_e = \mathbf{D}_e \Delta\boldsymbol{\varepsilon} \tag{5.5}$$

If the elastic part of the constitutive relation is linear, the stress-strain matrix $\mathbf{D}_e$ is independent of the stresses and it is trivial to compute the elastic trial state $\boldsymbol{\sigma}_e = \boldsymbol{\sigma}_0 + \Delta\boldsymbol{\sigma}_e$ (where $\boldsymbol{\sigma}_0$ is the initial stress state). For non-linear critical state elastic behavior, however, the above equation must in general be integrated to compute the proper value of $\Delta\boldsymbol{\sigma}_e$.

For non-linear critical state elasticity the elastic trial stress increment $\Delta\boldsymbol{\sigma}_e$ is used only to check if the stress state has changed from elastic to plastic. Such a change occurs

if $f(\boldsymbol{\sigma}_0) < 0$ and $f(\boldsymbol{\sigma}_0 + \Delta\boldsymbol{\sigma}_e) = f(\boldsymbol{\sigma}_e) > 0$, and it is then necessary to determine the fraction of $\Delta\boldsymbol{\varepsilon}$ that moves the stresses from $\boldsymbol{\sigma}_0$ to the stress state $\boldsymbol{\sigma}_{int}$ on the yield surface. This situation, shown in Figure 5.11, may arise many times during the course of an elastoplastic finite element analysis and needs to be handled efficiently and accurately. Note that in Figure 5.11 the exact yield condition $f(\boldsymbol{\sigma}) = 0$ is replaced by the approximation $|f(\boldsymbol{\sigma})| \leq F_{TOL}$, where F_{TOL} is a small positive tolerance. This allows for the effects of finite precision arithmetic and modifies the transition condition to $f(\boldsymbol{\sigma}_0) < -F_{TOL}$ and $f(\boldsymbol{\sigma}_e) > +F_{TOL}$. Suitable values for the yield surface tolerance are typically in the range 10^{-6} to 10^{-9}.

The problem of finding the stresses at the yield surface intersection point $\boldsymbol{\sigma}_{int}$ is equivalent to finding the scalar quantity α which satisfies the non-linear equation:

$$f(\sigma_0 + \alpha D_e \Delta\varepsilon_e) = f(\sigma_{int}) = 0 \qquad 5.6$$

A value of $\alpha = 0$ indicates that $\Delta\boldsymbol{\varepsilon}$ causes purely plastic deformation, while a value of $\alpha = 1$ indicates purely elastic deformation. Thus, for an elastic to plastic transition, we have $0 < \alpha < 1$ and the elastic part of the stress increment is given by $\alpha \mathbf{D}_e \Delta\boldsymbol{\varepsilon}$. For critical state models, the secant elastic stress-strain matrix $\mathbf{D}_e$ is evaluated using the initial stress $\boldsymbol{\sigma}_0$ and the strain increment $\alpha\,\Delta\boldsymbol{\varepsilon}$. This means the trial elastic stress state, for a given initial stress and imposed strain increment, is exact and leads to accurate estimates of the intersection stress $\boldsymbol{\sigma}_{int}$.

Equation 5.6 defines a single non-linear equation in the variable α and can be solved by a variety of numerical methods including the bisection, regula-falsi, modified regula-falsi, secant, and Newton-Raphson schemes. The Newton-Raphson scheme was used in this study.

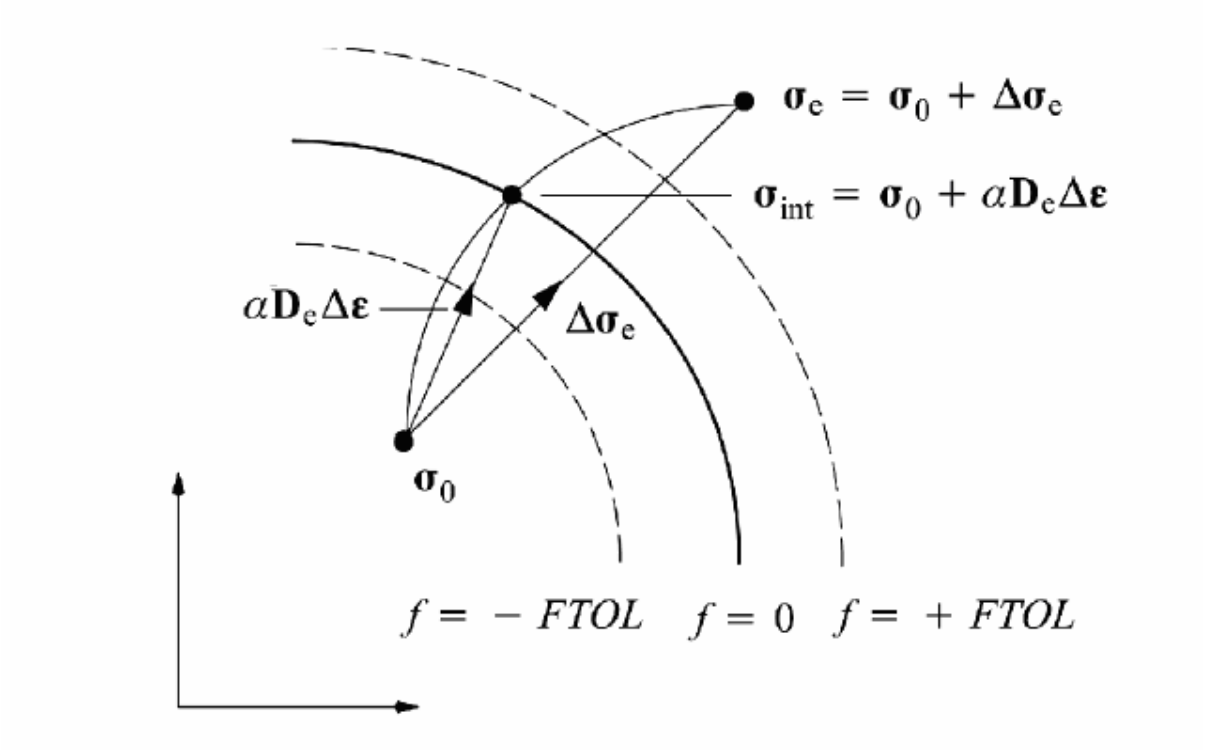

Figure 5.11 Yield Surface Intersections: Elastic to Plastic Transition (Sloan, 2001)

5.3.2 Correction of Stresses to Yield Surface

At the end of each sub-increment in an explicit integration process, the stresses may diverge from the yield condition so that $| f(\sigma, W) | \leq F_{TOL}$. The extent of this violation, which is commonly known as yield surface drift, depends on the accuracy of the integration scheme and the non-linearity of the constitutive relations.

Several methods have been proposed in the literature to correct for crossing the yield surface using any plasticity model. In this dissertation, a method proposed by Potts and Gens (1985) will be used. This method assumes that the total strain increment will be constant; however, the decomposed components (elastic and plastic) will be balanced to bring the stress back to the new yield surface within certain tolerance. Figure 5.12 shows an illustration for the correction technique, which will basically require the stress and the plastic work to be corrected.

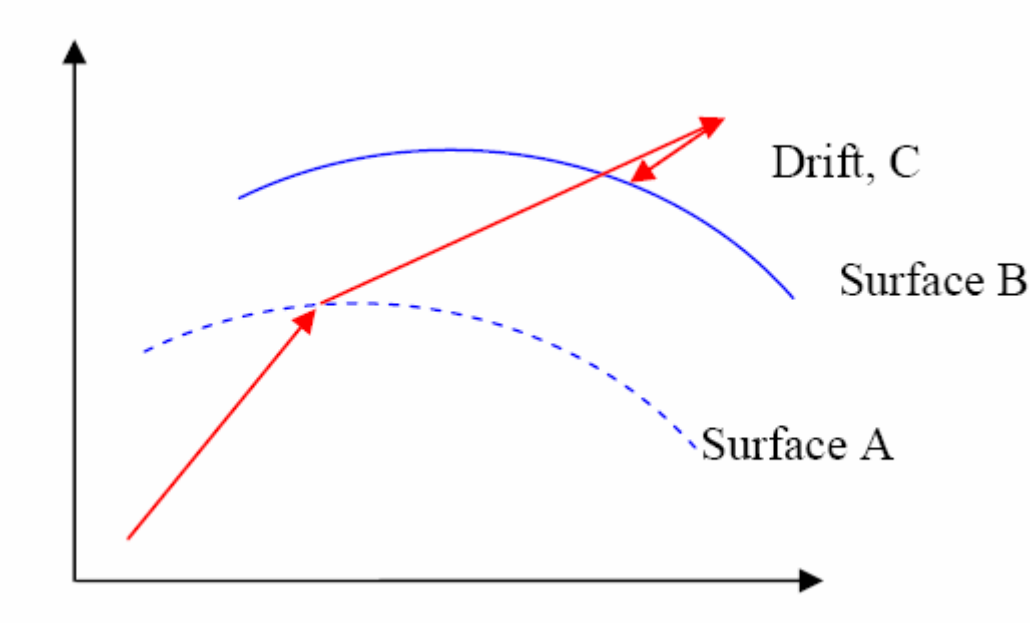

Figure 5.12 Illustration shows the Drift from the Yield Surface and the Correction Technique

For a point where the uncorrected stresses and hardening parameter, defined by $\boldsymbol{\sigma}_0$ and W_0, violate the yield condition so that $|f(\boldsymbol{\sigma}_0, W_0)| \leq F_{TOL}$, f may be expanded in a Taylor series about this stress point, to give:

$$f = f_0 + \frac{\partial f}{\partial \boldsymbol{\sigma}}\delta\boldsymbol{\sigma} + \frac{\partial f}{\partial W}\delta W \qquad 5.7$$

where $\partial\boldsymbol{\sigma}$ is a stress correction, ∂W is a hardening parameter correction, $f_0 = f(\boldsymbol{\sigma}_0, W_0)$, and $\frac{\partial f}{\partial \boldsymbol{\sigma}}$ is evaluated at $\boldsymbol{\sigma}_0$. The imposed strain increments remain unchanged provided the stress correction obeys the relation:

$$\delta\boldsymbol{\sigma} = \delta\lambda \mathbf{D}_e \frac{\partial g}{\partial \boldsymbol{\sigma}_0} \qquad 5.8$$

Where $\partial\lambda$ is an unknown multiplier.

The evolution of the work hardening parameter is found using the following equation:

$$\delta W = -\partial\lambda \frac{A_0}{\frac{\partial f}{\partial W}} \qquad 5.9$$

Where :

$$A = -\frac{\partial f}{\partial W}\frac{\partial W}{\partial \lambda} \tag{5.10}$$

Where A_0 is evaluated at $\boldsymbol{\sigma_0}$.

Combining Equations 5.7 through 5.9 and setting $f = 0$ gives the unknown multiplier as:

$$\partial\lambda = \frac{f_0}{A_0 + \frac{\partial f}{\partial \boldsymbol{\sigma}_0}\mathbf{D}_e\frac{\partial g}{\partial \boldsymbol{\sigma}_0}} \tag{5.11}$$

The corrections to the stresses and hardening parameter are thus given by:

$$\partial\boldsymbol{\sigma} = \frac{-f_0\mathbf{D}_e\frac{\partial g}{\partial \sigma}}{A_0 + \frac{\partial f}{\partial \boldsymbol{\sigma}_0}\mathbf{D}_e\ \frac{\partial g}{\partial \boldsymbol{\sigma}_0}} \tag{5.12}$$

$$\partial\mathbf{W} = \frac{-f_0\ \frac{A_0}{\frac{\partial f}{\partial \mathbf{W}}}}{A_0 + \frac{\partial f}{\partial \boldsymbol{\sigma}_0}\mathbf{D}_e\ \frac{\partial g}{\partial \boldsymbol{\sigma}_0}} \tag{5.13}$$

and an improved stress state, which is closer to the yield surface, can be obtained from:

$$\boldsymbol{\sigma} = \boldsymbol{\sigma}_0 + \partial\boldsymbol{\sigma} \tag{5.14}$$

$$\mathbf{W} = \mathbf{W}_0 + \partial\mathbf{W} \tag{5.15}$$

This type of scheme, which is known as a consistent correction, may be applied repeatedly until $| f(\boldsymbol{\sigma_0}, W_0) | \leq F_{TOL}$.

5.3.3 Modified Euler Scheme with Sub-Stepping

For a given strain increment, $\Delta\boldsymbol{\varepsilon}$, the constitutive relations to be integrated at each Gauss point are described by Equations 5.16 and 5.17 as:

$$\frac{\partial\boldsymbol{\sigma}}{\partial T} = D_{ep}\Delta\boldsymbol{\varepsilon} = \Delta\boldsymbol{\sigma}_e - \Delta\lambda\mathbf{D}_e\frac{\partial g}{\partial\boldsymbol{\sigma}} \tag{5.16}$$

$$\frac{\partial \mathbf{W}}{\partial \mathrm{T}} = \Delta\lambda \boldsymbol{\sigma} \frac{\partial \mathrm{g}}{\partial \boldsymbol{\sigma}} \tag{5.17}$$

$$\Delta\lambda = \frac{\frac{\partial f}{\partial \boldsymbol{\sigma}} \mathbf{D}_{\mathrm{e}} \Delta\boldsymbol{\varepsilon}}{\frac{\partial f}{\partial \boldsymbol{\sigma}} \mathrm{D}_{\mathrm{e}} \frac{\partial \mathrm{g}}{\partial \boldsymbol{\sigma}} - \frac{1}{\dot{\lambda}} \frac{\partial f}{\partial \mathbf{W}} \dot{\mathbf{W}}} \tag{5.18}$$

These equations describe a system of ordinary differential equations with initial conditions $\boldsymbol{\sigma} = \boldsymbol{\sigma}_0$ and $\mathrm{W} = \mathrm{W}_0$ at the start of the increment where $T = 0$ and $t = t_0$. The different integration scheme may be used to find the stresses and hardening parameter at the end of the increment (where $T = 1$). In this dissertation, the sub-stepping algorithm based on the method of modified Euler integration with error control proposed by Sloan et al. (2001) was used. This method is attractive for finite element applications because it attempts to control the errors in the stresses and hardening parameter arising from the approximate integration of the constitutive law.

The modified Euler integration with error control method proposed by Sloan et al. (2001) involves two steps. In the first step, a first approximation to the stress increments is calculated by multiplying the matrix of elastoplastic moduli (continuum Jacobian) by the vector of strain increments. Using the first approximation, the internal variables are temporarily updated and a second approximation to the stress increments is obtained by multiplying the matrix of updated elastoplastic moduli by the vector of strain increments. The relative error of each sub-step is estimated as the ratio between the norm of the difference between the two approximate stress increments and the norm of the updated stress calculated from the first approximation. The size of each sub-step is continually updated so that the relative error is less than a specified tolerance.

The above-mentioned procedure is illustrated by the following equations for calculation of stress increments at step k+1 of the analysis. The updated stress increment,

$\hat{\boldsymbol{\sigma}}_{\kappa+1}$ is calculated as follows:

$$\boldsymbol{\sigma}_{k+1} = \boldsymbol{\sigma}_k + \Delta\boldsymbol{\sigma}_1 \tag{5.19}$$

$$\Delta\boldsymbol{\sigma}_1 = D_{ep}(\boldsymbol{\sigma}_k, \kappa_k) \cdot \Delta\boldsymbol{\varepsilon}_k \tag{5.20}$$

$$\kappa_{k+1} = \kappa_k + \Delta\kappa_1 \tag{5.21}$$

$$\Delta\boldsymbol{\sigma}_2 = D_{ep}(\boldsymbol{\sigma}_{k+1}, \kappa_{k+1}) \cdot \Delta\boldsymbol{\varepsilon}_k \tag{5.22}$$

$$\kappa_{k+1} = \kappa_k + \Delta\kappa_1 \tag{5.23}$$

$$\hat{\boldsymbol{\sigma}}_{\kappa+1} = \boldsymbol{\sigma}_{\kappa} + 0.5(\Delta\boldsymbol{\sigma}_1 + \Delta\boldsymbol{\sigma}_2) \tag{5.24}$$

This updated stress increment is used to evaluate the relative error, *R*.

$$\mathbf{E} = 0.5(-\Delta\boldsymbol{\sigma}_1 + \Delta\boldsymbol{\sigma}_2) \tag{5.25}$$

$$R = \max\left\{EPS, \frac{\|\mathbf{E}\|}{\|\hat{\boldsymbol{\sigma}}_{\kappa+1}\|}\right\} \leq TOL \tag{5.26}$$

Here, R is the relative error and EPS is the smallest relative error that may be calculated by the utilized computer. If R is less than the specified tolerance, TOL, then the stresses and internal variables of the model may be updated and integration for the step is complete. Otherwise, it is necessary to reduce the size of the time step and repeat the calculations. The size of time step is adjusted according to the following equations:

$$q = \min\left\{0.8(TOL/R)^{1/2}, 2\right\} \tag{5.27}$$

$$T = q\Delta T \tag{5.28}$$

To begin the integration, a specified value is used for the size of the sub-step. The integration proceeds as described earlier. If the relative error, R, is less than the specified tolerance (TOL), then the stresses and internal variables of the model may be updated and

the integration for the step is complete. Otherwise, it is necessary to reduce the size of the time step and repeat the calculations. A tolerance of 10^{-5} is used in this study.

5.3.4 User Subroutine FORTRAN Code

The two surface critical state constitutive relations was implemented into a FORTRAN code used later in the USER MATERIAL (UMAT) subroutines for ABAQUS finite element program. The general structure of the FORTRAN code is presented in Figure 5.13

5.3.5 Verification of the Two Surface Critical State Model

To verify the prediction of the two surface critical surface model, the UMAT subroutine was used to predict the constitutive behavior of crushed limestone II material under monotonic and cyclic loading. For this purpose, monotonic and cyclic triaxial tests were conducted on crushed limestone II material prepared at the optimum moisture content and compacted at the maximum dry unit weight obtained from standard Proctor test. The monotonic tests included applying confining pressure of 21 kPa, then loading the sample at a constant strain rate (less than10% strain per hour) until failure was reached. While for the cyclic triaxial tests, a confining pressure of 14 kPa was first applied, the sample was then subjected to four cycles of loading and unloading at different strain level, and loaded at a constant strain till failure. Figure 5.14 and Figure 5.15 compare the results obtained from monotonic and cyclic triaxial tests conducted crushed limestone II material to those predicted using the two surface critical surface model for the same loading conditions. It can be seen that the model predictions were in good agreement with the experimental results.

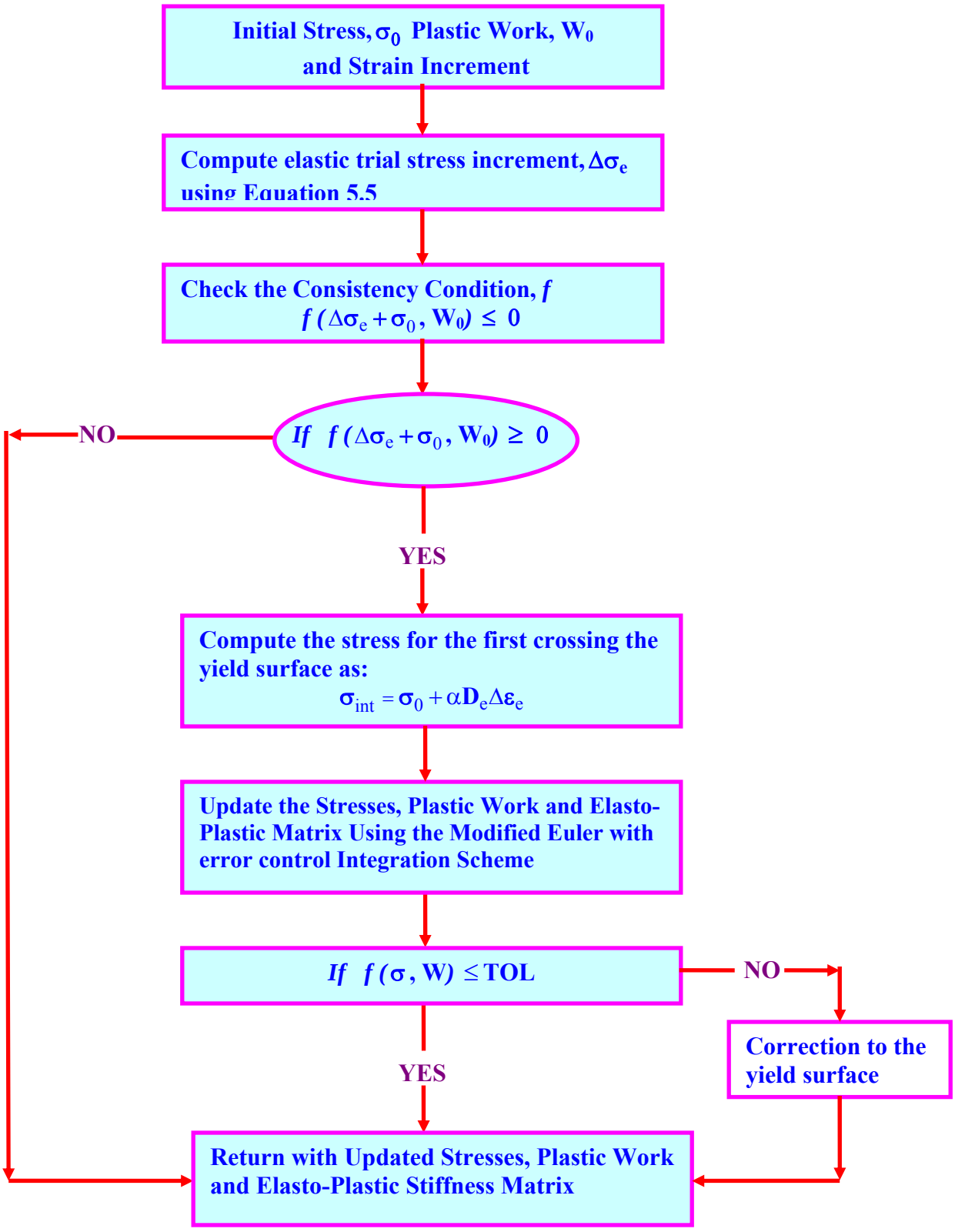

Figure 5.13 Schematic Flow Chart Describes the Structure for the Numerical Code

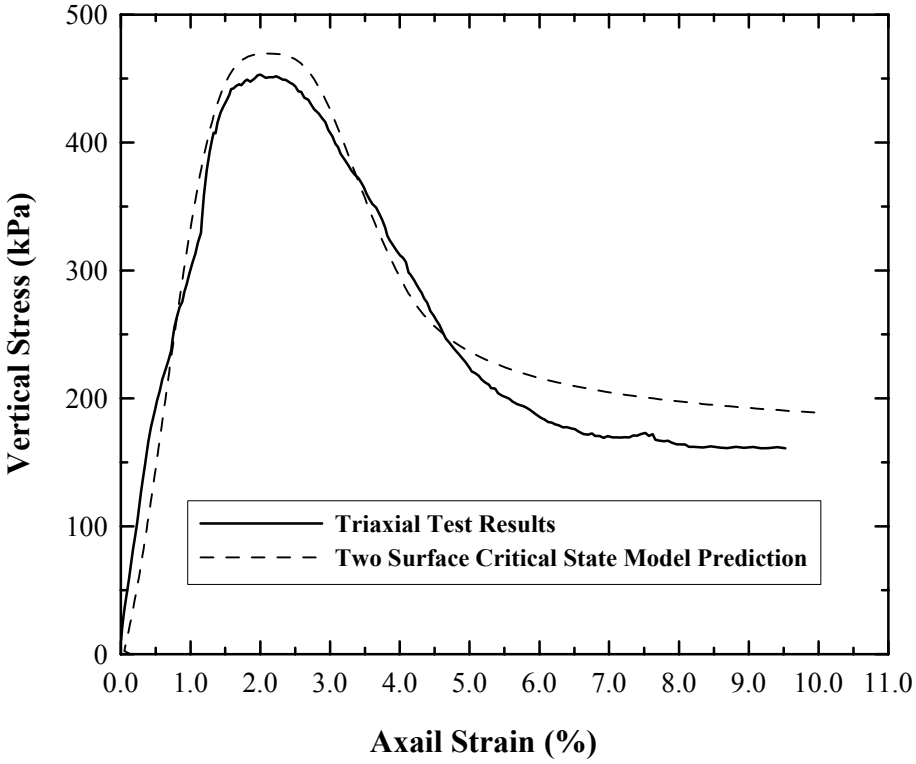

Figure 5.14 Verification of Two Surface Critical State Model Using Monotonic Triaxial

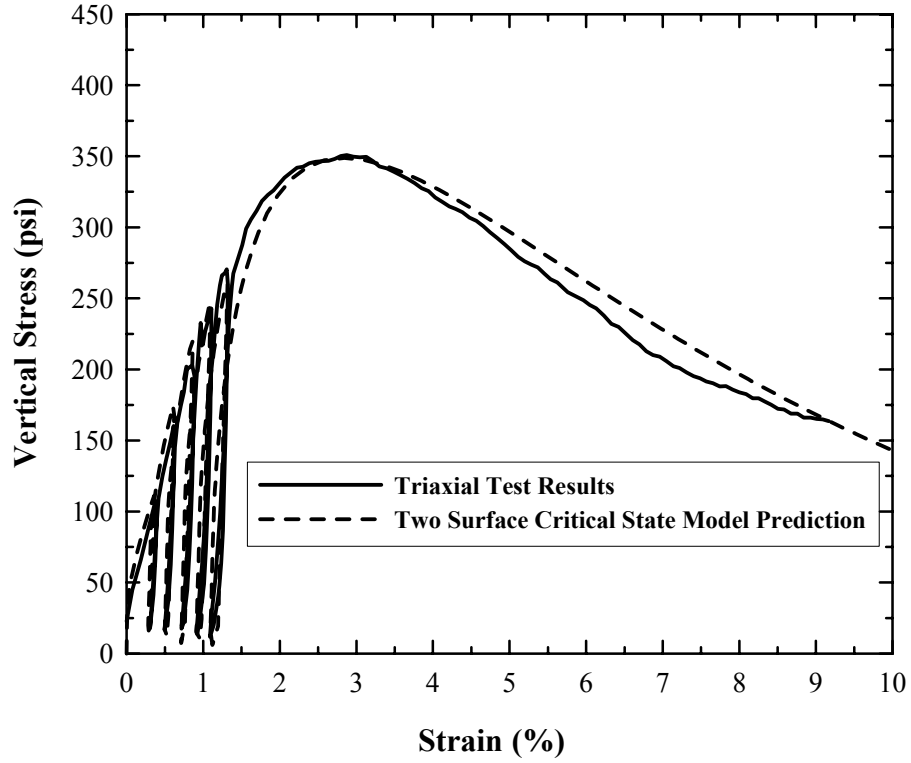

Figure 5.15 Verification of Two Surface Critical State Model Using Cyclic Triaxial

Chapter Six
Numerical Modeling of Geogrid Reinforced Base Layer in Flexible Pavement- Crushed Limestone I

This chapter presents the results of the numerical modeling study that was conducted to capture the impacts of the base course layers' parameters reflected by the granular base thickness, and subgrade strength, as well as stiffness and location of the geogrid reinforcement layer on the structural performance of geogrid reinforced flexible pavement systems.

6.1 Finite Element Numerical Model

A two-dimensional axisymmetric finite element model was developed using the ABAQUS finite element software package (ABAQUS, 2004) to analyze geogrid-reinforced flexible pavement structure. Hua (2000) showed that rutting in a flexible pavement can be modeled using two-dimensional finite element models rather than three-dimensional models without significant loss in accuracy. The following section describes finite element model features.

6.1.1 Finite Element Mesh

A typical finite element mesh that was used in the analysis is shown in Figure 6.1. The axi-symmetric mesh has a radius of 4500 mm and total depth of 4000 mm. The radius of the mesh was selected based on the distance at which the vertical and horizontal strains became insignificantly small in all layers. While, the depth of the mesh was chosen to be at the depth at which the maximum induced vertical stress in the subgrade became insignificantly small (< 0.01% of the applied tire pressure).

Conventional kinematic boundary conditions were adopted, such that the horizontal movement along the left and right boundaries and the vertical movement along

the bottom boundary were restrained by using roller supports. Such boundary conditions have been successfully used by Zaghloul and White (1993), and Kuo et al. (1995).

Eight-noded biquadratic axisymmetric quadrilateral elements were used for the subgrade, base, and asphalt concrete layers, while a three-noded quadratic axisymmetric membrane element with thickness of 1 mm was used for the geogrid reinforcement.

To determine the suitable element size for the 2D axisymmetric model, a series of finite element analyses were performed with decreasing element sizes. Mesh sensitivity was studied to determine the level of fine mesh needed for a stable finite element analysis. Based on this analysis, approximately 360, 1180, and 2480 elements were used for the AC, base course, and subgrade layer, respectively.

6.1.2 Interface Model

Full bonding was assumed between the different pavement layers. This assumption is acceptable for the case of a paved system where the allowed surface rutting of such a system surface is small and the slippage is not likely to occur unless excessive rutting takes place (Barksdale 1989; Espinoza 1994).

The geogrid was assumed to have full interlocking with materials surrounding it. However, the full interlocking interface model was compared to other interface models used in previous studies as will be discussed later in this chapter.

6.1.3 Load Model

The loading model in this study included applying gravity loads in the first load step of the analysis, then applying 100 cycles of loading representative of a 80 kN (18 kips) single axle wheel loading, which is the standard load known as equivalent single axle load (ESAL) recommended by AASHTO (1993). The wheel load was simulated by applying the contact pressure on a circular area with a radius of 152 cm (6 in.) at the

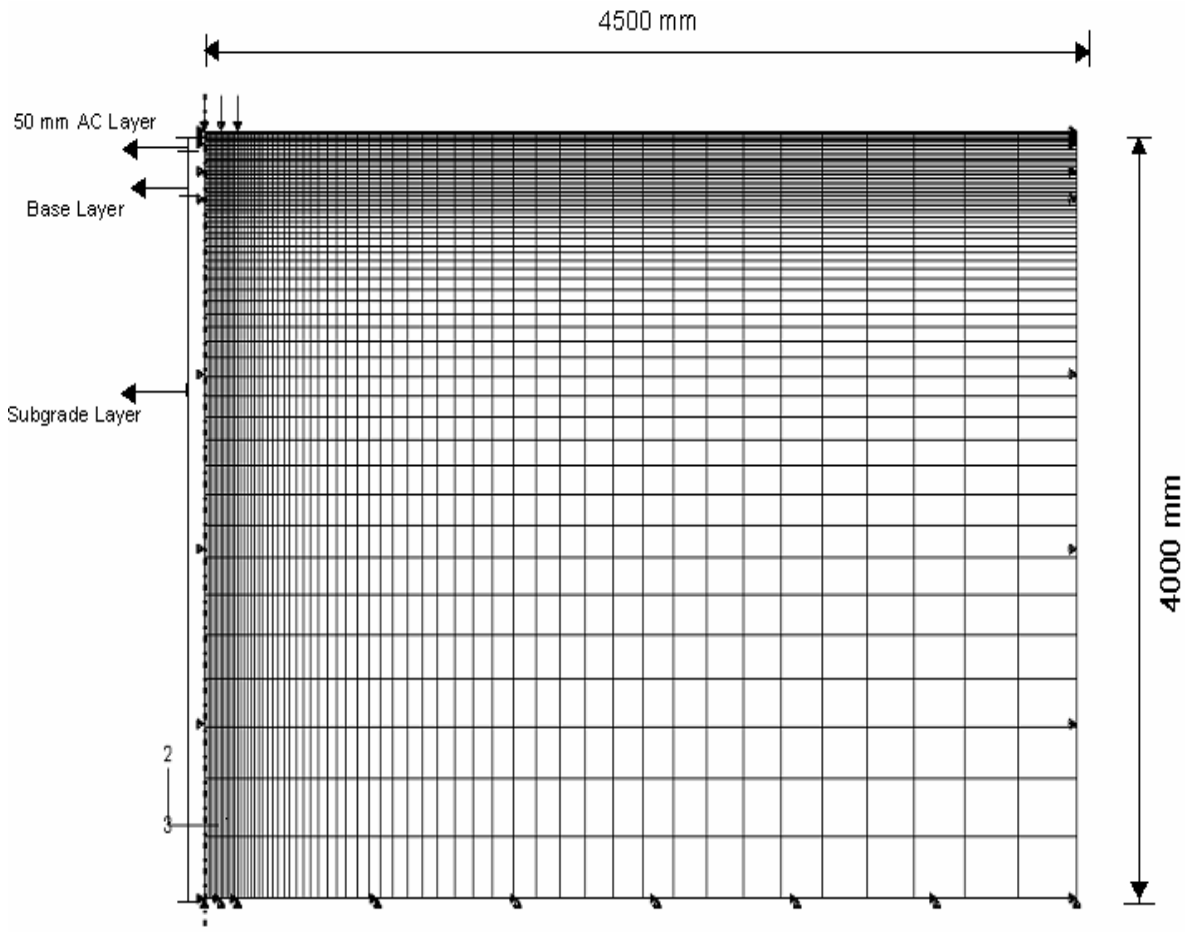

Figure 6.1 Mesh Used in Finite Element Analysis

surface, more information about the loading model used in this study is provided in Chapter Three. To account for compaction induced loads and suppress the initial stage of permanent deformation, the first four cycles were assumed to simulate the compaction stage and therefore their results were not considered in the analysis.

6.1.4 Material Constitutive Models

6.1.4.1 Asphalt Concrete (AC) layer

Given that AC is a viscous material and that it exhibits permanent strain, ideally a visco-plastic material model would be used. A number of factors precluded the use of a model of this type. These factors include the relatively small contribution to permanent

deformation due to the AC layer, the lack of relevance of properties pertaining to the development of permanent deformation in this material on benefits derived from the reinforcement, the difficulty in determining visco-plastic material parameters through established laboratory tests, the complexity of material models used for the other pavement layers and the desire to increase computational efficiency.

Many studies suggested that a linear elastic model is suitable for modeling the AC layer. Harold (1994) indicated that the AC layer behaves elastic or visco-elastic at low temperature, the plastic response of AC mixtures can be neglected. Also, Benedetto and La Roche (1998) concluded that AC mixtures exhibit a complex elasto-visco-plastic response but at small strain magnitude the plastic component can be neglected. Saad (2005) suggested that at when the time duration of this load affecting a pavement structure is small, the viscoelastic behavior of this structure becomes almost equivalent to an elastic structure.

Initially, a simple linearly elastic model was selected. However, after the initial use of this material model in the finite element model, it was observed that the rebound of this elastic layer after the applied load was returned to zero created vertical tensile stresses on the top of the base layer. For this reason, the model was extended to include a plasticity component. The plasticity was introduced by specification of an ultimate yield stress corresponding to a perfect plasticity hardening law. The parameters used for the AC layer is presented in Table 6.1.

6.1.4.2 Base Course Layer

Elastoplastic models like Drucker–Prager and Mohr–Coulomb are considered the simplest models that can represent the elasto-plastic soil and granular material behavior. In addition to their capacities to simulate the non-tensioning behavior and the hydrostatic

sensitivity response exhibited by the granular materials, such models reflect some other important characteristics of the granular material such as elastic response at lower stress level and plastic response at higher stress level, small material stiffness near failure, failure conditions (Baladi and Chen 1985). The Drucker-Prager is numerically easier to handle than Mohr-Coulomb, as convergence difficulty arises at the vertices of Mohr-Coulomb yield surface where the associative plasticity rule is not met.

In the study the base course was modeled using the Drucker-Prager model with isotropic hardening, which was previously described in Chapter Three of this dissertation. The base material used in the finite element analysis presented in this chapter was the crushed limestone I material. The Drucker Prager model parameter calibration and verification for this material was discussed in Chapter Five. Table 6.1 presents a summary of those parameters.

6.1.4.3 Subgrade Layer

The subgrade was modeled using the Drucker-Prager model with isotropic hardening. Three sets of the Drucker-Prager model parameters were selected for the subgrade materials from previous work to represent weak, moderate and stiff subgrades. The selected parameters are presented in Table 6.1

6.1.4.4 Geogrid Layer

A linear elastic model was used for the behavior of geogrid material. Such model proved to be efficient when used by other researchers (e.g., Dondi, 1994; and Ling and Liu, 2003, and Perkins, 2001), especially since the induced strain in the geogrid is very small and is considered within the elastic range. Four geogrid types with different equivalent elastic moduli were used. A summary of the properties of the geogrid types investigated in this study are shown in Table 6.1.

Table 6.1 AC, Base, Subgrade, and Geogrid Material Parameters

Material	Friction Angle	Cohesion (kPa)	Elastic Modulus (kPa)	v	CBR	Yield Stress (kPa)
AC*	-	-	3450000	0.35	-	770
Base	48	26	45000	0.35	-	-
Weak	6	10	7000	0.35	1.5	-
Moderate	14	20	15000	0.35	6	-
Stiff Subgrade**	28	22	35000	0.35	13	-
Geogrid Type I	-	-	135000	0.25	-	-
Geogrid Type II	-	-	158000	0.25	-	-
Geogrid Type III	-	-	255000	0.25	-	-
Geogrid Type IV	-	-	280000	0.25	-	-

- : Not applicable *: Masada et al. [16]; **: Mohammad et al. [17]

6.2 Parametric Study Matrix

The finite element model developed in this chapter was used to investigate the effects of different variables on the degree of improvement achieved by reinforcing the base course layer with a geogrid layer. These variables included the strength of the subgrade material, the thickness of the base course layer, as well as the stiffness, location and interface properties of the geogrid reinforcement material. To study these variables, finite element analyses were first conducted on 15 unreinforced sections with three different subgrade strength properties and five base course layer thicknesses for use as reference. The three different subgrades included: a weak subgrade with a CBR value less than 1.5, a moderate subgrade with a CBR value of 6, and a stiff subgrade with a CBR of 13. While the five different base course layer thicknesses varied from 150 mm (6 in.) to 254 mm (10 in.), and included: 150 mm (6 in.), 175 mm (7 in.), 200 mm (8 in.), 225 mm (9 in.), 250 mm (10 in.) base layer thicknesses. Table 6.2 presents a summary of the different sections investigated in this study. It should be noted that the different section

will be hereafter identified using the reference names provided in Table 6.2. Finite element analyses were then conducted on the different pavement sections reinforced with geogrid layer placed at the bottom of the base course layer. Four geogrid types with stiffness properties were used in this study.

Table 6.2 Investigated Pavement Sections

Section ID	Base Course Thickness (mm)	Subgrade Quality
Section 1a	150	Weak
Section 1b	150	Moderate
Section 1c	150	Stiff
Section 2a	175	Weak
Section 2b	175	Moderate
Section 2c	175	Stiff
Section 3a	200	Weak
Section 3b	200	Moderate
Section 3c	200	Stiff
Section 4a	225	Weak
Section 4b	225	Moderate
Section 4c	200	Stiff
Section 5a	250	Weak
Section 5b	250	Moderate
Section 5c	250	Stiff

The finite element model was also used to investigate the effect of the location of the geogrid reinforcement within the base course layer on the reinforced section performance. Four different locations were investigated in this study as shown in Figure 6.2. Generally, the optimum location of geogrid layer depends on the thickness of the base course layer and the subgrade strength (Perkins, 1997). Therefore, to investigat the geogrid location effect, finite element analysis were conducted on section 1a and section 5c, which represent sections that have the combination of the lowest and highest base

thickness and subgrade stiffness. Finally, the effects of the base course-geogrid interface properties were investigated by performing finite element analyses on pavement section 2b reinforced with geogrid type I placed at the bottom of the base layer. In these analyses the tie interface condition, which is used in this study to simulate the geogrid fully interlocking with the materials surrounding it, was compared to three other interface cases described in terms of a coulomb friction model with μ value of 1.475 and variable E_{slip} values ranging from 0.145 mm to 1 mm. These μ and E_{slip} values were selected to match the values used in previous finite element studies to adequately simulate the base course-geogrid interface.

6.3 Results of Finite Element Analysis

The following sections summarize the results of the finite element analysis conducted in this chapter. The response of different pavement sections computed from finite element analysis is first presented. The response is then used to evaluate the performance of those sections.

6.3.1 Stresses and Strain

6.3.1.1 Effect of Geogrid Reinforcement Placed at Bottom of Base Layer

Vehicular loads applied at the surface of a pavement section create a lateral spreading motion of the base course aggregate. As a result, tensile lateral strains are created in the base below the applied load as the material moves down and out away from the load. Lateral movement of the base allows for vertical strains to develop, leading to a permanent deformation in the wheel path. One of the main reinforcement mechanisms attributed to geosynthetics in paved roads is the direct prevention of lateral spreading of base course aggregate, which is called lateral restraint mechanism (Perkins, 2000). Figure 6.3 through Figure 6.6 present the lateral strain profiles computed at different

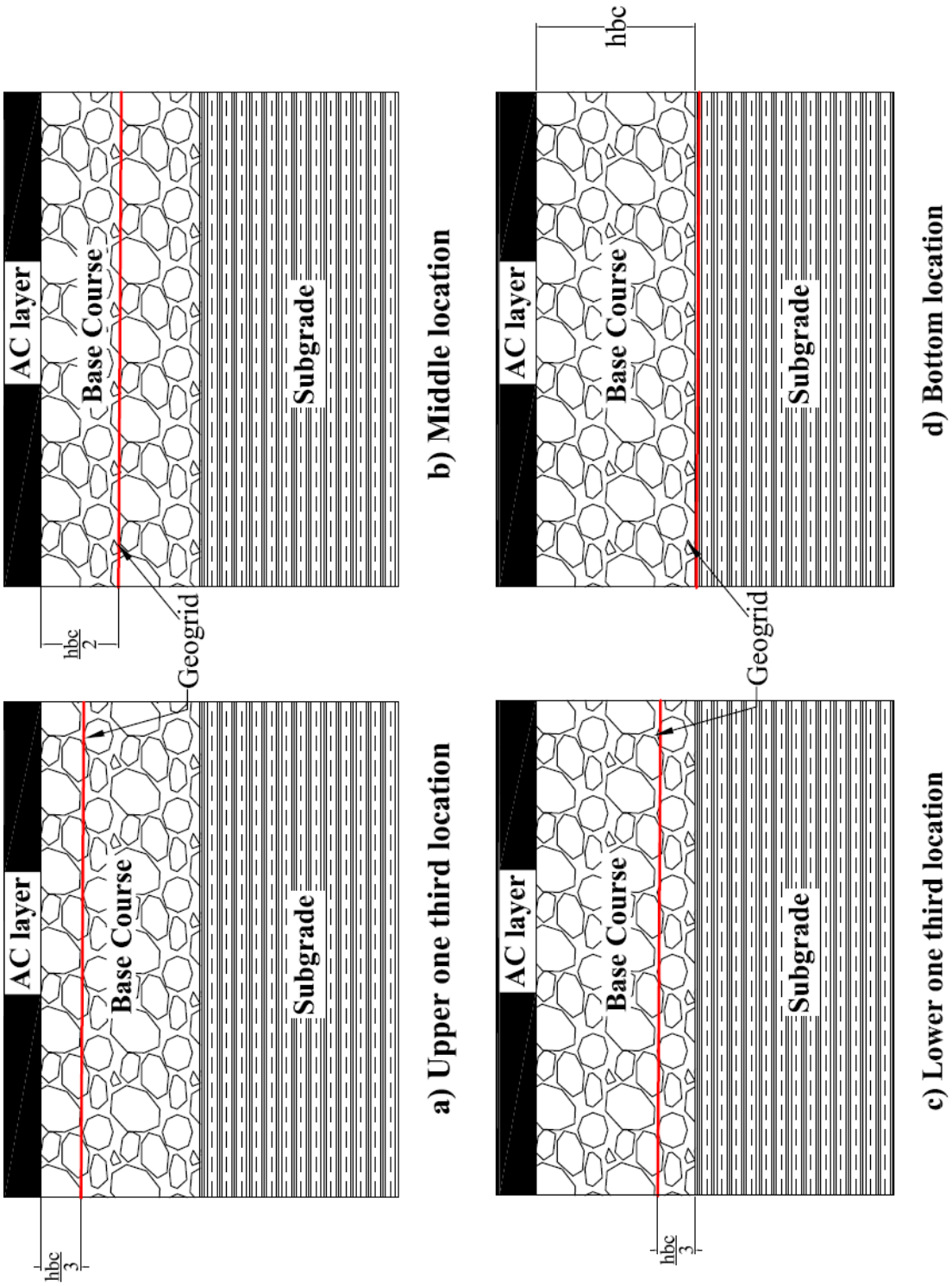

Figure 6.2 Geogrid Locations Investigated in the Parametric Study

distance from the center of the wheel load for sections 1a, 5a, 1c, and 5c reinforced with a layer of geogrid type I and IV placed at bottom of base course layer. In general, The figures show that the geogrid reinforcement constrained the lateral motiondifferent distance from the center of the wheel load for sections 1a, 5a, 1c, and 5c reinforced with a layer of geogrid type I and IV placed at bottom of base course layer. In general, the figures show that the geogrid reinforcement constrained the lateral motion of aggregate up into the base course layer and down into the subgrade. It is clear that the geogrid effect was mainly below the wheel load area and it almost vanished at distance of 304 mm from the center of the wheel load. The geogrid lateral constrain effect was more dominant in sections built with thin base course layer on top of weak subgrade layers, such as section 1a. This demonstrates that the geogrid effect on reducing the lateral tensile strain is controlled by the thickness of the base course layer and the stiffness of subgrade. However, the figures show that the subgrade stiffness has greater influence in this case. The figures also demonstrate that higher stiffness geogrids provided much greater reduction in lateral tensile strain.

The vertical strains profiles predicted from the finite element analysis at different locations within the subgrade layer for unreinforced and reinforced sections 1a, 1c, 5a, and section 5c, are shown in Figure 6.7 through Figure 6.10, respectively. It is that thegeogrid layer resulted in significant reduction in the vertical strain at the top of subgrade. However, this reduction is influenced by the base course thickness and subgrade stiffness, such that greater reduction is noticed for weaker subgrade and thinner base course layers Furthermore, the geogrid influence on the vertical strain was experienced within zone that extends to a depth of about 304 mm below the top of the subgrade layer. However, the greatest influence was encountered at the top of the

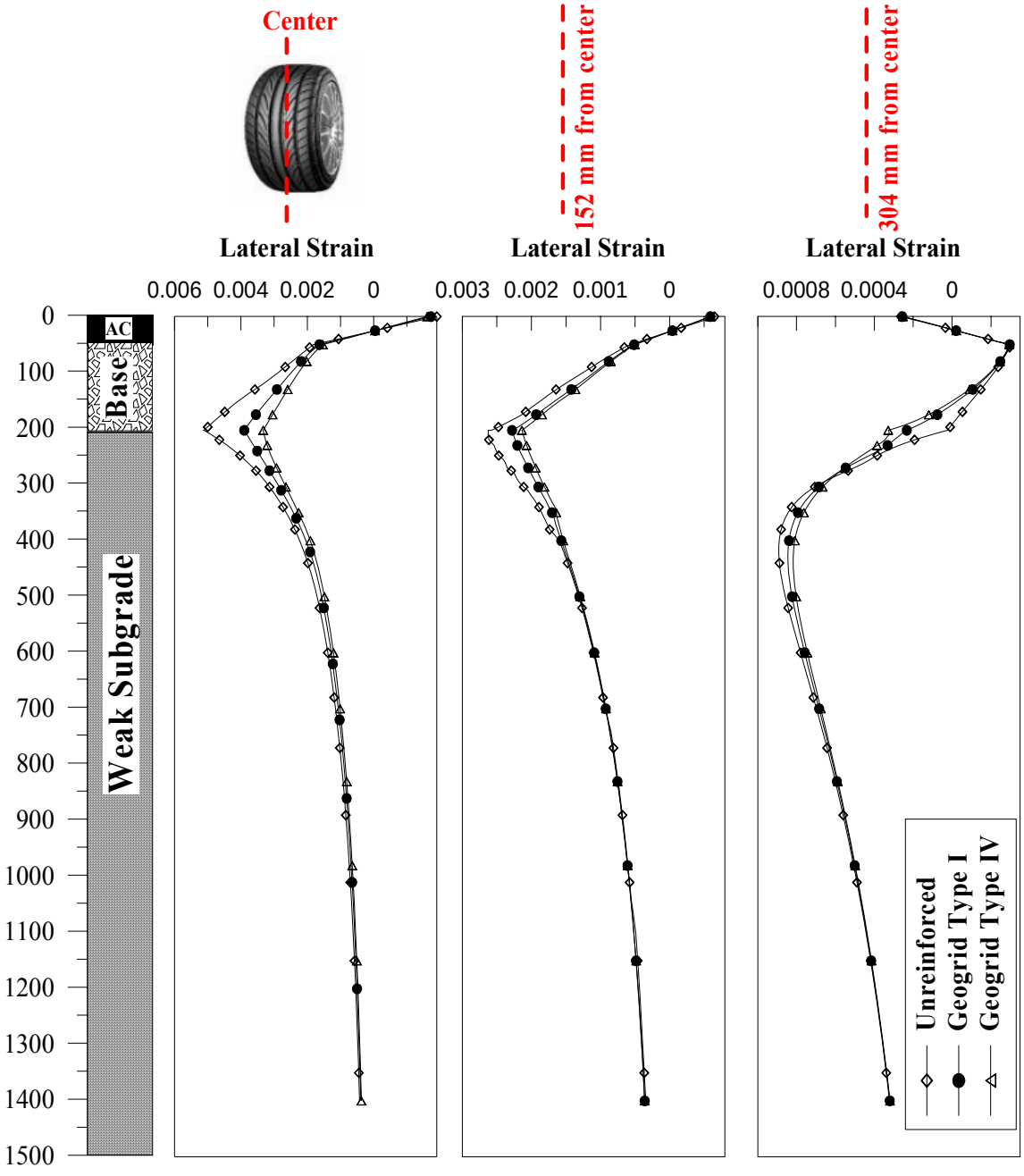

Figure 6.3 Lateral Strain Profile for Unreinforced Section 1a and Reinforced With Geogrid Layer Placed at the Bottom of the Base Layer

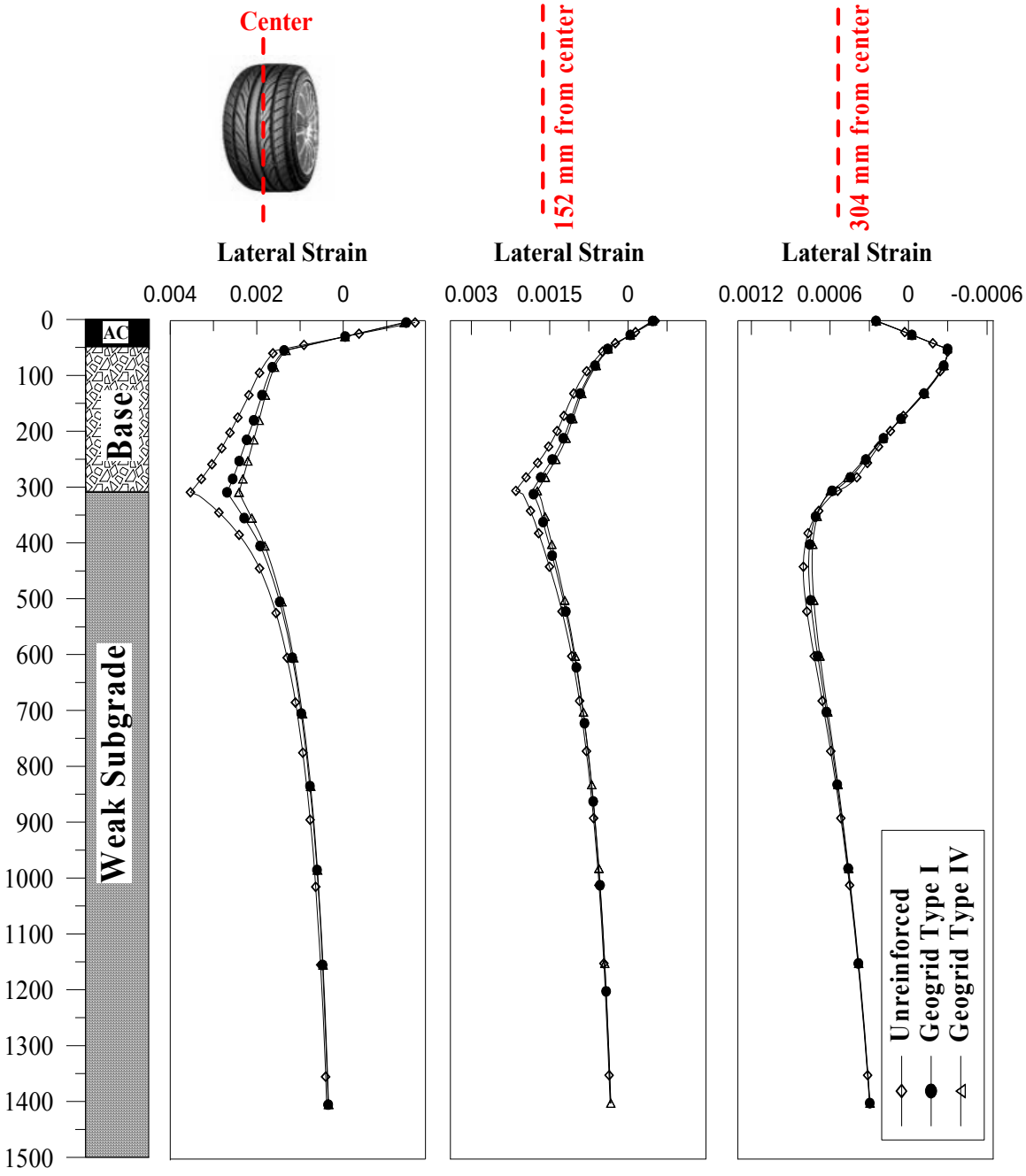

Figure 6.4 Lateral Strain Profiles for Unreinforced Section 5a and Reinforced With Geogrid Layer Placed at the Bottom of the Base Layer

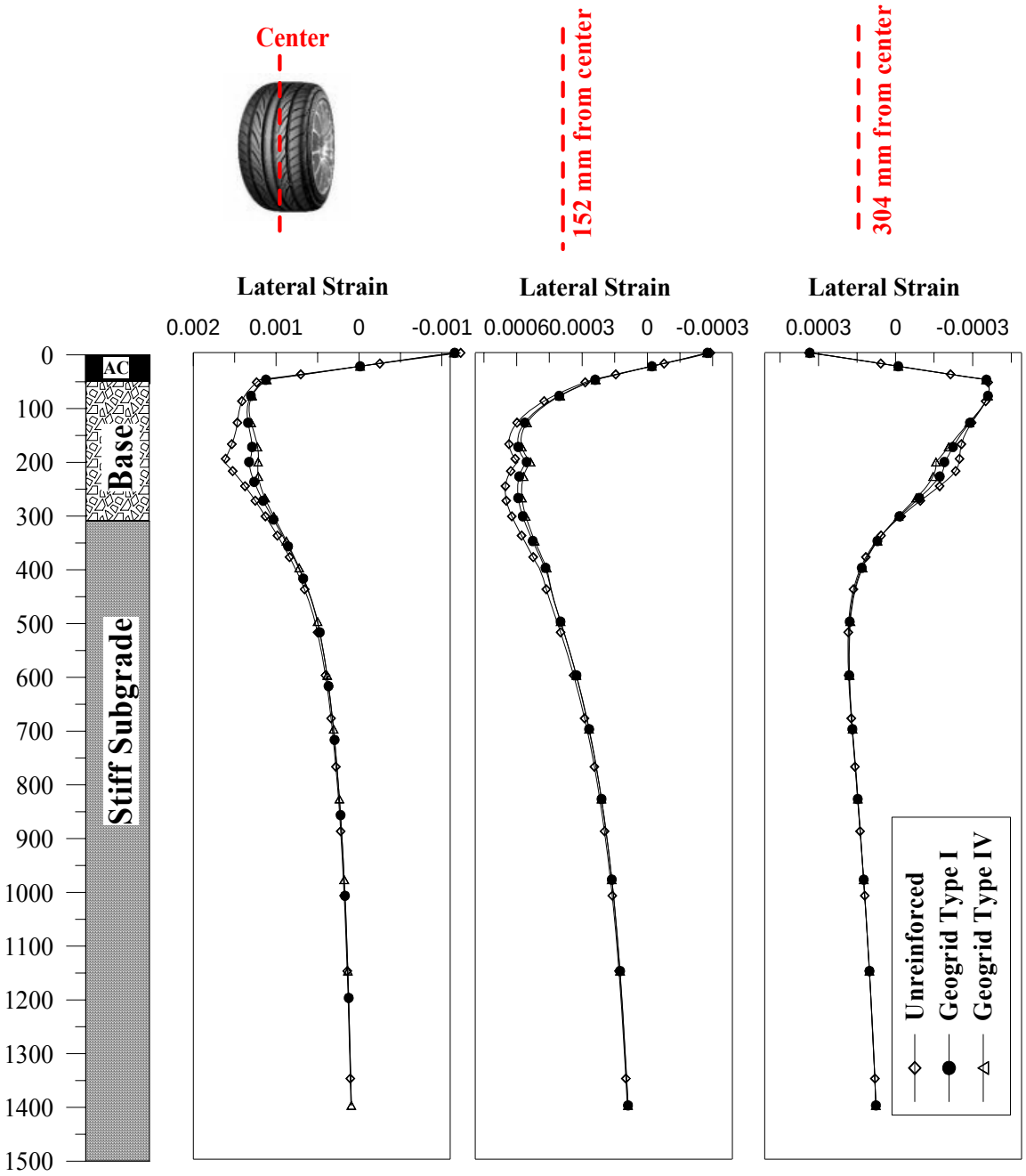

Figure 6.5 Lateral Strain Profile for Unreinforced Section 1c And Reinforced with Geogrid layer Placed at the Bottom of the Base Layer

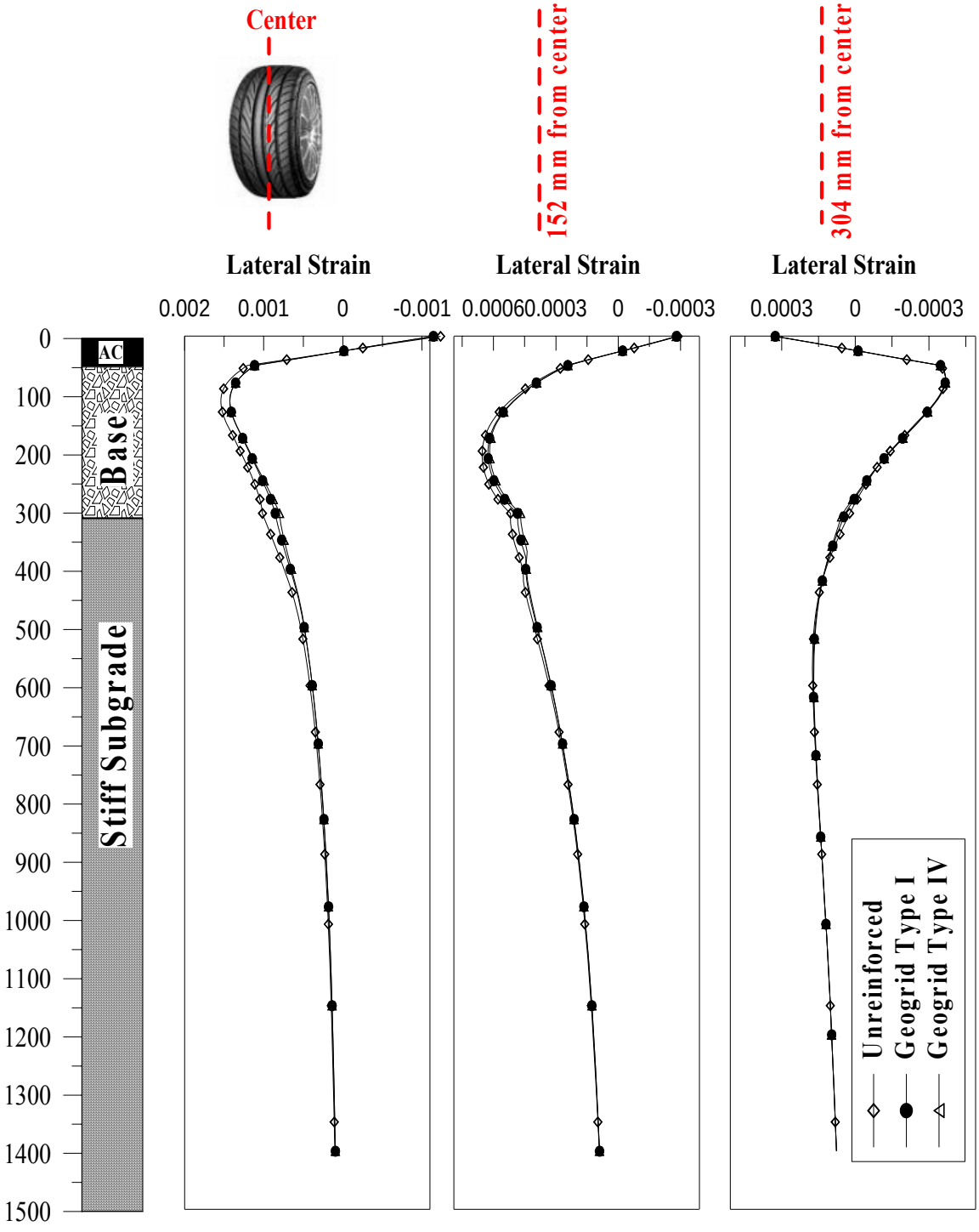

Figure 6.6 Lateral Strain Profile for Unreinforced Section 5c and Reinforced With Geogrid Layer Placed at the Bottom of the Base Layer

subgrade. The figures also clearly demonstrate the effect of geogrid stiffness on the induced vertical strain, such that stiffer geogrids exhibited lower vertical strain at top of the subgrade.

Figure 6.11 through Figure 6.14 show vertical stress profile at the top of the subgrade layer for unreinforced and reinforced sections 1a, 5a, 1c and 5c, respectively. It is noted that slight/no improvement in the vertical stresses at the top of subgrade was detected due to the geogrid reinforcement. For the first glance, this result seems to be contradicting with strain distribution. However, the finite element prediction of stresses in a material depends on the stress-strain relation, which is defined by the constitutive model used to describe the behavior of that material. In the classical theory of plasticity, the stress increment is computed using the following equation:

$$\Delta\boldsymbol{\sigma} = \mathbf{D}_e \Delta\boldsymbol{\varepsilon}^e = \mathbf{D}_e \left[\Delta\boldsymbol{\varepsilon} - \Delta\boldsymbol{\varepsilon}^p \right] \qquad 6.1$$

Where

$\Delta\boldsymbol{\sigma}$: is the increment in stress tensor; $\Delta\boldsymbol{\varepsilon}$, $\Delta\boldsymbol{\varepsilon}^e$, and $\Delta\boldsymbol{\varepsilon}^p$:are the increment in the total, elastic, and plastic strain tensor, respectively; and $\mathbf{D}_e$: is the elastic stiffness tensor.

Thus, the induced stress increment is dependant on the elastic portion of strain (recoverable) not on the total strain. So if an integration point of any element in a finite element model undergoes a totally plastic strain increment then the corresponding stresses increment will be equal to zero according to Equation 6.1 . Therefore, the plastic vertical strain (irrecoverable) at the top of the subgrade, which is responsible for the long-term permanent deformation, should be investigated.

Figure 6.15 through Figure 6.18 present the plastic strain distribution at the top of subgrade for section 1a, 5a, 1c and 5c, respectively. It can be seen that the plastic strains

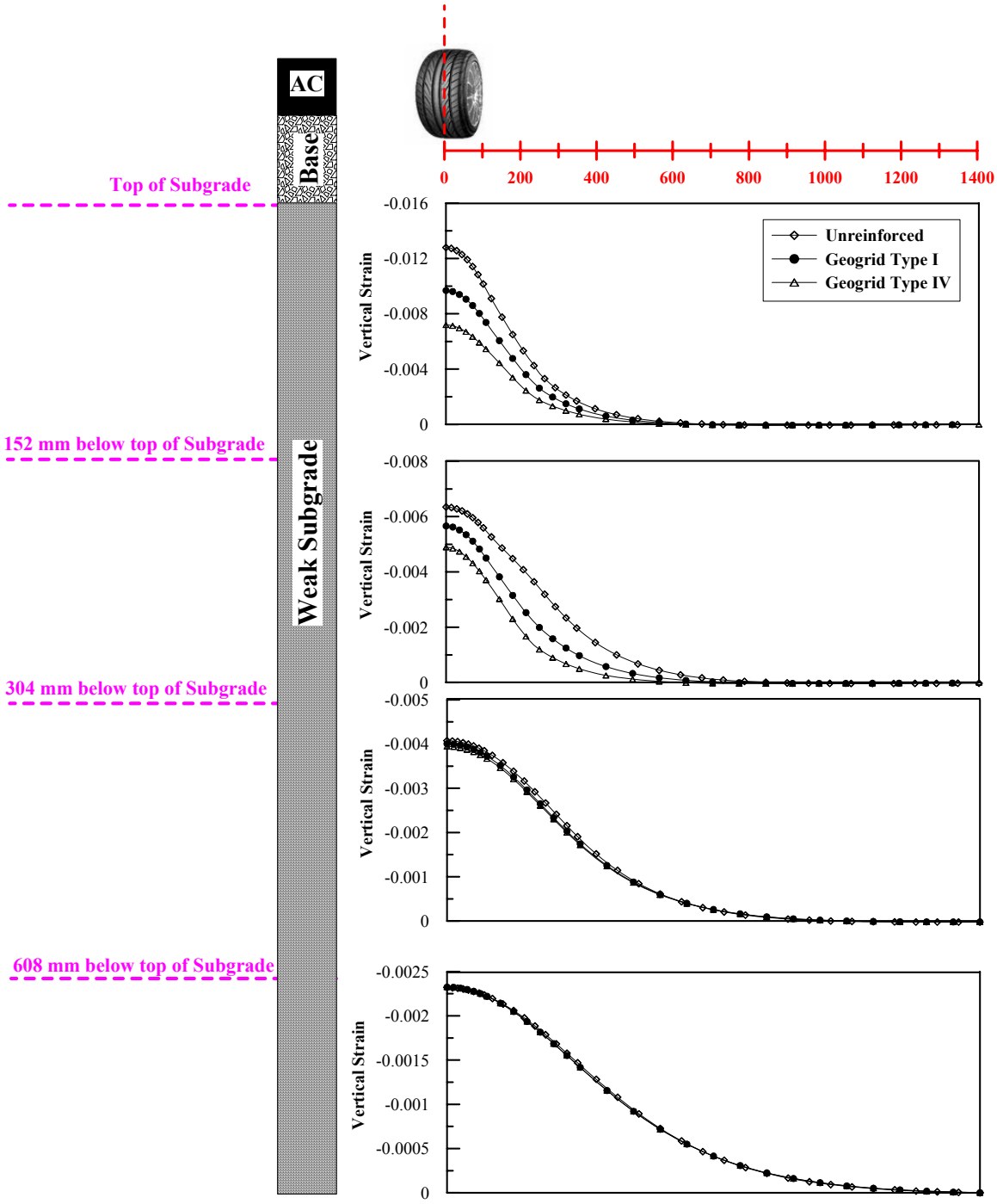

Figure 6.7 Vertical Strain Profiles within Subgrade Layer For Unreinforced Section 1a and Reinforced with Geogrid Place at the Bottom of the Base Layer

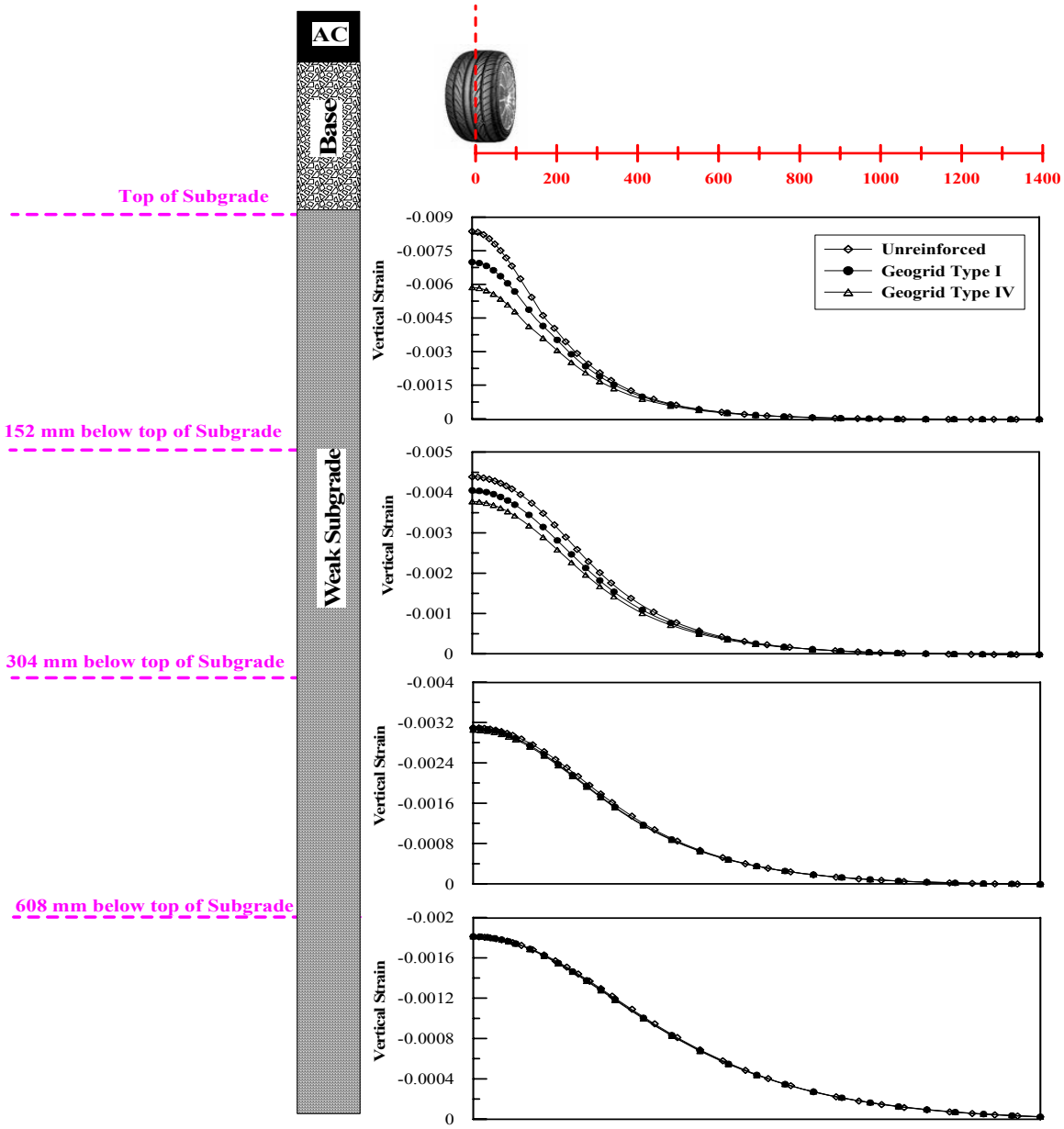

Figure 6.8 Vertical Strain Profiles within Subgrade Layer For Unreinforced Section 5a and Reinforced with Geogrid Place at the Bottom of the Base Layer

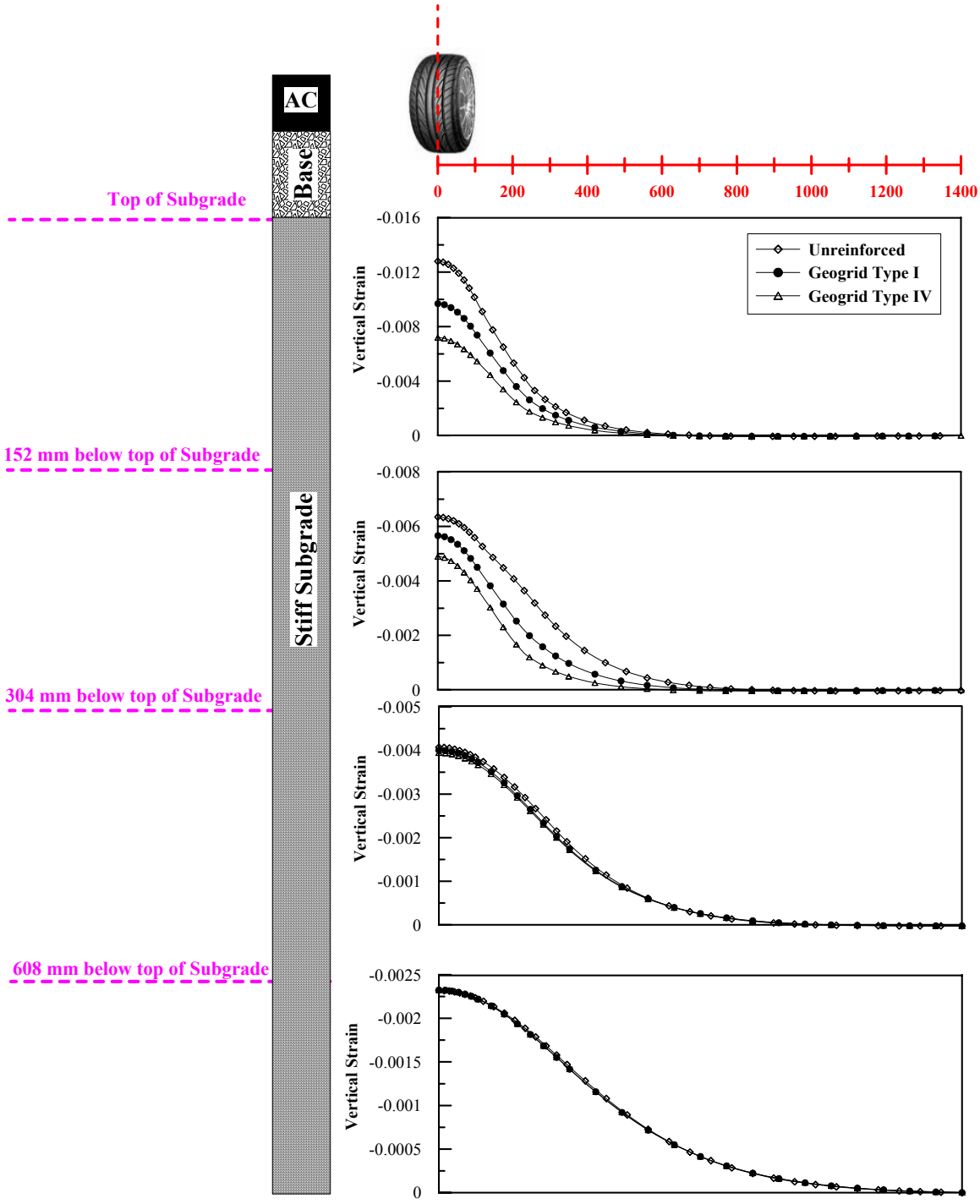

Figure 6.9 Vertical Strain Profiles within Subgrade Layer For Unreinforced Section 1c and Reinforced with Geogrid Place at the Bottom of the Base Layer

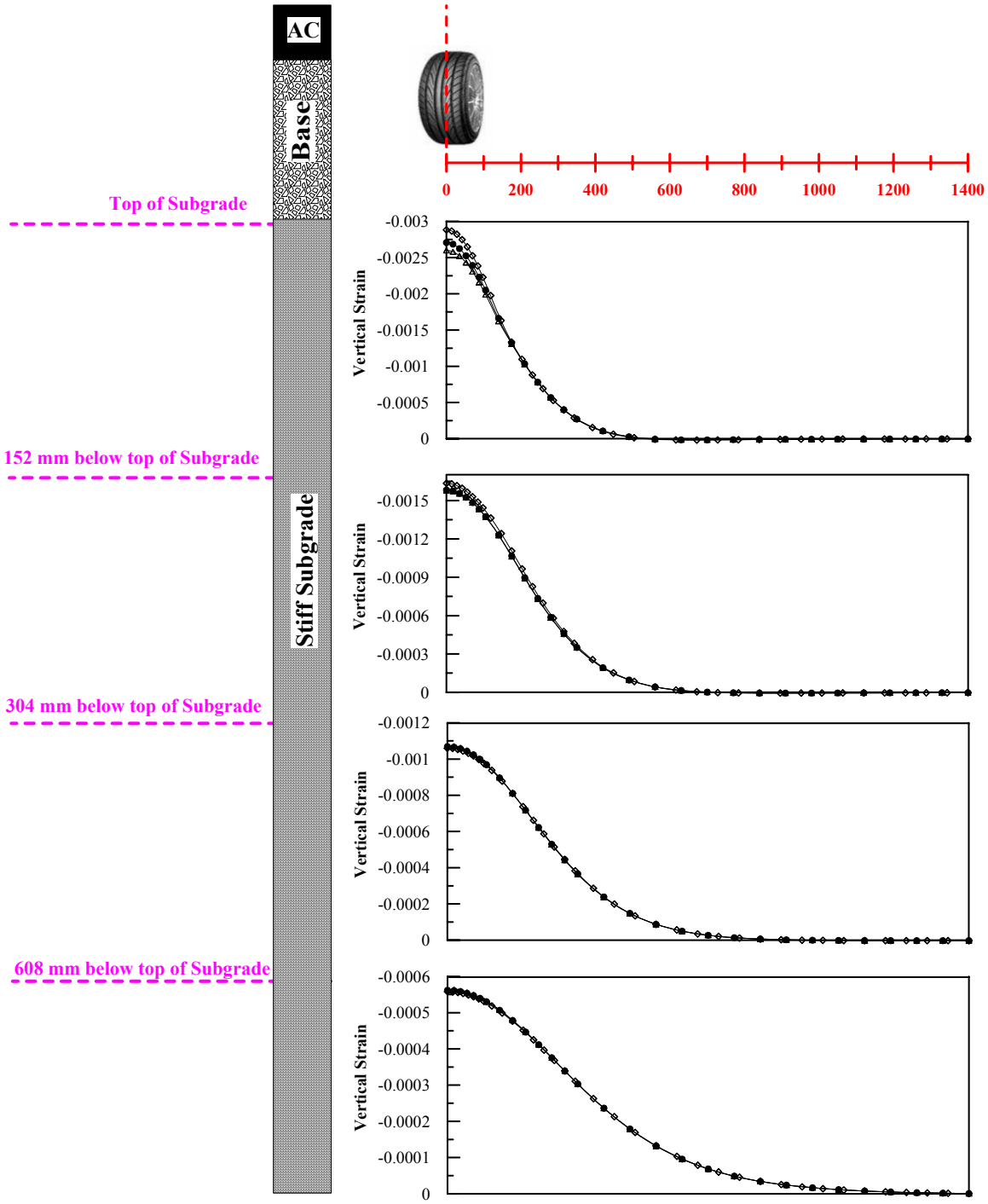

Figure 6.10 Vertical Strain Profiles within Subgrade Layer For Unreinforced Section 5c and Reinforced With Geogrid Place at the Bottom of the Base Layer

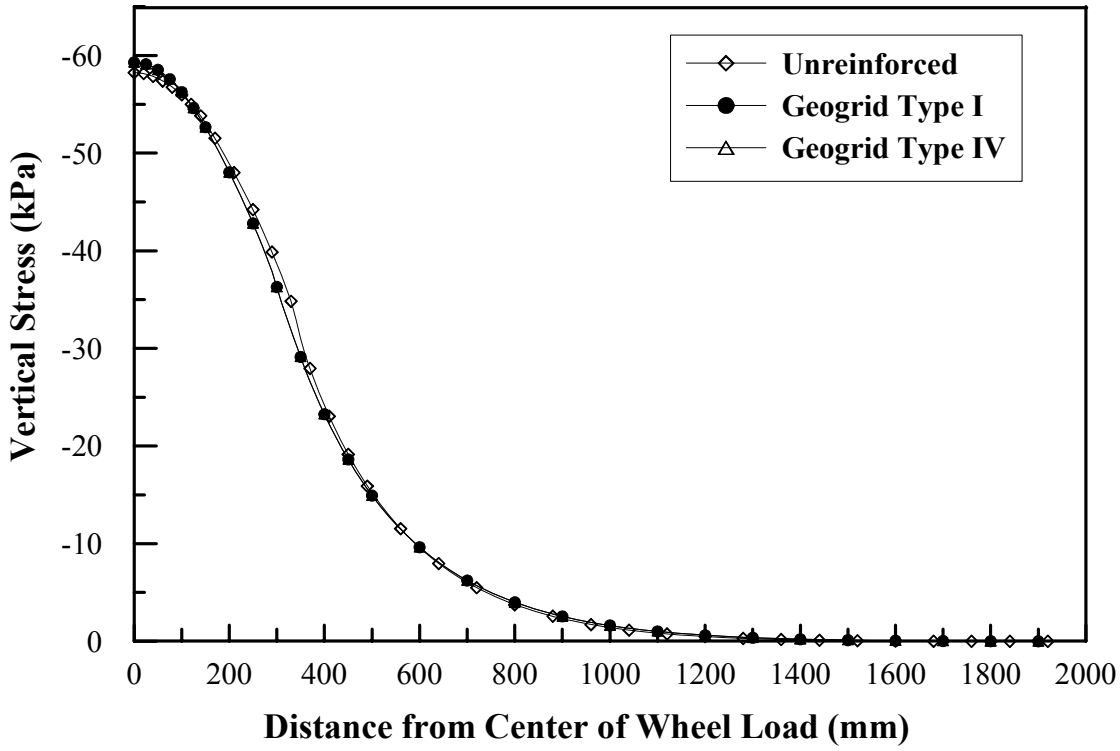

Figure 6.11 Vertical Stress Profile at top of Subgrade Layer for Unreinforced Section 1a and Reinforced With Geogrid Place at the Bottom of the Base Layer

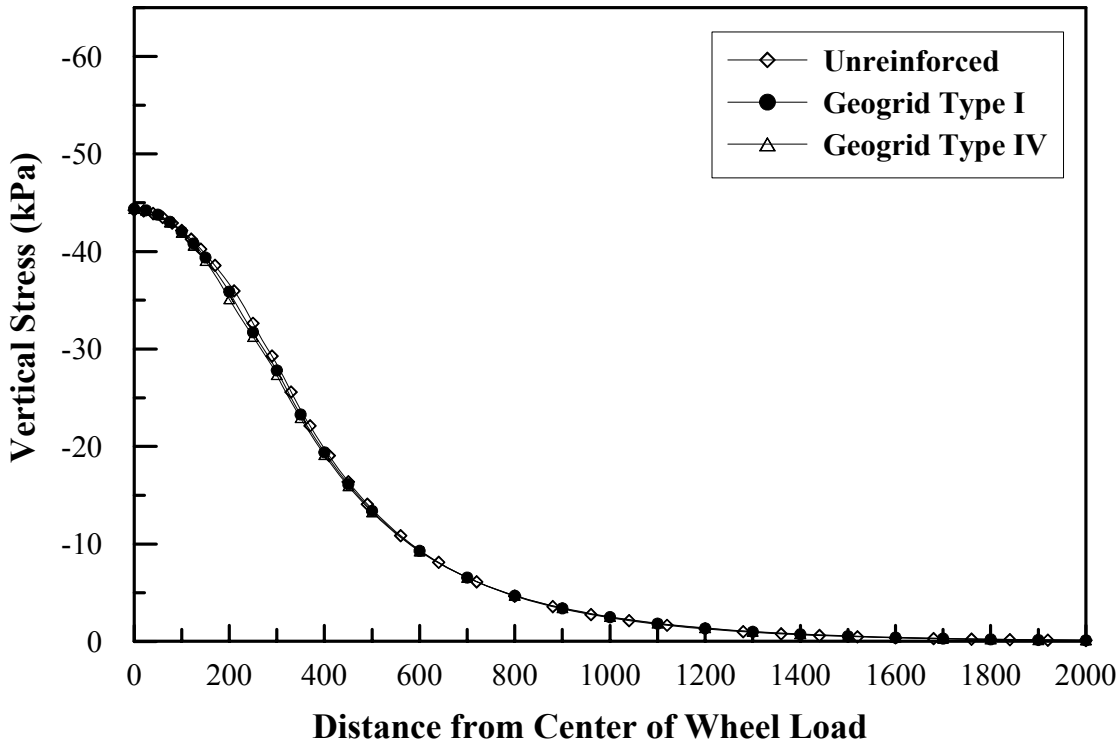

Figure 6.12 Vertical Stress Profile at top of Subgrade Layer for Unreinforced Section 5a and Reinforced with Geogrid Place at the Bottom of the Base Layer

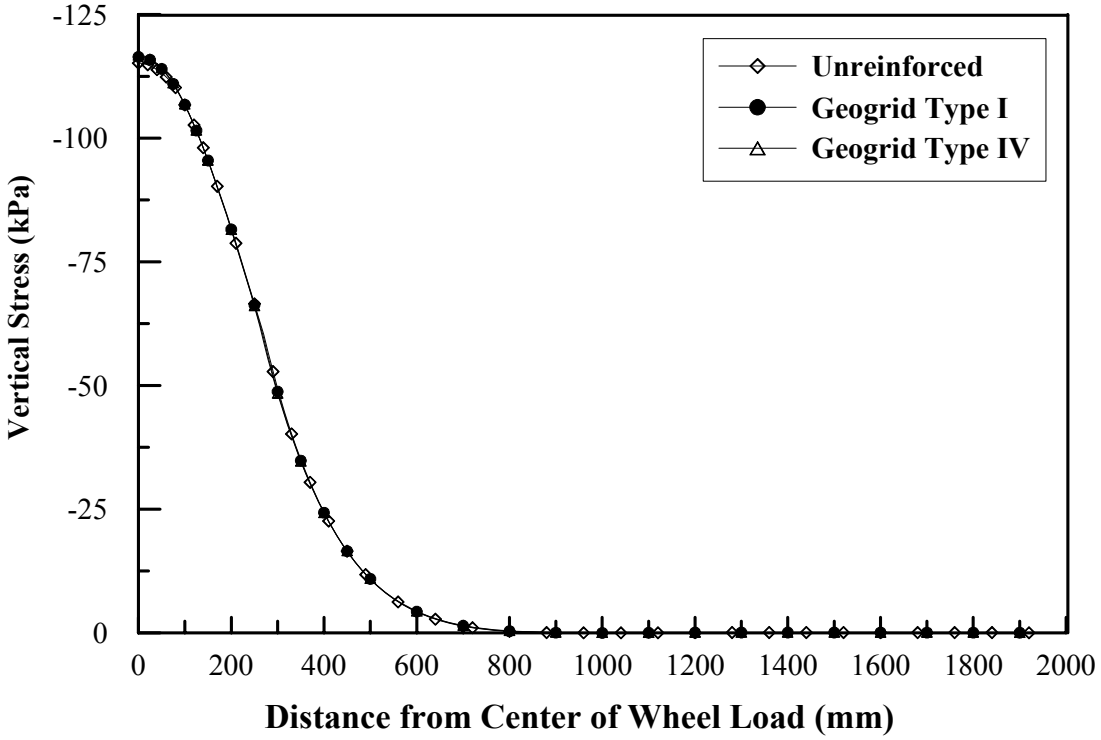

Figure 6.13 Vertical Stress Profile at top of Subgrade Layer for Unreinforced Section 1c and Reinforced with Geogrid Place at the Bottom of the Base Layer

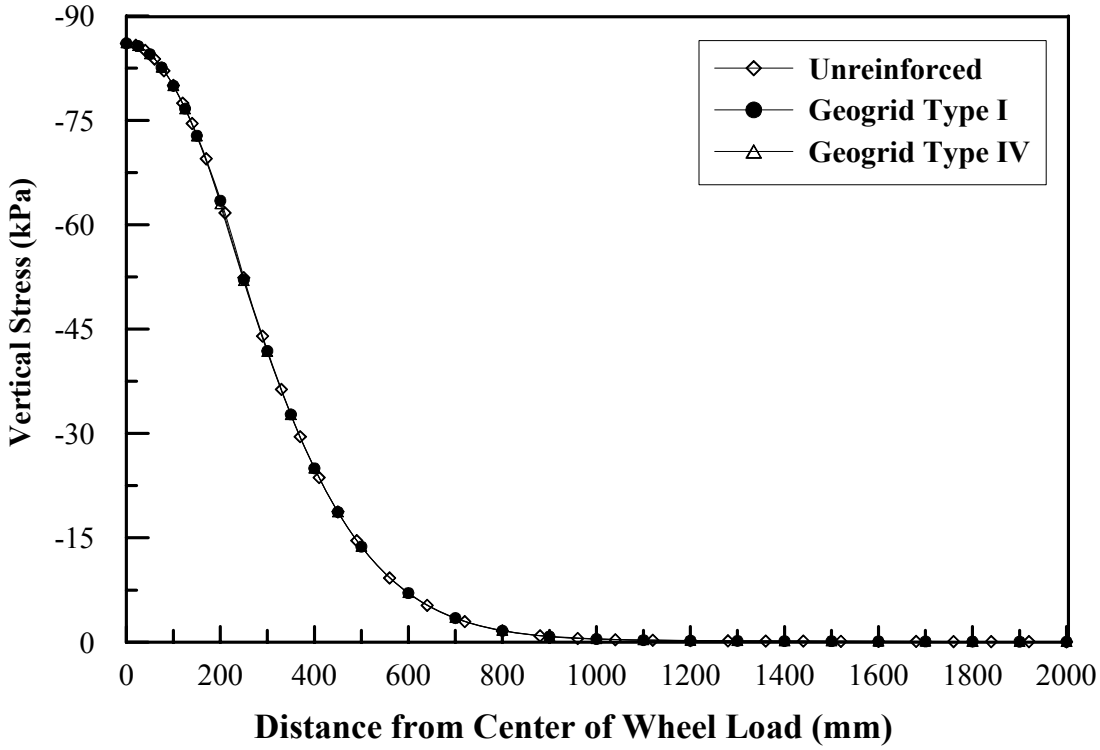

Figure 6.14 Vertical Stress Profile at top of Subgrade Layer for Unreinforced Section 5c and Reinforced with Geogrid Place at the Bottom of the Base Layer

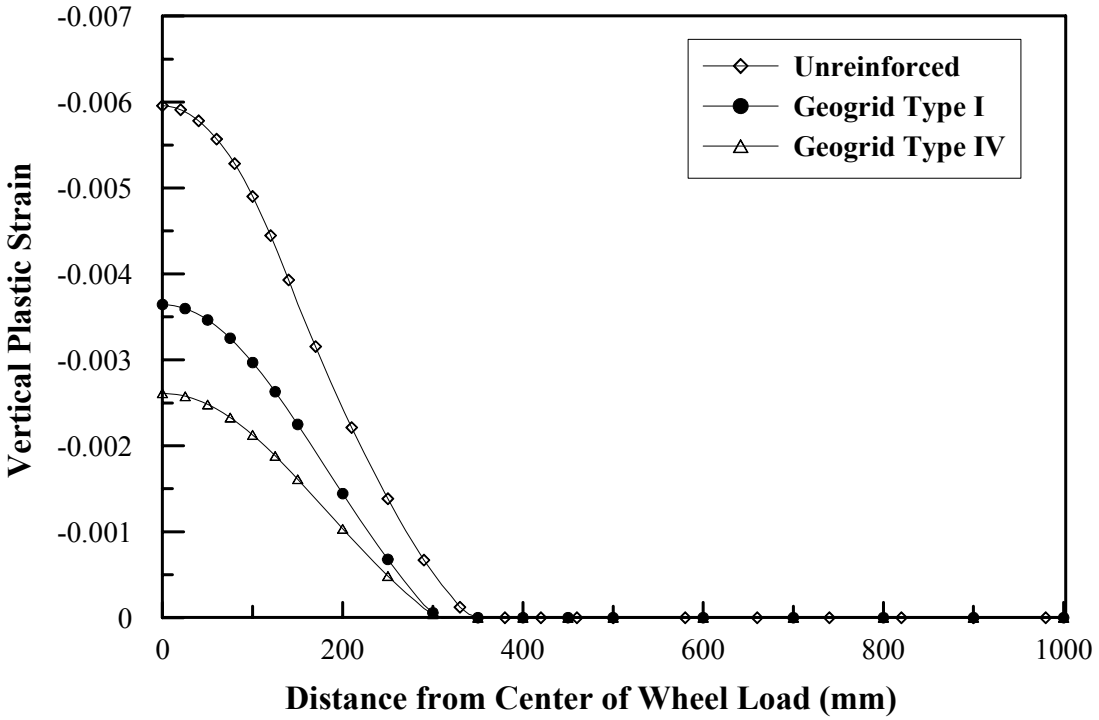

Figure 6.15 Vertical Plastic Strain Profile at top of Subgrade Layer for Unreinforced Section 1a and Reinforced with Geogrid Place at the Bottom of the Base Layer

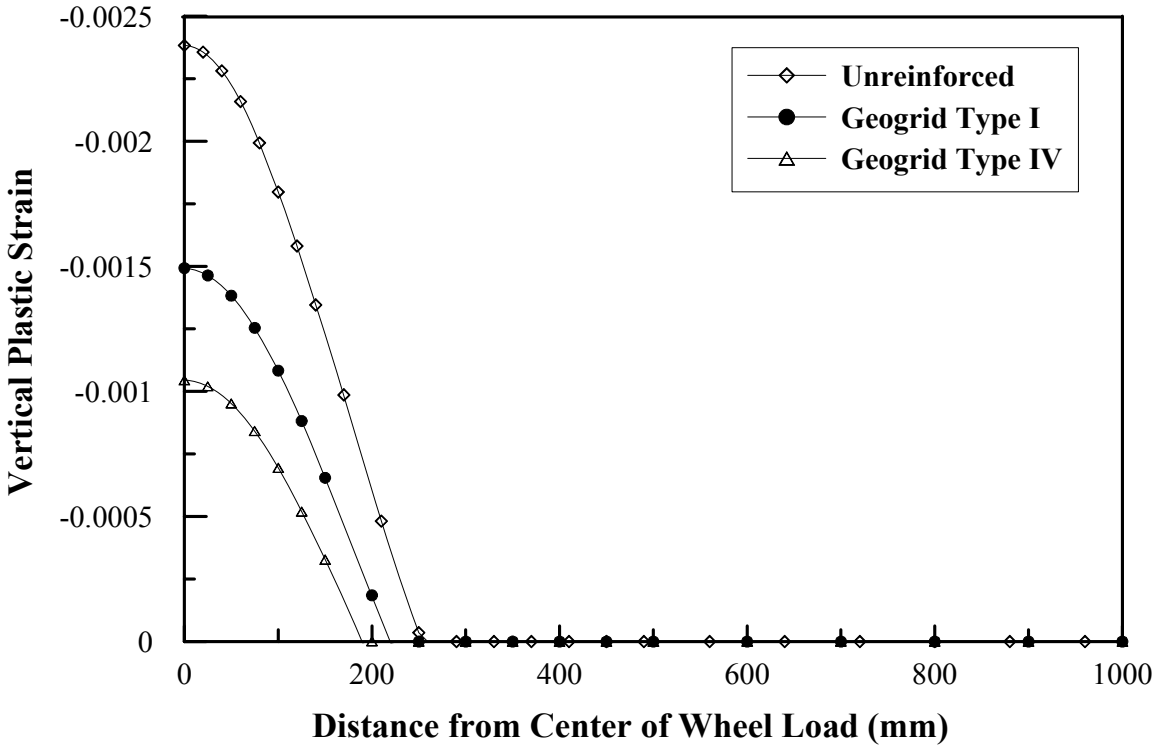

Figure 6.16 Vertical Plastic Strain Profile at top of Subgrade Layer for Unreinforced Section 5a and Reinforced with Geogrid Place at the Bottom of the Base Layer

obtained for the unreinforced section was much greater than those obtained for reinforced sections. This indicates that although the unreinforced section had larger vertical strains, the elastic portion of this strain that contributes to the stress is much less. This suggests that the geogrid layer influence is more pronounced on the development of the plastic strains than the resilient strain, which supports the findings of the experimental work of this study presented in Chapter Four.

Many studies indicated that the geogrid reinforcement benefits can be attributed to the reduction of shear strain at top the subgrade soil (Perkin, 2002; Berg et al, 2000; and Leng et al, 2003). Figure 6.19 through Figure 6.19 through Figure 6.22 presents the shear strain distributions at the top of the subgrade layer for sections 1a, 5a, 1c, and 5c, respectively. It is noticed that the geogrid resulted not only in decreasing the shear strains at the top of the subgrade layer, but also in providing a better distribution of these strains. This is expected since the shear strain transmitted from the base course layer to the subgrade would decrease as shearing of the base transmits tensile load to the geogrid reinforcement.

6.3.1.2 Effect of Geogrid Location

Figure 6.23 and Figure 6.24 present the lateral strain profiles computed at different distances from the center of the wheel load for sections 1a and 5c reinforced with a geogrid type IV layer placed at the different locations investigated in this study. In general, there is a slightly more reduction in the lateral strain at AC-base course layer interface when placing the geogrid layer at the upper one third locations compared to the other location; however, the bottom location had greater reduction within lower parts of the base course layer. Beyond a distance of 300 mm from the wheel load center, the geogrid location had the no effect on the lateral strains, mainly since the geogrid layer did

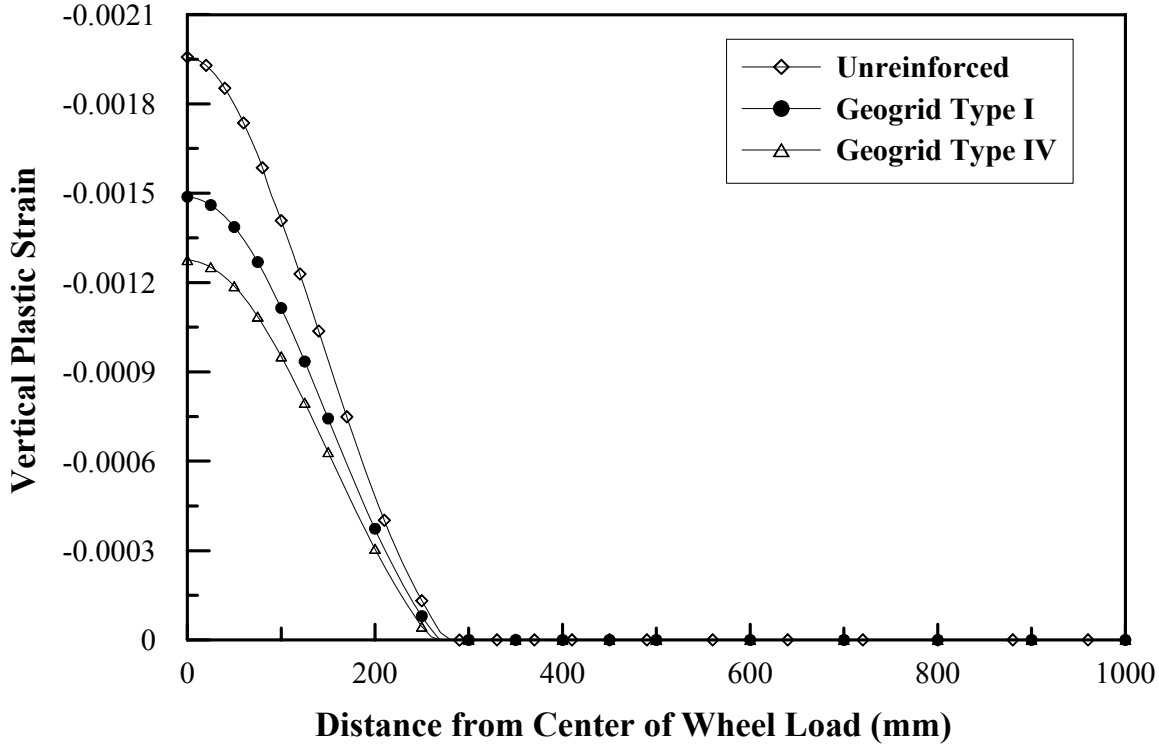

Figure 6.17 Vertical Plastic Strain Profile at top of Subgrade Layer for Unreinforced Section 1c and Reinforced with Geogrid Place at the Bottom of the Base Layer

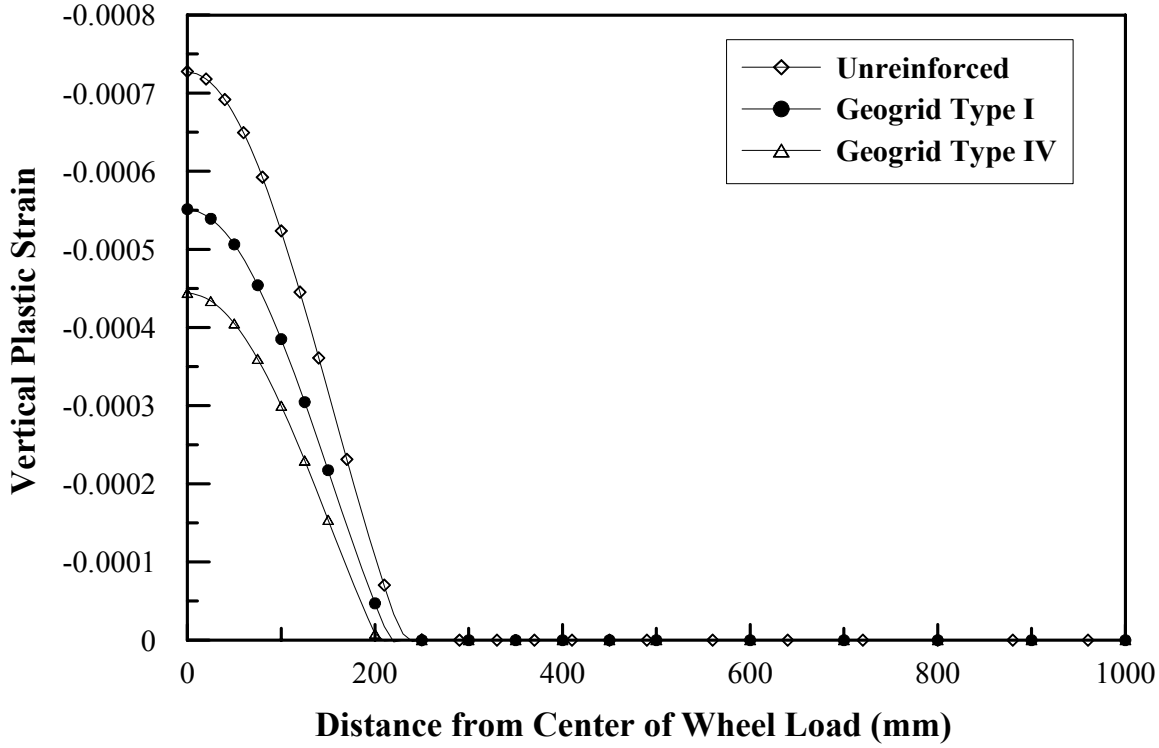

Figure 6.18 Vertical Plastic Strain Profile at top of Subgrade Layer for Unreinforced Section 5c and Reinforced with Geogrid Place at the Bottom of the Base Layer

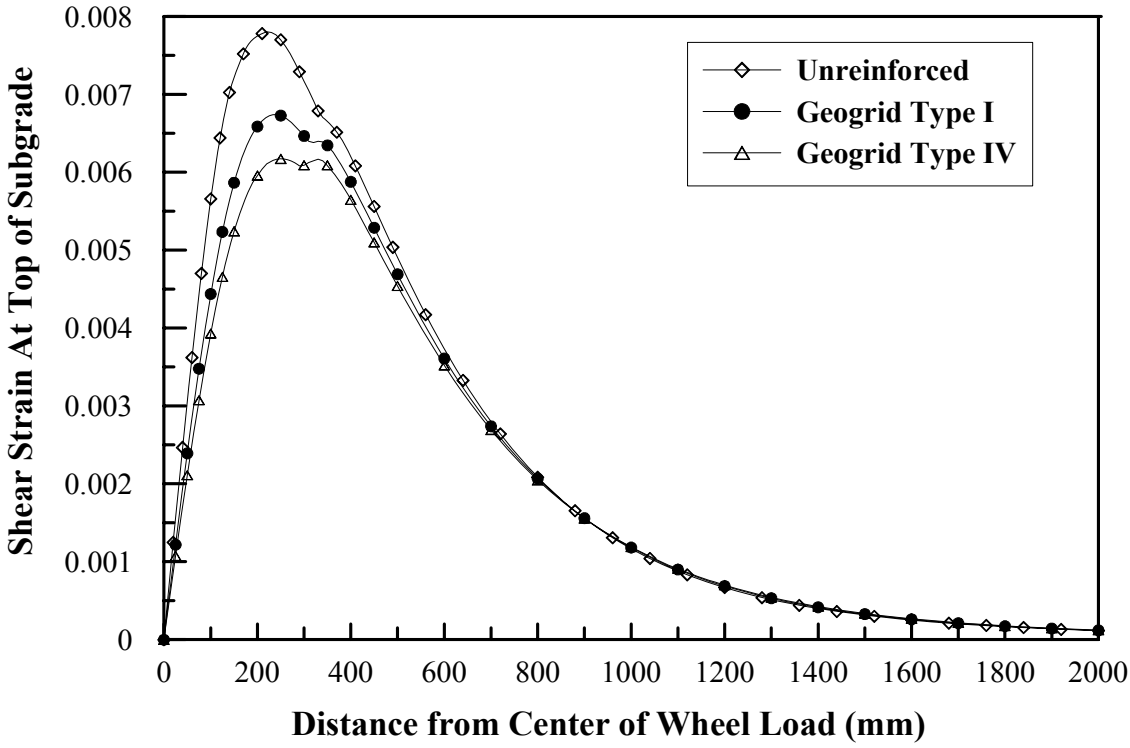

Figure 6.19 Shear Strain Profile at top of Subgrade Layer for Unreinforced Section 1a and Reinforced with Geogrid Place at the Bottom of the Base Layer

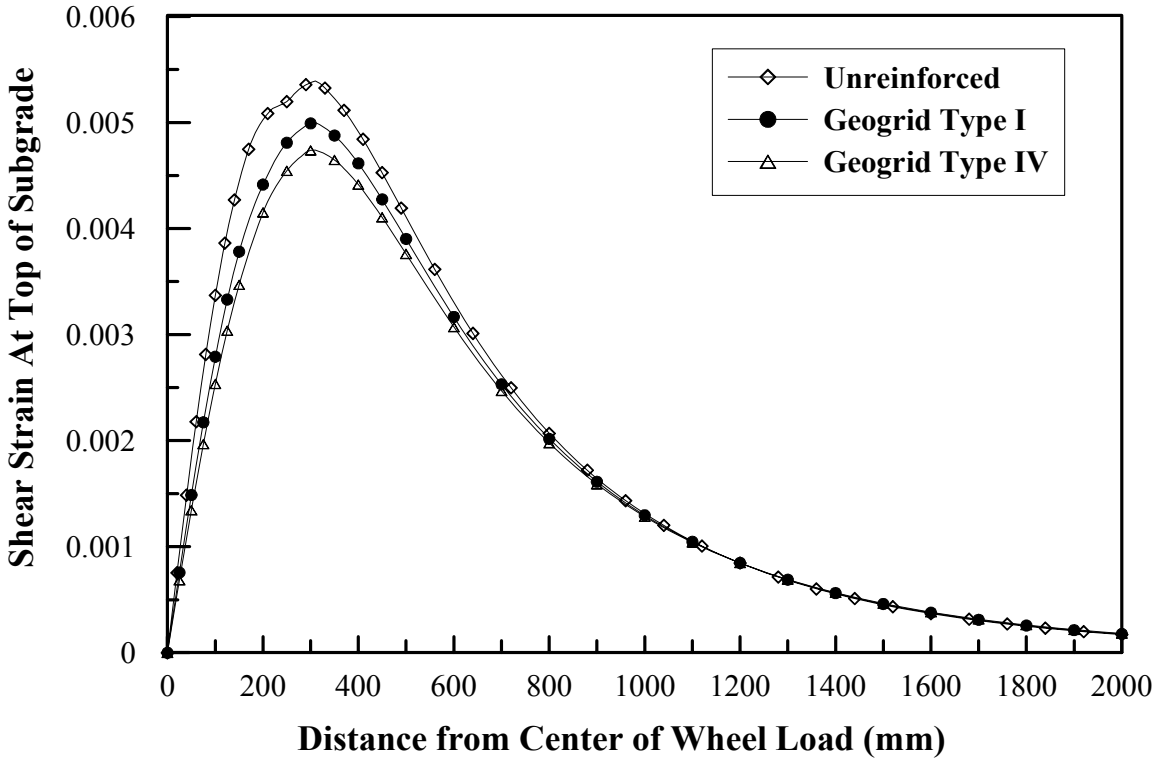

Figure 6.20 Shear Strain Profile at top of Subgrade Layer for Unreinforced Section 5a and Reinforced with Geogrid Place at the Bottom of the Base Layer

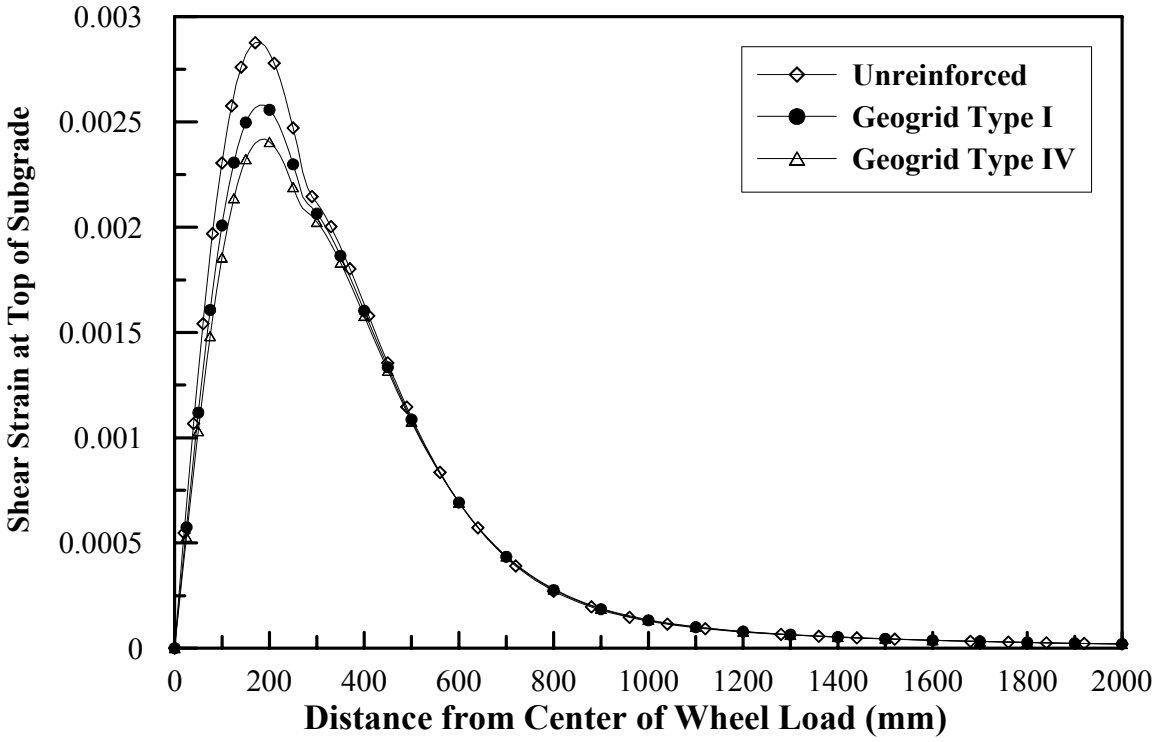

Figure 6.21 Shear Strain Profile at top of Subgrade Layer for Unreinforced Section 1c and Reinforced with Geogrid Place at the Bottom of the Base Layer

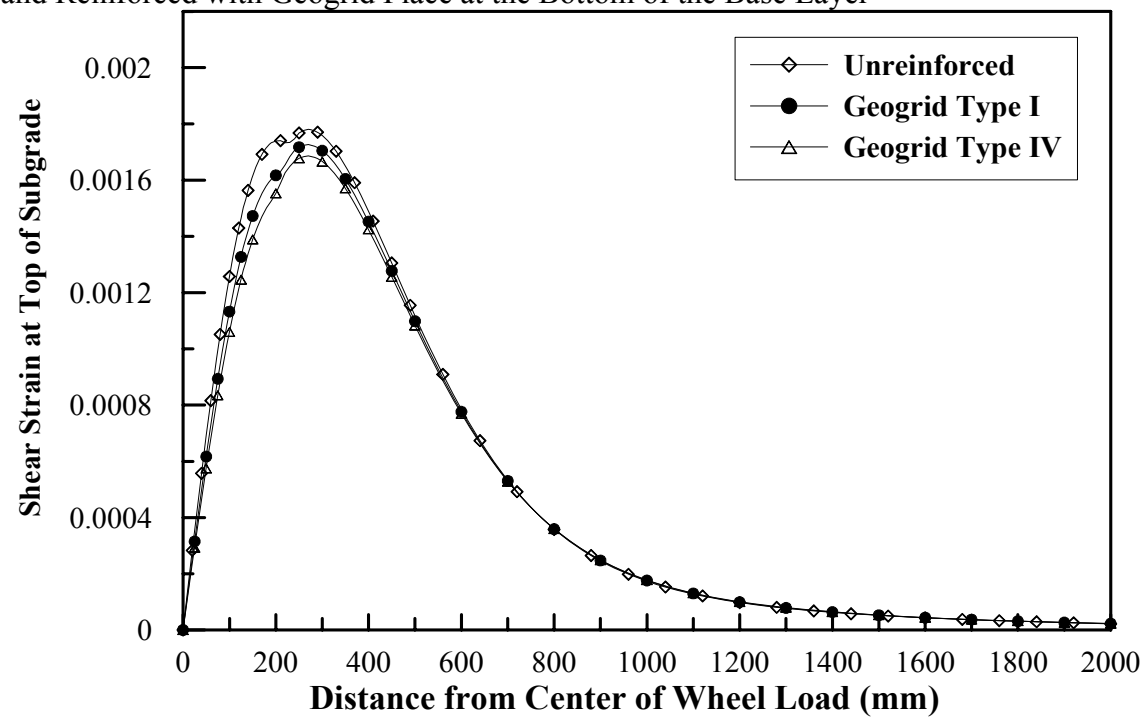

Figure 6.22 Shear Strain Profile at top of Subgrade Layer for Unreinforced Section 5c and Reinforced with Geogrid Place at the Bottom of the Base Layer

not have any contribution to the lateral strain beyond this point. A similar observation was noted for section 5c in Figure 6.24, however the differences between the different geogrid locations was smaller.

Figure 6.25 and Figure 6.26 show the vertical profile strain computed at different depths within the subgrade layer for sections 1a and 5c reinforced with a geogrid type IV layer placed at the different locations considered. It is noted that sections reinforced with a geogrid layer placed at the bottom of the base course had much greater reduction in vertical strain when compared to other locations. Furthermore, the reduction geogrid locations were more pounced in sections with thin base course layer built on top of weak subgrade layers.

Figure 6.27 and Figure 6.28 show the profile of vertical plastic strain obtained at the top of the subgrade layer for sections 1a and 5c reinforced at the different locations considered. It can bee seen that among all the location considered, the bottom location was had the most efficient effect in reducing the vertical plastic strain especially for section 5c. Similar observation was also noted in Figure 6.29 and Figure 6.30, which present the shear strain distribution at the top of the subgrade layer for sections 1a and 5c reinforced.

6.3.1.3 Effect of Geogrid Interface Properties

Figure 6.31 compares the lateral strain distribution under the center of the wheel load for section 3b reinforced with a layer of geogrid Type I placed at bottom of the base layer. In general, it is noted that the geogrid-base interface properties did not affect the distribution of lateral strain within the AC layer; however, a slight difference was observed within the base and subgrade layers, such that increasing Eslip value resulted in slight reduction in the lateral strain. It can also be noticed that the use of the frictional

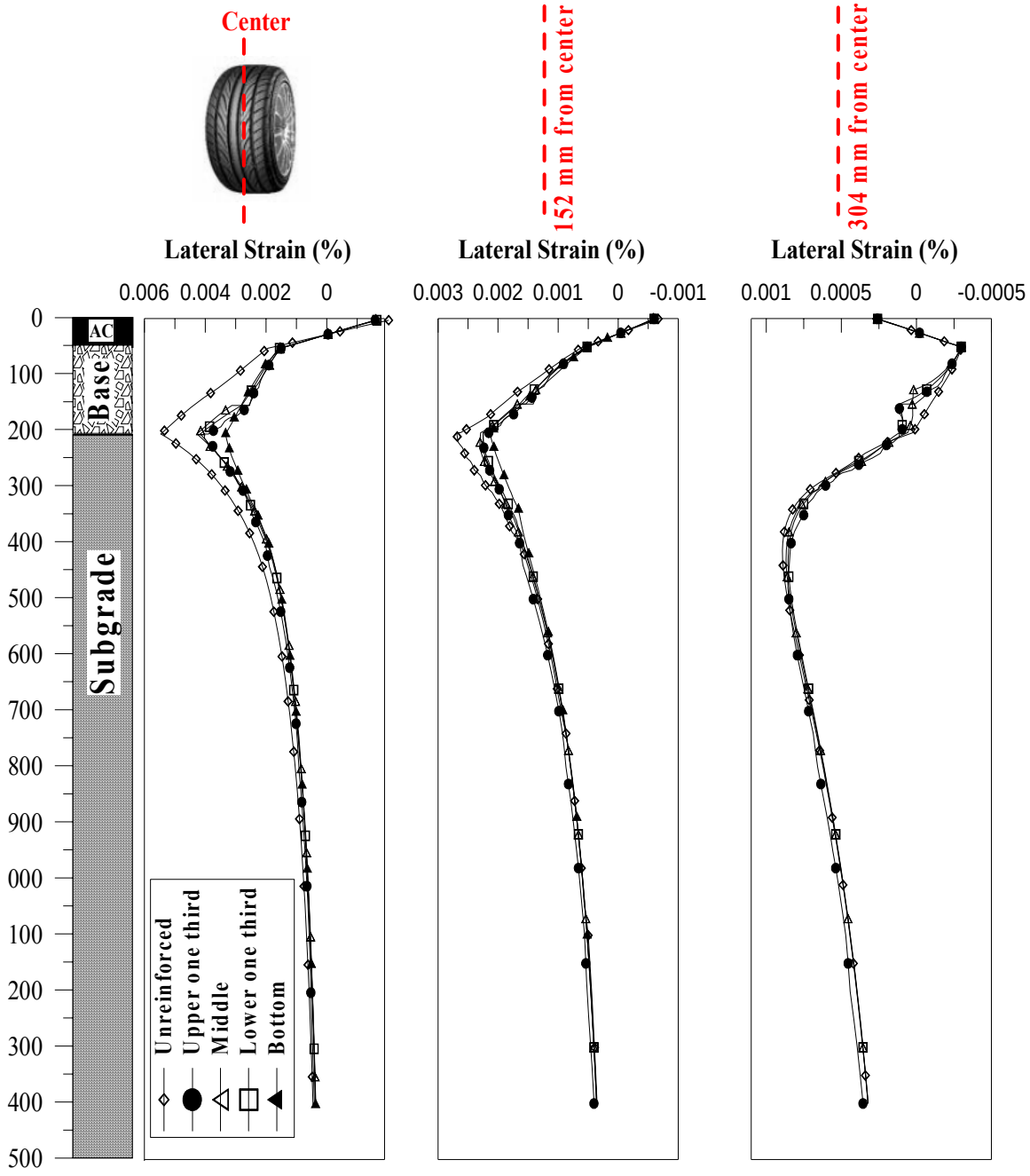

Figure 6.23 Lateral Strain Profile for Unreinforced Section 1a and Reinforced with Geogrid Type IV Layer Placed at Different Locations

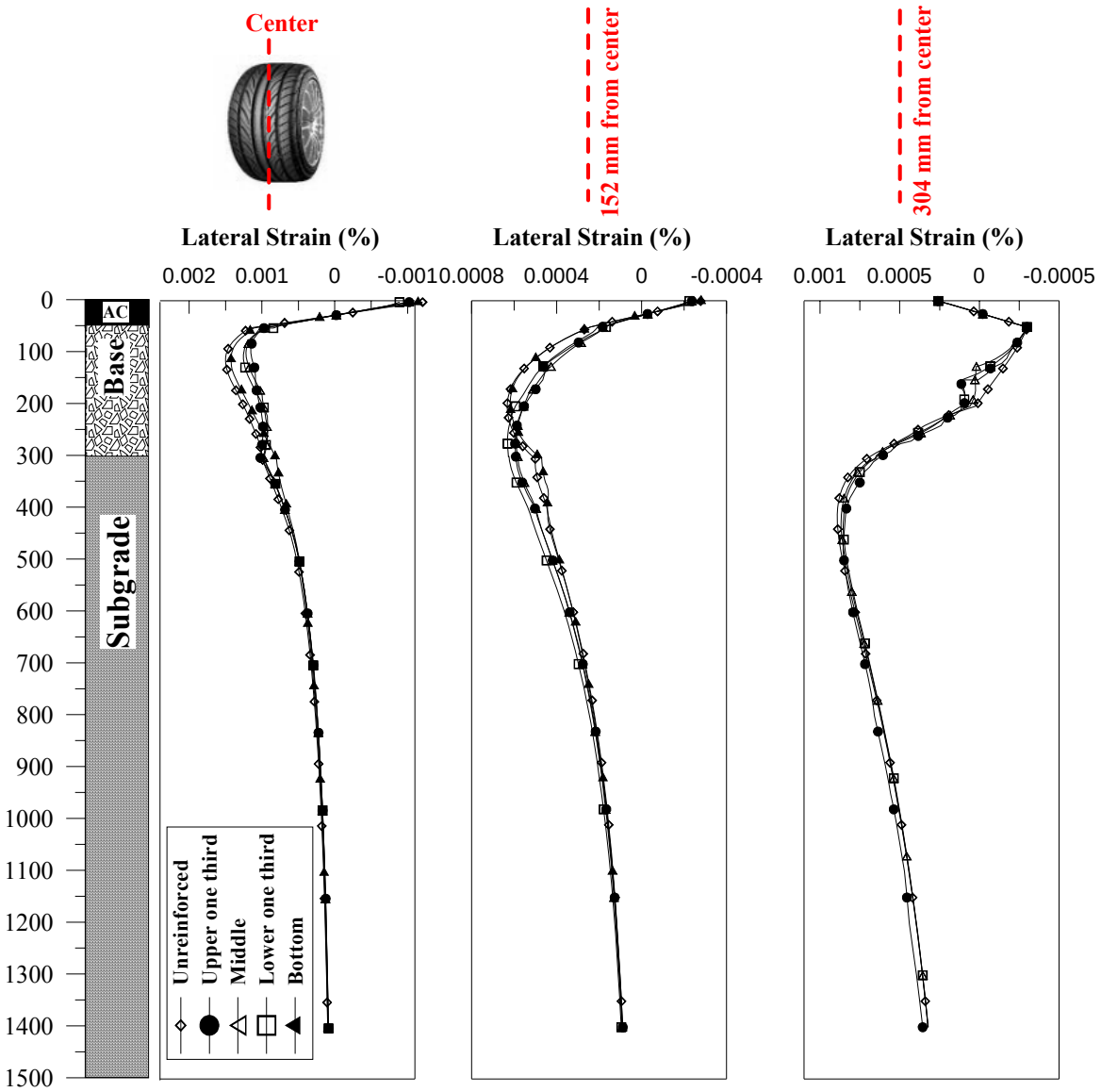

Figure 6.24 Lateral Strain Profile for Unreinforced Section 5c and Reinforced with a layer of Geogrid Type IV Placed at different locations

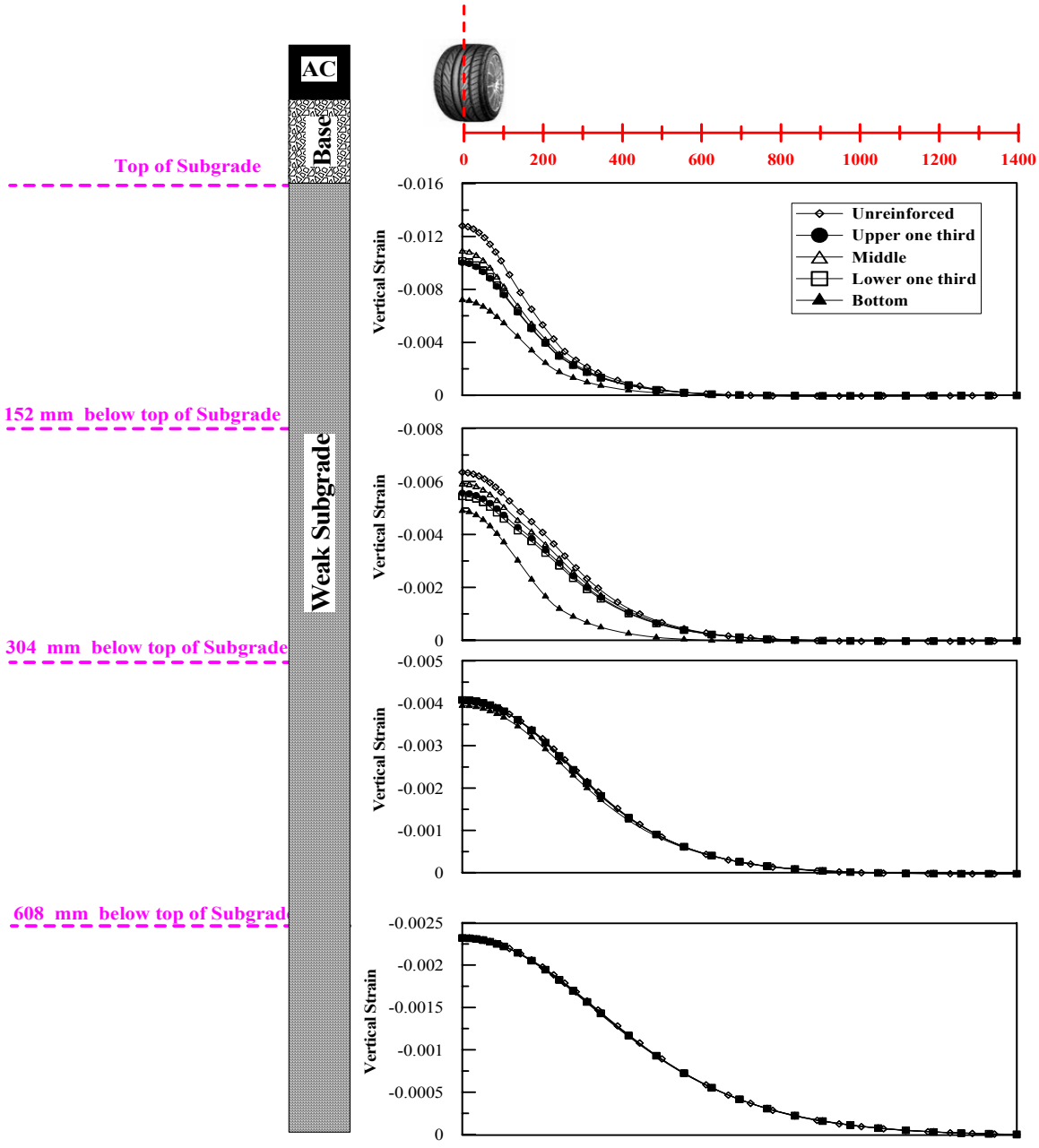

Figure 6.25 Vertical Strain Profiles within Subgrade Layer for Unreinforced Section 1a and Reinforced with a Layer of Geogrid Type IV Placed at Different Locations

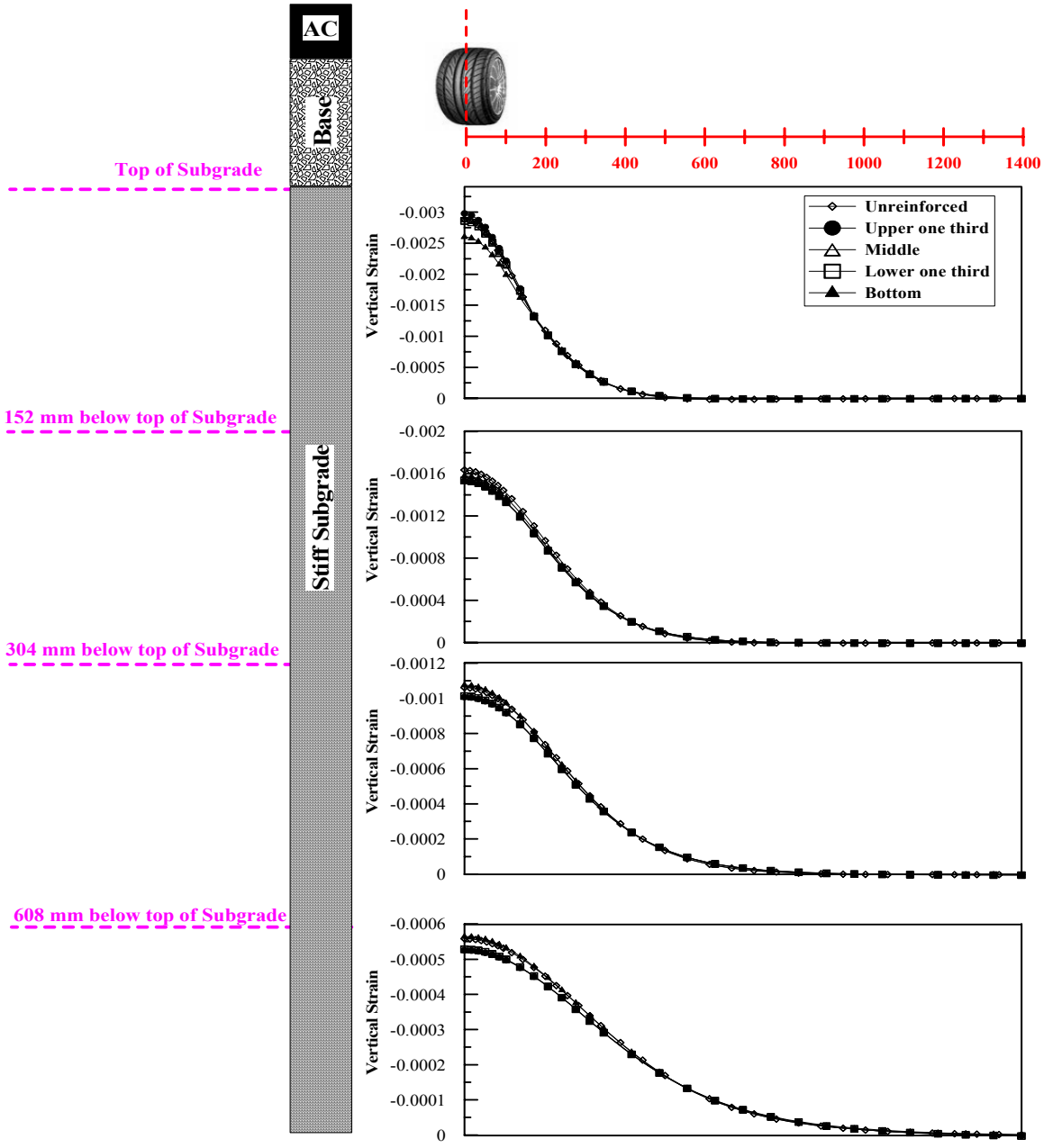

Figure 6.26 Vertical Strain Profiles within Subgrade Layer for Unreinforced Section 5c and Reinforced with a Layer of Geogrid Type IV Placed at Different Locations

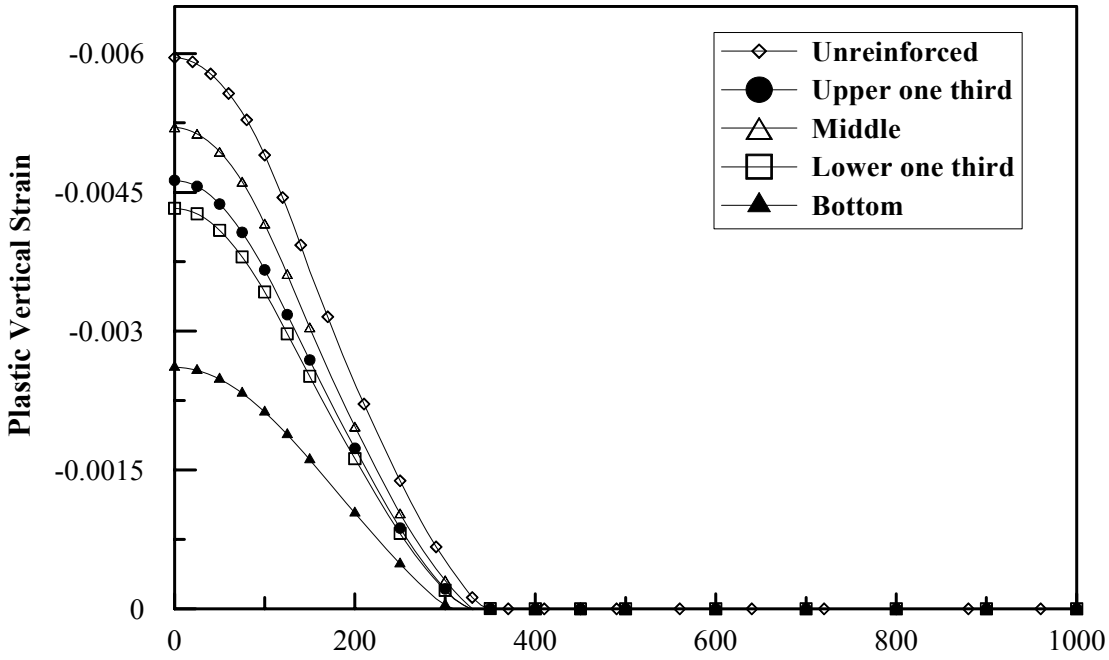

Figure 6.27 Vertical Plastic Strain Profile at top of Subgrade Layer for Unreinforced Section 1a and Reinforced with a layer of Geogrid Type IV Placed at different locations

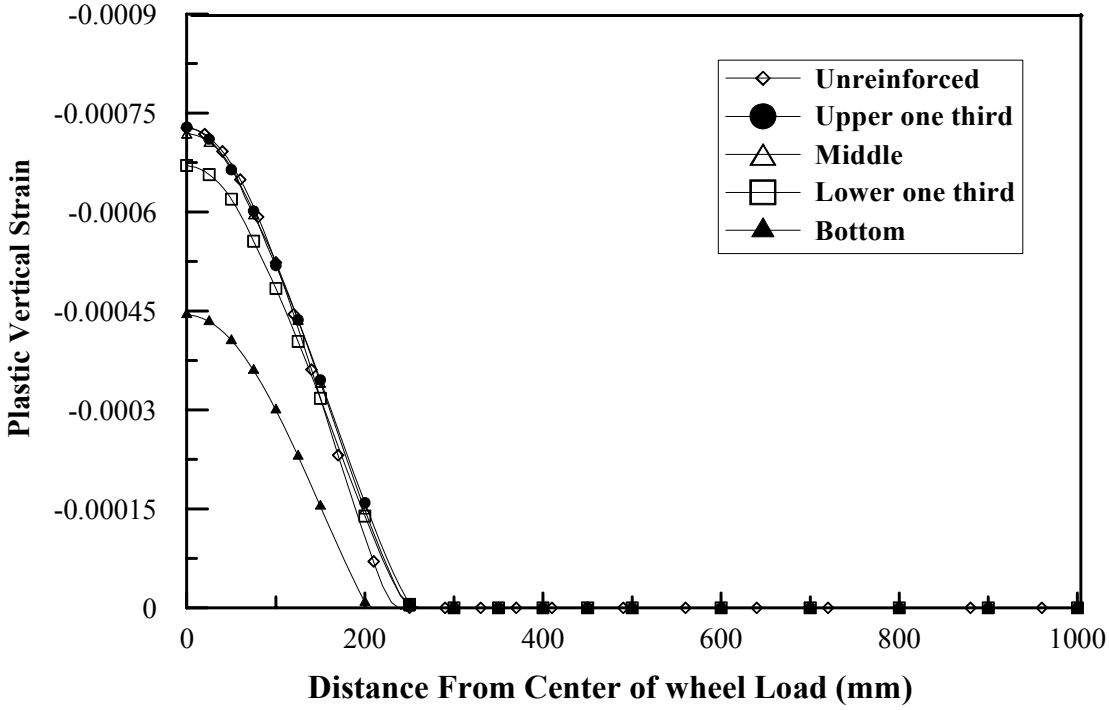

Figure 6.28 Vertical Plastic Strain Profile at top of Subgrade Layer for Unreinforced Section 5c and Reinforced with a layer of Geogrid Type IV Placed at different locations

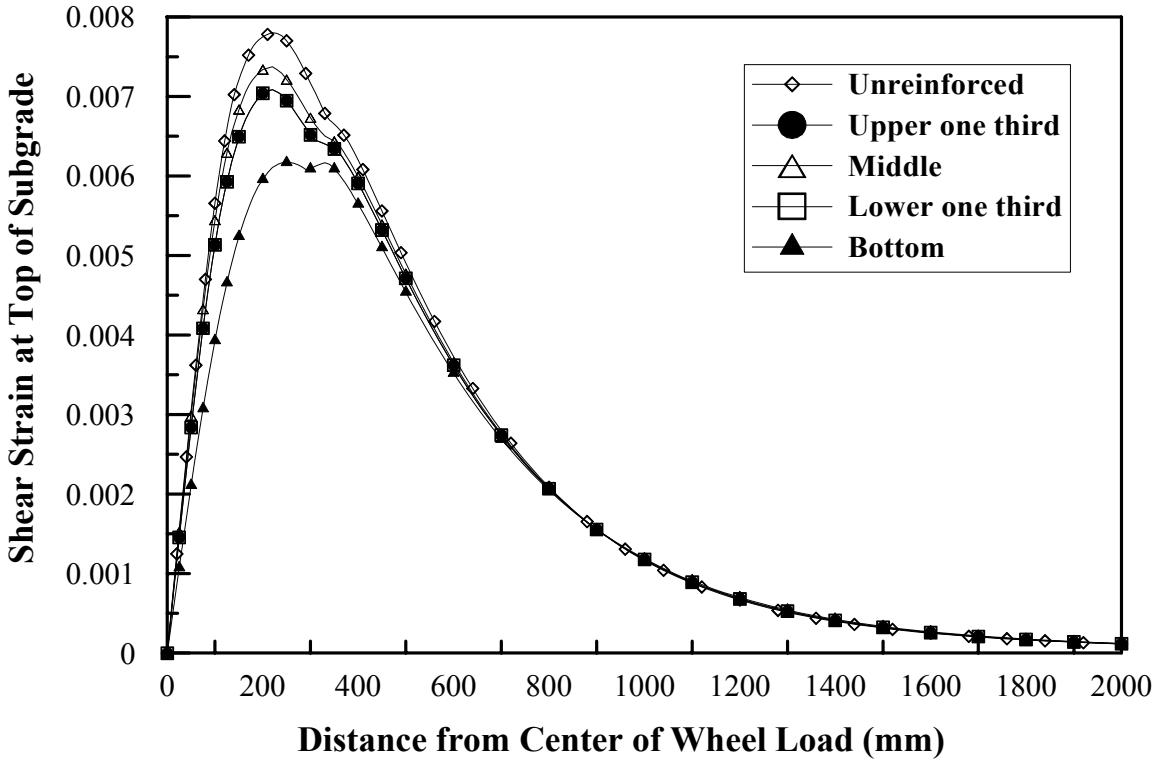

Figure 6.29 Shear Strain Profile at top of Subgrade Layer for Unreinforced Section 1a and Reinforced with a layer of Geogrid Type IV Placed at different locations

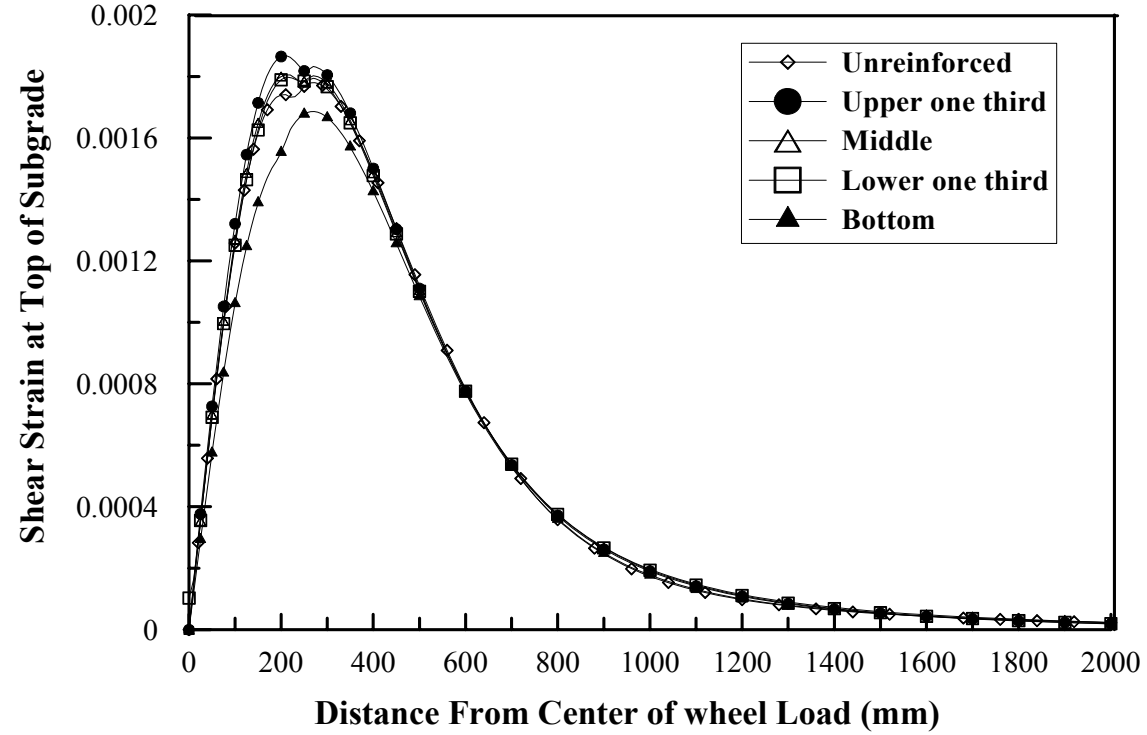

Figure 6.30 Shear Strain Profile at top of Subgrade Layer for Unreinforced Section 5c and Reinforced with a layer of Geogrid Type IV Placed at different locations

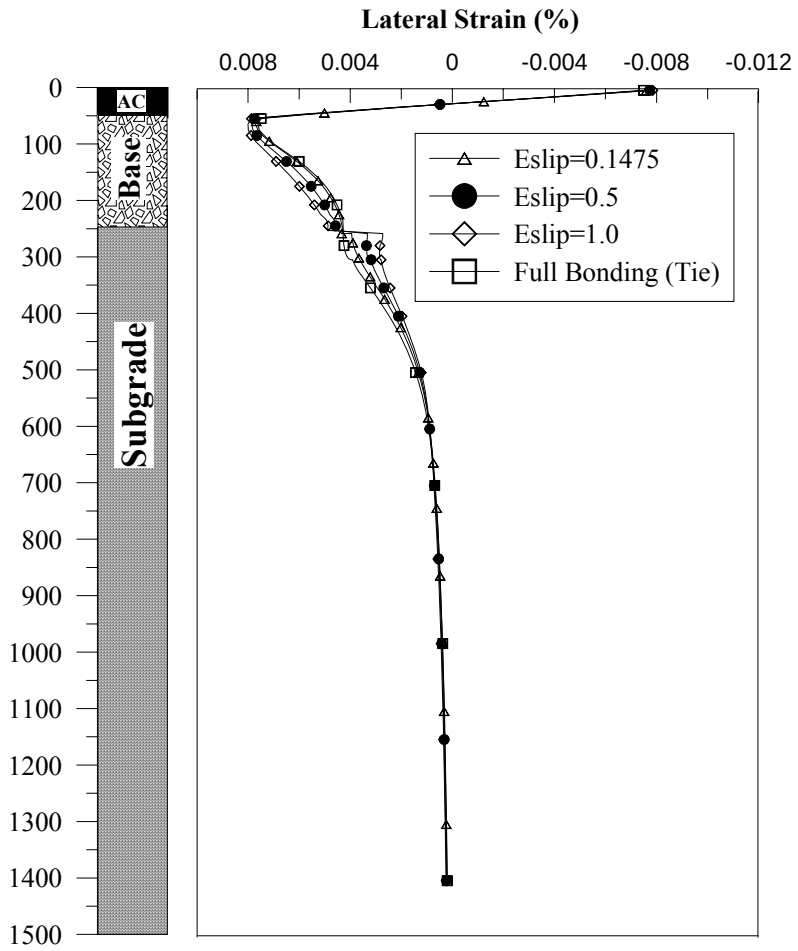

Figure 6.31 Lateral Strain Profile of Reinforced Section with Different Interface Properties

interface resulted in discontinuity in the lateral strain at base-subgrade interface. This discontinuity is mainly due to the shear-resistance interfacial strains.

Figure 6.32 and Figure 6.33 present the total and plastic vertical stain profiles at top of the subgrade layer for section 3b reinforced with a layer of geogrid Type I placed at bottom of the base layer. It is noticed that for reinforced sections, the increase in Eslip, and thus the decrease in the interface shear moduli, resulted in reducing both the total and plastic strain at the top of the subgrade. Figure 6.34 presents the shear strain distribution at value at top of the subgrade, it is noted that the different geogrid-base interface conditions resulted in the same trend, however lower Elsip values decreased the

magnitude of the shear strain In general, it was observed that the full bonding condition resulted in lateral, vertical, and shear strains close to those of the frictional interface condition with Eslip value of 0.5.

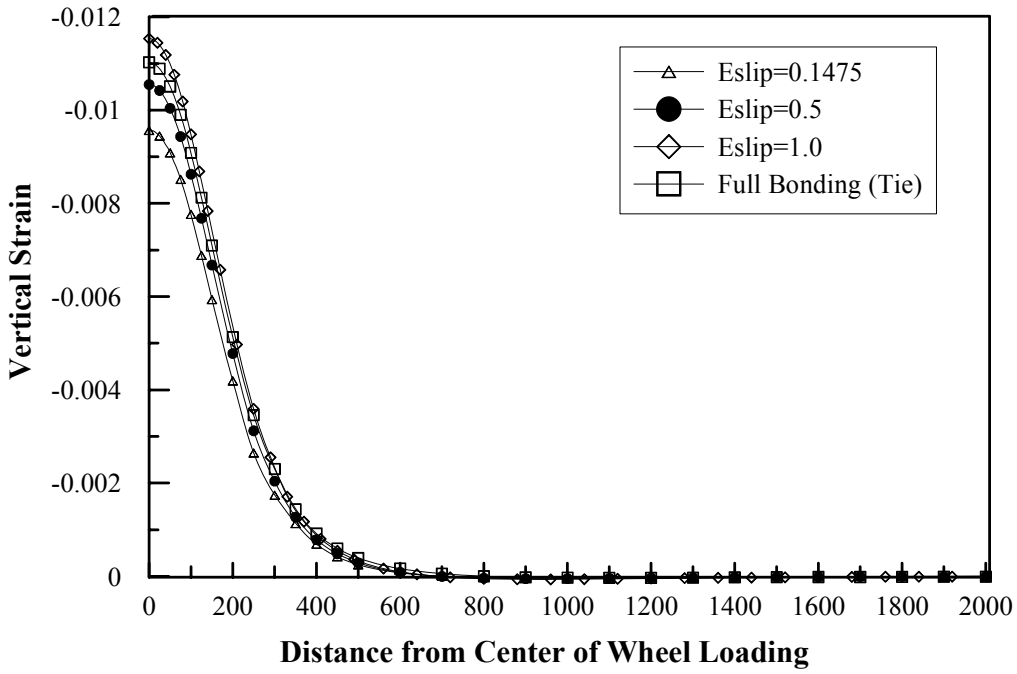

Figure 6.32 Vertical Strain Profile of Reinforced Section with Different Interface Properties

6.3.2 Permanent Deformation

Less shear strain, coupled with less vertical and lateral strains results in a less severe state of loading leading to lower permanent deformation accumulation. Figure 6.35 depict example of the permanent deformation curves computed using the finite element analysis for unreinforced and geogrid reinforced sections. It can clearly be seen that the geogrid reinforcement reduced the permanent deformation for reinforcedsections. However, the magnitude of reduction depended on the geogrid stiffness, and the subgrade strength, and the base course thickness.

Since the design of a pavement structure is evaluated at the end of its service life, the improvement due to the geogrid base reinforcement should be also evaluated at that

time. In this study, the pavement structure was assumed to have a moderate traffic volume, which is designed for 1 to 3 million single axle wheel load repetition. Therefore, the benefits of geogrid reinforcement in this study were evaluated at 2 million load cycles. The surface permanent deformation that accumulated during the application of 100 load cycles computed from the results of finite element analysis was used to develop regression models for each unreinforced and reinforced section to relate the permanent deformation to the number of load cycles. A power law of the number of load cycles was used to represent the permanent deformation response under repetitive loading for each section. Table 6.3 presents a summary of the permanent deformation regression models developed for the different sections in this study. The developed models were used to determine the permanent deformation values at 2 million load cycles.

The extrapolation of a regression model might cause unacceptable error in predicted value; therefore it was necessary to verify the prediction of permanent deformation-load cycles regression models. For this purpose, finite element analysis was conducted on section 3b in Table 6.3 to determine the permanent deformation value after 1500 load cycles. The permanent deformation obtained from the finite element analysis was then compared to those predicted using the regression model developed for the same section based on 100 load cycles. This comparison is shown in Figure 6.36. It was found that at 1500 load cycles the error in the predicted value was within 5% margin error, which is considered acceptable.

Figure 6.37 through Figure 6.39 depict the reduction in permanent deformation obtained at 2 million load cycles determined using the developed regression models for the different unreinforced sections and sections reinforced with the four different geogrid types placed at the bottom of the base course layer. It can be seen that an increase in the

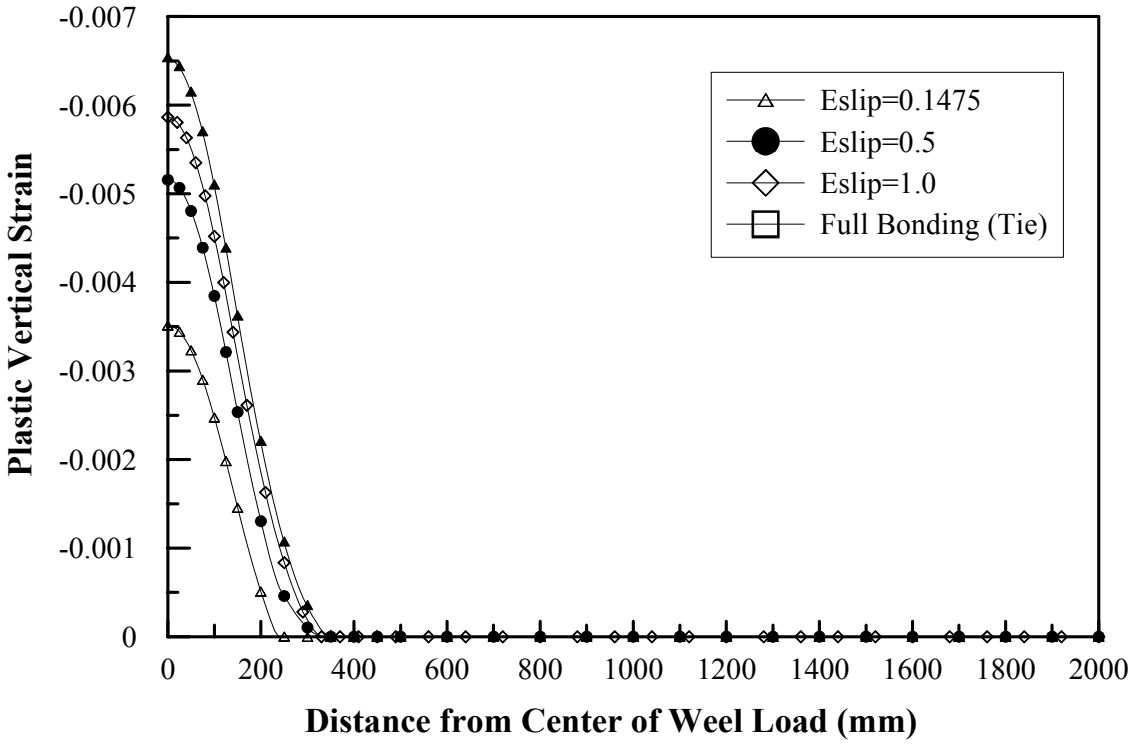

Figure 6.33 Vertical Plastic Strain Profile of Reinforced Sections with Different Interface Properties

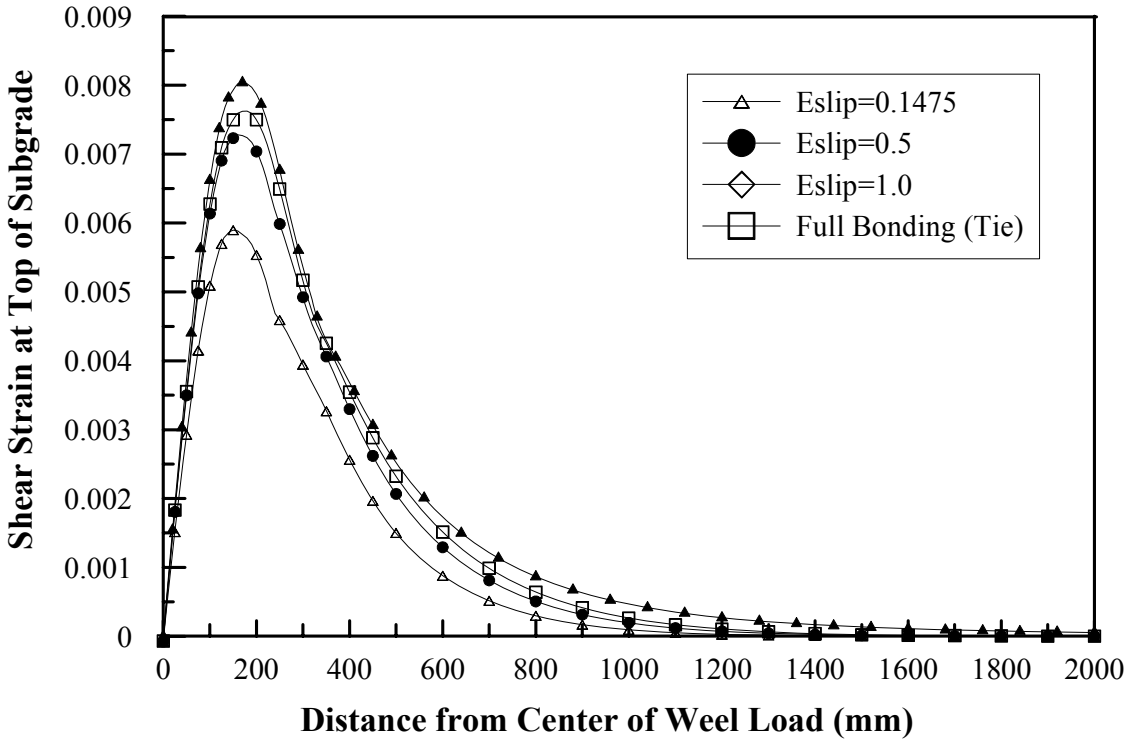

Figure 6.34 Shear Strain Profile of Reinforced Sections with Different Interface Properties

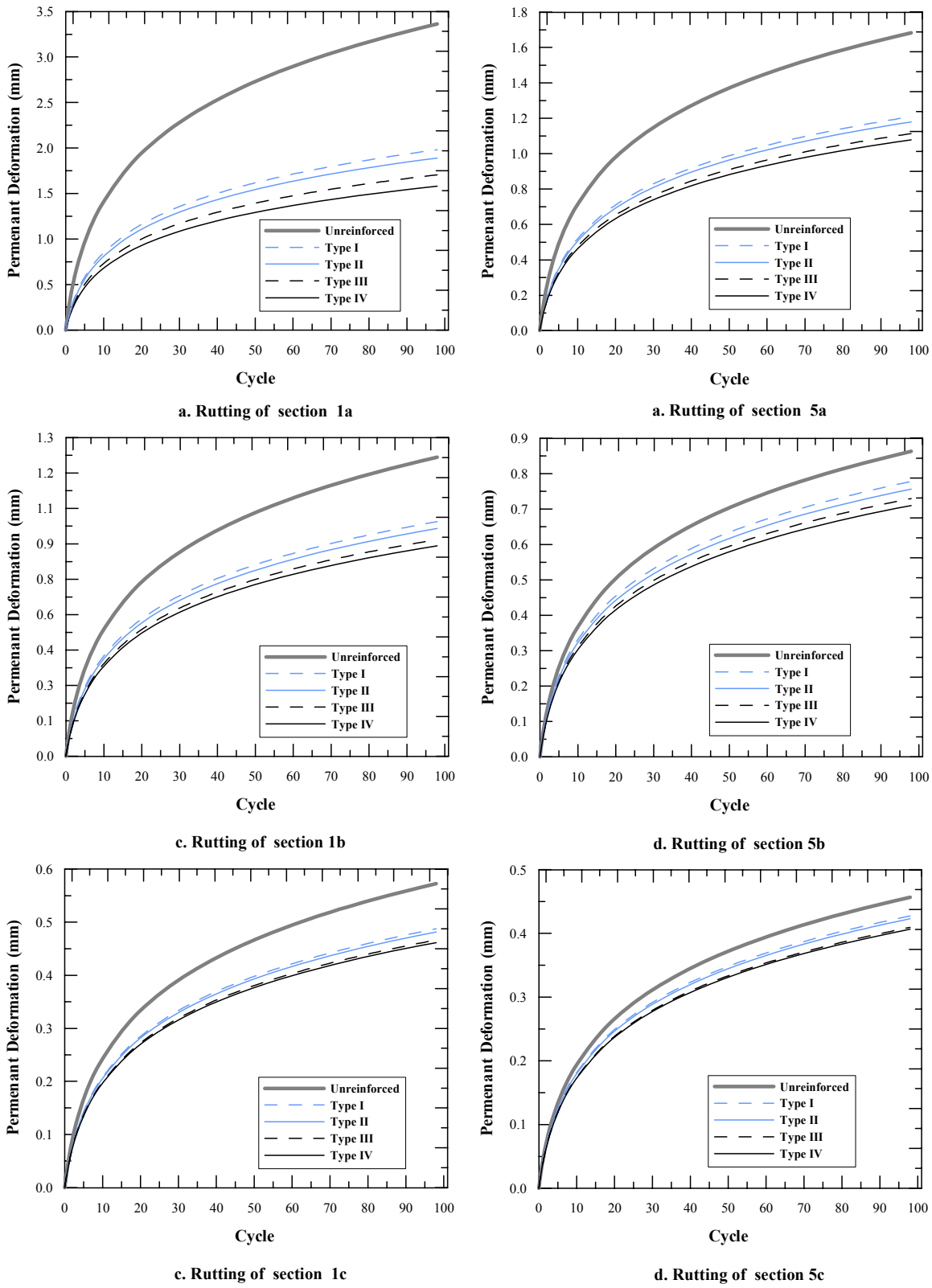

Figure 6.35 Rutting Curves of Different Pavement Sections

Table 6.3 Summary of Rutting Models of Sections Investigated

Section #	Type	Geogrid	δ_p Regression model	Section #	Type	Geogrid	δ_p Regression model
1a	Un	none	$9.45*N^{(0.074)}$	3b	Re	Type III	$2.69*N^{(0.061)}$
1b	Un	none	$4.21*N^{(0.066)}$	3c	Re	Type III	$1.42*N^{(0.063)}$
1c	Un	none	$1.95*N^{(0.063)}$	3a	Re	Type III	$4.85*N^{(0.055)}$
1a	Re	Type IV	$6.47*E5^{(0.054)}$	3b	Re	Type III	$2.72*N^{(0.062)}$
1b	Re	Type IV	$3.31*N^{(0.059)}$	3c	Re	Type III	$1.43*N^{(0.064)}$
1c	Re	Type IV	$1.69*N^{(0.06)}$	4a	Un	none	$4.65*N^{(0.061)}$
1a	Re	Type III	$6.56*N^{(0.057)}$	4b	Un	none	$2.64*N^{(0.064)}$
1b	Re	Type III	$3.35*N^{(0.06)}$	4c	Un	none	$1.39*N^{(0.066)}$
1c	Re	Type III	$1.70*N^{(0.059)}$	4a	Re	Type IV	$3.78*N^{(0.051)}$
1a	Re	Type II	$7.20*N^{(0.058)}$	4b	Re	Type IV	$2.30*N^{(0.061)}$
1b	Re	Type II	$3.57*N^{(0.059)}$	4c	Re	Type IV	$1.27*N^{(0.065)}$
1c	Re	Type II	$1.78*N^{(0.059)}$	4a	Re	Type III	$3.81*N^{(0.052)}$
1a	Re	Type I	$7.38*N^{(0.059)}$	4b	Re	Type III	$2.31*N^{(0.061)}$
1b	Re	Type I	$3.65* N^{(0.059)}$	4c	Re	Type III	$1.28*N^{(0.065)}$
1c	Re	Type I	$1.80*N^{(0.059)}$	4a	Re	Type III	$4.04*N^{(0.053)}$
2a	Un	none	$7.16*N^{(0.069)}$	4b	Re	Type III	$2.41*N^{(0.061)}$
2b	Un	none	$3.53*N^{(0.0642)}$	4c	Re	Type III	$1.31*N^{(0.065)}$
2c	Un	none	$1.71*N^{(0.063)}$	4a	Re	Type III	$4.12*N^{(0.054)}$
2a	Re	Type IV	$5.25*N^{(0.055)}$	4b	Re	Type III	$2.44*N^{(0.062)}$
2b	Re	Type IV	$2.87*N^{(0.060)}$	4c	Re	Type III	$1.32*N^{(0.065)}$
2c	Re	Type IV	$1.51*N^{(0.062)}$	5a	Un	none	$3.88*N^{(0.06)}$
2a	Re	Type III	$5.30*N^{(0.056)}$	5b	Un	none	$2.33*N^{(0.065)}$
2b	Re	Type III	$2.91*N^{(0.06)}$	5c	Un	none	$1.26*N^{(0.067)}$
2c	Re	Type III	$1.52*N^{(0.062)}$	5a	Re	Type IV	$3.29*N^{(0.049)}$
2a	Re	Type II	$5.79*N^{(0.056)}$	5b	Re	Type IV	$2.1* N^{(0.061)}$
2b	Re	Type II	$3.09*N^{(0.06)}$	5c	Re	Type IV	$1.19*N^{(0.067)}$
2c	Re	Type II	$1.58*N^{(0.062)}$	5a	Re	Type III	$3.30*N^{(0.052)}$
2a	Re	Type I	$5.90*N^{(0.057)}$	5b	Re	Type III	$2.10*N^{(0.063)}$
2b	Re	Type I	$3.14*N^{(0.06)}$	5c	Re	Type III	$1.19*N^{(0.067)}$
2c	Re	Type I	$1.60*N^{(0.062)}$	5a	Re	Type III	$3.47*N^{(0.054)}$
3a	Un	none	$5.62*N^{(0.064)}$	5b	Re	Type III	$2.17*N^{(0.062)}$
3b	Un	none	$3.01*N^{(0.064)}$	5c	Re	Type III	$1.22*N^{(0.067)}$
3c	Un	none	$1.51*N^{(0.065)}$	5a	Re	Type III	$3.51*N^{(0.055)}$
3a	Re	Type IV	$4.33*N^{(0.055)}$	5b	Re	Type III	$2.19*N^{(0.063)}$
3b	Re	Type IV	$2.54*N^{(0.061)}$	5c	Re	Type III	$1.22*N^{(0.068)}$
3c	Re	Type IV	$1.37*N^{(0.063)}$	6a	Un	none	$3.30*N^{(0.060)}$
3a	Re	Type III	$4.38*N^{(0.056)}$	6b	Un	none	$2.10*N^{(0.065)}$
3b	Re	Type III	$2.55*N^{(0.062)}$	6c	Un	none	$1.18*N^{(0.068)}$
3c	Re	Type III	$1.38*N^{(0.064)}$	7a	Un	none	$2.97*N^{(0.055)}$
3a	Re	Type III	$4.75*N^{(0.055)}$	7b	Un	none	$1.94*N^{(0.0656)}$
				7c	Un	none	$1.12*N^{(0.068)}$

Un is Unreinforced; Re is Reinforced

geogrid stiffness resulted in significant reduction of permanent deformation, and thus an increase in the achieved benefit. On the contrary, the reduction in permanent deformation due to geogrid reinforcement decreased with the increase in the thickness of the reinforced base course layer. The figures also demonstrate that the degree of improvement of a geogrid reinforcement at a given base course layer thickness depends on the strength of the subgrade layer. The geogrid benefit is more significant for weaker subgrades, and diminishes for very stiff subgrades. This is due to the fact that pavement sections on weak subgrades undergo large permanent deformation, which result in a better mobilization of the geogrid reinforcement.

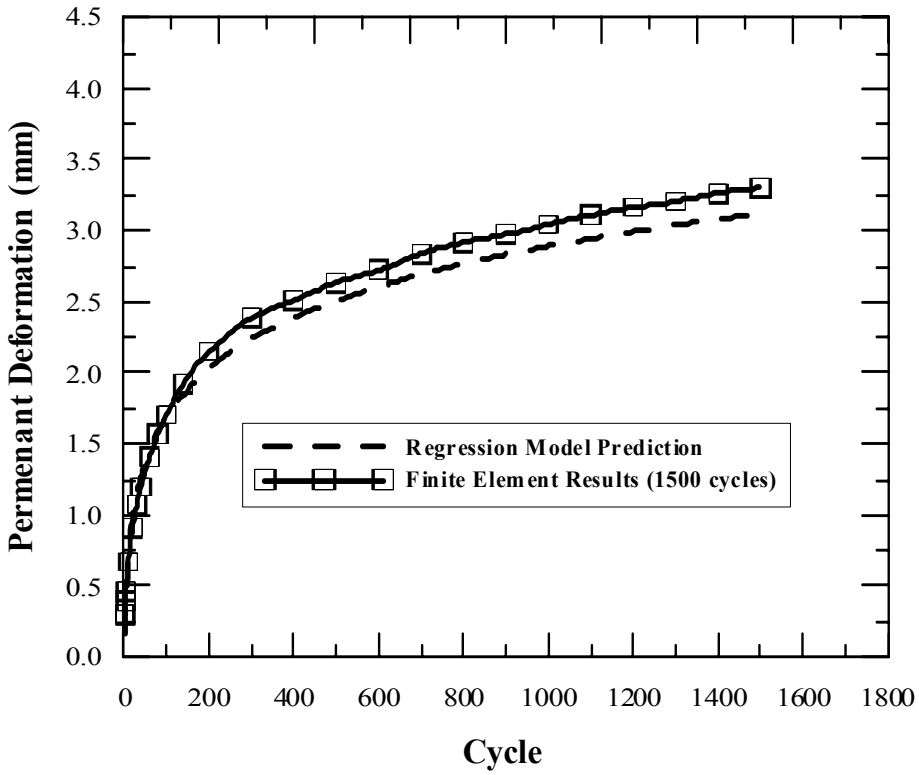

Figure 6.36 Regression model prediction vs. finite element results of (1500 cycles)

6.3.2.1 Effect of Geogrid Location on Permanent Deformation

Figure 6.40 presents the reduction in the permanent deformation predicted at 2 million cycles for the four geogrid locations investigated using the regression models for

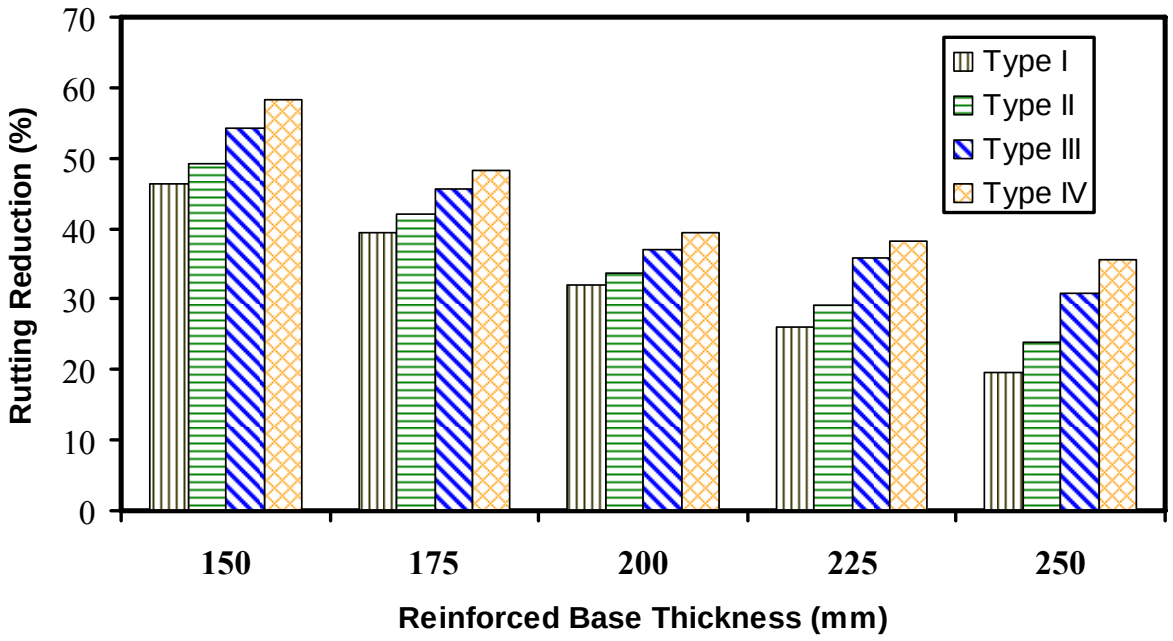

Figure 6.37 Reduction in Permanent Deformation for Sections with Weak Subgrade

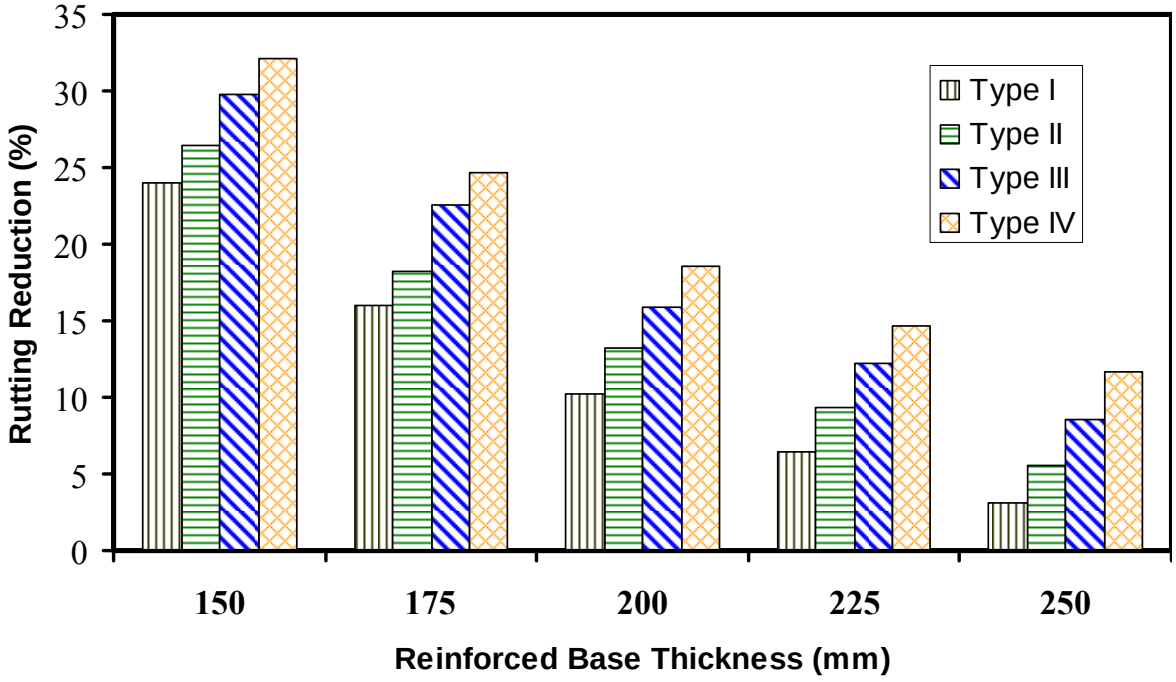

Figure 6.38 Reduction in Permanent Deformation for Sections with Moderate Subgrade

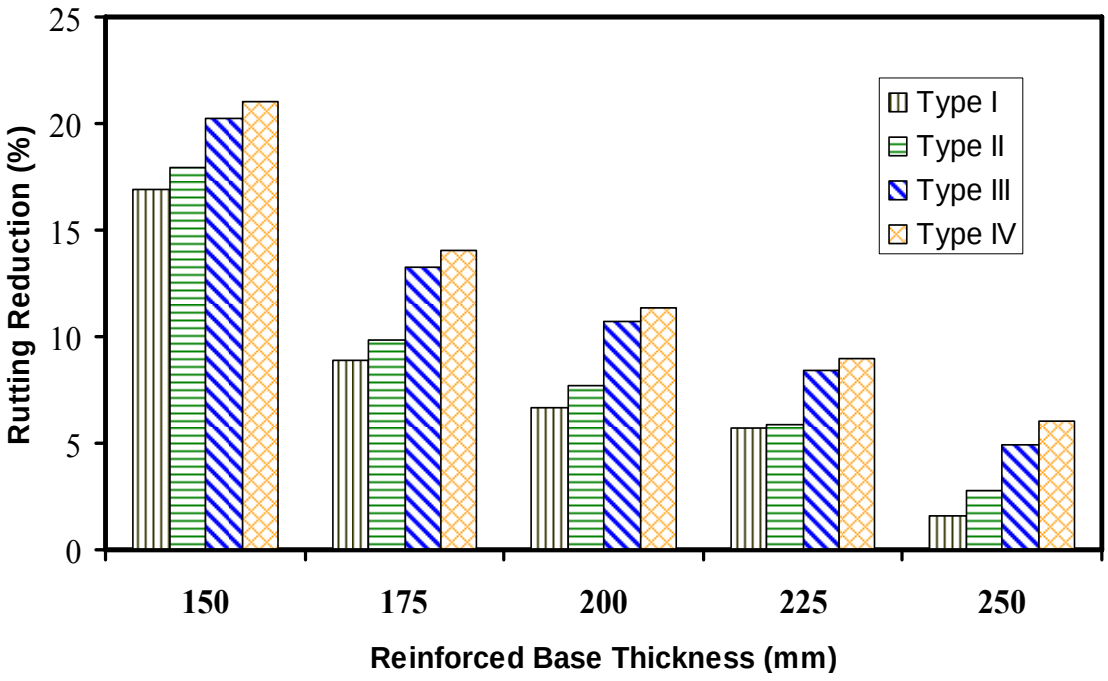

Figure 6.39 Reduction in Permanent Deformation for Sections with Stiff Subgrade

sections 1a and section 5c, respectively. The figure demonstrates that the optimum geogrid location for the two sections is at the bottom of the base layer. The difference in improvement between the different locations is very small for section 5c, which has the thickest base layer thickness and stiffest subgrades. The figure also shows that the upper one third and lower one third locations had almost the same permanent deformation reduction.

6.3.2.2 Effect of Base Course-Geogrid Interface Properties on Permanent Deformation

Figure 6.41 presents the reduction in permanent deformation estimated at 2 million cycles for the four different base course-geogrid interface cases investigated in this study. It is noticed that the Eslip value affected the accumulated permanent deformation, such that the decreasing Eslip values resulted in greater reduction in permanent deformation. It is also observed that the tie condition case was similar to case with Eslip value of 0.5 mm.

6.3.3 Base Course Reduction Ratio (BCR) Model

Many studies showed that the required base course thickness for a given design may be reduced when a geogrid is included in the design (e.g. Berg et al. 2000, Perkins, 2002; Leng et al, 2003). To determine the reduction in the base course thickness due to the geogrid reinforcement, it is necessary first to develop a relationship between the reinforced base thickness and unreinforced base thickness for the different sections. This was done by conducting a regression analyses on the finite element results of unreinforced sections to determine a relation between the permanent deformation at 2 million load cycles and the unreinforced base thickness for the different subgrade strengths. The analyses yielded the models shown in Equations 6.2, 6.3, and 6.4 for weak, moderate, and stiff subgrade sections, respectively. An equivalent unreinforced base thickness was then determined for the different geogrid reinforced base thicknesses by substituting the permanent deformation at two million cycles for each reinforced section in the suitable Equation 6.2, 6.3, and 6.4. The Base Course Reduction Ratio (BCR) ratio was determined for each reinforced section.

$$BaseThickness = 522.54 \times \delta_p^{-0.4334} \quad \text{(weak subgrade)} \quad R^2 = 0.997 \qquad (6.2)$$

$$BaseThickness = 731.23 \times \delta_p^{-0.8639} \quad \text{(moderate subgrade)} \quad R^2 = 0.996 \qquad (6.3)$$

$$BaseThickness = 784.83 \times \delta_p^{-1.812} \quad \text{(stiff subgrade)} \quad R^2 = 0.996 \qquad (6.4)$$

Where

δ_p : is the surface permanent deformation in mm.

A multiple regression analysis was conducted on the results to develop a model that can predict the BCR ratio as a function of the thickness of reinforced base layer, the geogrid stiffness, and the subgrade CBR value. A general model shown in Equation 6.5 was used.

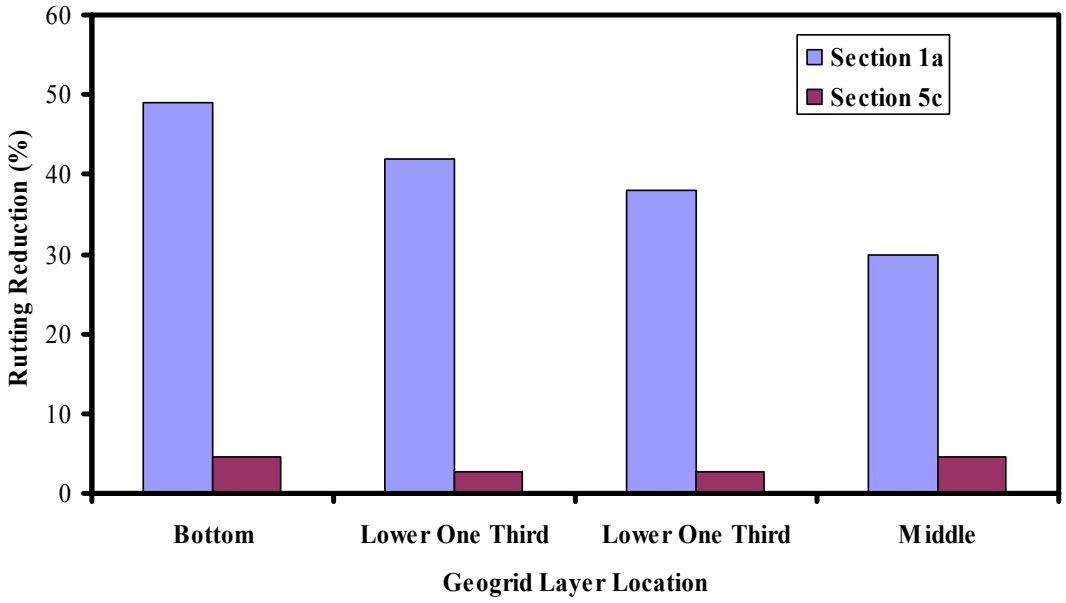

Figure 6.40 Reduction in permanent deformation for the different geogrid layer location

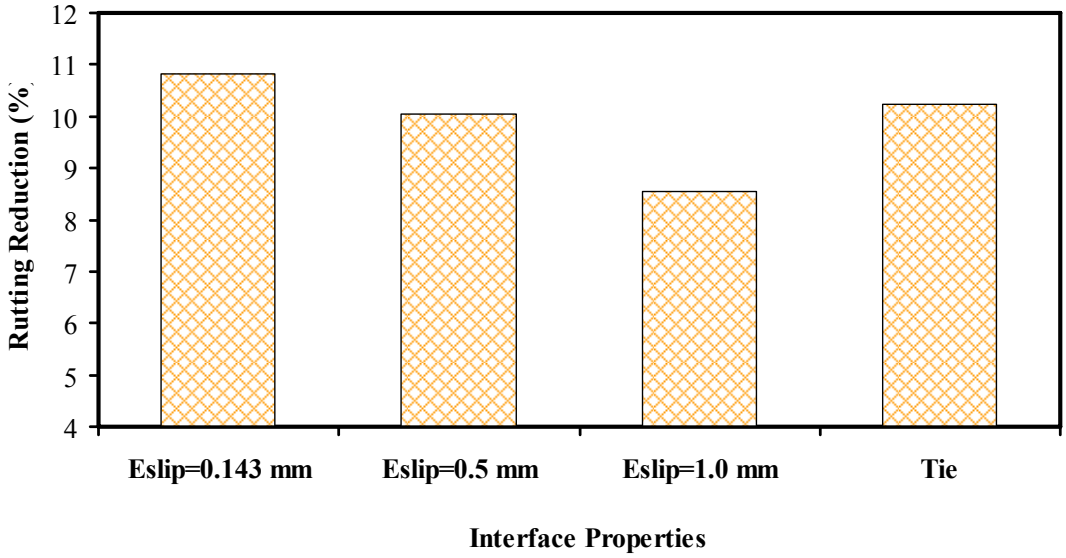

Figure 6.41 Base-Geogrid Interface Properties Effect on Rutting Reduction

$$BCR = \beta_0 + \beta_1 X_1 + \beta_2 X_2 + \beta_3 X_3 + \beta_4 X_1 X_2 + \beta_5 X_1 X_3 + \beta_6 X_2 X_3 \quad 6.5$$

Where

X_1: is the reinforced base layer thickness in mm

X_2: is the geogrid modulus (kPa) used in the finite element models normalized to a modulus value of 135000 (kPa);

X_3: is subgrade CBR value;

X_1X_2: is the interaction between the effect of the reinforced thickness and normalized geogrid modulus;

$X_1 X_3$: is the interaction between the effect of the reinforced thickness and subgrade CBR value; and

X_2X_3: is the interaction between the effect of the subgrade strength and normalized geogrid modulus.

A stepwise variable selection analysis was conducted to eliminate insignificant variables from the general model. Table 6.4 presents a summary of the stepwise variable selection analysis. It is noted that the reinforced thickness (X_1), geogrid stiffness modulus (X_2), and the subgrade CBR value (X_3) were the only significant variables at 95% confidence level.

A multiple regression analysis was conducted using reduced model determined from the stepwise variable selection. The results of this analysis are shown Table 6.5 and Table 6.6. In addition, Equation 6.6 presents the prediction model developed from results of this analysis. The results of the regression analysis conform with the conclusion that the benefit of geogrid reinforcement is inversely proportional to the reinforced base layer thickness and subgrade CBR values and is proportional to the geogrid stiffness modulus. This is consistent with the earlier finite element analysis. Figure 6.36 illustrates the

Table 6.4 Summary of Stepwise Selection for BCR Model

Variable Entered	Variable Removed	Number Vars In	Partial R-Square	Model R-Square	C(p)	F Value	Pr > F
X_1		1	0.6027	0.6027	2025.1	88.00	<.0001
X_2		2	0.2078	0.8105	938.69	62.50	<.0001
X_3		3	0.1714	0.9819	42.598	531.65	<.0001

comparison between the BCR obtained using the finite element analysis and those predicted using the regression model. It can be seen that the regression line well fits the data.

Finite element analyses were conducted on new nine unreinforced and reinforced pavement sections in order to verify the capability of the regression models, developed in this study, to predict the reduction in permanent deformation and hence the equivalent unreinforced base thickness.

$$BCR= 1.459 - 0.04225*X_1 + 0.07644*X_2 - 0.00557 *X_3 \quad 6.6$$

Table 6.5 Summary of the Analysis of Variance of the BCR Model

Source	DF	Sum of Squares	Mean Square	F Value	Pr > F
Model	3	0.34895	0.11632	1015.05	<.0001
Error	56	0.00642	0.00011459		
Corrected Total	59	0.35537			
Root MSE	0.01070		R-Square	0.9819	
Dependent Mean	1.19819		Adj R-Sq	0.9810	
Coeff Var	0.89341				

Table 6.6 Summary of the BCR Model Parameters Estimate

Label	DF	Parameter Estimate	t Value	Pr > |t|	Standardized Estimate	Variance Inflation
Intercept	1	1.45876	16.05	<.0001	0	0
X_1	1	-0.04225	-33.23	<.0001	-0.77635	1.
X_2	1	0.07644	25.38	<.0001	0.45583	1.
X_3	1	-0.00557	-23.06	<.0001	-0.41405	1.

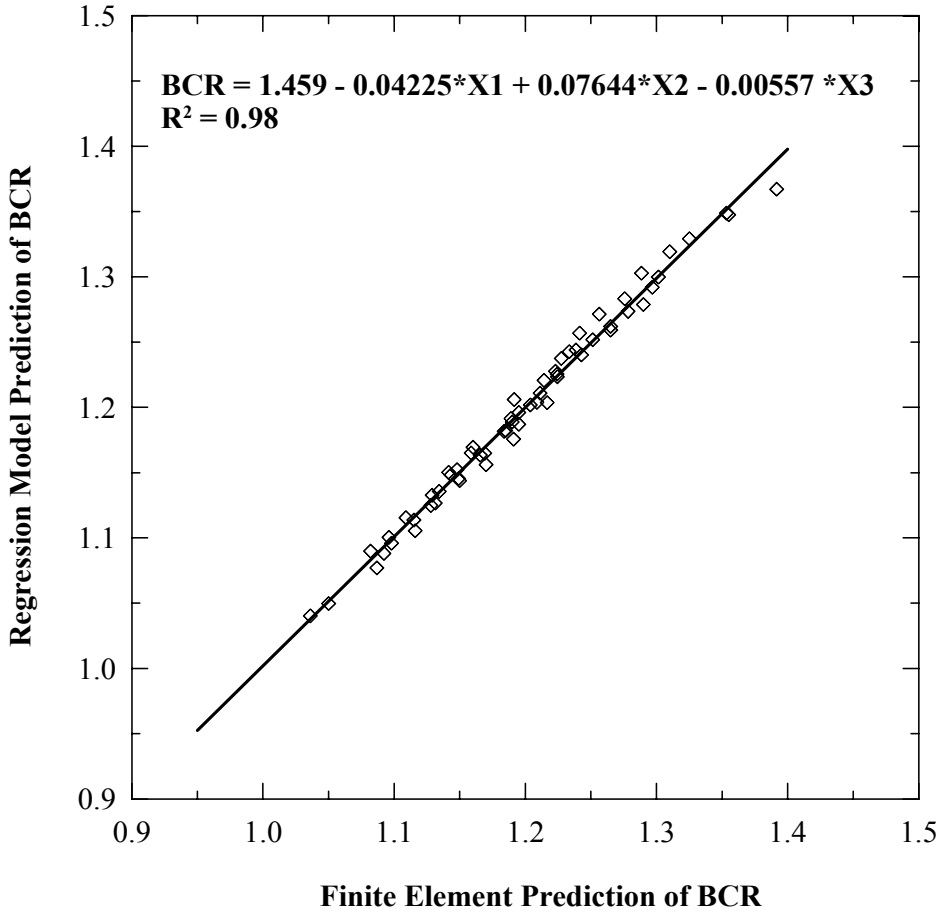

Figure 6.42 Regression Model of BCR

The sections used a new base course layer thickness of 188 mm (7.5 in) and two new geogrid reinforcement moduli. To verify the reliability of the suggested models, the BCR values determined using the finite element analyses were compared with the values predicted using the proposed regression model (Equation 6.6). The results of this

comparison are presented in Table 6.7. The error in predicting the BCR values ranged from 0.63% to 4.68%. This result suggests that the predicted BCR values are within acceptable accuracy.

Table 6.7 Verification of BCR Regression Models

Subgrade	Elastic Modulus (MPa)	BCR (FE)	BCR (REG)	Error (%)
Weak	209	1.26	1.26	0.63
moderate	209	1.23	1.24	0.6
Stiff	209	1.18	1.23	4.68
Weak	179	1.25	1.21	3.54
moderate	179	1.21	1.19	1.32
Stiff	179	1.16	1.17	1.09

6.3.4 Evaluation of the Geogrid Reinforced Sections Using a Mechanistic Empirical Approach

The improvement of the inclusion of the geogrid layer within the base course layer was also evaluated using the mechanistic empirical approach. In this approach, the response parameters computed from the finite element analysis results are used to determine the pavement structure distresses based on empirical models. Two types of distresses were considered to control the flexible pavement performance, namely, permanent deformation (rutting), and fatigue cracking.

The permanent deformation of pavement structures was determined by first dividing each pavement layer into sub-layers. Damage models are then used to relate the vertical compressive strain, computed from the finite element analysis, at the mid-depth of each sub-layer and the number of traffic applications to layer plastic strains. The overall permanent deformation is then computed using Equation 6.7 as sum of permanent deformation for each individual sub-layer.

$$PD = \sum_{i}^{NS} \varepsilon^{i}_{p} \cdot h^{i} \qquad 6.7$$

where:

PD = Pavement permanent deformation

NS = Number of sub-layers

ε^{i}_{p} = Total plastic strain in sub-layer i

h^{i} = Thickness of sublayer i

Three main damage models were used in this study, namely, one for the asphalt concrete material (Equation 6.8), one for the base(Equation 6.10), and one for subgrade materials (Equation 6.11). The parameters of these models were determined through national calibration efforts using the Long-Term Pavement Performance (LTPP) database, and laboratory tests conducted on the different pavement materials used.

$$\frac{\varepsilon_p}{\varepsilon_v} = k_1 10^{-3.4488} T^{1.5606} N^{0.473844} \qquad \text{(Asphalt concrete layer)} \qquad 6.8$$

Where

ε_p = Accumulated plastic strain at N repetitions of load

ε_v = vertical strain of the asphalt material

N = Number of load repetitions

T = Pavement temperature

k_1 = function of total asphalt layer(s) thickness and depth to computational point, to correct for the variable confining pressures that occur at different depths and is expressed as:

$$k_1 = (C_1 + C_2 * \text{depth}) * 0.328196^{\text{depth}} \qquad 6.9$$

Where

C_1=-0.1039*h_{ac}^2+2.4868*h_{ac}-17.342

C_2=0.0172*h_{ac}^2-1.7331*h_{ac} - 27.428

h_{ac}= is the asphalt layer thickness

$$\frac{\varepsilon_p}{\varepsilon_v} = \beta_{GB}\left(\frac{\varepsilon_o}{\varepsilon_r}\right)\cdot e^{-\left(\frac{\rho}{N}\right)^{\beta}} \quad \text{(Base course layer)} \quad 6.10$$

$$\frac{\varepsilon_p}{\varepsilon_v} = \beta_{SG}\left(\frac{\varepsilon_o}{\varepsilon_r}\right)\cdot e^{-\left(\frac{\rho}{N}\right)^{\beta}} \quad \text{(Subgrade layer)} \quad 6.11$$

Where

β_{GB} = is national model calibration factor for unbound base course material and is equal to 1.673

β_{SG} = is national model calibration factor for subgrade material and is equal to 1.35

ε_0, β, and ρ = Material parameters

ε_r = Resilient strain imposed in laboratory test to obtain material properties

The other major distress type occurring in flexible pavement that will be evaluated in this section is load associated fatigue cracking. Several model forms are available in the literature to characterize the fatigue damage in asphalt layer. The most commonly used model form to predict the number of load repetitions to fatigue cracking is a function of the tensile strain and mix stiffness (modulus). The model used in this study for the prediction of the number of repetitions to fatigue cracking was the national field calibrated model adopted in the MEPDG that was determined by numerical optimization and other modes of comparison and is expressed as follows:

$$N_f = 0.00432 \cdot k_1 \cdot C\left(\frac{1}{\varepsilon_t}\right)^{3.9492}\left(\frac{1}{E}\right)^{1.283} \quad 6.12$$

Where

N_f: is traffic repetitions to AC fatigue

ε_t : is resilient horizontal tensile strain from the response model taken as the maximum tensile value with the AC layer

C: is a laboratory to field adjustment factor

E: is AC complex modulus used in response model (psi)

k_1: is a correction factor to adjust for AC layer thickness (h_{ac}) effects and can be expressed in the following form:

$$k_1 = \frac{1}{0.000398 + \frac{0.003602}{1 + e^{(11.02 - 3.49 \cdot h_{ac})}}} \quad 6.13$$

6.3.4.1 Permanent Deformation

The effect of geogrid stiffness, subgrade strength, and base thickness on the performance of sections reinforced with geogrid layer placed at the bottom of the base course layer was evaluated using the mechanistic empirical approach describe above. Nine sections (sections 1a-c, 3a-c, and 5a-c in Table 6.2) combining the bracketing combination of three base course thicknesses and three subgrade stiffness, and three geogrid types, namely, geogrid types II, IV, and V were used in this evaluation. Table 6.8 presents the number of traffic passes to 25 mm of permanent surface deformation and fatigue life for each of the different evaluated unreinforced and reinforced pavement. The TBR values in this table corresponds to the ratio of the number of load cycles to achieve a rut depth of 25 mm in reinforced section to that of an unreinforced. While N_R/N_U corresponds to the ratio of the traffic repetitions to reach AC fatigue for reinforced to that of unreinforced sections. The results in Table 6.8 are graphically represented in Figure 6.43 through Figure 6.48.

Table 6.8 Summary of Rutting and Fatigue Life of Unreinforced and Reinforced Sections

Section	Geogrid	N_f Rutting	N_f Fatigue	TBR	N_R/N_u
Section 1a	None	2.7E+04	5922	NA	NA
Section 1a	Type II	4.9E+04	13269	1.80	2.24
Section 1a	Type III	6.0E+04	18169	2.23	3.03
Section 1a	Type IV	8.0E+04	17924	2.95	3.07
Section 1b	None	1.6 E+05	22789	NA	NA
Section 1b	Type II	2.5E+05	39058	1.61	1.71
Section 1b	Type III	3.0 E+05	40336.5	1.91	1.77
Section 1b	Type IV	3.2 E+05	41111	2.08	1.80
Section 1c	None	6.3E+05	45786	NA	NA
Section 1c	Type II	8.8E+05	79925	1.41	1.75
Section 1c	Type III	9.8E+05	83056	1.57	1.81
Section 1c	Type IV	1.0E+06	83344	1.65	1.82
Section 3a	None	4.9E+04	14187	NA	NA
Section 3a	Type II	8.5E+04	24860	1.72	1.75
Section 3a	Type III	9.7E+04	26176	1.96	1.85
Section 3a	Type IV	1.0E+05	26498	2.11	1.87
Section 3b	None	3.0E+05	28154	NA	NA
Section 3b	Type II	4.2E+05	49509	1.42	1.76
Section 3b	Type III	5.0E+05	50393	1.68	1.79
Section 3b	Type IV	5.3E+05	51277	1.77	1.82
Section 3c	None	7.4E+05	52106	NA	NA
Section 3c	Type II	9.4E+05	83448	1.27	1.60
Section 3c	Type III	9.9E+05	84151	1.33	1.61
Section 3c	Type IV	1.0E+06	84317	1.37	1.62
Section 5a	None	7.8E+04	12044	NA	NA
Section 5a	Type II	1.1E+05	31259	1.42	2.60
Section 5a	Type III	1.3E+05	36088	1.65	3.00
Section 5a	Type IV	1.3E+05	35753	1.71	2.97
Section 5b	None	3.0E+05	35660	NA	NA
Section 5b	Type II	4.0E+05	58063	1.35	1.63
Section 5b	Type III	4.5E+05	58972	1.53	1.65
Section 5b	Type IV	4.7E+05	59179	1.59	1.66
Section 5c	None	8.2E+05	52170	NA	NA
Section 5c	Type II	8.9E+05	82911	1.08	1.59
Section 5c	Type III	8.9E+05	83284	1.08	1.60
Section 5c	Type IV	9.3E+05	83373	1.13	1.60

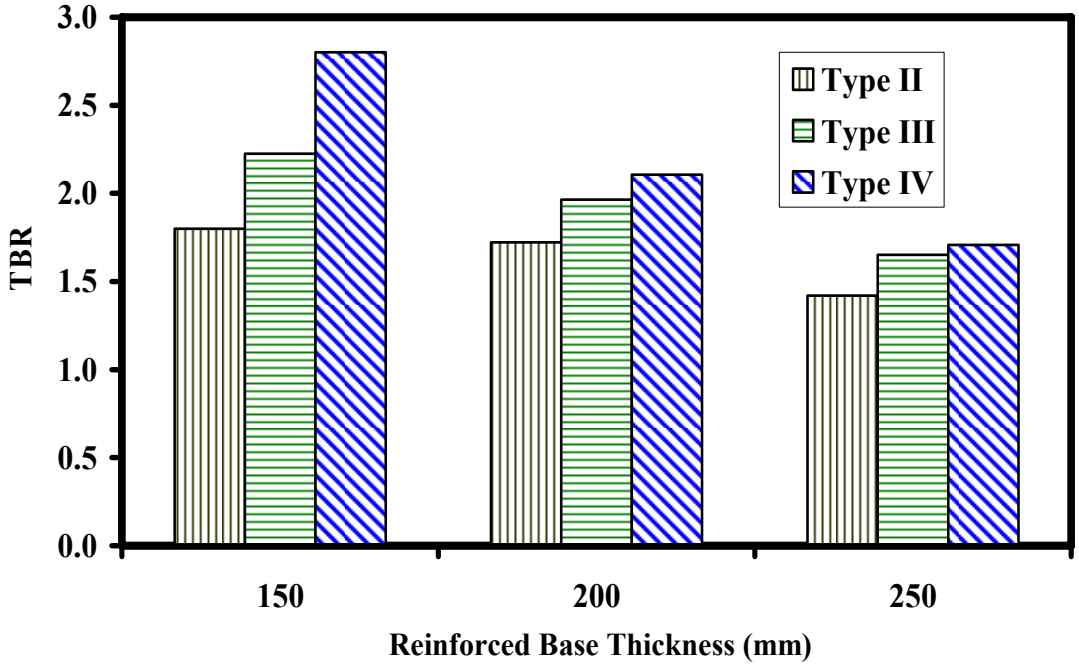

Figure 6.43 TBR of Reinforced Section with Weak Subgrade

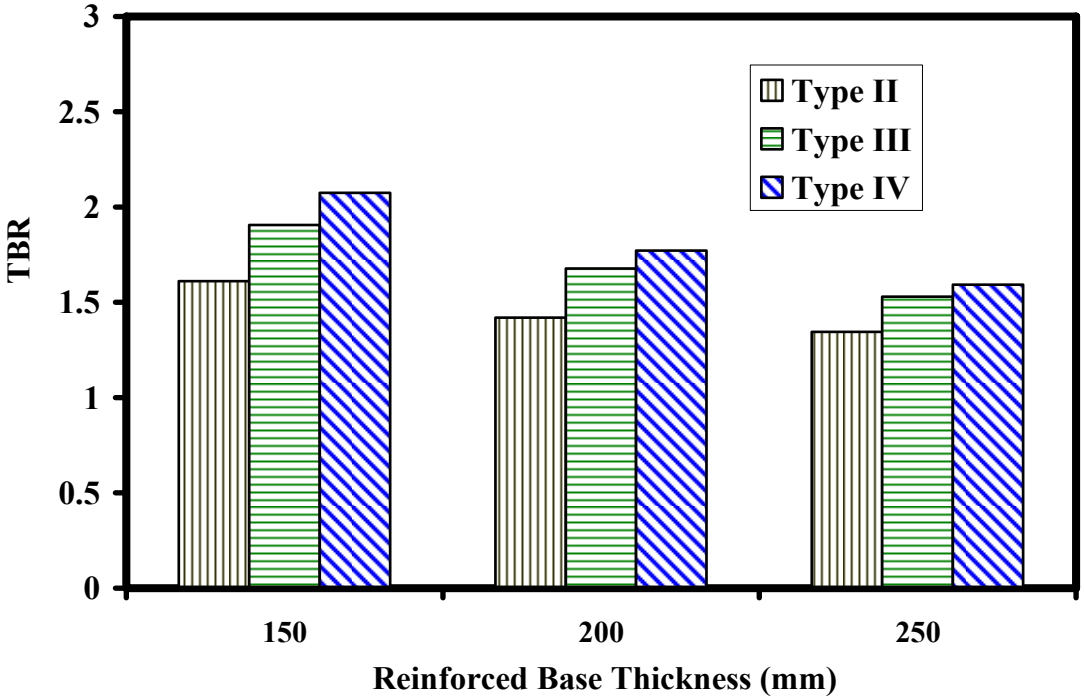

Figure 6.44 TBR of Reinforced Section with Moderate Subgrade

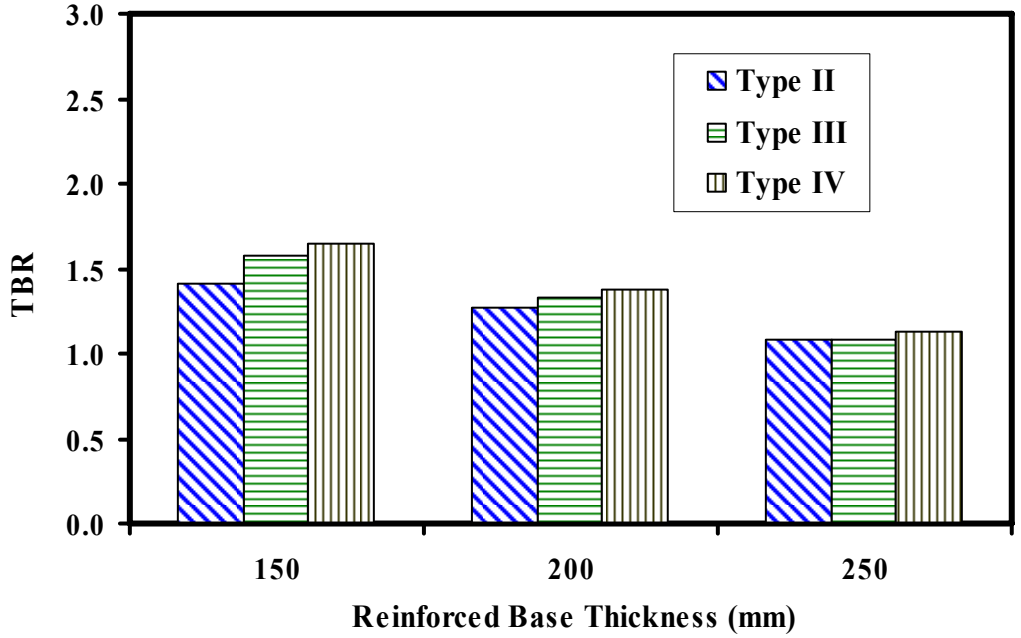

Figure 6.45 TBR of Reinforced Section with Stiff Subgrade

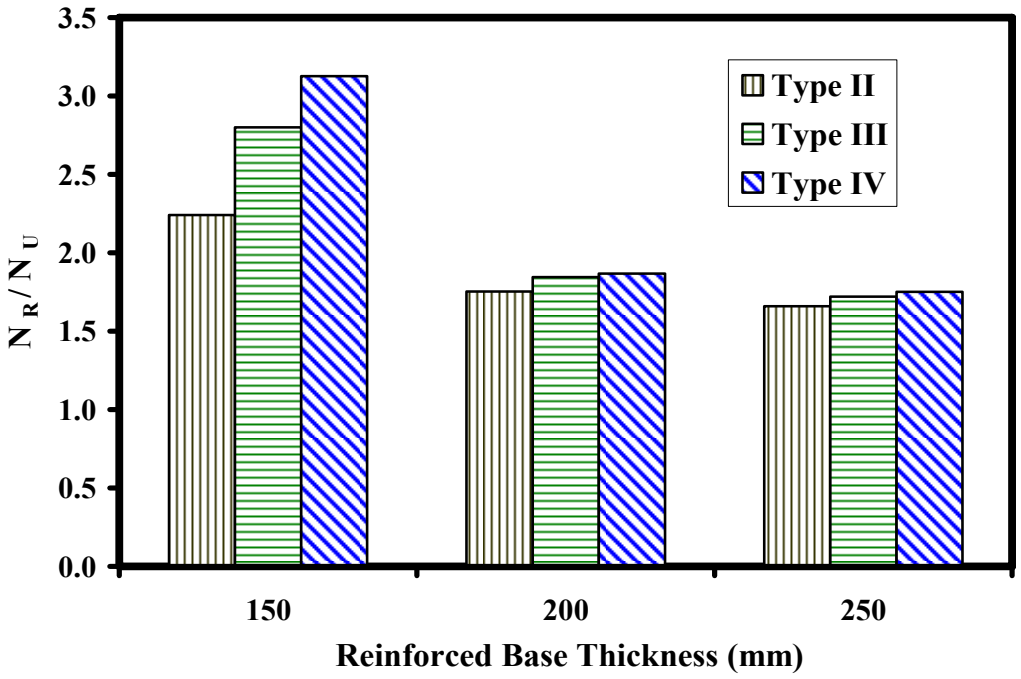

Figure 6.46 N_f / N_U of Reinforced Section with Weak Subgrade

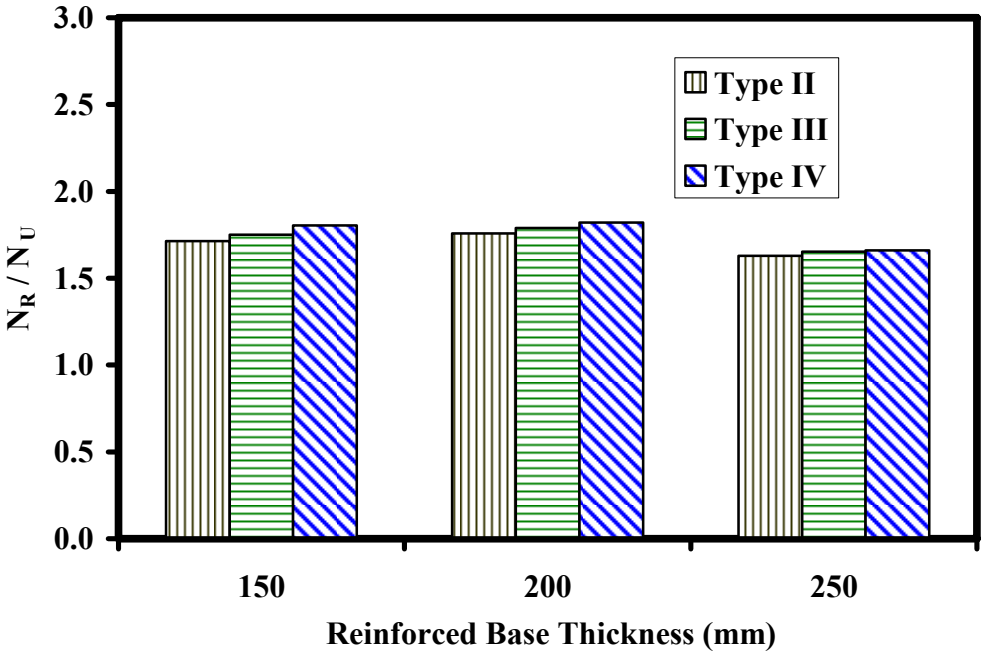

Figure 6.47 N_f / N_U of Reinforced Section with Moderate Subgrade

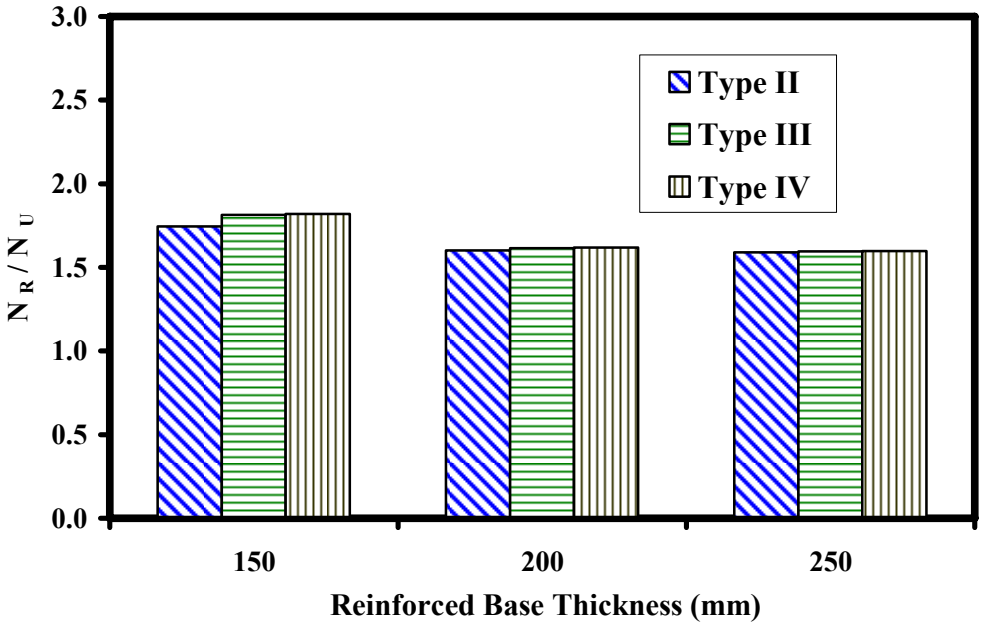

Figure 6.48 N_f / N_U of Reinforced Section with Stiff Subgrade

The results show a clear and marked difference between the different geogrid reinforcement types. The pavement sections on a weak subgrade with medium to thin base layer thickness demonstrate appreciable reduction on rutting due to geogrid reinforcement with the thin base layer thickness showing the greater values of improvement. These improvement levels are consistent with those observed in test section reported in different studies. However, negligible to modest reinforcement effects on rutting was obtained for sections having a firm subgrade or thick base layer thickness. These results are consistent with observations and recommendations reported in section 6.2.3 of this dissertation. They are also consistent with conventional wisdom that geogrid reinforcement has less benefit for sections having a firm subgrade or thick base layer.

The results also demonstrate that the geogrid reinforcement had modest to high values of improvement on fatigue life, which show great promise of reinforcement for controlling fatigue cracking. However these results have not been validated in test sections, which is due mainly to the fact that most constructed test sections reported in the literature have failed by rutting. It is noted that the increase in geogrid stiffness influenced the improvement in the fatigue life of section-1a only, which is the pavement sections with thin base layer built on top of weak subgrade soil. Furthermore, the increase base course thickness had much less adverse effect on the fatigue life improvement, especially for the moderate and stiff subgrades. While some differences in the geogrid benefits were observed between sections built on top weak subgrade to those built on top of moderate and stiff subgrades.

The mechanistic empirical approach was also used to evaluate the performance of sections 1a and 5c reinforced with geogrid type IV placed at the middle, upper one third, lower one third locations. Table 6.9 lists the results of traffic passes to 25 mm surface

Table 6.9 Summary of Rutting and Fatigue Life of Sections Reinforced with Layer of Geogrid Type IV Placed at the Different locations

Section	Geogrid Location	N_f Rutting	N_f Fatigue	TBR	Nf/Nu
Section 1a	Upper one third	4.9E+04	21597	1.80	3.64699
Section 1a	Middle	5.9E+04	19709	2.19	3.32815
Section 1a	Lower one Third	7.0E+04	18401	2.59	3.10726
Section 1a	Bottom	7.6E+04	18169	2.80	3.06808
Section 5c	Upper one third	9.6 E+05	158162	1.16	3.03164
Section 5c	Middle	1.0 E+6	157101	1.21	3.01131
Section 5c	Lower one Third	9.7 E+05	122050	1.18	2.33946
Section 5c	Bottom	9.4E+05	83373	1.13	1.60

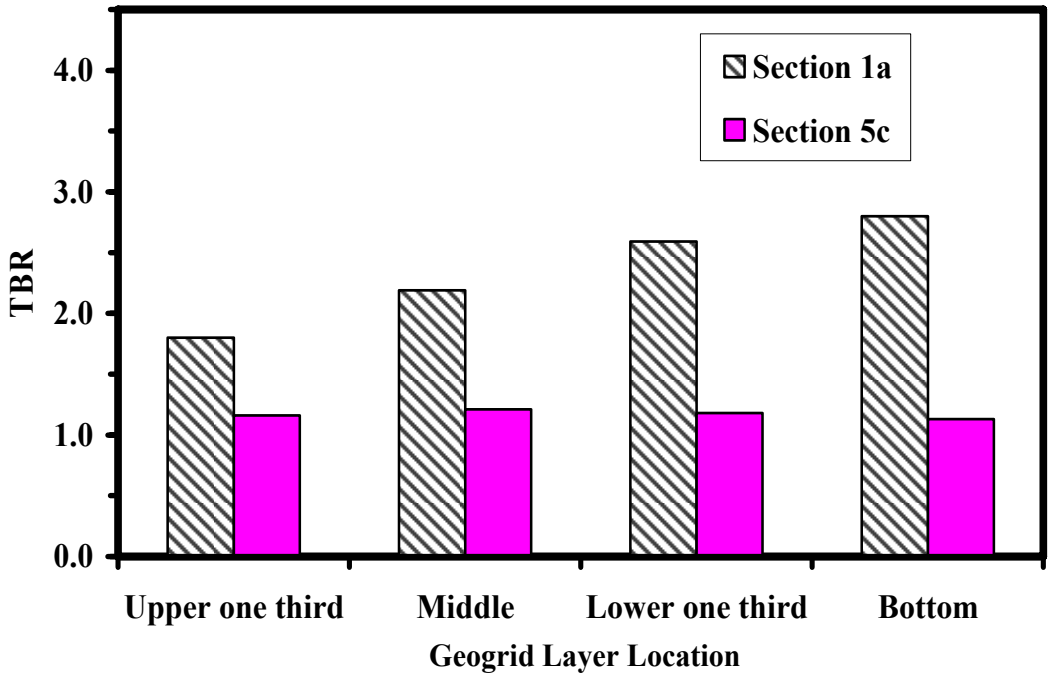

Figure 6.49 TBR of Sections Reinforced with Geogrid Layer Placed at Different Locations

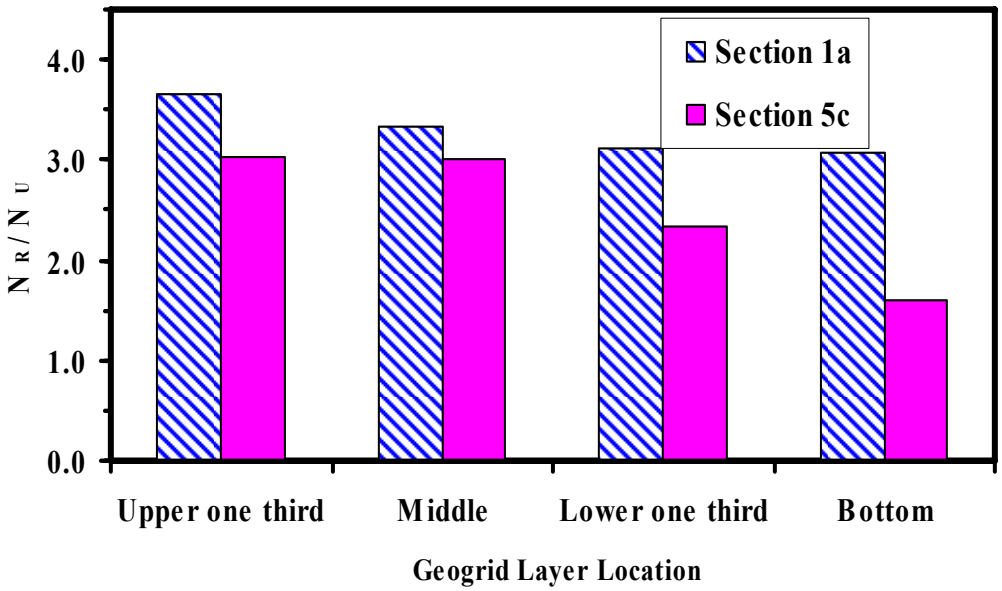

Figure 6.50 N_f / N_U of Sections Reinforced with Geogrid Layer Placed At Different Location

deformation and fatigue life for these sections. Figure 6.49 through Figure 6.50 present a graphical illustration of Table 6.9 results. The results show that in terms of rutting, maximum benefit is seen when the geogrid reinforcement is at the bottom of the base for section with thin base course thickness and weak subgrade soil, while placing the geogrid within the base course layer had a better performance when the base layer have the greatest contribution to the total permanent deformation of the pavement structure as in section 5c. For fatigue, elevating the reinforcement provides more benefit.

In terms of overall design, placement of the reinforcement at the lower one third base position can be optimal when having a thick base course layer (greater than 250 mm), since it provides the greatest number of traffic passes for the controlling mode of failure (rutting) and fatigue.

6.3.5 Development of TBR Model

A multiple regression analysis was conducted on the results to develop a prediction model of the TBR. Initially, a general model that includes all of the

investigated variables and their interactions was selected (Equation 6.14). A stepwise variable selection procedure was conducted on the selected model to eliminate any insignificant variable. Table 6.10 presents a summary of the results of the stepwise selection analysis. It is noted that the best model includes the normalized geogrid modulus, the interaction between the reinforced thickness and normalized geogrid modulus, the interaction between the subgrade strength and normalized geogrid modulus. The general TBR model is given as:

$$TBR = \beta_0 + \beta_1 X_1 + \beta_2 X_2 + \beta_3 X_3 + \beta_4 X_1 X_2 + \beta_5 X_1 X_3 + \beta_6 X_2 X_3 \quad 6.14$$

Where

X_1: is the reinforced base layer thickness in mm

X_2: is the geogrid modulus (kPa) used in the finite element models normalized to a modulus value of 135000 (kPa);

X_3: is subgrade CBR value;

X_1X_2: is the interaction between the effect of the reinforced thickness and normalized geogrid modulus;

$X_1 X_3$: is the interaction between the effect of the reinforced thickness and subgrade CBR value; and

X_2X_3: is the interaction between the effect of the subgrade strength and normalized geogrid modulus.

Based on the results of stepwise selection analysis, multiple regression analysis was conducted on finite element data to develop a TBR prediction model. Table 6.11 and Table 6.12 present the results of the regression analysis, while Equation 6.15 shows the TBR model obtained from the analysis.

Table 6.10 Summary of the Variable Stepwise Selection Analysis

Step	Variable Entered	Variable Removed	Number Vars In	Partial R-Square	Model R-Square	C(p)	F Value	Pr > F
1	X_1X_3		1	0.5192	0.5192	78.025	27.00	<.0001
2	X_1		2	0.1414	0.6606	50.313	10.00	0.0042
3	X_2		3	0.1360	0.7966	23.736	15.38	0.0007
4	X_2X_3		4	0.0791	0.8757	9.1210	13.99	0.0011
5		X_1X_3	3	0.0079	0.8678	8.7712	1.39	0.2510
6	X_1X_2		4	0.0267	0.9145	5.1578	5.57	0.0275
7		X_1	3	0.0015	0.9330	3.4763	0.32	0.5796

Table 6.11 Summary of the Analysis of Variance of the TBR Model

Source	DF	Sum of Squares	Mean Square	F Value	Pr > F
Model	3	1	3.039	3.039	624.75
Error	23	25	0.121	0.00487	
Corrected Total	26	26	3.1609		

Root MSE	0.07106	R-Square	0.96
Dependent Mean	1.63	Adj R-Sq	0.959
Coeff Var	6.01		

Table 6.12 Summary of the TBR Model Parameters Estimate

Variable	Parameter Estimate	Standard Error	Pr > |t|	Variance Inflation
Intercept	1.0	0.08477	<.0001	0
X_2	1.08394	0.04010	<.0001	2.27157
X_2X_3	-0.02395	0.00136	<.0001	1.07806
X_1X_2	-0.00274	0.00019058	<.0001	2.19352

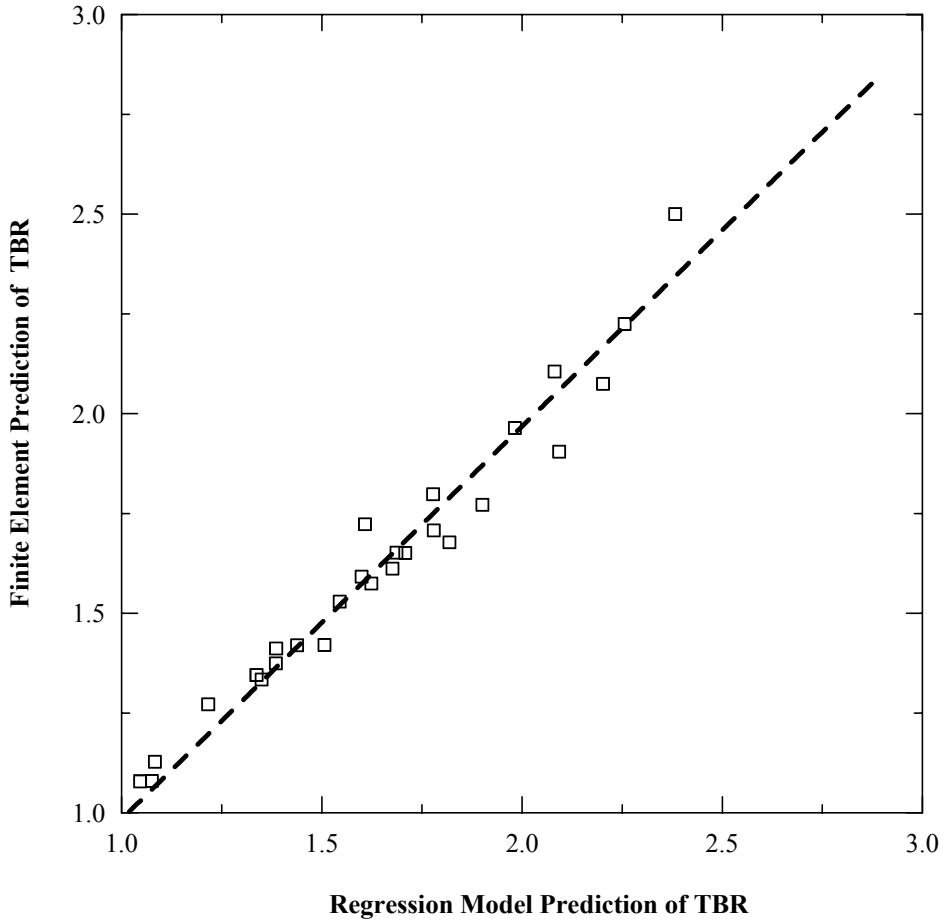

Figure 6.51 Prediction of TBR Model

The results show that the model had a high R^2 of 0.94, and low RMSE value of 0.098 suggesting that the model well fits the data. This is also illustrated in Figure 6.51, which the compares the TBR obtained using the finite element analysis and those predicted using the regression model. The results in Table 6.12 indicate that all parameters had similar significance effect on the prediction of the model, as indicated by the t-value. In addition, all three variables have VIF values less than 5, which indicate that these variables are not collinear.

$$TBR = 1.0 + 1.08 \cdot X_2 - 0.00274 \cdot X_1 X_2 - 0.0239 \cdot X_1 X_3 \qquad 6.15$$

Equation 6.15 suggests that the predicted TBR decreases with increasing in the geogrid stiffness and decreasing of the base layer thickness and the subgrade stiffness

strength. Furthermore it is noted that the beneficial effect of the geogrid stiffness decreases with the increase in the base course layer thickness and the subgrade stiffness/strength.

6.3.6 Development of Fatigue Life Improvement Model

Statistical analysis was also conducted to develop model that predict the improvement in fatigue life described by N_f/N_u ratio. Stepwise variable selection analysis was conducted on a general model similar to that Equation . The results of this analysis are provided in Table 6.13. It is noted that, the geogrid stiffness or any of its interactions was selected, indicating the geogrid stiffness did not have any affect on the fatigue life improvement.

Based on the results of the stepwise analysis, a multiple regression analysis was conducted on the results obtained from finite element analysis to develop a model that predicts N_f/N_u ratio. The results of this analysis are presented in Table 6.14 and Table 6.15. It can be seen that the developed model had a low R^2 value of 0.43, suggesting that the variables in that model are poorly correlated with N_f/N_u ratio, which suggests that the base thickness and subgrade stiffness did not have an appreciable effect on the fatigue life of reinforced section.

$$TBR = 2.94 - 0.00458 \cdot X_1 - 0.0267 \cdot X_3 \qquad 6.16$$

Table 6.13 Summary of Stepwise Selection

Step	Variable Entered	Variable Removed	Number Vars In	Partial R-Square	Model R-Square	C(p)	F Value	Pr > F
1	X_1		1	0.2586	0.2586	12.63	8.72	0.0068
2	X_3		2	0.1723	0.4309	6.35	7.27	0.0126

Table 6.14 Summary of the Analysis of Variance of the N_f/N_u Model

Source	DF	Sum of Squares	Mean Square	F Value	Pr > F
Model	2	1.5714	0.78569	9.09	0.0012
Error	24	2.075	0.08646		
Corrected Total	26	3.646			
Root MSE		0.29404	R-Square		0.4309
Dependent Mean		1.83370	Adj R-Sq		0.3835
Coeff Var		16.03540			

Table 6.15 Summary of the N_f/N_u Model Parameters Estimate

Variable	Parameter Estimate	t Value	Pr > |t|	Standardized Estimate	Variance Inflation
Intercept	2.94038	10.08	<.0001	0	0
X_1	-0.00458	-3.30	0.0030	-0.50854	1.00000
X_3	-0.02667	-2.70	0.0126	-0.41512	1.00000

Chapter Seven
Numerical Modeling of Geogrid Reinforced Base Layer In Flexible Pavement- Crushed Limestone II

This chapter presents the results of the numerical modeling program that was conducted to investigate the benefits of placing a geogrid layer at the bottom of a crushed lime stone II base layer. The chapter describes a new approach that was developed based on the shakedown theory to evaluate and design unreinforced and geogrid reinforced flexible pavement structures. A comparison between the results obtained using the mechanistic approach described in previous chapter and the new approach that accounts for the stability of the base course layer based on a shakedown concept is also provided in this chapter.

7.1 Finite Element Numerical Model

A two-dimensional axisymmetric finite element model similar to that developed in Chapter 6 was used in this chapter to analyze the geogrid-reinforced flexible pavement structure. The model had similar mesh properties, interface and loading models. However, the thickness of the asphalt layer was 75 mm instead of 50 mm. In addition, some features were incorporated in the finite element model to enhance it. These features are described in the following sections.

7.2 Material Constitutive Models

7.2.1 Base Course Layer

The base course material used in the finite element model in this chapter was the crushed limestone II. As discussed in Chapter five of this dissertation, the Drucker Prager model was unable to predict the stress-strain behavior of the crushed limestone II.

Therefore, it was necessary to select a model that can adequately predicts this behavior. The two-surface model was used to model the crushed limestone II base material. The features of this model are described in details in chapter three of this dissertation. Furthermore, the calibration of the model parameters and verification of the model prediction were presented in Chapter five. presents a summary of the calibrated model parameters used in the finite element analysis conducted in this chapter.

Table 7.1 Two Surface Model Parameter for Crushed Limestone II Base Material

Elastic Parameters	
K_0	103.4 MPa
ν	0.3
b	0.72
Critical state Parameters	
M_c/M_e	1.91/1.14
λ	0.0165
$e_{cs,ref}$, pref	0.52, 21 kPa
Model Parameters	
k^bc/k^be	4.5/1.74
k^dc /k^de	2.3/0.72
h_0	800
c_m	0.01
m	0.19
A_0	0.36
F_{max}	100
C_f	100
Suction Parameters	
n_1	0.0263
n_2	1.975
n_3	2.363

7.2.2 Subgrade Layer

The subgrade was modeled using the Modified Cam clay model. Three sets of the Modified Cam clay model parameters were selected to describe the behavior of subgrade materials from previous work to represent weak, moderate and stiff subgrades. The selected parameters are presented in Table 7.2

7.2.3 Geogrid Layer

A linear elastic model was used to describe the behavior of geogrid material. In this chapter it was intended to use the properties of the three geogrid types investigated in the experimental work of this dissertation. However, since the three types has an orthotropic linear elastic behavior, it was required to determine an equivalent isotropic elastic properties that can be used in the finite element analysis. The following section describes the method used to convert the orthotropic to isotropic linear elastic properties.

7.2.3.1 Conversion of Orthotropic to Isotropic Linear Elastic Properties

The constitutive equation for an orthotropic linear-elastic material containing the elastic constants described is given by Equation 7.1 .

$$\begin{Bmatrix} \varepsilon_{xm} \\ \varepsilon_{m} \\ \varepsilon_{n} \\ \gamma_{xm-m} \\ \gamma_{xm-n} \\ \gamma_{m-n} \end{Bmatrix} = \begin{bmatrix} 1/E_{xm} & -\nu_{m-xm}/E_{xm} & -\nu_{n-xm}/E_{n} & 0 & 0 & 0 \\ -\nu_{xm-m}/E_{xm} & 1/E_{m} & -\nu_{n-m}/E_{n} & 0 & 0 & 0 \\ -\nu_{xm-n}/E_{xm} & -\nu_{m-n}/E_{m} & 1/E_{n} & 0 & 0 & 0 \\ 0 & 0 & 0 & 1/G_{xm-m} & 0 & 0 \\ 0 & 0 & 0 & 0 & 1/G_{xm-n} & 0 \\ 0 & 0 & 0 & 0 & 0 & 1/G_{m-n} \end{bmatrix} \cdot \begin{Bmatrix} \sigma_{xm} \\ \sigma_{m} \\ \sigma_{n} \\ \tau_{xm-m} \\ \tau_{xm-n} \\ \tau_{m-n} \end{Bmatrix} \quad 7.1$$

Where the subscripts xm and m denote the in-plane cross-machine and machine directions, and n denotes the direction normal to the plane of the geosynthetic. The model contains 9 independent elastic constants, of which 4 (E_{xm}, E_m, ν_{xm-m}, G_{xm-m}) are pertinent to a reinforcement sheet modeled by membrane elements in a pavement response model.

Poisson's ratio, $\nu_{m\text{-}xm}$, is related to $\nu_{xm\text{-}m}$ through Equation 7.2. When using membrane elements, values for the remaining elastic constants can be set to any values that ensure stability of the elastic matrix. Stability requirements for the elastic constants are given by Equations 7.3– 7.7 (Hibbitt, 2004).

Table 7.2 Modified Cam-Clay Model Parameter for Different Subgrade Soils

Subgrade	G (kPa)	M	λ	κ	e_0	CBR
Soft	5170	0.65	0.225	0.11	1.35	1.5
Medium	20000	1	0.11	0.084	0.95	7
Stiff	35000	1.56	0.022	0.005	0.54	15

$$\nu_{m-xm} = \nu_{xm-m}\frac{E_m}{E_{xm}} \tag{7.2}$$

$$E_{xm}, E_m, E_n, G_{xm-m}, G_{xm-n} > 0 \tag{7.3}$$

$$\left|\nu_{xm-m}\right| = \left(\frac{E_{xm}}{E_m}\right)^{\frac{1}{2}} \tag{7.4}$$

$$\left|\nu_{xm-n}\right| = \left(\frac{E_{xm}}{E_n}\right)^{\frac{1}{2}} \tag{7.5}$$

$$\left|\nu_{m-n}\right| = \left(\frac{E_m}{E_n}\right)^{\frac{1}{2}} \tag{7.6}$$

$$1-\nu_{xm-m}\nu_{m-xm} - \nu_{xm-n}\nu_{n-xm} - 2\nu_{xm-n}\nu_{m-xm}\nu_{m-n} > 0 \tag{7.7}$$

The constitutive matrix for an isotropic linear-elastic constitutive matrix is given by Equation 7.8 and contains 2 independent elastic constants (E, ν). The third elastic constant in Equation 7.8 is the shear modulus (G), which is expressed in terms of E and ν by Equation 7.9.

$$\begin{Bmatrix} \varepsilon_{xm} \\ \varepsilon_{m} \\ \varepsilon_{n} \\ \gamma_{xm-m} \\ \gamma_{xm-n} \\ \gamma_{m-n} \end{Bmatrix} = \begin{bmatrix} 1/E & -\nu/E & -\nu/E & 0 & 0 & 0 \\ 1/E & 1/E & -\nu/E & 0 & 0 & 0 \\ -\nu/E & -\nu/E & 1/E & 0 & 0 & 0 \\ 0 & 0 & 0 & 1/G & 0 & 0 \\ 0 & 0 & 0 & 0 & 1/G & 0 \\ 0 & 0 & 0 & 0 & 0 & 1/G \end{bmatrix} \cdot \begin{Bmatrix} \sigma_{xm} \\ \sigma_{m} \\ \sigma_{n} \\ \tau_{xm-m} \\ \tau_{xm-n} \\ \tau_{m-n} \end{Bmatrix} \quad 7.8$$

$$G = \frac{E}{2(1+\nu)} \quad 7.9$$

An equivalency of measured orthotropic elastic constants (E_{xm}, E_m, ν_{xm-m}, G_{xm-m}) to isotropic constants (E, ν) can be determined using work-energy equivalency formulation, such that two materials, one containing orthotropic properties and the second containing isotropic properties, are assumed to experience an identical general state of stress given in Figure 7.1

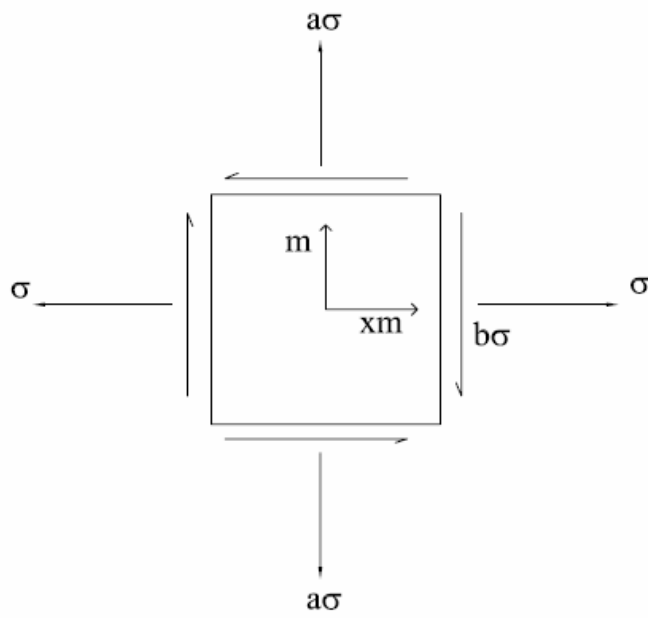

Figure 7.1 General State of Stress Experienced By a Reinforcement Element

The work energy produced by the application of the stress state shown in can be determined in general by Equation 7.10. Substitution of Equations 7.1 and 7.8 into

Equation 7.10 results in the work energy for the orthotropic and isotropic materials given by Equations 7.11 and 7.12, respectively.

$$W = \frac{1}{2}\left(\sigma\varepsilon_{xm} + a\sigma\varepsilon_{m} + b\sigma\varepsilon_{xm-m}\right) \quad 7.10$$

$$W = \frac{\sigma^2}{2}\left(\frac{1}{E_{xm}} + \frac{a^2}{E_m} - \frac{2a\nu_{m-xm}}{E_m} + \frac{b^2}{G_{xm-m}}\right) \quad 7.11$$

$$W = \frac{\sigma^2}{2E}\left(1 - 2a\nu + a^2 + 2b^2(1+\nu)\right) \quad 7.12$$

Setting Equations 7.11and 7.12 equal to each other and solving for equivalent isotropic elastic modulus (E_{equ}) that produce same work energy by the orthotropic and isotropic materials results in Equation 7.13.

$$E_{equ} = \frac{1 - 2a\nu + a^2 + 2b^2(1+\nu)}{\frac{1}{E_{xm}} + \frac{a^2}{E_m} - \frac{2a\nu_{m-xm}}{E_m} + \frac{b^2}{G_{xm-m}}} \quad 7.13$$

Assuming a value Pioson's ratio of $\nu = 0.25$ and substitution of Equation 7.2 into Equation 7.13 results in Equation 7.14.

$$E_{equ} = \frac{1 - 0.5\nu + a^2 + 2.5b^2}{\frac{1}{E_{xm}} + \frac{a^2}{E_m} - \frac{2a\nu_{m-xm}}{E_m} + \frac{b^2}{G_{xm-m}}} \quad 7.14$$

Based on finite element and field testing programs, Perkins et al. (2004) suggested that $a = 0.35$ and $b = 0.035$ values were appropriate. Based on these values, equivalent isotropic elastic properties for the geogrids used in this chapter were computed. A summary of these properties are shown in Table 7.3.

7.3 Study Matrix

Since this chapter compares the two approaches that are used to evaluate unreinforced and geogrid reinforced pavement sections, a factorial that incorporates all

Table 7.3 Geogrid Material Properties

Geogrid Type	Reference Name	Elastic Modulus (kPa)	v
BX 1100	Geogrid Type I	426000	0.25
BX 1200	Geogrid Type	928000	0.25
BX 1500	Geogrid Type	1118000	0.25

the variables that were found to affect the performance of the reinforced sections should be investigated. For this purpose, finite element analyses were conducted on nine pavement sections with three different subgrade strength properties and three base courselayer thicknesses, and a fixed AC layer thickness of 75mm. The sections were evaluated before and after placing geogrid reinforced layer at the bottom of the base course layer. Three types of geogrids representing the properties of Tensar BX 1100, Tensar BX 1200, and Tensar BX 1500 were used in this study. Table 7.4 presents a summary of the different sections investigated in this study. It should be noted that the different section will be hereafter identified using the reference names provided in Table 7.4.

Table 7.4 Pavement Sections investigated

Section ID	Base Course Thickness (mm)	Subgrade Quality
Section 1a	150	Weak
Section 1b	150	Moderate
Section 1c	150	Stiff
Section 2a	200	Weak
Section 2b	200	Moderate
Section 2c	200	Stiff
Section 3a	250	Weak
Section 3b	250	Moderate
Section 3c	200	Stiff

7.4 Results of Finite Element Analysis

The following sections summarize the results of the finite element analysis conducted in this chapter. The response of different pavement section computed from finite element analysis is first presented. The response is then used to evaluate the performance of those sections based on a mechanistic empirical approach previously described and a new approach that are described later in this chapter.

7.4.1 Stresses and Strain

Figure 7.2 and Figure 7.3 present the lateral strain profiles computed at different distance from the center of the wheel load for sections 1a, and 3c reinforced with a layer of geogrid type I and III placed at the bottom of base course layer. It is noted that the geogrid reinforcement significantly constrained the lateral strains within the base course and subgrade layers. The maximum reduction in lateral strain was observed at the base-subgrade interface. It is clear that the geogrid effect was mainly below the wheel loading area and it almost vanished at a distance of 304 mm from the center of the wheel load. The geogrid effect on lateral strain was much more appreciable in sections with thin base layer built on top of weak subgrade layers compared to sections built with thick base layer on stiff subgrade soils. Finally, Figure 7.2 and Figure 7.3 demonstrate that higher stiffness geogrids provided much greater reduction in lateral tensile strain.

The vertical strains profiles computed from the finite element analyses at different locations within the subgrade layer for unreinforced and reinforced sections 1a and 3c, are presented in Figure 7.4 and Figure 7.5, respectively. The figures demonstrate that the inclusion of the geogrid layer resulted in significant reduction in the vertical strain at top of subgrade. However, this reduction is influenced by the base course thickness and subgrade stiffness, such that greater reduction is noticed for weaker subgrade and thinner

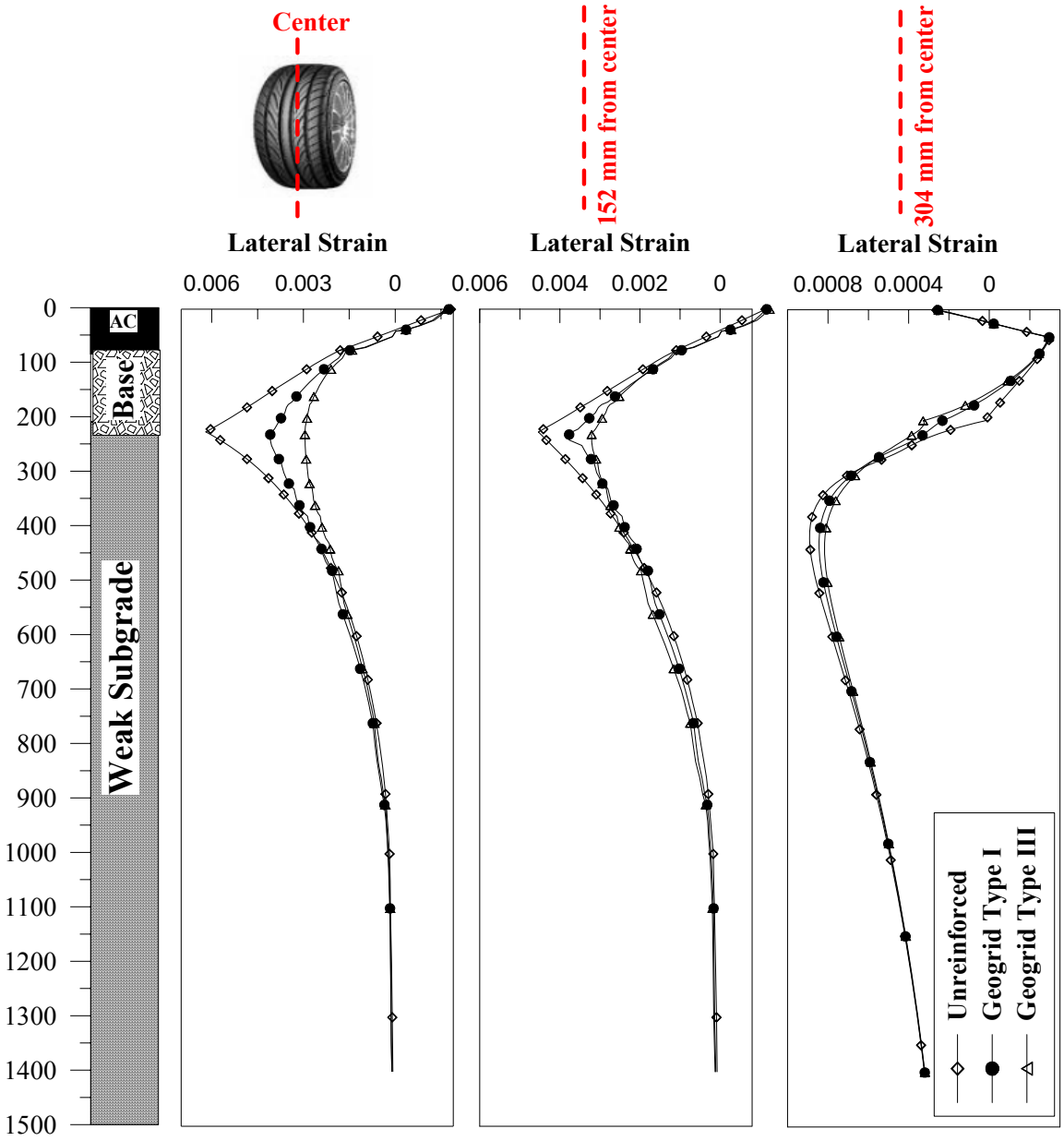

Figure 7.2 Lateral Strain Profile for Unreinforced Section 1a and Reinforced With Geogrid Layer Placed at the Bottom of the Base Layer

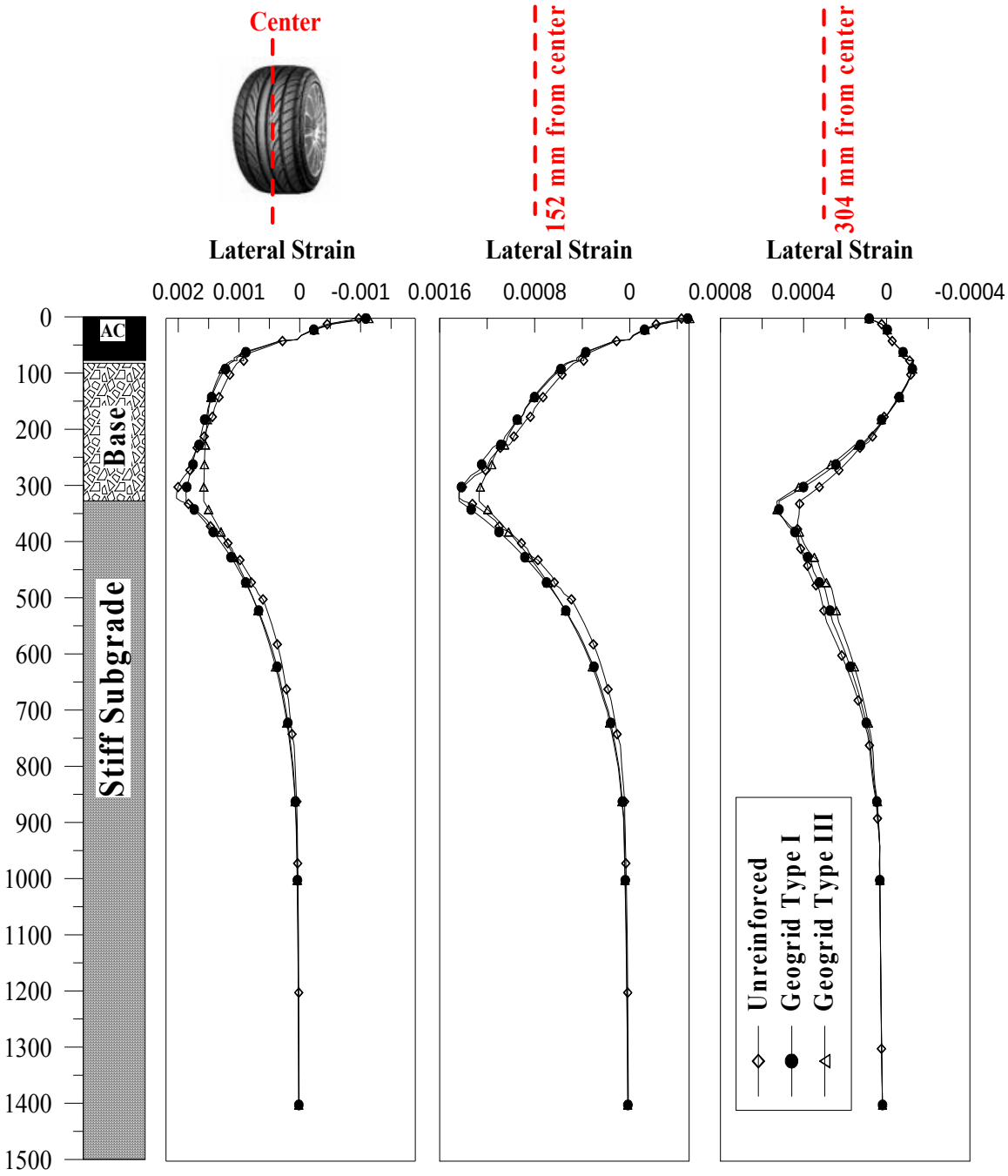

Figure 7.3 Lateral Strain Profile for Unreinforced Section 5c and Reinforced With Geogrid Layer Placed at the Bottom of the Base Layer

base course layers Furthermore, the geogrid influence on the vertical strain was experienced within a zone that extends to a depth of about 304 mm below the top of the subgrade layer. However, the greatest influence was encountered at the top of the subgrade. The figures clearly demonstrate the effect of the geogrid types/stiffness on the vertical strain, such that stiffer geogrids exhibited lower vertical strain at the top of the subgrade.

Figure 7.6 and Figure 7.7 present the plastic strain distribution at the top of subgrade for section 1a and 3c, respectively. It is clearly noted that the plastic strains for the unreinforced section was much greater than those obtained for reinforced sections. Furthermore, the reduction in the vertical plastic strain was more appreciable than that in the total vertical strain. This confirms the findings in previous chapters which suggested that the geogrid reinforcement effect is more pronounced on the development of the plastic strains than the resilient strain.

Figure 7.8 and Figure 7.9 present the shear strain distribution at the top of the subgrade layer for sections 1a and 3c, respectively. It is noted that the shear strains decreased due to the inclusion of the geogrid reinforcement within a distance of 800 mm from the center of the wheel load, beyond this distance the shear strain experienced by unreinforced and reinforced sections were similar in magnitude.

7.4.2 Permanent Deformation

Of all finite element analyses that were conducted in this chapter, only those performed on unreinforced and reinforced section 2b included applying one hundred cycles was those. The reason for this is that very long time was required to complete the finite element analysis when a hundred load cycles was applied. This shows the limitation of using cyclic plasticity models in finite element modeling of pavement structures, and

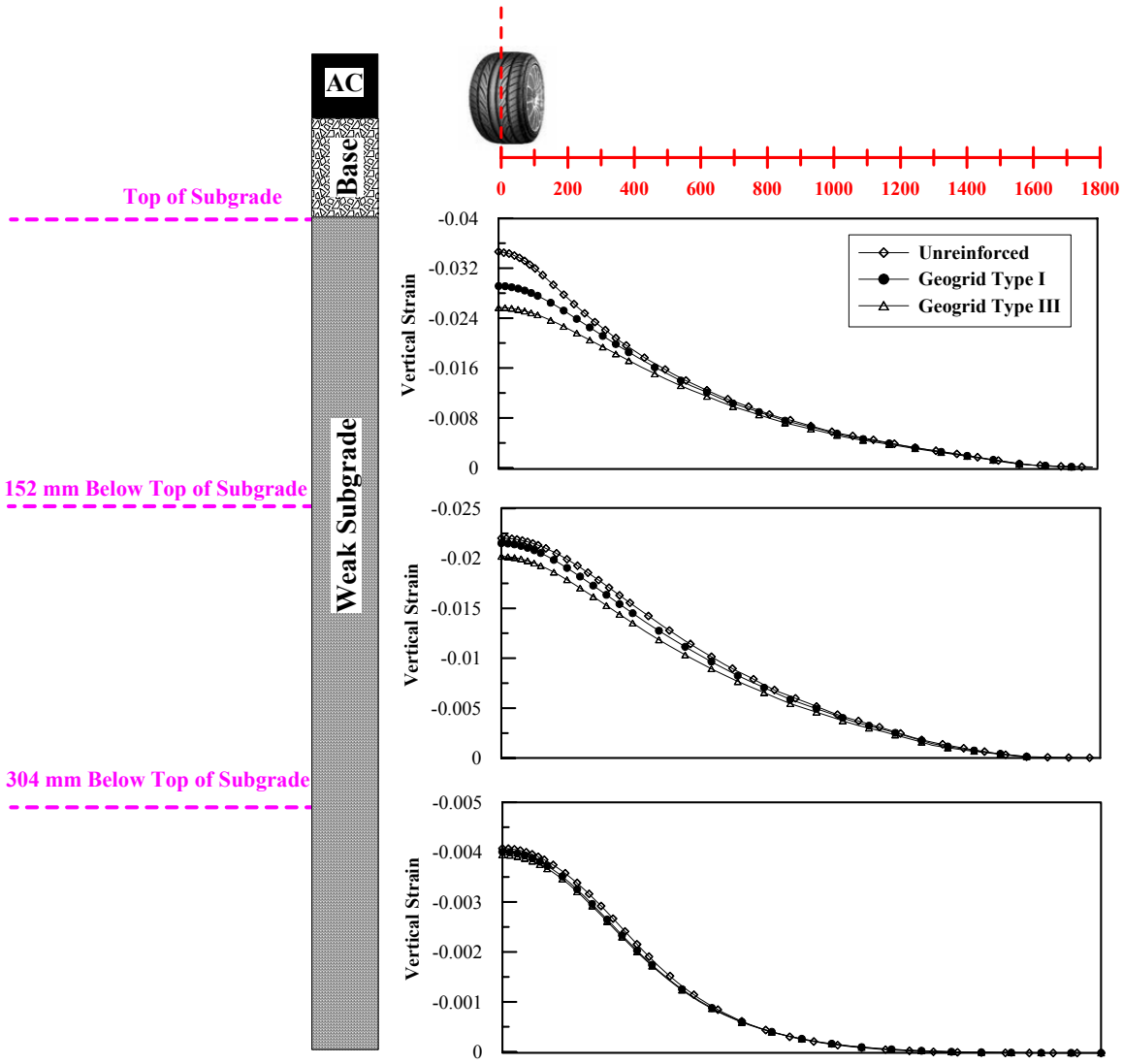

Figure 7.4 Vertical Strain Profiles within Subgrade Layer For Unreinforced and Reinforced Section 1a

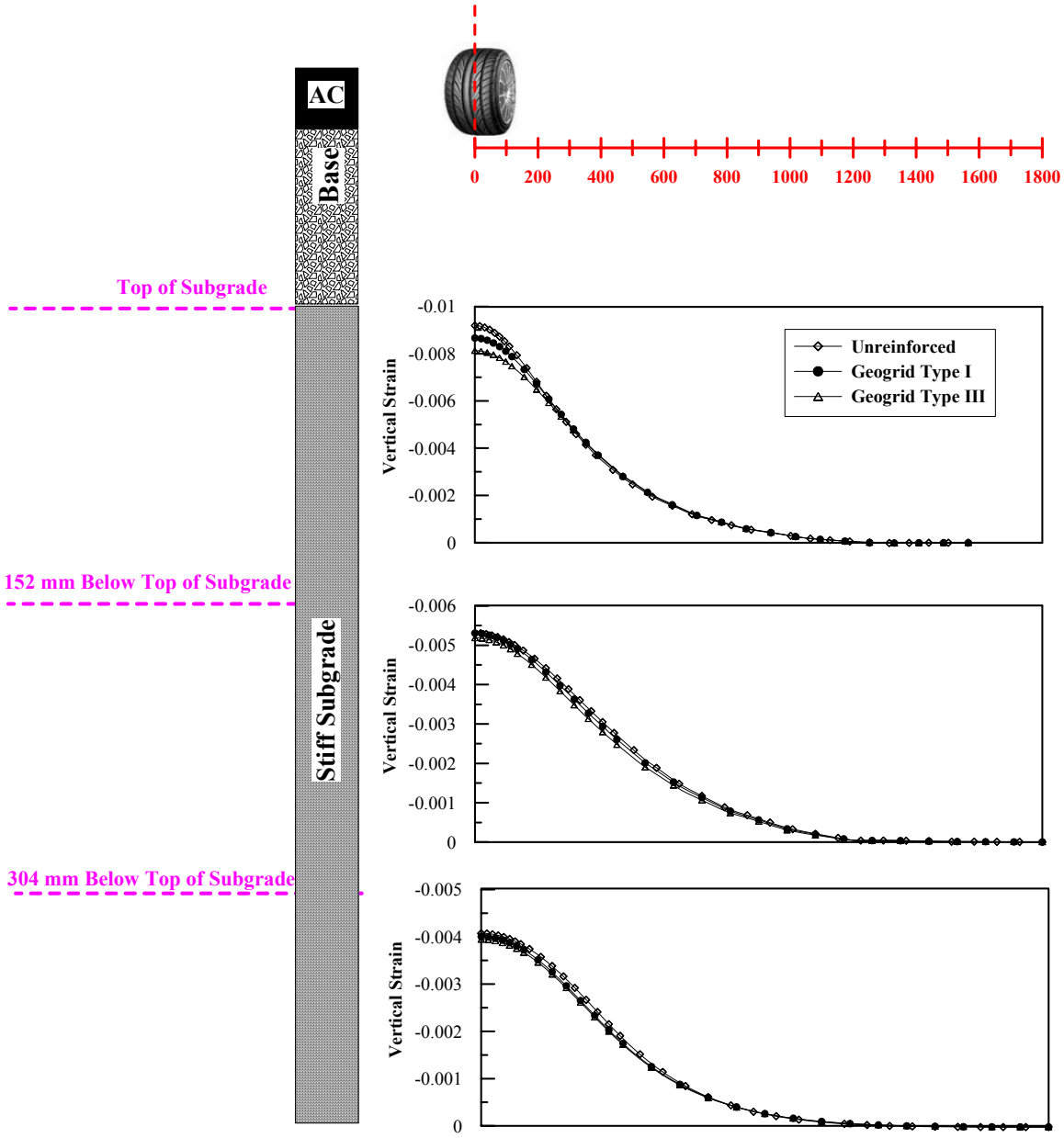

Figure 7.5 Vertical Strain Profiles within Subgrade Layer For Unreinforced and Reinforced Section 3c

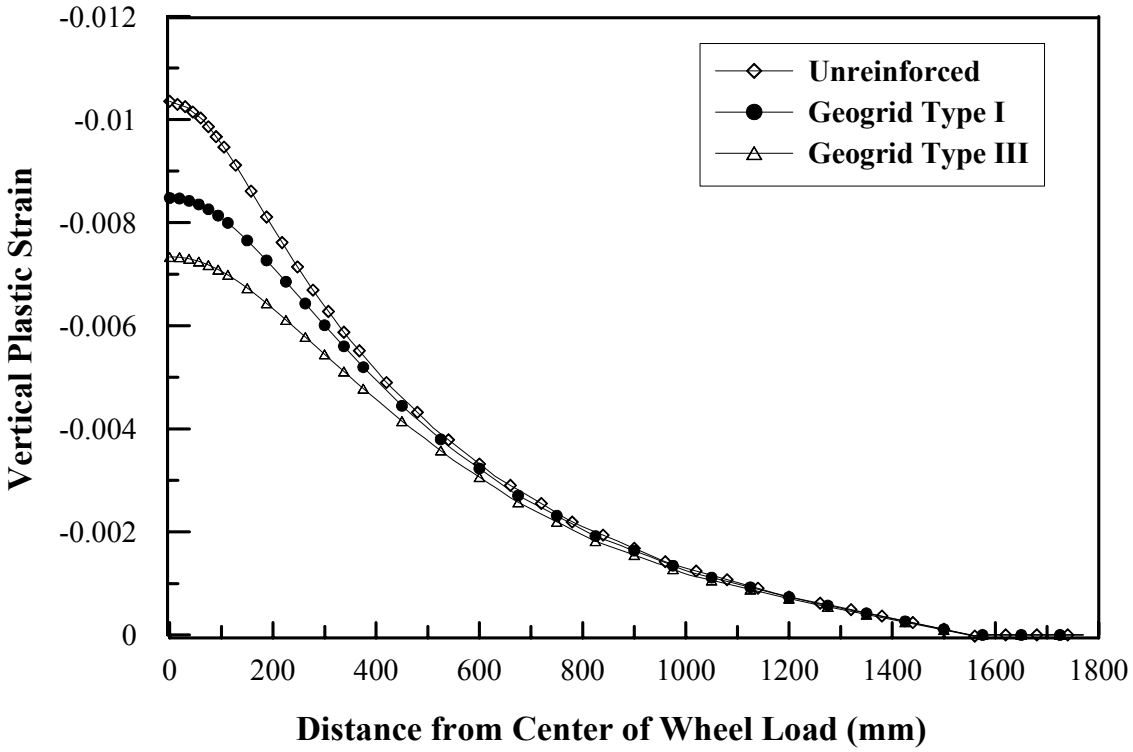

Figure 7.6 Vertical Plastic Strain Profile at top of Subgrade Layer for Unreinforced and Reinforced Section 1a

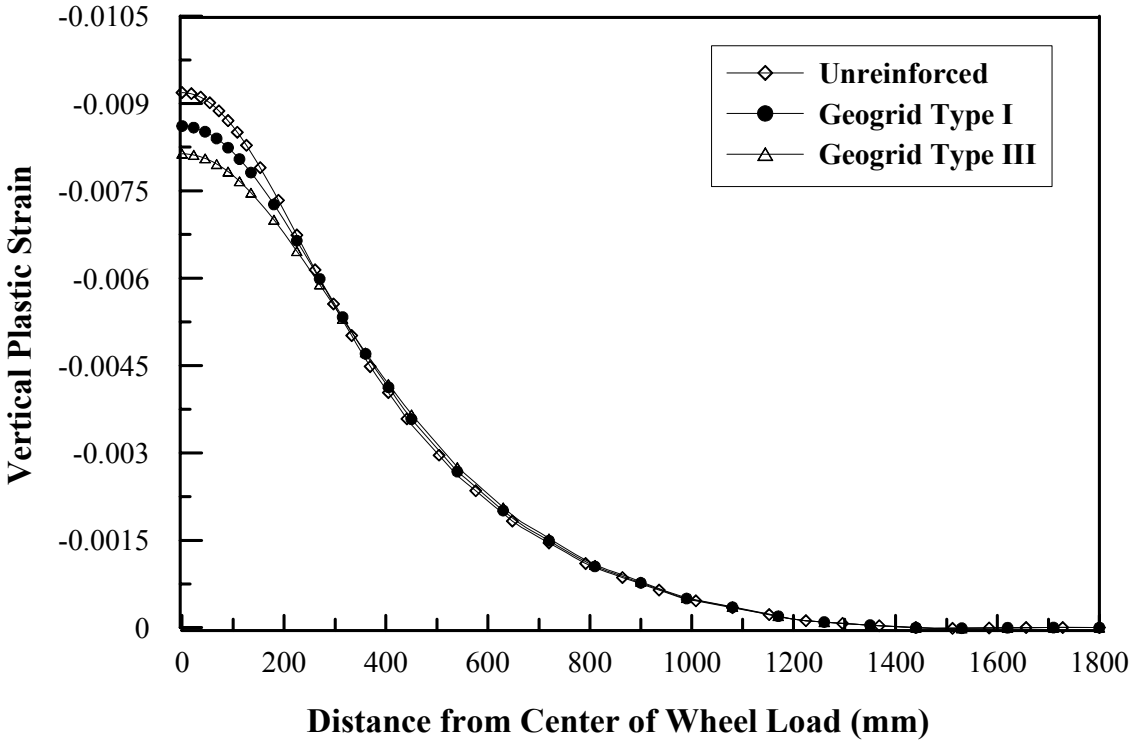

Figure 7.7 Vertical Plastic Strain Profile at top of Subgrade Layer for Unreinforced and Reinforced Section 3c

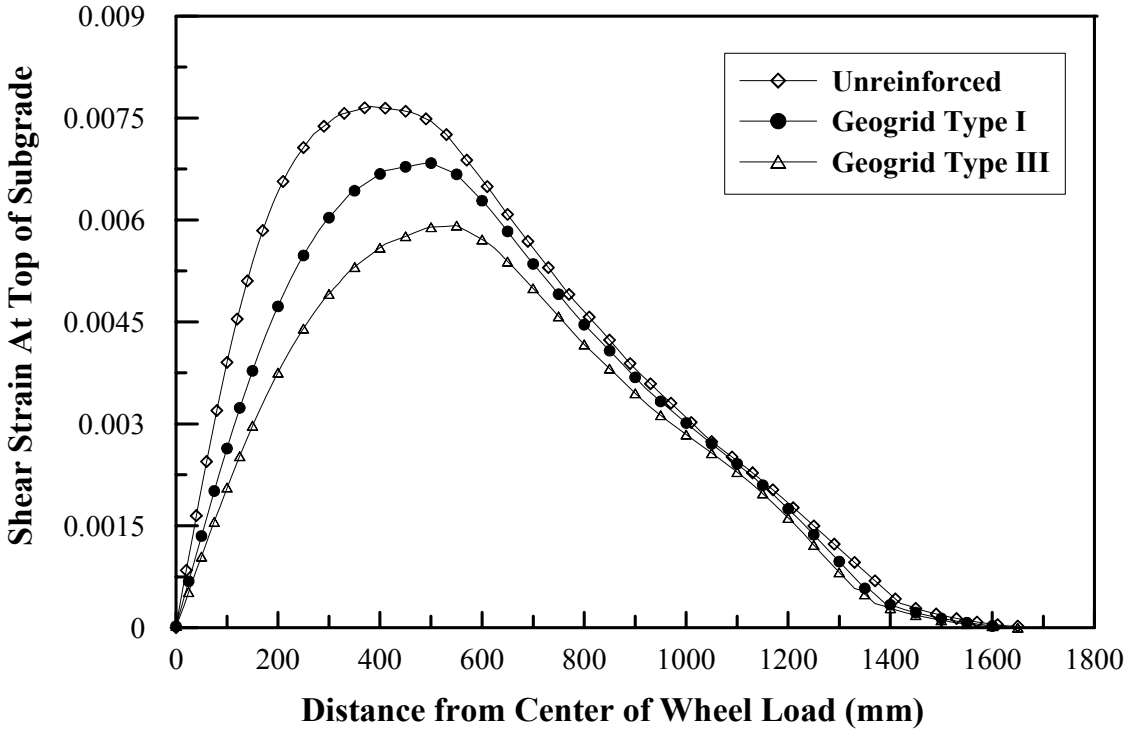

Figure 7.8 Shear Strain Profile at top of Subgrade Layer for Unreinforced and Reinforced Section 1a

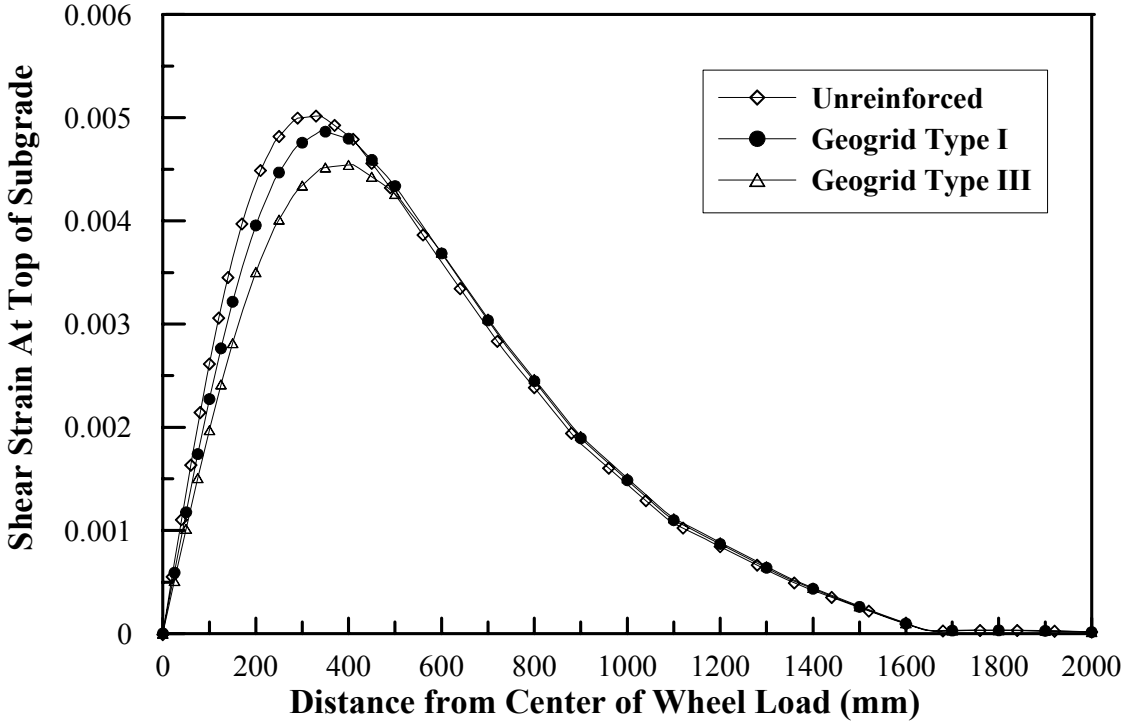

Figure 7.9 Shear Strain Profile at top of Subgrade Layer for for Unreinforced and Reinforced Section 3c

hence, suggests that a new approach that avoids the step-by-step calculation should be developed. It is worth mentioning here that recent research work reached to a similar conclusion (Allou et al, 2006; Chazallon et al., 2006).

Figure 7.10 depicts the permanent deformation curves computed using the finite element analysis for unreinforced and geogrid reinforced section 2b. It is noted that the geogrid reinforcement reduced the permanent deformation for reinforced sections. The magnitude of this reduction increased with the increase in the geogrid stiffness.

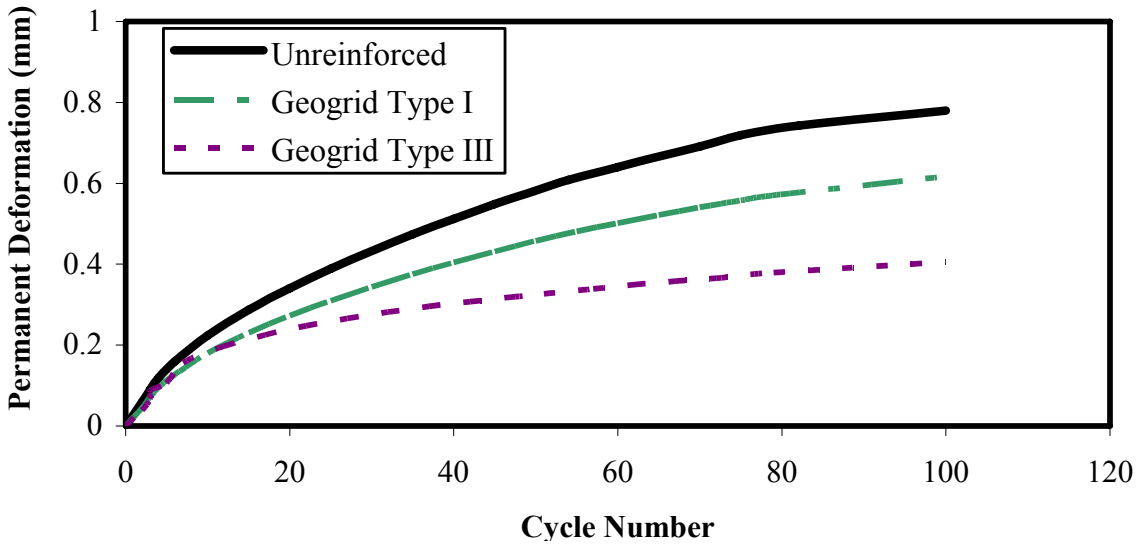

Figure 7.10 Rutting Curves of Unreinforced and Reinforced Section 2b

7.5 Evaluation of the Benefits of Geogrid Reinforcement Using a Mechanistic Empirical Approach

The improvement due to the inclusion of the geogrid layer within the base course layer was also evaluated using the mechanistic empirical approach described in Chapter 6 for crushed limestone I base material. Two performance criterions were used in this evaluation, namely, permanent deformation (rutting), and fatigue cracking. The permanent deformation was determined using the procedure described in Section 6.3.4 of Chapter six. Similar permanent deformation equation were used for all layer; however,

since a different material (crushed limestone II) was used in the base course layer, the material parameters of the permanent deformation prediction models were different, such that a $\varepsilon_0 / \varepsilon_r$ and β parameters value of 62.42 and 0.175 were used, respectively. The fatigue life was determined using Equation 6.1.

Table 7.5 presents the number of traffic passes to 25 mm of permanent surface deformation and fatigue life for each of the different unreinforced and reinforced pavement cross sections evaluated using the aforementioned mechanistic empirical approach. The table also presents the geogrid improvements in the rutting and fatigue life expressed in terms of TBR and N_R/N_U defined in Chapter 6 of this dissertation. The results in Table 7.5 are illustrated in Figure 7.11 through Figure 7.16.

The results demonstrate that the increase of the geogrid stiffness resulted in greater reduction in the permanent deformation of reinforced section, and hence increasing the number of load repetition needed to reach the maximum allowable rutting value of 25 mm. The reason for this is that the higher geogrid stiffness the lower the deformation and strain needed to mobilize the geogrid strength. The results in Table 7.5 and Figure 7.11 through Figure 7.13 demonstrate that the improvement due to the geogrid decreased with the increase in base course thickness and subgrade stiffness. This is expected since for weak subgrade and thin base course thickness great deformation will be encountered, and hence significant portion of the geogrid strength will be effective. It is clear that the geogrid improvement for sections built on top of stiff subgrade did not change when increasing the base course thickness from 200mm to 250 mm.

In general, the aforementioned results are consistent with those obtained in the previous chapter and the findings of field studies, which demonstrated that for a given geogrid location the reinforcement mechanism in reducing the permanent deformation

Table 7.5 Summary of Rutting and Fatigue Life of Unreinforced and Reinforced Sections

Section	Geogrid	Nf Rutting	Nf Fatigue	TBR	Nf/Nu
Section 1a	None	5.62E+04	4.710E+04	NA	NA
Section 1a	Type II	1.11E+05	9.307E+04	1.97	1.98
Section 1a	Type III	1.70E+05	1.117E+05	3.03	2.37
Section 1a	Type IV	1.96E+05	1.208E+05	3.50	2.57
Section 1b	None	2.14E+05	9.621E+04	NA	NA
Section 1b	Type II	3.63E+05	1.729E+05	1.69	1.80
Section 1b	Type III	4.74E+05	1.853E+05	2.21	1.93
Section 1b	Type IV	5.91E+05	1.993E+05	2.76	2.07
Section 1c	None	1.14E+06	2.671E+05	NA	NA
Section 1c	Type II	1.50E+06	4.298E+05	1.31	1.61
Section 1c	Type III	1.86E+06	4.724E+05	1.63	1.77
Section 1c	Type IV	2.27E+06	4.998E+05	1.99	1.87
Section 3a	None	8.82E+04	7.321E+04	NA	NA
Section 3a	Type II	1.47E+05	1.071E+05	1.67	1.46
Section 3a	Type III	1.84E+05	1.188E+05	2.09	1.62
Section 3a	Type IV	2.09E+05	1.266E+05	2.37	1.73
Section 3b	None	3.30E+05	1.528E+05	NA	NA
Section 3b	Type II	5.08E+05	2.133E+05	1.54	1.40
Section 3b	Type III	6.23E+05	2.296E+05	1.89	1.50
Section 3b	Type IV	6.92E+05	2.493E+05	2.10	1.63
Section 3c	None	1.28E+06	4.252E+05	NA	NA
Section 3c	Type II	1.39E+06	5.624E+05	1.09	1.32
Section 3c	Type III	1.55E+06	6.355E+05	1.21	1.49
Section 3c	Type IV	1.63E+06	6.748E+05	1.27	1.59
Section 5a	None	3.82E+05	1.134E+05	NA	NA
Section 5a	Type II	5.46E+05	1.616E+05	1.43	1.43
Section 5a	Type III	7.31E+05	1.850E+05	1.91	1.63
Section 5a	Type IV	8.29E+05	1.935E+05	2.17	1.71
Section 5b	None	1.02E+06	2.548E+05	NA	NA
Section 5b	Type II	1.42E+06	3.326E+05	1.39	1.31
Section 5b	Type III	1.72E+06	3.593E+05	1.68	1.41
Section 5b	Type IV	1.86E+06	3.871E+05	1.82	1.52
Section 5c	None	2.41E+06	6.999E+05	NA	NA
Section 5c	Type II	2.56E+06	8.652E+05	1.06	1.24
Section 5c	Type III	2.83E+06	9.077E+05	1.17	1.30
Section 5c	Type IV	2.91E+06	9.334E+05	1.21	1.33

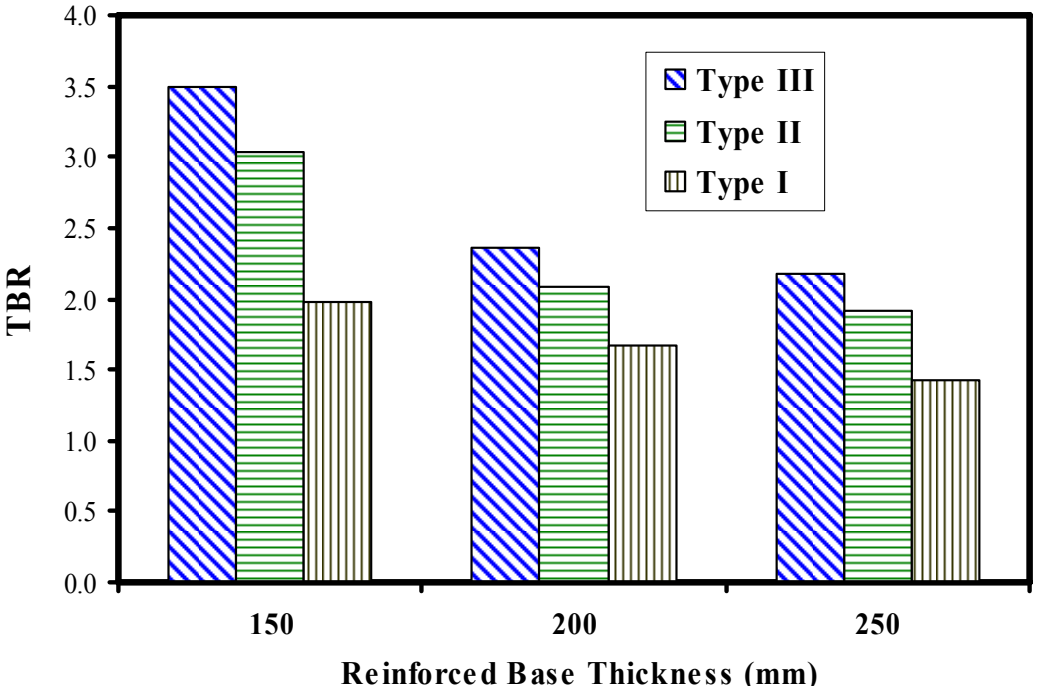

Figure 7.11 TBR of Reinforced Section with Weak Subgrade

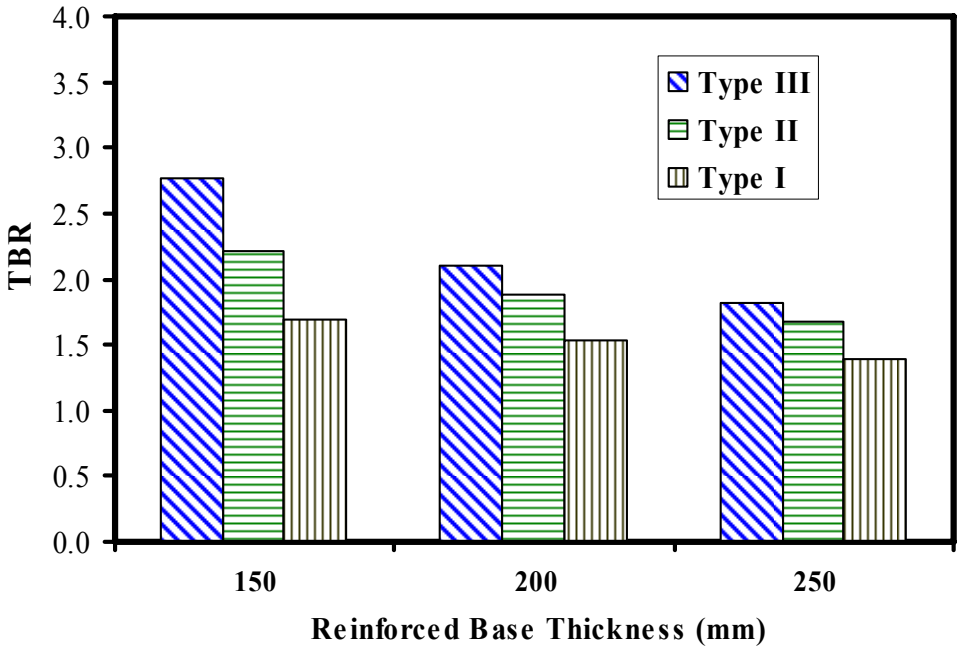

Figure 7.12 TBR of Reinforced Section with Moderate Subgrade

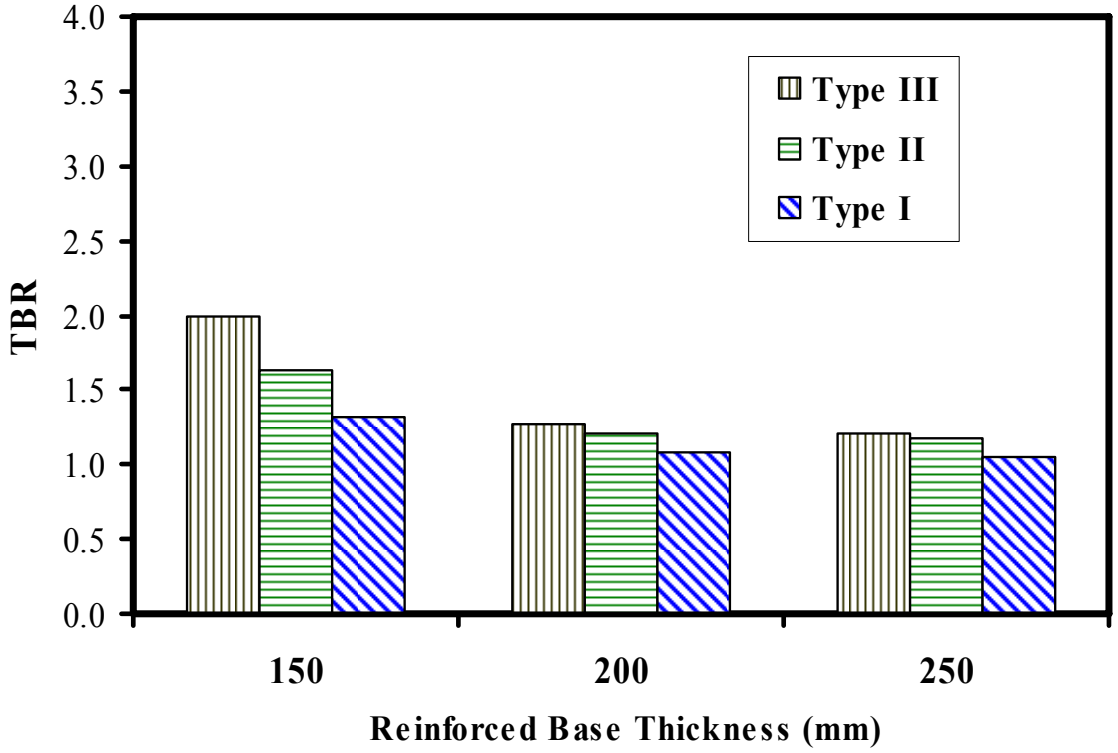

Figure 7.13 TBR of Reinforced Section with Stiff Subgrade

depends on three main factors, namely, geogrid stiffness, subgrade strength, and base course thickness. However, the effect of these factors can interact with each other, and the combined effect should be studied.

Figure 7.14 through Figure 7.16 present the N_R/N_U obtained for the different reinforced sections investigated in this chapter. It is noted that geogrid reinforcement had high values of improvement on fatigue life for sections built on top of weak subgrade soils. The improvement significantly decreased as base course thickness increased from 150 mm to 200mm, while small difference was observed between sections with 200 mm and 250 mm base layer thicknesses built. This results show that geogrid stiffness has some effect in improving the fatigue life, however this effect is not appreciable. In general, the results demonstrate the geogrid had a rather good ability to control fatigue cracking. However, these results should be further verified in test sections.

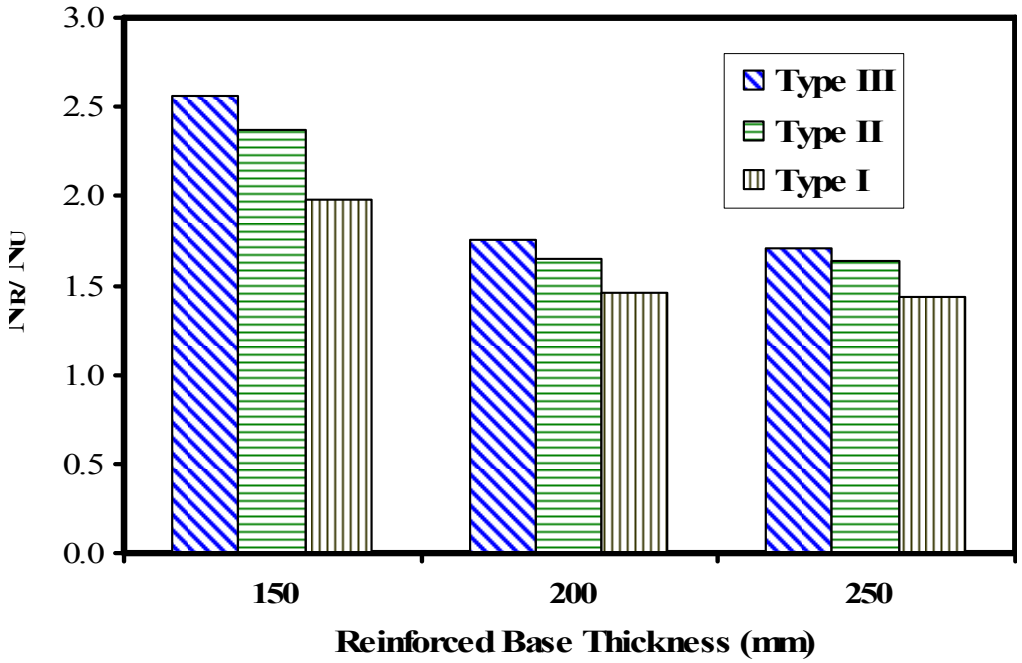

Figure 7.14 N_f / N_U of Reinforced Section with Weak Subgrade

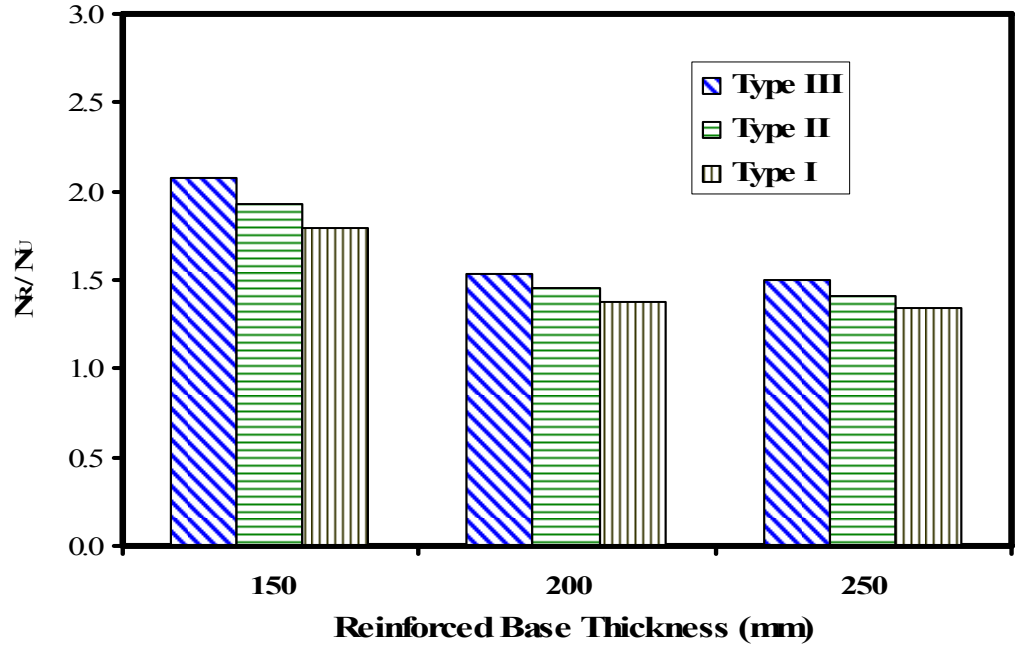

Figure 7.15 N_f / N_U of Reinforced Section with Moderate Subgrade

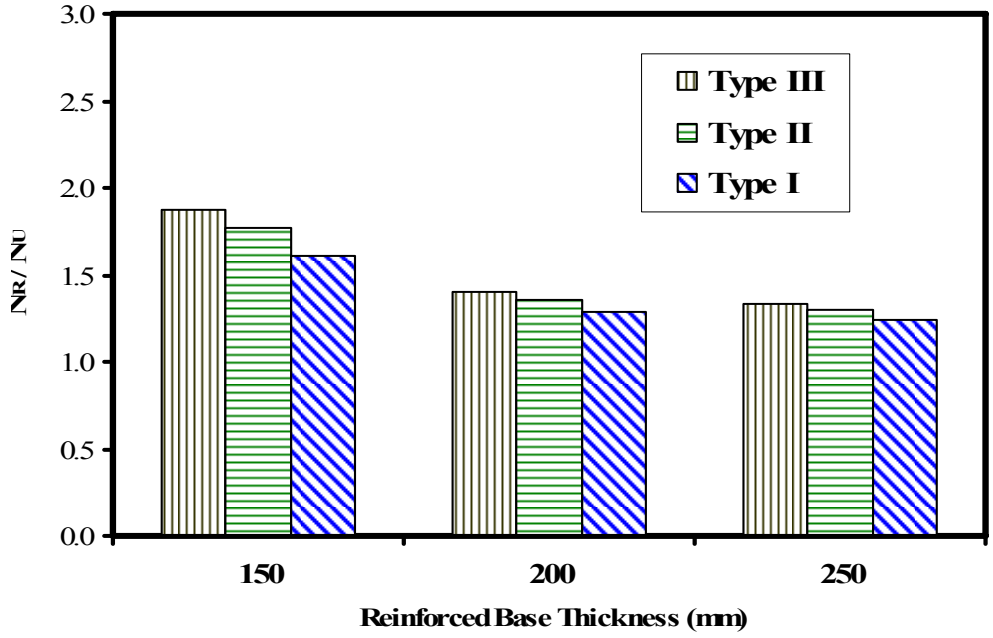

Figure 7.16 N_f / N_U of Reinforced Section with Stiff Subgrade

7.5.1 Development of TBR Model

A multiple regression analysis was conducted on the results of the finite element analysis to develop a prediction model of the TBR. Initially, a general model that includes all of the investigated variables and their interactions was selected. A stepwise variable selection procedure was conducted on the selected model to eliminate any insignificant variable. Based on the results of this procedure, only the normalized geogrid modulus, the interaction between the reinforced thickness and normalized geogrid modulus, the interaction between the subgrade strength and normalized geogrid modulus were found significant. Based on the results stepwise selection analysis, multiple regression analyses were conducted on finite element data to develop the TBR model. Table 7.6 and Table 7.7 present the results of the regression analysis, while Equation 7.15 shows the TBR model obtained from the analysis. The results show that the model had a high R^2 of 0.953, and a low RMSE value of 0.172, suggesting that the model well fits

the data. The results in Table 7.7 indicate that all parameters had similar significance effect on the prediction of the model, as indicated by the t-value. In addition, all three variables have variance inflation factor (VIF) values less than 5, which indicate that these variables are not collinear.

$$TBR = 1.0 + 1.3 \cdot X_2 - 0.00343 \cdot X_1 X_2 - 0.0305 \cdot X_2 X_3 \qquad 7.15$$

where

X_2: is the geogrid modulus (kPa) used in the finite element models normalized to a modulus value of 428000 (kPa);

X_1X_2: is the interaction between the effect of the reinforced thickness and normalized geogrid modulus;

X_2X_3: is the interaction between the effect of the subgrade strength and normalized geogrid modulus.

Equation 7.15 suggests that the predicted TBR decreases with increasing in the geogrid stiffness and decreasing of the base layer thickness and the subgrade stiffness strength. Furthermore it is noted that the effect of the geogrid stiffness decreases with the increase in the base course layer thickness and the subgrade stiffness/strength.

Figure 7.17 compares the TBR determined using the finite element analysis and those predicted using the regression model. It can be observed that a good agreement was obtained between the predicted and measured values. Moreover, the model was able to provide good prediction of the TBR data that were not used in the development of the model.

7.6 Stability of the Base Course Layer Using Shakedown Theory

The aforementioned mechanistic empirical design approach utilizes permanent deformation prediction models that only consider the primary and secondary stages of

Table 7.6 Summary of the Analysis of Variance of the TBR Model

Source	DF	Sum of Squares	Mean Square	F Value	Pr > F
Model	3	26.76787	8.92262	301.33	<.0001
Error	24	0.71064	0.02961		
Corrected Total	27	27.4785			

Root MSE	0.17209	R-Square	0.953
Dependent Mean	0.82074	Adj R-Sq	0.949
Coeff Var	21.29		

Table 7.7 Summary of the TBR Model Parameters Estimate

Variable	Parameter Estimate	Standard Error	Pr > |t|	Variance Inflation
Intercept	1.	0.084	<.0001	0
X_2	1.30016	0.07988	<.0001	4.33
X_1X_2	-0.03049	0.00264	<.0001	1.2
X_2X_3	-0.00343	0.00038071	<.0001	3.97

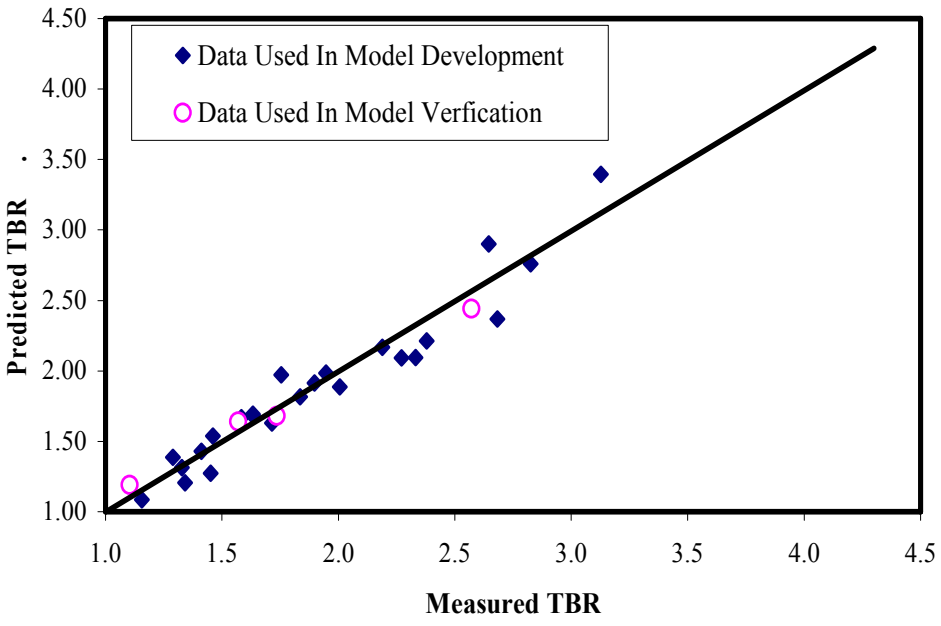

Figure 7.17 Prediction of TBR Model

permanent deformation, with the primary stage modeled using an extrapolation of the secondary stage trend. The tertiary stage of permanent deformation, though very important, is not taken into account in the mechanistic empirical design. This presents a major limitation in the current design practice. The main emphasize of this study was to characterize the behavior of the base course layer within flexible pavement structure. Therefore, the main purpose was to provide serviceability pavement design method that can ensure the adequacy of the permanent deformation prediction of the base layer.

Shakedown analysis can be used to identify the material response under cyclic loads. The shakedown theory is concerned with the evolution of the plastic deformation in the material. It predicts that a structure is liable to show progressive accumulation of plastic strains under repeated loading if the magnitude of the applied loads exceeds a certain limiting value, the so-called "shakedown limit" or "limit load". The pavement structure is then said to exhibit an incremental collapse, and thus the tertiary stage of permanent deformation will occur. On the other hand, if the amplitude of the applied cyclic loads is lower than the shakedown limit, the residual stresses will frequently develops such that the resultant stress cycle can be accommodated within the yield surface after a finite number of load applications. The resultant stress at a point is the residual stress remaining after the previous load application plus the elastic stress induced by the current load cycle. Once this stress accommodation occurred the pavement structure is said to have shakedown or undergone elastic shakedown and the maximum load amplitude at which this phenomenon occurs is called the (elastic) shakedown load. In this case the plastic rate will reach a stabilized value, and hence the assumption of the mechanistic empirical design approach to have the primary and secondary stages of permanent deformation will be valid.

Based on the mentioned assumption, the behavior of unbound granular base materials can be divided into three different shakedown ranges:

- Range A–elastic shakedown range: The response is plastic only for a finite number of load applications, and becomes purely resilient after completion of the post-compaction. The permanent strain rate quickly decreases to a very small level.
- Range B–intermediate response (plastic creep): The level of permanent strain rate decreases to a low and nearly constant level after several loading cycles depending on the applied stress level.
- Range C–incremental collapse: The permanent strain rate decreases very slowly or not at all and there is no cessation of permanent strain accumulation.

For design purposes, it is very important to determine within which shakedown range the applied loads of pavement layer can be classified, in order to examine its stability. In this dissertation the stability of the base course layer was only examined. To achieve that goal, the results of the multi-stage permanent deformation tests, described in Chapters three and four, were used to define the elastic and plastic shakedown limits. Equations 7.16 and 7.17 were found to adequately describe the elastic and plastic shake down limits., respectively.

$$q = 1.6p \qquad \text{(Elastic shakedown Limit)} \qquad 7.16$$

$$q = 2.22 + 24.48 \qquad \text{(Plastic shakedown Limit)} \qquad 7.17$$

Equations 7.16 and 7.17 were implemented in a FORTRAN subroutine that was developed and incorporated in the UMAT code in order to determine the shakedown range of the stresses encountered in the base course layer under traffic loading. At the end

of the loading step, the FORTRAN subroutine returns a value of a designated internal state variable (SDV2) that was included in the UMAT for this purpose. The subroutine basically verifies if the elastic or plastic shakedown limits are exceeded. If the elastic shakedown limit is exceeded, SDV2 is assigned a value of one, while if the elastic shakedown limit is exceeded and the plastic shakedown limit was not, a value of two is assigned for SDV2, finally if the plastic shakedown limit is exceeded then a value of three is assigned. Table 7.8 provides a summary of the shakedown analysis for all sections. While Figure 7.18 through Figure 7.23 show examples of contour plots of the SDV2 that was obtained for unreinforced and geogrid reinforced sections 1a and 3c. In Table 7.8 , Range B/C indicate that stresses within base course layer were classified within Ranges B and C, but more stresses lie within Ranges B. It can be noted that unreinforced and reinforced sections built on top of weak subgrades (sections 1a, 2a, and 3a) were structurally unstable, thus these sections should be redesigned. Furthermore, the geogrid reinforcement did not improve the base behavior from unstable to stable. However, it reduced the area within the base layer that had an unstable behavior. One reason that explains this result is that the confinement of the geogrid that was reported in some field studies was not completely included in the modeling of these layers.

7.7 Permanent Deformation Prediction Based on Shakedown Concept

The determination of the stability of base course layer is important. However, another key aspect of pavement design involves predicting the permanent deformation and service life of the pavement structure. Therefore, in order to implement the shakedown concept in the current pavement design procedures, it is necessary to modify the method used to predict the permanent deformation.

Table 7.8 Shakedown Ranges of Stresses Within Base layer

Section	Geogrid Type	Shakedown Range
Section 1a	NA	Range C
Section 1a	Type I	Range C
Section 1a	Type II	Range C
Section 1a	Type III	Range C
Section 1b	NA	Range C/B
Section 1b	Type I	Range B/ C
Section 1b	Type II	Range B/ C
Section 1b	Type III	Range B/ C
Section 1c	NA	Range B/ C
Section 1c	Type I	Range B
Section 1c	Type II	Range B
Section 1c	Type III	Range B
Section 3a	NA	Range C
Section 3a	Type I	Range C
Section 3a	Type II	Range C
Section 3a	Type III	Range C
Section 3b	NA	Range C/ B
Section 3b	Type I	Range B/ C
Section 3b	Type II	Range B/ C
Section 3b	Type III	Range B
Section 3c	NA	Range B
Section 3c	Type I	Range B
Section 3c	Type II	Range B
Section 3c	Type III	Range B
Section 5a	NA	Range C
Section 5a	Type I	Range C/B
Section 5a	Type II	Range C/B
Section 5a	Type III	Range C/B
Section 5b	NA	Range B/Range C
Section 5b	Type I	Range B
Section 5b	Type II	Range B
Section 5b	Type III	Range B
Section 5c	NA	Range B
Section 5c	Type I	Range B
Section 5c	Type II	Range B
Section 5c	Type III	Range B

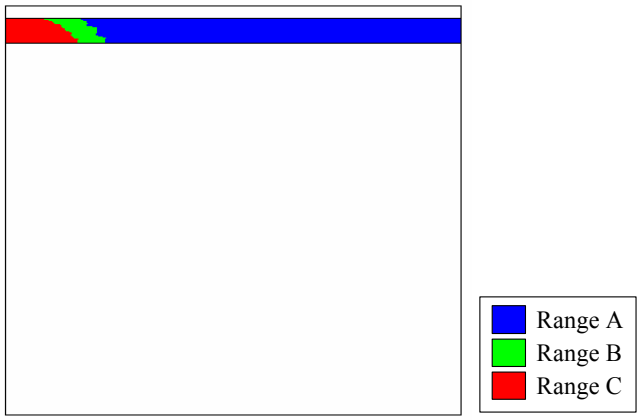

Figure 7.18 Contour Map of Base Layer Shakedown Behavior for Unreinforced Section 1a

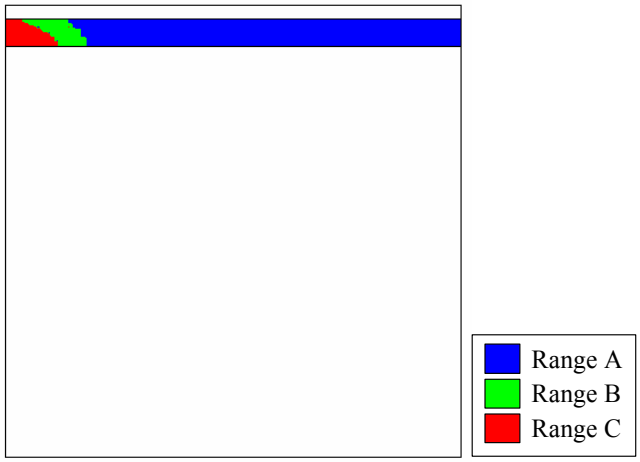

Figure 7.19 Contour Map of Base Layer Shakedown Behavior for Section 1a Reinforced with Geogrid Type I

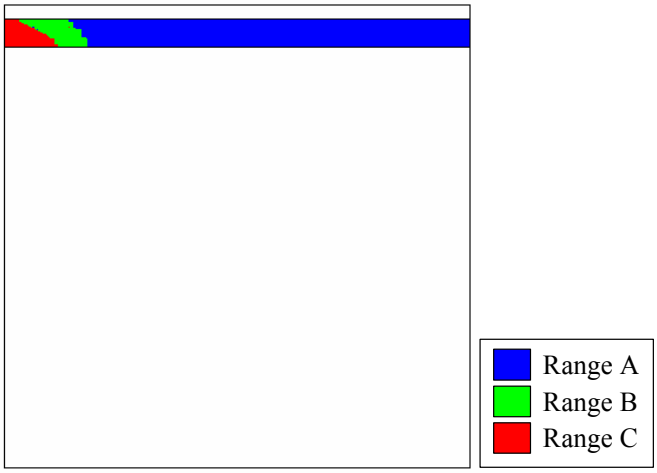

Figure 7.20 Contour Map of Base Layer Shakedown Behavior for Section 1a Reinforced with Geogrid Type III

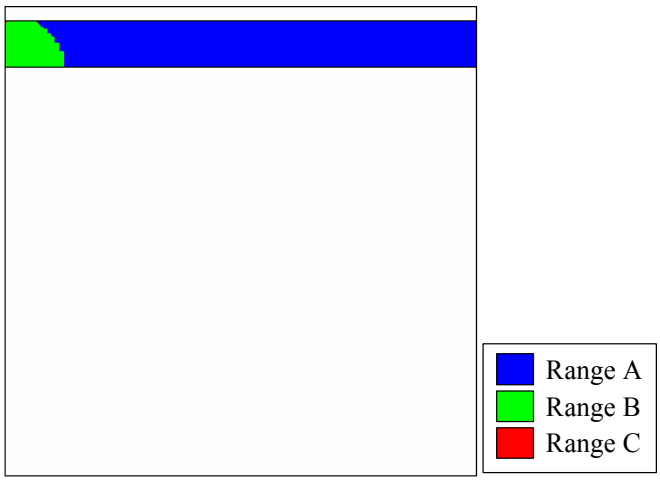

Figure 7.21 Contour Map of Base Layer Shakedown Behavior for Unreinforced Section 3c

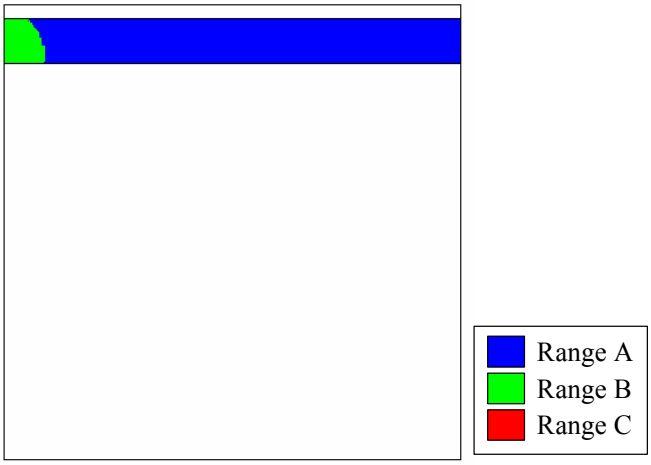

Figure 7.22 Contour Map of Base Layer Shakedown Behavior for Section 3c Reinforced with Geogrid Type I

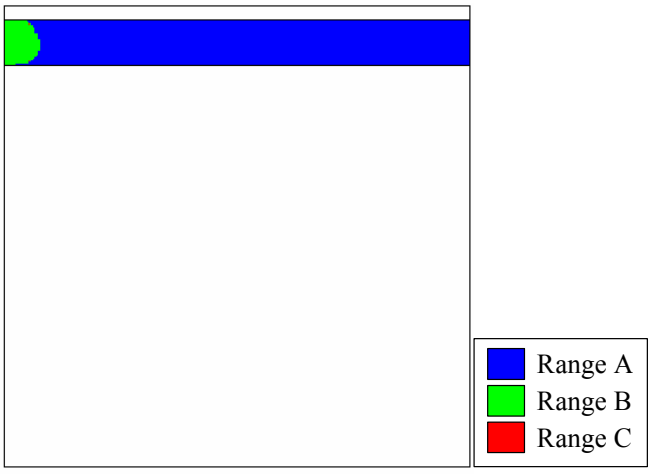

Figure 7.23 Contour Map of Base Layer Shakedown Behavior for Section 3c Reinforced with Geogrid Type IIII

According to the shakedown theory, the permanent deformation behavior of the material is depends on its material stress state. Therefore, any equation used to predict permanent deformation of base course layer should consider the stresses encountered in this layer. Looking at the base course prediction model (Equation 6.9), the equation requires two material parameters to define permanent deformation curve. Therefore, to account for the stress dependency of the permanent deformation, the definition of the two parameters was modified to incorporate the material's stress state.

Many studies that used the shakedown concept to characterize the permanent deformation behavior of the unbound granular base course materials, suggested that the ratio of deviatoric to mean stress (q/p) was the most dominant factor affecting the permanent deformation curve (Arnold, 2004; Werkmeister, 2005). Some studies indicated that the stress path length can also have a significant affect on the material response under cyclic loading (Gidel et al., 2001). Therefore, the relation between each of the two parameters with the q/p and stress length had to be examined.

The two parameters in Equation 6.9 were obtained for each stage in the different multi-stage RLT tests described in Chapter four of this dissertation. Figure 7.24 and Figure 7.25 depicts the relation between the $\varepsilon_0/\varepsilon_r$ and β parameters and q/p ratio, respectively. It is clear that there is a strong relationship between $\varepsilon_0/\varepsilon_r$ and q/p ratio, such that the $\varepsilon_0/\varepsilon_r$ increases exponentially with the increase in q/p. Figure 7.25 demonstrates a good agreement between the β and q/p ratio; however, it is difficult to express β parameter in term of q/p ratio individually.

Figure 7.26 and Figure 7.27 show the relation between the $\varepsilon_0/\varepsilon_r$ and β parameters and stress path length, respectively. It is noted that no clear relationship is

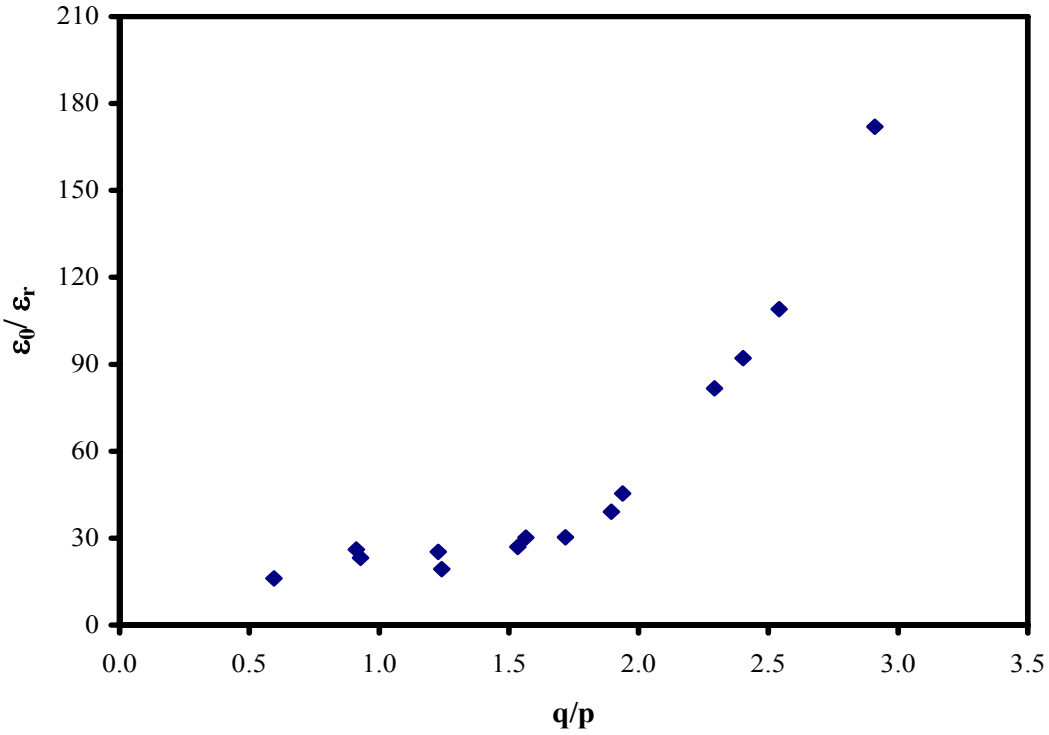

Figure 7.24 $\varepsilon_0 / \varepsilon_r$ Versus q/p Relation

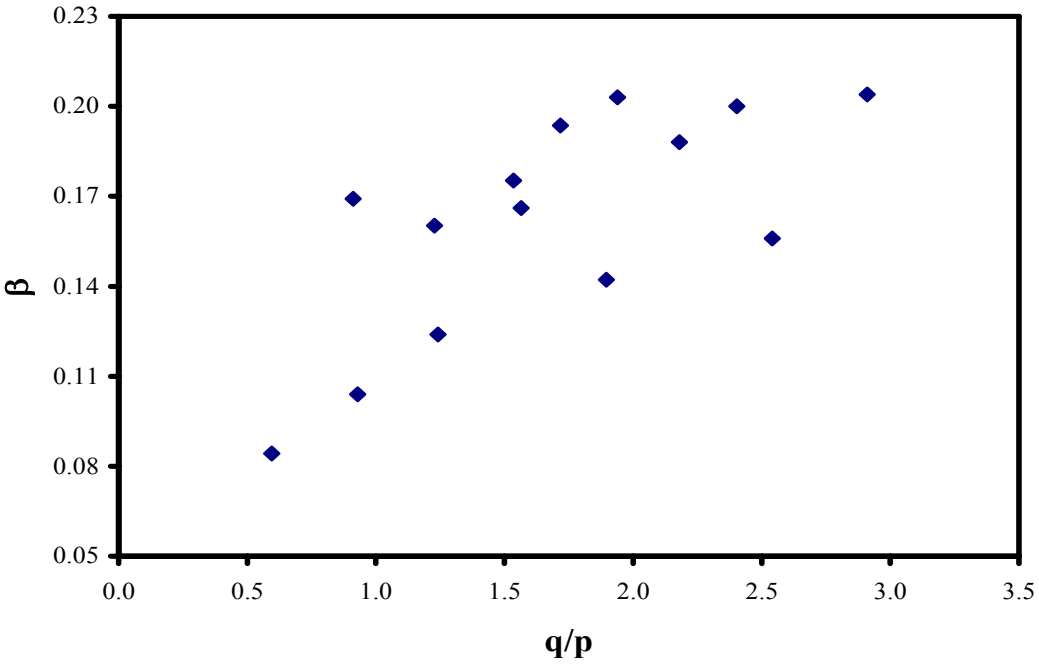

Figure 7.25 β Versus q/p Relation

observed between $\varepsilon_0/\varepsilon_r$ and stress path length, such that the $\varepsilon_0/\varepsilon_r$ points are widely scattered. However, a relationship do exist between the β and stress path length as shown in Figure 7.27.

Different models were examined to select the most appropriate model that can adequately predicts $\varepsilon_0/\varepsilon_r$ and β obtained from different stages and hence at different stress states. Accordingly, the two general models shown in Equations 7.18 and 7.19 were selected to predict the $\varepsilon_0/\varepsilon_r$ and β, respectively. It is noted that $\varepsilon_0/\varepsilon_r$ model was based only on q/p since the stress path length was not found to significantly affect this parameter, as noticed in Figure 7.25.

$$\varepsilon_0/\varepsilon_r = a \cdot e^{b\left(\frac{q}{p}\right)} \tag{7.18}$$

$$\beta = c\left[\left(\frac{q}{p}\right)^2 + 1\right]^{\frac{1}{2}} + d \cdot L \tag{7.19}$$

Where

L: is the stress path length

a, b, c and d are material parameters

A regression analyses were conducted to determine the parameters in Equations 7.18 and 7.19. The results of the regression analyses yielded the following equations:

$$\varepsilon_0/\varepsilon_r = 7.21 \cdot e^{1.0176\left(\frac{q}{p}\right)} \tag{7.20}$$

$$\beta = 0.054\left[\left(\frac{q}{p}\right)^2 + 1\right]^{\frac{1}{2}} + .00124 \cdot L \tag{7.21}$$

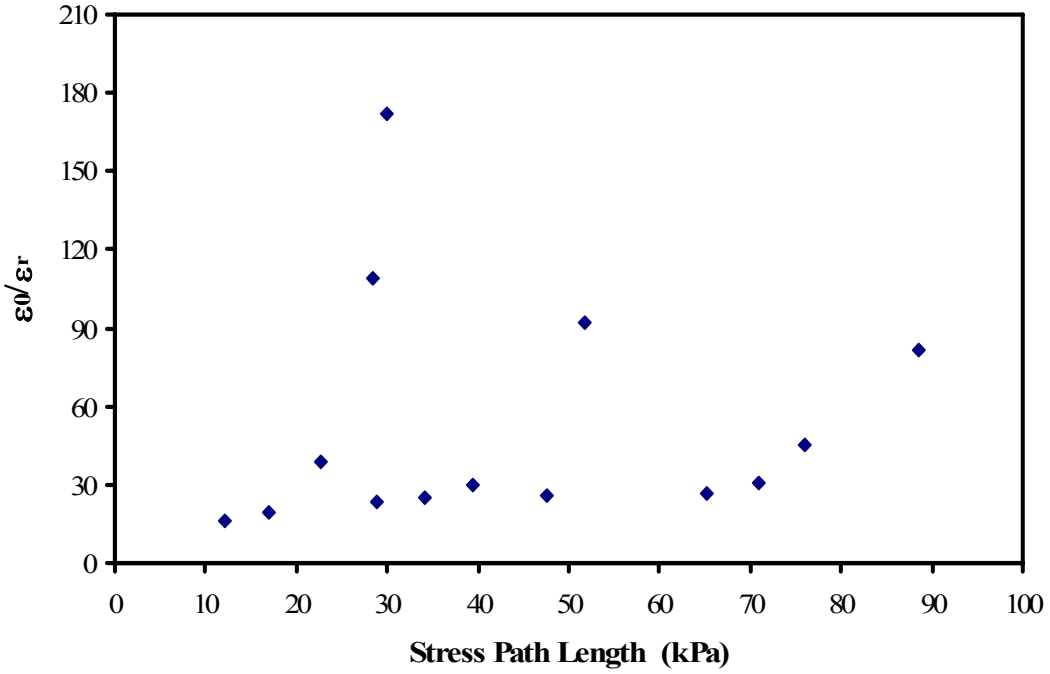

Figure 7.26 $\varepsilon_0 / \varepsilon_r$ Versus Stress Length Relation

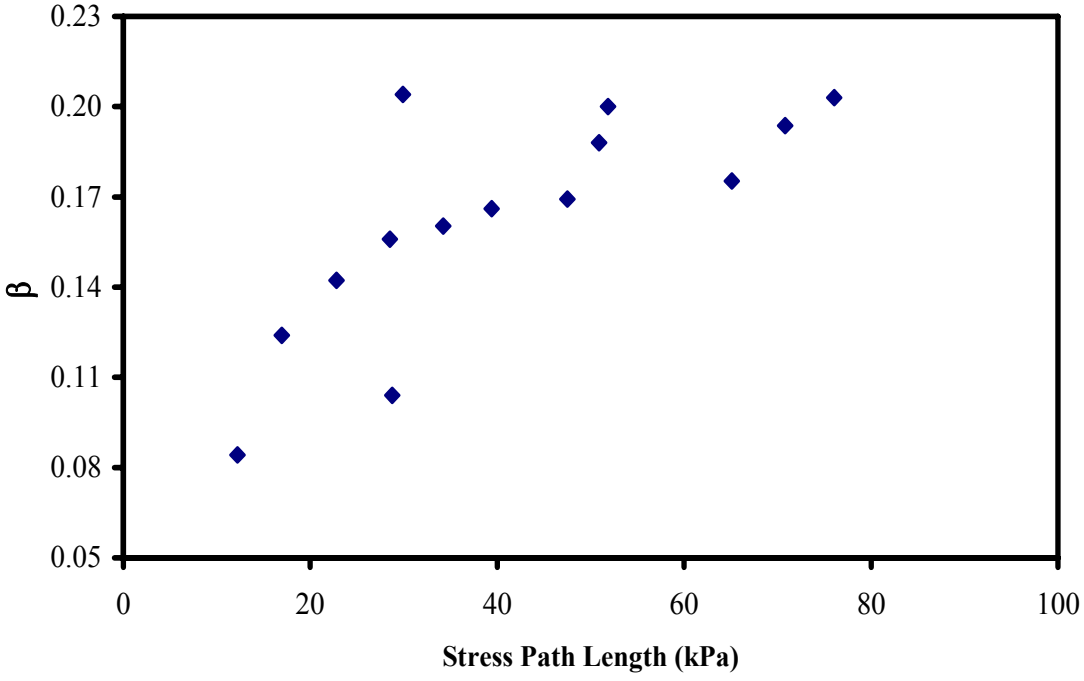

Figure 7.27 β Versus Stress length Relation

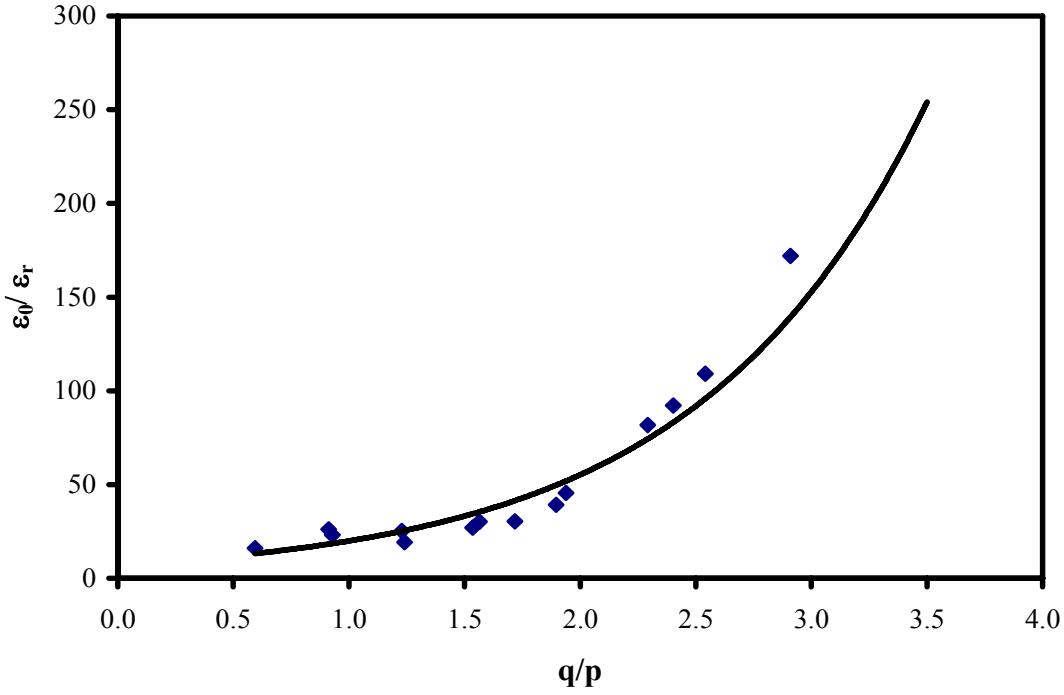

Figure 7.28 Prediction of the Developed $\varepsilon_0/\varepsilon_r$ Model

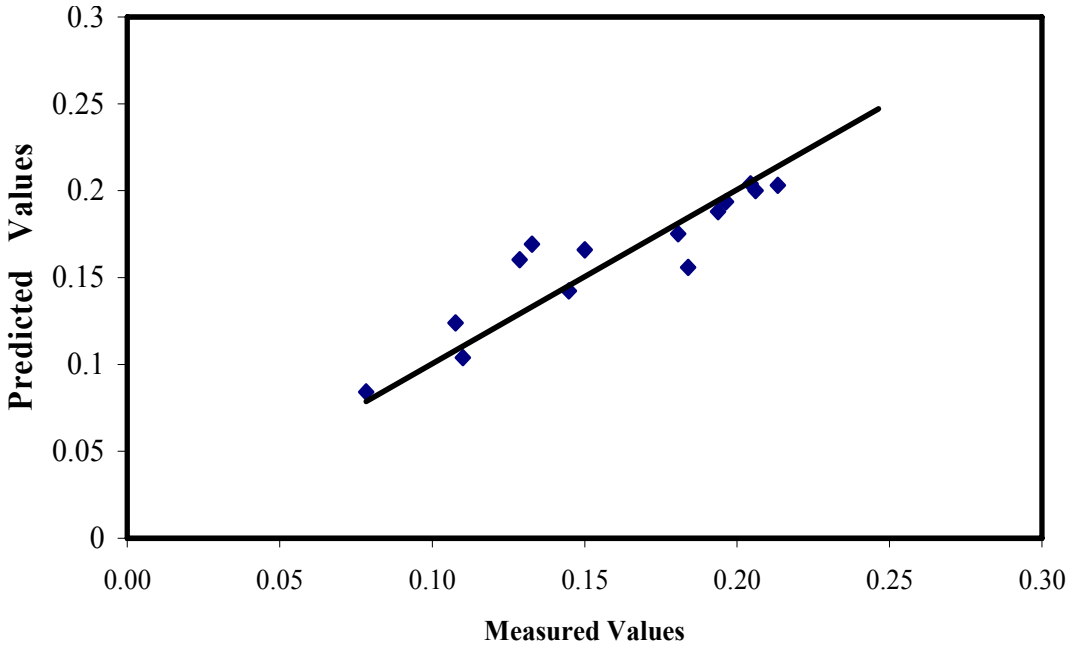

Figure 7.29 Prediction of the Developed β Model

The models in Equations and had R^2 values of 0.91 and 0.84, respectively. Furthermore the RMSE values for those models were, respectively. This indicates that both models were highly significant and well fit the data. This can also be noted in Figure 7.28 and Figure 7.29, which compares the predicted and measured $\varepsilon_0 / \varepsilon_r$ and β values.

Using Equations 7.20 and 7.21, the permanent deformation of the base course layers were recomputed considering the different stresses encountered in the base layer due to traffic loading. Table 7.9 presents the number of repetition needed to reach a permanent deformation of 25 mm for the different sections that were evaluated using the modified permanent deformation prediction models. It is worth mentioning here that sections with all the base course layer stresses classified within Range C, were not evaluated, since those sections are instable and should be redesigned. It should be mentioned that two options can be considered for overcoming the base course layer instability, namely, increasing the AC layer thickness, or using a better quality base course material.

Table 7.9 shows that the number of repetition needed to reach permanent deformation of 25 mm were reduced when using considering the stresses encountered in the base course layer. This reduction is much more pronounced in section built on moderate strength subgrade than those built on stiff subgrades. Some sections built on moderate strength subgrades had Range C stresses (see Table 7.8), which significantly affected the predicted permanent deformation values of these sections. This is obvious where the contribution of base layer to the total permanent deformation is larger.

Table 7.9 also demonstrates that improvement in the permanent deformation due to the geogrid reinforcement was enhanced when considering the stress state of the base course layer. This indicates that the geogrid had some affects on the stress state

Table 7.9 Summary of Rutting Life of Unreinforced and Reinforced Sections Predicted Using Modified Permanent deformation prediction Equation

Section	Geogrid Type	Nf Rutting	TBR
Section 1b	None	1.54E+05	NA
Section 1b	Type I	2.82E+05	1.93
Section 1b	Type II	4.29E+05	2.78
Section 1b	Type III	5.07E+05	3.29
Section 1c	None	1.12E+06	NA
Section 1c	Type I	1.74E+06	1.56
Section 1c	Type II	2.39E+06	2.14
Section 1c	Type III	2.94E+06	2.64
Section 3b	None	1.88E+05	NA
Section 3b	Type I	3.15E+05	1.68
Section 3b	Type II	4.87E+05	2.59
Section 3b	Type III	5.30E+05	2.82
Section 3c	None	1.28E+06	NA
Section 3c	Type I	1.64E+06	1.29
Section 3c	Type II	1.90E+06	1.49
Section 3c	Type III	2.00E+06	1.57
Section 5b	None	5.65E+05	NA
Section 5b	Type I	8.12E+05	1.44
Section 5b	Type II	1.29E+06	2.28
Section 5b	Type III	1.49E+06	2.63
Section 5c	None	2.17E+06	NA
Section 5c	Type I	2.95E+06	1.36
Section 5c	Type II	3.20E+06	1.48
Section 5c	Type III	3.31E+06	1.53

encountered in the base layer, which demonstrates the importance of using the shakedown concept in the design of unreinforced as well as reinforced pavement sections.

7.8 Modeling of Residual Stresses Effect in Pavement Structure

During construction the compaction of the granular pavement layers is usually achieved by the application of large vertical stresses. This will cause significant amount of lateral residual stresses to develop and become locked into the granular bases layer. The inclusion of the geogrid provides additional lateral residual stresses through the enhanced aggregate interlocking and the improved confinement it provides. These residual stresses should be properly quantified and considered in determining the initial stress state of the granular base course layer. This section primarily focuses on the investigation of geogrid confinement and its interlocking effects on pavement response by introducing the lateral residual stress distributions as initial stress states in the aggregate base.

The finite element model that was developed in the previous sections was modified to incorporate the effects of the residual stresses developed due to compaction and inclusion of geogrid reinforcement in base course layer. The model included applying initial lateral stresses within the base course layer. Two different horizontal residual stress distributions were considered in the finite element model for analyzing the unreinforced and geogrid reinforced pavement sections. These distributions are illustrated in Figure 7.30. For unreinfoced section in Figure 7.30a, a residual stress of 21 kPa was assumed to exist along the depth of the granular base in accordance with the field measurements reported in different studies. More details about the selection of this value can be found is section 2.2.1 of this dissertation.

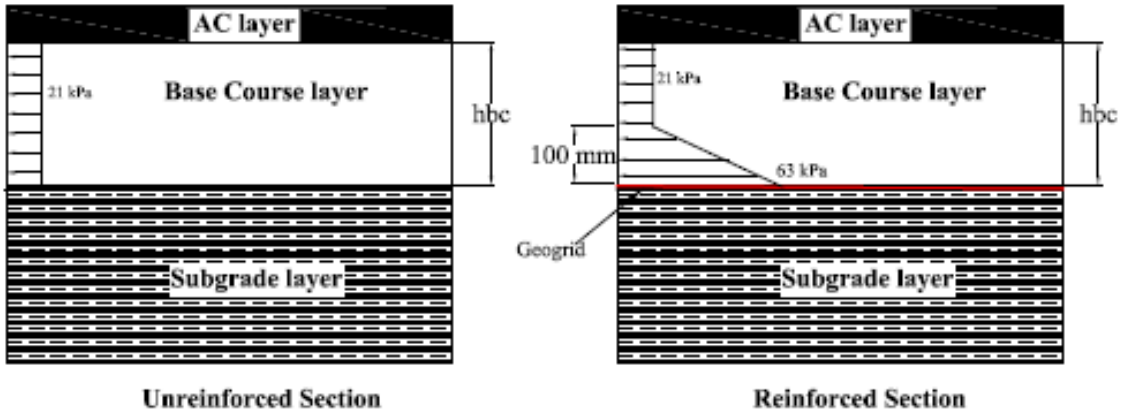

Figure 7.30 Residual Stress Distributions Used In Finite Element Model for Unreinforced and Reinforced Sections

The nature and the distribution of the locked-in horizontal residual stresses in the base course around the geogrid reinforcement are still unknown. However, a recent discrete element analyses (DEM) of the geogrid reinforced base course layer showed that the zone of the lateral confinement effect of geogrid tends extend to approximately 10 cm from geogrid side. Furthermore, the confinement effect of geogrid was shown to be great at the immediate vicinity of the geogrid, and decreased linearly within the influence zone. Based on the results of DEM the distribution shown in Figure 7.30 (b) was assumed in this analysis.

All the residual stresses were applied as initial stress conditions. However, since the residual stress distribution for reinforced sections shown in Figure 7.30 is not readily available in ABAQUS, a user defined subroutine (SIGINI) was developed for this purpose.

The developed finite element model was used to evaluate sections 1a, 1c, 3a, and 3c in Table 7.4. The finite element analyses were conducted on unreinforced sections and sections reinforced with geogrid Type I and III placed at the bottom of the base course layer. Figure 7.31 and Figure 7.32 illustrate the lateral strain profiles obtained from finite

element analyses for unreinforced and reinforced sections 1a and 3c, respectively. It is clear that the lateral strains of unreinforced as well as reinforced sections were reduced when the residual stresses were incorporated in the finite element model. However, the reduction in reinforced section was more appreciable than in unreinforced sections.

Figure 7.33 and Figure 7.34 present the vertical strain profiles within the subgrade layer for sections 1a and 3c, respectively. In general, the vertical strains within the subgrade layer were significantly reduced when considering the residual stresses, especially in the upper portions of this layer.

The permanent deformation was also computed using the mechanistic empirical models described in section 7.5 of this chapter. Table 7.10 presents the results of this computation for the selected pavement sections. By comparing Table 7.10 with Table 7.5 , one can notice that the number of repetition to reach 25 mm rutting for the analyzed pavement sections was significantly increased when considering the residual stresses. Furthermore, the effect of residual stresses on the pavement structures' permanent deformation was more appreciable when the structure was built on top of weak subgrades. The effect of the geogrid improvement on reducing the permanent deformation and hence increasing the pavement structures' service life was also significantly enhanced. It is interesting to note that the differences between the improvement achieved using the different geogrids types was reduced.

Shakedown stability analysis similar to those presented in section 7.6 were conducted to examine the stability of the different sections when considering the residual stresses effect within base course layer. Table 7.11 summarizes the results of this analysis. It is clear that the residual stresses significantly affected stress state of the base course layer and thus the shakedown range of stresses encountered within this layer. In addition, the

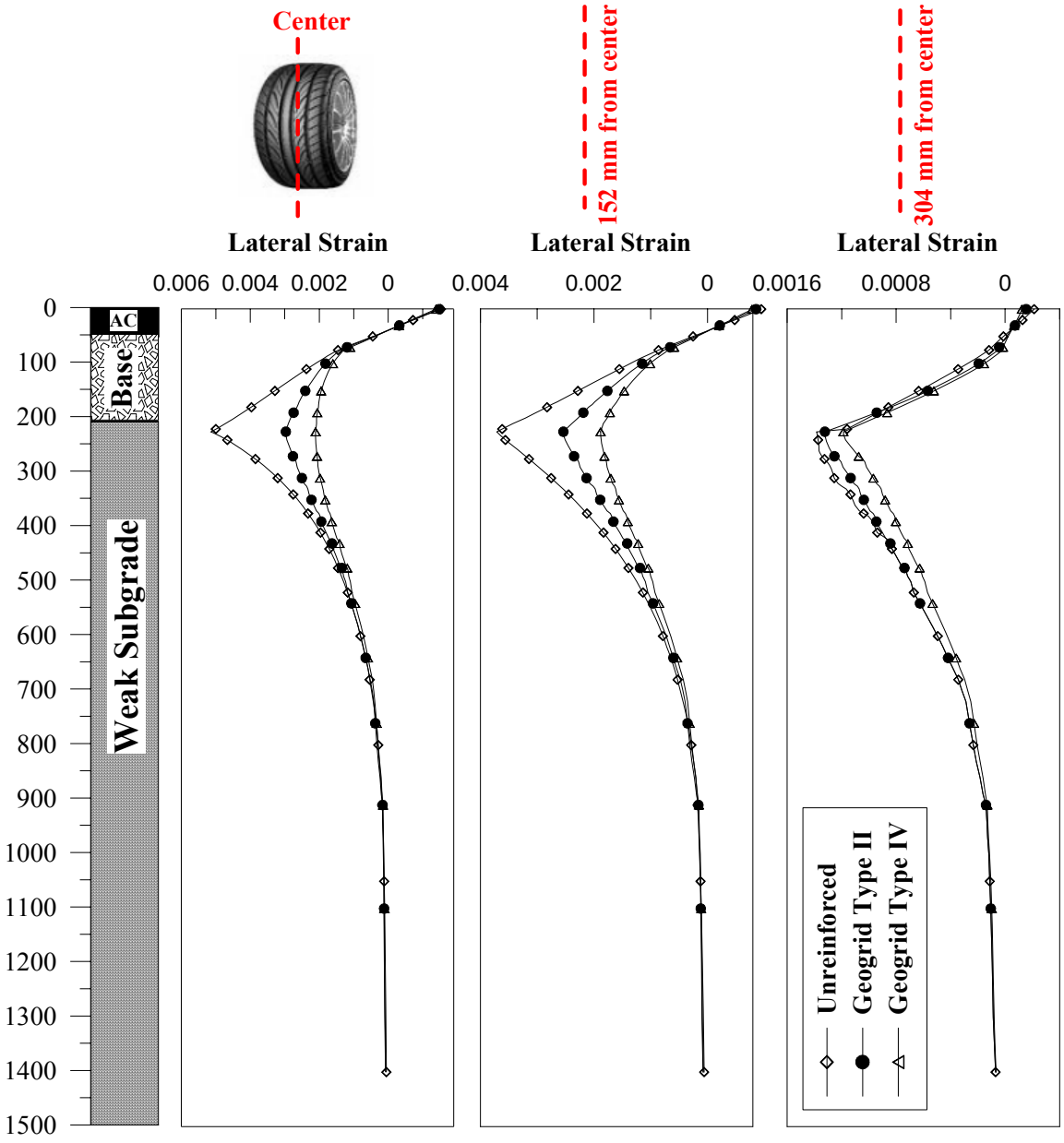

Figure 7.31 Lateral Strain Profile for Unreinforced and Reinforced Section 1a Considering the Residual Stress Effect

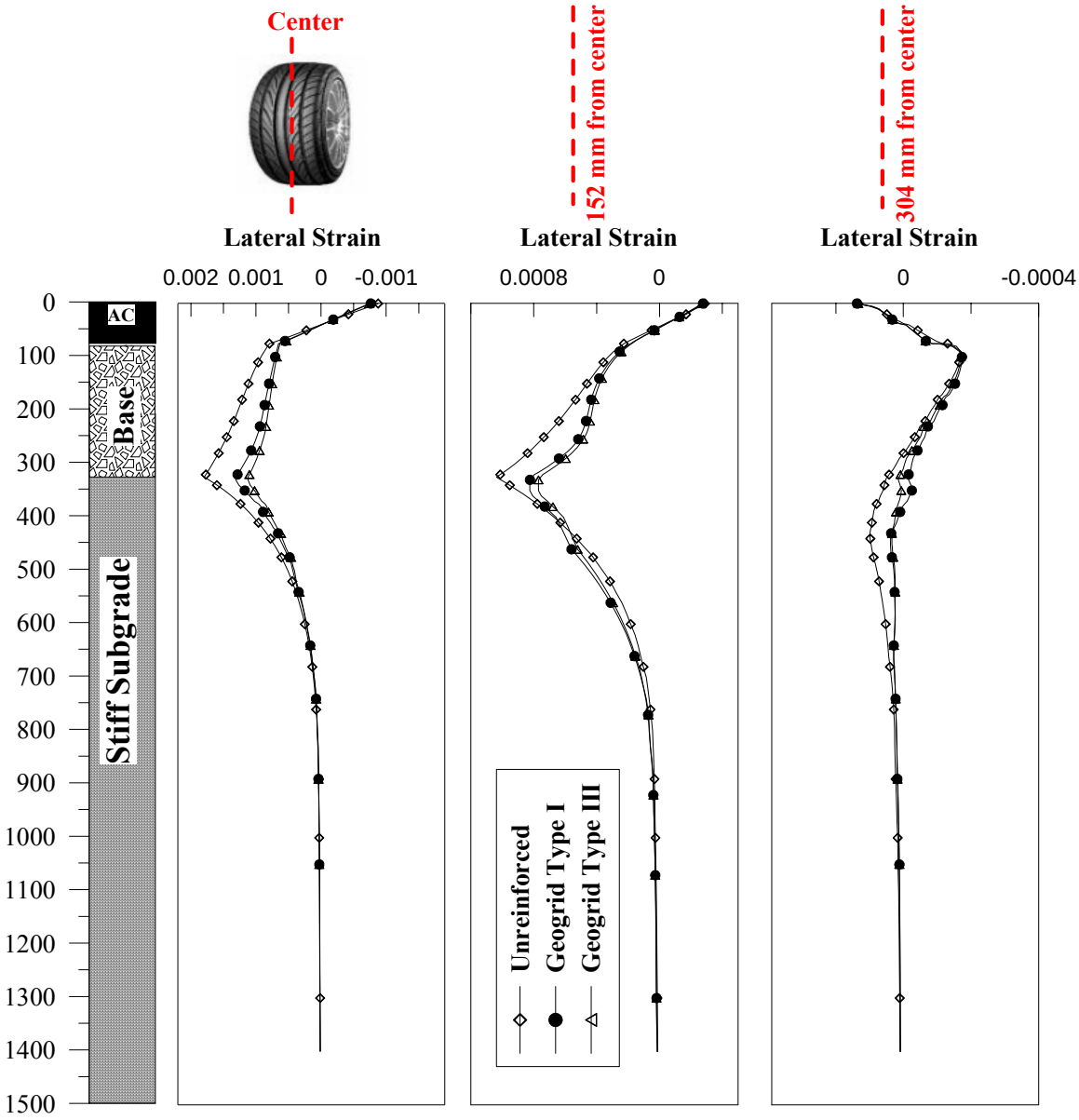

Figure 7.32 Lateral Strain Profile for Unreinforced and Reinforced Section 3c Considering the Residual Stress Effect

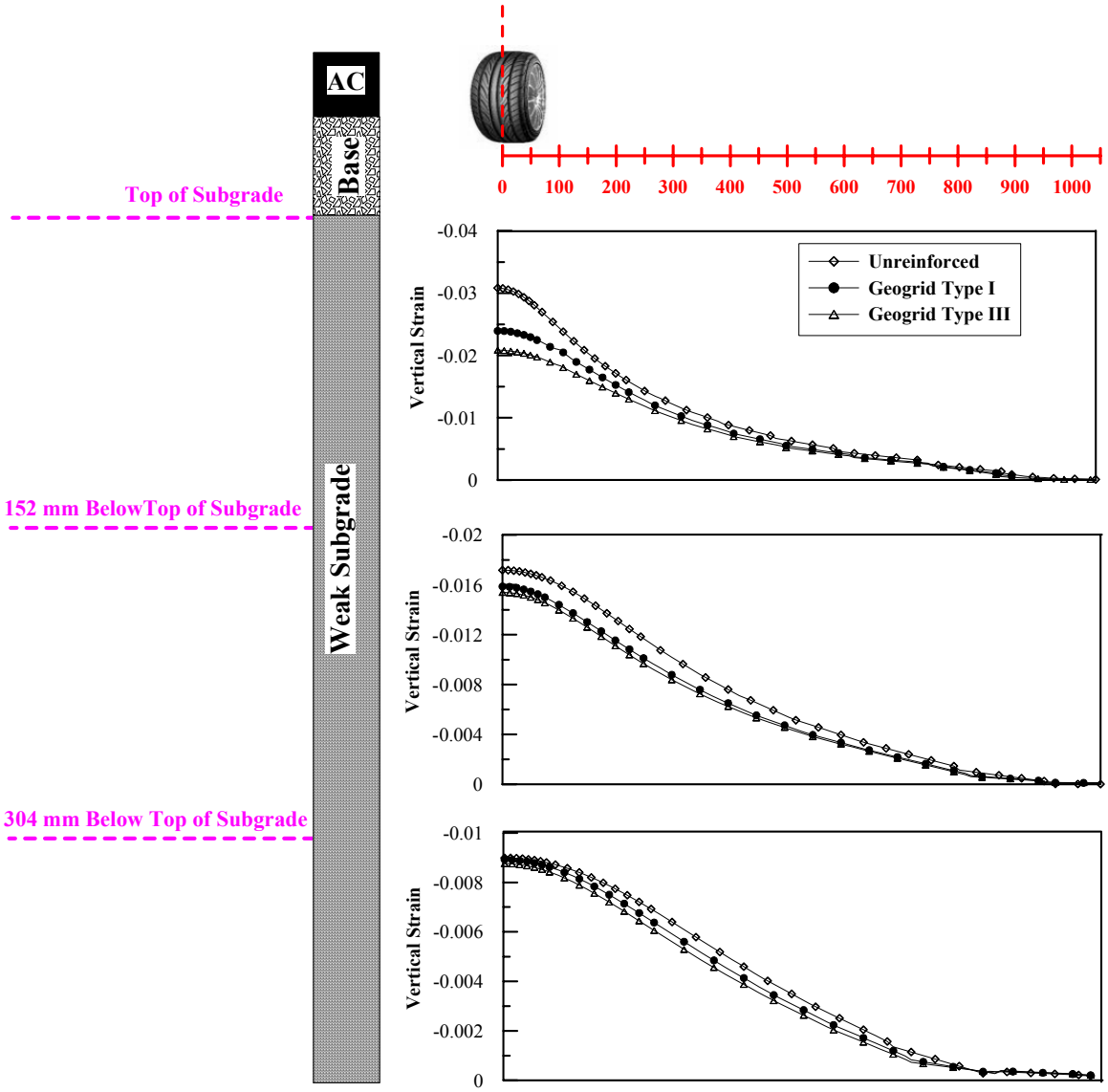

Figure 7.33 Vertical Strain Profile Within Subgrade layer for Unreinforced and Reinforced Section 1a Considering the Residual Stress Effect

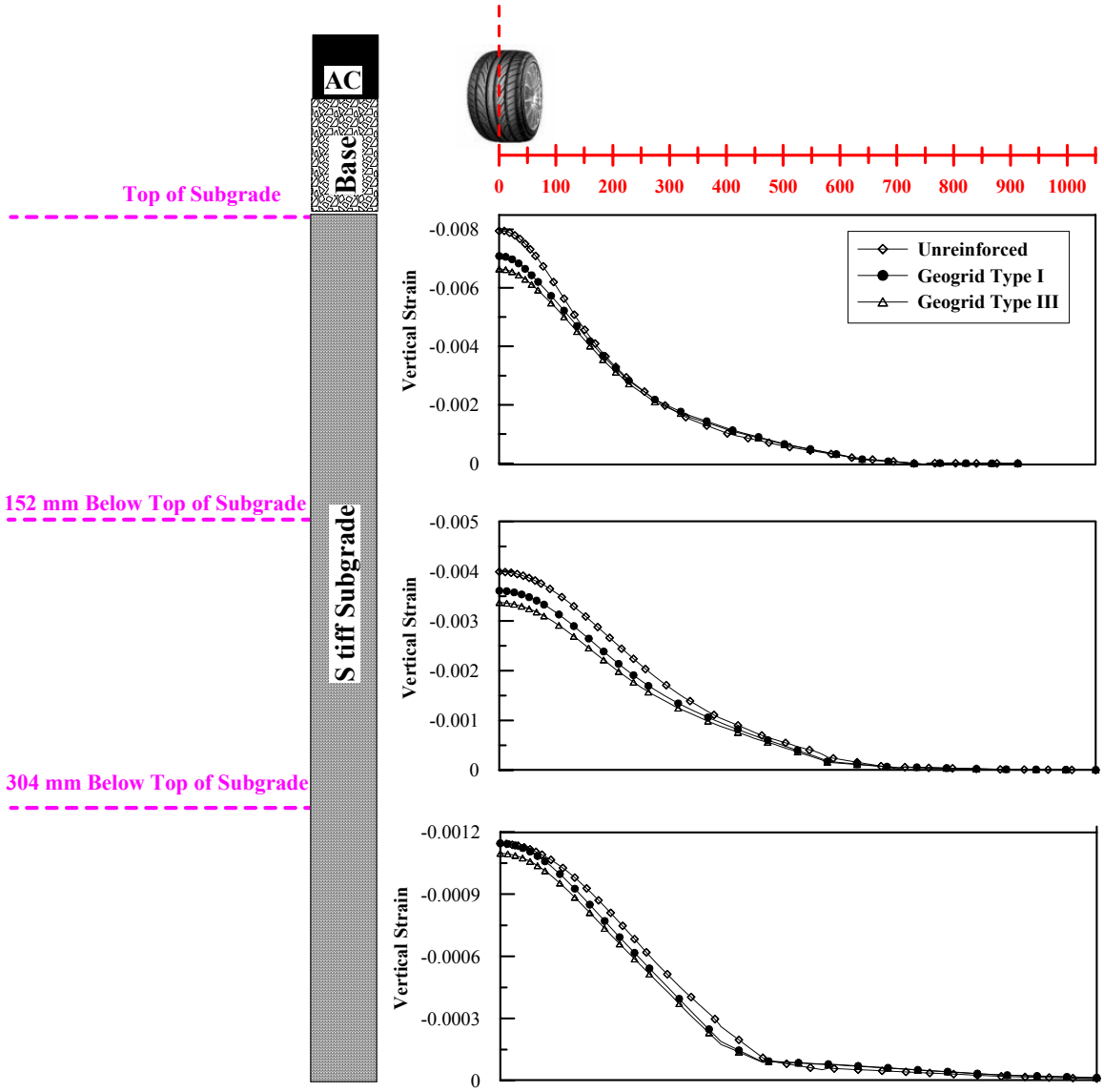

Figure 7.34 Vertical Strain Profile Within Subgrade layer for Unreinforced and Reinforced Section 3c Considering the Residual Stress Effect

Table 7.10 Summary of Rutting Life of Unreinforced and Reinforced Sections When Considering the Residual Stresses

Section	Geogrid Type	Nf Rutting	TBR
Section 1a	None	1.28E+05	NA
Section 1a	Type I	3.90E+05	3.06
Section 1a	Type III	6.01E+05	4.71
Section 1c	None	2.60E+06	NA
Section 1c	Type I	5.06E+06	1.95
Section 1c	Type III	5.93E+06	2.28
Section 3a	None	1.72E+06	NA
Section 3a	Type I	3.40E+06	1.98
Section 3a	Type III	5.09E+06	2.96
Section 3c	None	5.39E+06	NA
Section 3c	Type II	8.50E+06	1.58
Section 3c	Type III	9.12E+06	1.69

geogrid layer was found to be more effective in improving the stability of the base course layer. For example, the behavior of the base course layer for section 3c built on top of stiff subgrades soils was improved from Range B shakedown behavior to Range B/A.

The permanent deformation prediction equation developed in section 7.7 of this chapter, was used here to evaluate the permanent deformation service life of the unreinforced and geogrids reinforced pavement sections that exhibited stable base course behavior, as indicated from the results shown in Table 7.11. Table 7.12 present the results of this evaluation. The results indicate that for sections with base course layer exhibiting a Range C shakedown behavior, showed a reduction in the rutting service life when using the modified permanent deformation models. However, for base course layers having Range A or B shakedown behavior, and hence a more stable behavior, the pavement

Table 7.11 Shakedown Ranges of Stresses Within Base layer When Considering Residual Stresses

Section	Geogrid Type	Shakedown Range
Section 1a	NA	Rang C
Section 1a	Type I	Rang B/ C
Section 1a	Type III	Rang B/ C
Section 1c	NA	Rang B
Section 1c	Type I	Rang B/A
Section 1c	Type III	Rang B/A
Section 3a	NA	Rang B/ C
Section 3a	Type I	Rang B
Section 3a	Type III	Rang B
Section 3c	NA	Rang B/A
Section 3c	Type I	Rang A/B
Section 3c	Type III	Rang A/B

structure service life (N_f) was enhanced. This can be clearly noticed in unreinforced and geogrid reinforced section 3c, such that the N_f values were increased by more than 50% when using the modified models.

Table 7.12 also shows that when considering the material state of stress in the permanent deformation, the geogrid benefits presented in terms of TBR value, was enhanced for section with base course layer behavior of range B or range C, while the geogrid improvement was not affected when the base course layer behavior was within range A .

The results presented in this section demonstrate the importance of considering the residual stresses in numerical modeling of pavement structures, especially those reinforced with geogrid layers. It also emphasizes the significance of considering the shakedown concept in designing the pavement structures.

Table 7.12 Summary of Rutting Life Predicted Using Modified Permanent Deformation Model of When Considering the Residual Stresses prediction Equation

Section	Geogrid Type	Nf Rutting	TBR
Section 1c	None	3.29E+06	NA
Section 1c	Type I	6.53E+06	1.99
Section 1c	Type III	7.58E+06	2.31
Section 3a	None	1.27E+06	NA
Section 3a	Type I	2.75E+06	2.17
Section 3a	Type III	4.32E+06	3.41
Section 3c	None	7.78E+06	NA
Section 3c	Type II	1.21E+07	1.56
Section 3c	Type III	1.30E+07	1.68

Chapter Eight
Conclusions And Recommendations

8.1 Conclusions

This dissertation documents the findings of an extensive research study that was conducted to characterize the behavior of geogrid reinforced bases in flexible pavements. The objectives of this study were achieved through conducting an experimental testing and numerical modeling programs. The following sections summarize the findings and conclusions of each of these programs.

8.1.1 Experiential Testing Program

The experimental testing program in this study included performing different laboratory tests to characterize the performance of unreinforced and geogrid reinforced base course materials. The test factorial included two types of base course materials and five types of geogrid reinforcements that are typically used in the construction of base course layers. The laboratory tests conducted in this study included: drained compression triaxial test, resilient modulus repeated loading triaxial (RLT) test, single-stage RLT test, and multi-stage RLT test. Drained compression triaxial test was used to evaluate the static strength properties and stress-strain response parameters of tested samples. While the different types of RLT were used to study the resilient and permanent deformations under conditions that simulate the physical conditions and stress states in base layers subjected to traffic loads.

The effects of different factors associated with geogrid base course materials were investigated in this part of the study. Some of these factors were directly related to the properties of geogrids: geogrid stiffness, location, and number of layers. Others were

related to the properties of the base course material; such as its state of stress and moisture content. Comprehensive statistical analyses were conducted on the data obtained from the different laboratory tests. Based on the results of the experimental testing program, the following conclusions can be drawn:

- The inclusion of geogrid reinforcement layer/s improves the compressive strength and stiffness of base course materials under static loading. In general, the geogrid improvement was not mobilized until certain strain levels were reached, which differed between the two crushed limestone materials investigated. For crushed limestone I, this strain limit was 1%; while for crushed limestone II it was 2%.
- The geogrid improvement under static loading was more pronounced at higher strain levels. Such that for crushed limestone I, the maximum improvement was demonstrated at the ultimate shear strength that happened to be similar to the residual strength for this material. However, for crushed limestone II, the geogrid layer(s) had the maximum improvement in the residual post peak strength.
- The improvement due to the geogrid in the compressive strength and stiffness response parameters under static loading were found to be a function of the geogrid location, type, and number of layers.
- At a certain geogrid location, stiffer geogrids exhibited greater benefits.
- For a specific geogrid stiffness/type, the highest improvement was always achieved when using two geogrid layers placed at the upper and lower third of the sample height. While the lowest improvement was encountered when placing the geogrid layer at the sample's mid height for crushed limestone I samples, while it differed for crushed limestone II material with different response parameters.
- For samples compacted at the dense state, the use of the geogrid reinforcement layers

changed the pattern of deformation in the collapse mechanism of reinforced samples, and altered the development of shear bands.

- The inclusion of geogrid reinforcement layer(s) significantly reduces the accumulation of permanent deformation accumulation under cyclic loading of base course materials.
- The reduction in permanent deformation under cyclic loading due to the geogrid reinforcement was found to be a function of the geogrid stiffness, geogrid arrangement, and number of load cycles. However, the geogrid arrangement was found to be the dominant factor influencing this reduction.
- The reinforcing capacity of the double layers of geogrid was mobilized at much lower load cycles than the single layer of geogrid.
- The showed that the shakedown approach can be used to characterize the deformation behavior of unbound granular base materials in pavement constructions.
- The behavior of base course materials can be categorized into three possible Ranges A, B or C. If the base course materials behavior was within Range A, the pavement will "shakedown". After post-compaction deformations, no further permanent strains develop and the material subsequently responds elastically. Thus Range A is permitted in a pavement, provided that the accumulated strain before the development of fully resilient behavior is sufficiently small. The material in Range B does not "shakedown", instead it will achieve failure at a very high number of load repetitions. In such a case the resilient strains are no longer constant and will increase slowly with increasing number of load cycles (decrease of stiffness). Range C behavior, i.e. incremental collapse or failure, should not be allowed to occur in a well designed pavement.

- For stresses less than plastic shakedown limit and higher than elastic shakedown limit, the geogrid had a minimal contribution to the permanent deformation resistance during primary stage; however, it significantly increased the permanent deformation resistance during the secondary stage.
- The geogrid reinforcement mechanism did not significantly affect the permanent deformation accumulation in for stresses higher than plastic shakedown limit.
- The dominant geogrid reinforcement mechanism that influences the permanent deformation is the geogrid-aggregate interlocking mechanism. While the membrane tension reinforcement mechanism was found to be much less effective.
- Moisture content was found to alter the material state of stress; which significantly affected the geogrid improvement.
- The geogrid inclusion did not show appreciable effect on the resilient deformation of reinforced samples.
- The behavior of unbound granular base material has an important influence on rut build-up in pavement structure and can not readily modeled solely by ultimate shear strength parameter.
- Multi-stage RLT test provides a good approach to minimize the time and effort needed to define the shakedown limits, and to investigate the permanent deformation at different stress levels.

8.1.2 Numerical Modeling Program

Finite element analyses were conducted to assess the benefits of using geogrids to reinforce the base course layer in a flexible pavement structure, and to evaluate the effects of subgrade strength, thickness of the base course layer, and stiffness and location of the reinforcement layer on these benefits. Different constitutive models were used to

describe the behavior of the pavement layers, which included: Extended Drucker Prager, Modified Cam Clay, and Elastic–Perfectly Plastic models. In addition, a two surface critical state elasto-plastic model that was originally proposed by Manzari and Daflias (1997) was calibrated and implemented in the ABAQUS using a User subroutine UMAT to represent the behavior of crushed limestone base course material.

The stresses, strains, and permanent deformation obtained from the results of finite element analysis were used to evaluate the effect of the different variables associated with geogrid reinforced base layers. The improvement due to the geogrid reinforcement was also assessed using a mechanistic empirical approach. In this approach, the response parameters computed from the finite element analyses were used to determine the pavement structure distresses based on empirical models. Two types of distresses were considered to control the flexible pavement performance, namely, permanent deformation (rutting), and fatigue cracking.

The shakedown concept was successfully applied to analyze the performance of unreinforced and geogrid reinforced sections, and was used to develop a new approach to analyze and design pavement systems.

Multiple regression analyses were conducted on the results of the finite element analyses to develop models that predict geogrid benefits as a function of the different variables investigated in this study. Based on the results of this numerical modeling program, the following conclusions can be drawn:

- The geogrid reinforcement reduced the lateral strains within the base course and subgrade layers. The maximum reduction in lateral strain was observed at the base subgrade interface. The geogrid effect was mainly below the wheel loading area and it almost vanished at a distance of 304 mm from the center of the wheel load.

- The inclusion of the geogrid layer resulted in significant reduction in the vertical strains at top of subgrade. Moreover, the geogrid influence on the vertical strain was experienced within a zone that extends to a depth of about 304 mm below the top of the subgrade layer. However, the greatest influence was encountered at the top of the subgrade.
- The improvement of geogrid layer was found to be more pronounced in the development of the plastic strains rather than the resilient strains.
- The geogrid layer resulted not only in decreasing the shear strains at the top of the subgrade layer, but also in providing a better distribution of these strains.
- The geogrid benefits in improving the developed strains were more appreciable in sections with weak subgrades compared to those in sections with stiff subgrades. In addition, these benefits were reduced as the thickness of the base layer increased, and were enhanced as the stiffness of the geogrid layer increased.
- More reduction in the lateral strain at AC-base course layer interface was achieved when placing the geogrid layer at the upper one third location compared to the other locations; however, the bottom location had greater reduction in lateral strains encountered within the lower parts of the base course layer.
- The bottom location was the most efficient in reducing the total and plastic vertical strain at the top of the subgrade layer.
- The geogrid-base interface properties did not affect the distribution of lateral strains within the AC layer; however, a slight difference was observed within the base and subgrade layers, such that increasing shear interface modulus resulted in slight reduction in the lateral strain.
- The geogrid reinforcement demonstrated appreciable reduction in the permanent

deformation for pavement sections built on top of weak subgrade soils with medium to thin base layer thickness; with the thin base layer thickness showing greater values of improvement. However, negligible to modest reinforcement effects on rutting was obtained for sections having a firm subgrade or thick base layer thickness.

- The increase in the geogrid stiffness resulted in significant reduction of permanent deformation. However, the geogrid stiffness effect decreased with the increase in the thickness of the reinforced base course layer.
- The interface shear modulus value affected the accumulated permanent deformation, such that the increasing it resulted in greater reduction in permanent deformation.
- The results obtained from the finite element analysis concerning the permanent deformation of geogrid reinforced sections were consistent with those observed in test section reported in different studies.
- Regression models that predict the benefits of reinforcing base course layers in terms of traffic benefit ratio (TBR), and base course reduction ratio (BCR) were successfully developed for readily use in design of reinforced flexible pavement structure. In general these models showed that the geogrid improvement decreases with increasing the geogrid stiffness and decreasing the base layer thickness and the subgrade stiffness.
- In terms of rutting, the maximum benefit is attained when the geogrid reinforcement is at the bottom of the base for section with thin base course thickness and weak to moderate subgrade soil, while placing the geogrid within the base course layer had a better performance when the base layer have the greatest contribution to the total permanent deformation of the pavement structure.
- The geogrid reinforcement had modest to high values of improvement in fatigue life

of pavement structure, which shows great promise of reinforcement for controlling AC fatigue cracking.

- The increase in geogrid stiffness only improved the fatigue life of pavement sections with thin base layer built on top of weak subgrade soil.
- The increase in base course thickness had much less adverse effect on the fatigue life improvement, especially for the moderate and stiff subgrade.
- The closer the geogrid layer to the AC-base interface, the better the improvement in the fatigue life of reinforced pavement structures.
- The geogrid reinforcement did not improve the base course layer behavior from unstable to stable. However, it reduced the area that had an unstable behavior within the base course layer.
- The improvement in the permanent deformation due to the geogrid reinforcement was enhanced when considering the stress state of the base course layer. Due to the fact that the geogrid affected the stress state encountered in the base layer.
- The results demonstrate great importance of using the shakedown concept in the design of unreinforced as well as reinforced pavement sections. The application of concept can help to prevent under-designing or over-designing pavement structures.
- The use of constitutive cyclic plasticity models in finite element analysis of pavement sections requires unrealistic computational time to simulate the application of large number of load cycles. This shows the limitation of using such models in finite element modeling of pavement structures.
- The results of the mechanistic pavement analysis indicated that the benefits of the inclusion of geogrid layer at the granular base-subgrade interface could be successfully modeled by considering the residual stress concentrations above the

geogrid reinforcement in the numerical model. Considering such stresses is important to account for fundamental mechanisms and processes involved in reinforced pavement structures that are otherwise missing from numerical model.

- The residual stresses considerably changed the base course layer state of stress, resulting in significant increase in the geogrid benefits.

8.2 Recommendations

- Additional research effort is needed to investigate the interaction between aggregate size and geogrid aperture.
- Models that are based on the plasticity framework, the shakedown concept and avoid the step-by-step calculation should be developed and used in modeling pavement structure.
- More research is required to develop more appropriate material models that can simulate the build up of residual stresses due to the compaction of base aggregate.
- Further investigation is required to characterize the geogrid-aggregate interlocking mechanism and provide a better models to quantify the resulting residual stresses reinforced base course layer.
- Additional research effort is required to characterize the geogrid influenced zone.
- The benefit of reinforcement on asphalt concrete fatigue life should be established and experimentally verified to validate the large benefit values seen in this study.
- It is strongly recommended that the findings of this research are evaluated and verified using large scale testing facilities such as the Louisiana Accelerated Loading Facility (ALF). This will provide the opportunity to monitor the performance of geogrid reinforced pavement sections under field conditions.
- Further investigations on proposed linkage between shakedown range boundaries

defined via the RLT test and in-situ performance are necessary to confirm predictions made by the approach introduced in this study.

- Further research effort is recommended to implement the shakedown concept in the design of pavement structures.

References

- AASHTO (1993). *AASHTO Guide for Design of Pavement Structures*, Washington, DC.
- AASHTO T307-99 (2003). Standard method of test for determining the resilient modulus of soils and aggregate materials. *American Association Of State Highways And Transportation Office*.
- Allen, J. (1973). ‘‘The effect of non-constant lateral pressures of the resilient response of granular materials,’’ PhD thesis, University of Illinois at Urbana-Champaign, Urbana, Ill.
- Allen, J. J., and Thompson, M. R. (1974). ‘‘Resilient response of granular materials subjected to time dependent lateral stresses.’’ Transp. Res. Rec. 510, Transportation Research Board, Washington, D.C., 1–13.
- Allou, F., Chazallon, C., (2006) “A numerical model for flexible pavements rut depth evolution with time” *International Journal for Numerical and Analytical Methods in Geomechanics*, Vol 31, Issue 1 , Pages 1 – 22.
- Almeida, J. R. de. (1986). Structural Analysis of Rigid Pavements by the Finite Element Method. MSc Thesis, Technical University of Lisbon (in Portuguese).
- Alonso, E. (2003). “Exploring The Limits Of Unsaturated Soil Mechanics: The Behavior Of Coarse Granular Soil And Rockfill.” *The Eleventh Spencer J. Buchanan Lecture*.
- Al-Qadi, I. L., Brandon, T.L, Valentine, R J., Lacina, B.A., and Smith, T.E. (1994). “Laboratory evaluation of geosynthetic reinforced pavement sections.” *Transportation Research Record*, *No. 1188*, 25-31.
- Al-Qadi, I.L., Brandon, T.L. and Bhutta, A. (1997). "Geosynthetic Stabilized Flexible Pavements," Proceedings of the Conference Geosynthetics ’97, Long Beach, CA, USA, March, Vol. 2, pp. 647-662.
- Al-Qadi, I.L., Coree, B.J., Brandon, T.L., Bhutta, S.A. and Appea, A.K., (1998). "Quantifying the Separation Characteristic of Geosynthetics in Flexible Pavements," Proceedings of the Sixth International Conference on Geosynthetics, Atlanta, GA, USA, Vol. 2, pp. 945-950.
- Al-Qadi, IL, Brandon, TL, and Bhutta, SA (1997). “Geosynthetics stabilized flexible pavements.” *Proc., Geosynthetics’ 97,* Long Beach, CA, Vol. 2, 647-661.
- Anderson and Collins, I.F. (1995). “Plane strain stress distributions in discrete and blended coated solids under normal and sliding contact.” *Wear* 185, pp. 23-33.

- Ansell, P., and Brown, S. F. (1978). ‘‘Cyclic simple shear apparatus for dry granular material.’’ Geotech. Testing J., 1(2), 82–91.
- Armstrong, P. J. and Frederick, C. O. (1966). “A Mathematical Representation of the Multiaxial Bauschinger Effect.” CEGB Report, RD/B/N731, Berkeley Nuclear Laboratories.
- Arnold G, Dawson A, Hughes D, Robinson D. The application of shakedown approach to granular pavement layers. Journal of Transportation Research Board 2003; 1819(2):194–200.
- Arnold, G. (2000). Performance based specifications for road construction and materials. UNBAR 5. University of Nottingham, UK.
- Arnold, G. K., (2004). *Rutting of granular pavements,* Ph.D. dissertation, School of Civil Engineering, The University of Nottingham, The United Kingdom.
- ASTM, 1998, Annual Books of ASTM Standards, West Conshohocken, PA.
- Ashby, M. and Jones, D., Engineering Materials 1, Pergamon Press, 1980.
- Ashmawy, A.K, Bourdeau, P.L., Drnevich, V.P., Dysli, M., (1999) "Cyclic Response of Geotextile- Reinforced Soil," *Journal of Soils and Foundations*, Vol. 39, No. 1, February, pp.
- Baladi, G. Y., and Chen, W. F. (1985). Soil plasticity: Theory and implementation, Elsevier, Amsterdam, The Netherlands
- Barksdale, R. D. (1972). ‘‘Laboratory evaluation of rutting in basecourse materials.’’ Proc., 3rd Int. Conf. on Struct. Des. of Asphalt Pavements, 161–174.
- Barksdale, R. D. (1991). The aggregate handbook. National Stone Association, Washington, D.C.
- Barksdale, R. D., and Itani, S. Y. (1989). ‘‘Influence of aggregate shape on base behavior.’’ Transp. Res. Rec. 1227, Transportation Research Board, Washington, D.C., 173–182.
- Barksdale, R.D., Brown, S. F., and Chan, F. (1989). “Potential benefits of geosynthetics in flexible pavement systems”, *National Cooperative Highway research Program Report* No. 315, Transportation Research Board, National Research Council, Washington, DC, USA, 56 p.
- Benedetto, H., and La Roche, C. (1998). "State of art on stiffness modulus and fatigue of bituminous mixtures." RILEM Rep. 17, Bituminous Binders and Mixes, London.

- Berg, R. R., Christopher, B.R., and Perkins, S.W. (2000). "Geosynthetic reinforcement of the aggregate base course of flexible pavement structures." GMA White paper II, Geosynthetic material Assoiation, Roseville, MN, USA, 130 p.

- Binquet, J. A. and Lee, K. L. (1975), "Bearing Capacity Analysis on Reinforced Earth Slabs", Journal of Geotechnical Engineering, ASCE, Vol. 101, pp. 1257-1276.

- Bishop, A. W. (1959).*The principle of effective stress*. Tecknish Ukeblad 106 (39), 859–863.

- Borja, R.I. (1991), "Cam-clay plasticity. Part II: implicit integration of constitutive equations based on a non-linear elastic stress predictor.'' Computer Methods in Applied Mechanics and Engineering, Vol. 88, pp. 225-40.

- Borja, R.I. and Lee, S.R. (1990), "Cam-clay plasticity. Part I: implicit integration of elasto-plastic constitutive relations", *Computer Methods in Applied Mechanics and Engineering*, Vol. 78, pp. 49-72.

- Boulbibane, M. and Weichert, D. (1997). "Application of shakedown theory to soils with non associated flow rules." Mechanics Research Communications, Vol. 24, No. 5, pp. 516-519.

- Boyce, J. R. (1976). The behaviour of granular material under repeated loading. PhD Thesis, University of Nottingham, UK.

- Britto, A.M. and Gunn, M.J. (1987), Critical State Soil Mechanics via Finite Elements, Ellis Horwood, Chichester.

- Brown, S. F. (1996). 36th Rankine Lecture: Soil Mechanics in Pavement Engineering, Géotechnique, Vol. 46, No. 3, 1996, pp 383-426.

- Brown, S. F., and Hyde, A. F. L. (1975). ''Significance of cyclic confining stress in repeated-load triaxial testing of granular material.'' Transp. Res. Rec. 537, Transportation Research Board, Washington, D.C., 49– 58.

- Cancelli, A., and Montanelli, F. (1996). "In-ground test for geosynthetic reinforced flexible paved roads", Proc. Of the Conference Geosynthetics '99, Boston, MA, USA, Vol. 2, pp. 863-878.

- Cancelli, A., Montanelli, F., Rimoldi, P., and Zhao, A (1996). "Full scale laboratory testing on geosynthetics reinforced paved roads", Earth reinforcement, Ochiai, H., Yasufuku, N., and Omine, K., Editors, Balkema, Proceedings of the International Symposium on Earth Reinforcement, Fukuoka, Kyushu, Japan, November, 1996, pp. 573-578.

- CEN (2004). Unbound and hydraulically bound mixtures – Test methods – Part 7:Cyclic load triaxial test for unbound mixtures. European Committee for Standardisation, No. prEN 13286-7, Brussels, Belgium.

- Chazallon, C., Hornych, P., and Mouhoub, S. (2006) "Elastoplastic Model for the Long-Term Behavior Modeling of Unbound Granular Materials in Flexible Pavements" *Int. J. Geomech*., Vol 6, Issue 4, pp. 279-289.

- Collins, I. F., Wang, A. P., and Saunders, L. R. (1993). ''Shakedown theory and the design of unbound pavements.'' Rd. and Transp. Res.,2(4), 28–37.

- Crisfield, M.A. (1991), *Non-linear Finite Element Analysis of Solids and Structures*, Volume 1, John Wiley & Sons, Chichester.

- Crisfield, M.A. (1997), *Non-linear Finite Element Analysis of Solids and Structures*, Volume 2, John Wiley & Sons, Chichester.

- Dafalias, Y. F., and Herrmann, L. R. Bounding surface plasticity II: Application to isotropic cohesive soils. Journal of Engineering Mechanics, ASCE 112, 12 (December 1986), 1263—1981.

- Dafalias, Y. F., and Popov, E. (1976)." Plastic internal variables formalism of cyclic plasticity." Journal of Applied Mechanics, ASME 98, 4, 645—651.

- Dawson, A. R. (1990). ''Introduction to soils & granular materials.'' Lecture Notes from Residential Course, Bituminous Pavements: Materials, Design and Evaluation, University of Nottingham, Nottingham, England

- Dawson, A. R., Thom, N. H., and Paute, J. L. (1996). ''Mechanical characteristics of unbound granular materials as a function of condition.'' Flexible Pavements, Proc., Eur. Symp. Euroflex 1993, A. G. Correia, ed., Balkema, Rotterdam, The Netherlands, 35–44.

- Davies, M. C. R., and Bridle, R. J. (1990). "Predicting the Permanent Deformation of Reinforced Flexible Pavement Subject to Repeated Loading," Performance of Reinforced Soil Structures, McGown, A., Yeo, K., and Adrawes, K. Z., Editors, Thomas Telford, 1991, Proceedings of the International Reinforced Soil Conference, Glasgow, Scotland, pp. 421-425.

- Dehlen, G. L. (1969). ''The effect of non-linear material response on the behavior of pavements subjected to traffic loads,'' PhD thesis, University of California, Berkeley, Berkeley, Calif.

- Desai, C. S., Somasundaram, S., and Frantziskonis, G. (1986). ''A hierarchical approach for constitutive modeling of geologic materials.'' Int. J. Numer. and Analytical Methods in Geomechanics, 10, 225–257.

- Duncan, J. M., and Chang, C. Y. (1970). ‘‘Nonlinear analysis of stress and strain in soils.’’ J. Soil Mech. and Found. Div., ASCE, 96(5), 1629–1653.
- Dondi, G. (1994). “Three dimensional finite element analysis of a reinforced paved road”, Proc. Of the Fifth International Conference on Geotextiles, Geomembranes and Related Products, Singapore, pp. 95-100.
- Drucker D. C. and W. Prager (1952) Soil Mechanics and Plastic Analysis of Limit Design, Quart. Applied Mathematics, Vol.10, No.2
- Dunlap, W. A. (1966). ‘‘Deformation characteristics of granular materials subjected to rapid repetitive loading,’’ PhD thesis, Texas A&M University, College Station, Tex.
- Espinoza, R. D. (1994), “Soil-geotextile Interaction: Evaluation of Membrane Support”, Geotextiles and Geomembranes, Vol. 13, pp. 281-293.
- García-Rojo, R. and Herrmann, H. J. (2005). “Shakedown of unbound granular material.” Granular Matter, Vol. 7, No. 2-3, 2005, pp. 109-11
- Gerrard, C. M., Morgan, J. R., and Richards, B. G. (1975). ‘‘An approach to the design of flexible pavements for Australian conditions.’’ ARRR, 5(8).
- Gidel, G, Hornych, P.; Chauvin, J.J., Breysse, D. and Denis, A. (2001). NouvelleApproche pour l’Étude de Déformations Permanentes des Graves non Traitées àl’Appareil Triaxial à Chargement Répétés. Bulletin de Liaison des Laboratoires desPonts et Chaussées, No. 233, pp. 5-21.
- Goodman RE, Taylor RL, Brekke TL (1968) A model for the mechanics of jointed rock. Journal of the Soil Mechanics and Foundations Division ASCE, 94(SM3): 637
- Gray, J. E. (1962). ‘‘Characteristics of graded base course aggregates determined by triaxial tests.’’ Engrg. Res. Bull., No. 12, National Crushed Stone Association.
- Gray, DH, and Al-Refeai, T. (1986). “Behavior of fabric- versus fiber-reinforced sand.” *Journal of Geotechnical Engineering*, Vol. 112, No. 8, 804-820.
- Guide for Mechanistic-Empirical Design of New and Rehabilitated Pavement Structures.National Cooperative Highway Research Program Final Report for NCHRP 1-37A Project. (2004). http://www.NCHRP 1-37A Designdesignguide.com. Accessed July 10, 2004.

- Haas, R., Walls, J. and Carroll, R.G. (1988). "Geogrid Reinforcement of Granular Bases in Flexible Pavements," *Transportation Research Record 1188*, pp. 19-27.

- Haliburton, Lawmaster and King, (1970) Potential Use of Geotextile Fabric in Airfield Runway Design, Air Force Office of Scientific Research, AFOSR Report 79-00871.

- Haliburton, T.A. and Barron, J.V., (1983) "Optimum-Depth Method for Design of Fabric-Reinforced Unsurfaced Roads," Transportation Research Record 916, TRB, National Research Council, Washington, DC, USA, pp. 26-32.

- Halliday, A.R. and Potter, J.F., (1984) "The Performance of a Flexible Pavement Constructed on a Strong Fabric," Transport and Road Research Laboratory, Report 1123, Crowthorne, Berkshire, 15 p.

- Heydinger A G, Xie, Q L, Randolph B W, Gupta J D, Analysis of resilient modulus of dense and open-graded aggregates. Transportation Research Record 1547, Transportation Research Board, Washington, D.C., pp 1–6, 1996.

- Haynes, J. G., and Yoder, E. J. (1963). ''Effects of repeated loading on gravel and crushed stone base course materials used in the AASHO road test.'' Hwy. Res. Rec. 39.

- Heath, A. C. (2002). "*Modeling unsaturated granular pavement materials using bounding surface plasticity*." Ph. D. thesis, University of California at Berkeley, 2002.

- Heath, A.C., J.M. Pestana, J.T. Harvey and M.O. Bejarano, "Normalizing Behavior of Unsaturated Granular Pavement Materials," J. Geotech. Geoenviron. Eng., January 2004, Vol. 130, No. 9, pp. 896-904.

- Hibbitt, Karlson and Sorensen (2004), *ABAQUS Standard User's Manuals*, Version 6.5, Pawtucket, RI, USA.

- Hicks, R. G. (1970). Factors influencing the resilient properties of granular materials, PhD thesis, University of California, Berkeley, Berkeley, Calif.

- Hicks, R. G., and Monismith, C. L. (1971). Factors influencing the resilient properties of granular materials. Highway Research Record 345, 15-31. Highway Research Board. Washington, DC

- Holubec, I. (1969). ‘‘Cyclic creep of granular materials.’’ Rep. No. RR147, Department of Highways, Ontario, Canada. Jouve, P., Martinez, J., Paute, J. L., and Ragneau, E. (1987). ‘‘Rational model for the flexible pavement deformations.’’ Proc., 6th Int. Conf. on Struct. Des. of Asphalt Pavements, Vol. 1, 50–64.

- Harold, L. V. (1994). "Performance prediction models in the SuperPave Mix design system." SHRP-A-699, Strategic Highway Research Program, National Research Council, Washington, D.C.

- Hoyos, L. R., and Macari, E. J. Nature of principal strain response of unsaturated soils under multi-axial stress states. In Advances In Unsaturated Geotechnics : Proceedings of Sessions of Geo-Denver 2000 (August 2000), Geo- Institute of the American Society of Civil Engineers, pp. 333—343.

- Hua, J. Finite Element Modeling and Analysis of Accelerated Pavement Testing Devices and Phenomenon. Thesis submitted to Purdue University, 2000.

- Hossain, M.Z. & Yu, H.S. 1996. Shakedown analysis of mult-ilayer pavements using finite element and linear programming. Proc. 7th Australia- New Zealand Conference on Geomechanics, Adelaide: 512-520.

- Johnson K L. (1986). Plastic flow, residual stresses and shakedown in rolling contact. Pro-ceedings of the 2nd International Conference on Contact Mechanics and Wear of Rail/Wheel Systems, University of Rhode Island, Waterloo Ontario.

- Khalili, N. & Khabbaz, M.H. (1998). “A unique relationship for c for the determination of the shear strength of unsaturated soils.” Géotechnique 48, No. 5, 681-687

- Kamal, M. A., Dawson, A. R., Farouki, O. T., Hughes, D. A. B., and Sha’at, A. A. (1993). ‘‘Field and laboratory evaluation of the mechanical behavior of unbound granular materials in pavements.’’ Transp. Res. Rec. 1406, Transportation Research Board, Washington, D.C., 88– 97.

- Katona, M. G. (1983). “A simple contact-friction interface element with application to buried culverts.” Int. J. Num. Anal. Meth. Geomech., Vol. 7, 1983, 371–384.

- Khedr, S. (1985). ‘‘Deformation characteristics of granular base course in flexible pavement.’’ Transp. Res. Rec. 1043, Transportation Research Board, Washington, D.C., 131–138.

- Khogali, W. E., and Mohamed, E. H. (2004) “Novel Approach for Characterization of Unbound Materials.” Transportation Research Record 1874, 38–46, 2004.

- Koerner, R.M., (1998). *Designing With Geosynthetics*, 4th Edition, Prentice-Hall Inc., Englewood Cliffs, NJ, 761 p.

- Kolisoja, P. (1998). ‘‘Large scale dynamic triaxial tests.’’ III. Delprosjektrapport 20, Arbeidsfelleskapet KPG, Oslo, Norway. Lashine, A. K., Brown, S. F., and Pell, P. S. (1971). ‘‘Dynamic properties of soils.’’ Rep. No. 2, Submitted to Koninklijke/Shell Laboratorium, Dept. of Civ. Engrg., University of Nottingham, Nottingham, England.

- Konietzky, H., Kamp, L., Groeger, T., and Jenner, C. (2004) “ Use of DEM To Model The Interlocking Effect Of Geogrids Under Static And Cyclic Loading”. *In Numerical Modelling in Micromechanics via Particle methods*, Balkema, Rotterdam, pp. 3-11.

- Kuo, M. C., Hall, K. T., and Darter, M. (1995). "Three-dimensional finite element model for analysis of concrete pavement support." Transportation Research Record 1505, Transportation Research Board, National Research Council, Washington, D.C., 119–127.

- Kwon, J., Tutumluer, E., and Kim, M. (2005). “Development of a Mechanistic Model for Geosynthetic-Reinforced Flexible Pavements,” Geosynthetics International, 12, No. 6, pp. 310-320.

- Laguros, J.G. and Miller, G.A., (1997) “Stabilization of Existing Subgrades to Improve Constructibility During Interstate Pavement Reconstruction”, National Cooperative Highway Research Program, Synthesis of Highway Practice 247, Transportation Research Board, National Academy Press, Washington, D.C., 75p.

- Lashine, A.K., Brown, S.F., and Pell, P.S. (1971). Dynamic properties of soils. Report No. 2 Submitted to Koninklijke/Shell Laboratorium, Department of Civil Engineering, University of Nottingham, UK.

- Lekarp, F. (1997). ‘‘Permanent deformation behaviour of unbound granular materials,’’ Licentiate thesis, Royal Institute of Technology, Stockholm.

- Lekarp, F., and Dawson, A. (1998). ‘‘Modelling permanent deformation behaviour of unbound granular materials.’’ Constr. and Build. Mat.,

- Lekarp, F., Isacsson, U., and Dawson, A. (2000). ‘‘State of the art. I: Resilient response of unbound aggregates.’’ J. Transp. Engrg., ASCE, 126(1), 66–75.

- Lekarp, F., Richardson, I. R., and Dawson, A. (1996). ‘‘Influences on permanent deformation behavior of unbound granular materials.’’Transp. Res. Rec. 1547, Transportation Research Board, Washington, D.C., 68–75.

- Leng, J. and Gabr, M. (2003) "Numerical Analysis of Stress-Deformation Response in Reinforced Unpaved Road Sections". Presented at 83rd Annual Meeting of the Transportation Research Board, Washington, D.C.

- Leng, J. and M. Gabr, (2003) "Characteristics of Geogrid-Reinforced Aggregate under Cyclic Load," *Journal of Transportation Research Board,* No. 1786, National Research Council, Washington, D.C., pp. 29-35

- Lentz, R. W., and Baladi, G. Y. (1981). ''Constitutive equation for permanent strain of sand subjected to cyclic loading.'' Transp. Res. Rec.810, Transportation Research Board, Washington, D.C., 50–54.

- Manzari, M. T., and Dafalias, Y. F. A critical state two-surface plasticity model for sands. *Geotechnique* 47, 2 (1997), 255—272.

- Maree, J. H. (1982). ''Aspects of the design and behaviour of road pavements with granular material base layers,'' PhD thesis, Dept. of Civ. Engrg., University of Pretoria, Pretoria, South Africa (in Afrikaans).

- Maree, J. H., Freeme, C. R., Van Zyl, N. J., and Savage, P. F. (1982). ''The permanent deformation of pavements with untreated crushed stone bases as measured in heavy vehicle simulator tests.'' Proc., 11th ARRB Conf., Part 2, 16–28.

- Marek, C. R. (1977). ''Compaction of graded aggregate bases and subbases.'' Transp. Engrg. J. of ASCE, 103(1), 103–113. Morgan, J. R. (1966). ''The response of granular materials to repeated loading.'' Proc., 3rd Conf., ARRB, 1178–1192.

- Mayhew, H. C. (1983). Resilient properties of unbound road base under repeated triaxial loading. Lab. Rep. 1088, TRRL, Crowthorne, U.K.

- Mcdowell, G.R., Harireche , O., Konietzky, H., Brown, S., Thom, N. (2006) "Discrete element modeling of geogrid-reinforced aggregates". *Proceedings of the Institution of Civil Engineers. Geotechnical Engineering*, 159, pp. 35-48.

- McGown, A., Andrawes, K.Z., Pradhan, S., Khan, A.J., (1998) "Limit state design of geosynthetic reinforced soil structures, *Proc. of 6th Int. Conf. on Geosynthetics*, Atlanta, Vol. 1, pp.143-179.

- McGown, A., K.C. Yeo, and I. Yogarajah (1990). "Identification of a Dynamic Interlock Mechanism." Performance of Reinforced Soil Structures", *Proc., International Reinforced Soil Conference*, Glasgow, 377-379.

- McGown, A., Yeo, K.C. and Yogarajah, I. (1990). "Identification of a Dynamic Interlock Mechanism." Performance of Reinforced Soil Structures, *Proc., International Reinforced Soil Conference*, Glasgow, 377-379.

- Mitry, F. G. (1964). ''Determination of the modulus of resilient deformation of untreated base course materials,'' PhD thesis, University of California, Berkeley, Berkeley, Calif.

- Miura, N., Sakai, A., Taesiri, Y., Yamanouchi, T., and Yasuhara, K. (1990). "Polymer grid reinforced pavement on soft clay grounds", *geotextiles and geomembranes*, Vol. 9, No. 1, pp. 99-123.

- Moghaddas-Nejad, F. and Small, J.C. (1996). "Effects of Geogrid Reinforcement in Model Track Tests on Pavements", *Journal of Transportation Engineering*, Vol. 122, No. 6, pp. 468-474.

- Moghaddas-Nejad, F. and Small, J.C. (2003). "Resilient and Permanent Characteristics of Reinforced Granular Materials by Repeated Load Triaxial Tests", *ASTM Geotechnical Testing Journal,* Vol. 26, No. 2, pp. 152-166.

- Mohammad, L. N., Puppala, A. J., Alavilli, P. (1994)."Investigation of the Use of Resilient Modulus for Louisiana Soils in Design of Pavements," Louisiana Transportation Research Center, FHWA, LADOTD, Report No. 283.

- Mohammad, L.N., Herath, A., Rasoulian, M., and Zhongjie, Z. (2006). "Laboratory Evaluation of Untreated and Treated Pavement Base Materials from a Repeated Load Permanent Deformation Test." *Transportation Research Record*.

- Mohammad, L.N., Puppala, A.J., and Alavalli, P. (1994). "Influence of Testing Procedure and LVDT Location on Resilient Modulus of Soils," Transportation Research Record, No. 1462, pp. 91-101.

- Monismith, C. L., Seed, H. B., Mitry, F. G., and Chan, C. K. (1967). 'Prediction of pavement deflections from laboratory tests.'' Proc., 2nd mInt. Conf. Struct. Des. of Asphalt Pavements, 109–140.

- Morgan, J.R. (1966). The response of granular materials to repeated loading. Proc., 3rd Conf., ARRB, 1178-1192.

- Moore, W. M., Britton, S. C., and Schrivner, F. H. (1970). ''A laboratory study of the relation of stress to strain for a crushed limestone base material.'' Res. Rep. 99-5F, Study 2-8-65-99, Texas Transp. Inst., Texas A&M University, College Station, Tex.

- Nazzal M., M. Y. Abu-Farsakh, and L. Mohammad. Laboratory Characterization of Reinforced Crushed Limestone under Monotonic and Cyclic Loading. *ASCE Journal of Materials* (in press).

- Nazzal, M.D., Abu-Farsakh, M., and Mohammad, L.(2006) " Numerical Analyses of Geogrid Reinforced Flexible Pavements." *Proc., GeoCongress Conference*, Atlanta.

- NCHRP (2004), NCHRP Project 1-37A, *Development of NCHRP 1-37A Design Guide, Using Mechanistic Principles to Improve Pavement Design*, http://www.NCHRP 1-37A Designdesignguide.com/.

- NCHRP (2004). *"Guide for Mechanistic-Empirical Design of New and Rehabilitated Pavement Structures"* NCHRP Final Report for NCHRP 1-37A Project. www.NCHRP 1-37A Designdesignguide.com (July 20, 2005).

- NCHRP (2004). "*Laboratory Determination of Resilient Modulus for Flexible Pavement Design."* NCHRP Research Results Digest for NCHRP 1-28A Project.

- Niekerk, A. Scheers, J. Muraya, P. Kisimbi,A. 2000. The effect of compaction on the mechanical behaviour of mix granulate basecourse materials and on pavement performance. Unbound aggregates in roads - Proceedings of the international symposium, UNBAR 5, Nottingham, UK, 21-23 June 2000, pp 125-136.

- Notes from Residential Course, Bituminous Pavements: Materials, Design and Evaluation, University of Nottingham, Nottingham, England.

- Ortiz, M, Simo, J. C. (1986). "An analysis of a new class of integration algorithms for elastoplastic constitutive relations." Int. J. Num. Meth. Engrg., 23, 353–366

- Pappin, J. W. (1979). Characteristics of granular material for pavement analysis. PhD Thesis, University of Nottingham, UK.

- Paute, J. L., Hornych, P., and Benaben, J. P. (1996). ''Repeated load triaxial testing of granular materials in the French network of Laboratoires des Ponts et Chausse´es.'' Flexible Pavements, Proc., Eur. Symp. Euroflex 1993, A. G. Correia, ed., Balkema, Rotterdam, The Netherlands, 53–64.

- Penner, R., (1985), "*Geogrid Reinforcement of the Granular Base Layer in Conventional Three-Layer Pavement Sections*", M.S. Thesis, University of Waterloo, August, 130 p.

- Penner, R., Haas, R., Walls, J. and Kennepohl, G., (1985), "Geogrid Reinforcement of Granular Bases," Paper Presented at the Roads and Transportation Association of Canada Annual Conference, Vancouver, Canada, September.

- Perkins, S.W (2002) "Evaluation of Geosynthetic Reinforced Flexible Pavement Systems Using Two Pavement Test Facilities". Report No. FHWA/MT-02-008/20040, U.S. Department of Transportation, Federal Highway Administration.

- Perkins, S.W. (2001) "Mechanistic-empirical modeling and design model development of geosynthetic reinforced flexible pavements", Montana Department of transportation, Helena, Montana, Report No. FHWA/MT-01-002/99160-1A.

- Perkins, S.W. and Edens, M.Q. (2002), "Finite Element and Distress Models for Geosynthetic-Reinforced Pavements", *International Journal of Pavement Engineering*, Vol. 3, No. 4,NCHRP 1-37A Design, pp. 239-250.

- Perkins, S.W. and Ismeik, M. (1997a). "A Synthesis and Evaluation of Geosynthetic Reinforced Base Layers in Flexible Pavements: Part I," *Geosynthetics International*, Vol. 4, No. 6, pp. 549- 605.

- Perkins, S.W. and Ismeik, M. (1997b). "A Synthesis and Evaluation of Geosynthetic Reinforced Base Layers in Flexible Pavements: Part II," *Geosynthetics International*, Vol. 4, No. 6, pp. 549- 605.

- Perkins, S.W. and M.Q. Edens (2002). "Finite Element and Distress Models for Geogrid-Reinforced Pavements", *International Journal of Pavement Engineering*, Vol. 3, No. 4, pp. 239-250.

- Perkins, S.W., (1999a), "Mechanical Response of Geosynthetic Reinforced Pavements," Geosynthetics International, Industrial Fabrics Association International, Roseville, MN.

- Perkins, S.W., (1999b) , "Geosynthetic Reinforcement of Flexible Pavements: Laboratory Based Pavement Test Sections, Federal Highway Administration Report FHWA/MT-99-001/8138, Montana Department of Transportation, 140 p.

- Perkins, S.W., and M. Ismeik (1997a). "A Synthesis and Evaluation of Geogrid Reinforced Base Layers in Flexible Pavements: Part I", *Geogrids International*, Vol. 4, No. 6, 1997, pp. 549- 605.

- Perkins, S.W., and M. Ismeik. (1997b) "A Synthesis and Evaluation of Geogrid Reinforced Base Layers in Flexible Pavements: Part II" ,*Geogrids International*, Vol. 4, No. 6, 1997, pp. 549- 605.

- Perkins, S.W., Christopher, B., Cuelho, E.L., Eiksund, G.R., Hoff, I., Schwartz, C.W., Svano, G., and Want, A. (2004). "Development of design methods for geosynthetic reinforced flexible pavements". A report prepared for the U.S. Department of transportation, Federal Highway Administration, FHWA/DTFH61-01-X-00068.

- Perkins, S.W., Christopher, B., Cuelho, E.L., Eiksund, G.R., Hoff, I., Schwartz, C.W., Svano, G., and Want, A. (2004). "Development of design methods for geosynthetic reinforced flexible pavements." A report prepared for the U.S. Department of transportation, Federal Highway Administration, FHWA/DTFH61-01-X-00068, p. 263.

- Perkins, S.W., Ismeik, M. and Fogelsong, M.L., (1998a), "Mechanical Response of Geosynthetic-Reinforced Pavement System to Cyclic Loading," Proceedings of the Fifth International Conference on the Bearing Capacity of Roads and Airfields, Trondheim, Norway, Vol. 3, pp. 1503-1512.

- Perkins, S.W., Ismeik, M. and Fogelsong, M.L., (1999), "Influence of Geosynthetic Placement Position on the Performance of Reinforced Flexible Pavement Systems," Proceedings of the Conference Geosynthetics '99, Boston, MA, USA, Vol. 1, pp. 253-264.

- Perkins, S.W., Ismeik, M., Fogelsong, M.L., Wang, Y., Cuelho, E.V., (1998b), Proceedings of the Sixth International Conference on Geosynthetics, "Geosynthetic-Reinforced Pavements: Overview and Preliminary Results," Atlanta, GA, March, 1998, Vol.2, pp. 951-958.

- Puppala, A. J., Mohammad, L. N., and Allen, A. (1999). "Permanent Deformation Characterization of Subgrade Soils from RLT Test." *Journal of Materials in Civil Engineering*, Vol. 11, No. 4, pp. 274-282.

- Plaistow, L. C. (1994). ''Non-linear behaviour of some pavement unbound aggregates,'' MS thesis, Dept. of Civ. Engrg., University of Nottingham, Nottingham, England.

- Potts, D.M. and Ganendra, D. (1994), ``An evaluation of substepping and implicit stress point algorithms'', *Computer Methods in Applied Mechanics and Engineering*, Vol. 119, pp. 341-54.

- Potts, D.M. and Gens, A. (1985), ``A critical assessment of methods of correcting for drift from the yield surface in elastoplastic finite element analysis'', *International Journal for Numerical and Analytical Methods in Geomechanics*, Vol. 9, pp. 149-59.

- Puppala, A. J., S. Chomtid, and V. Bhadriraju. (2005) "Evaluation of Plastic Strain Potentials in Subgrade Soils Using Repeated Load Triaxial Tests." *The 84th Transportation Research Board Annual Meeting. CD-ROM*, National Research Council, Washington, D.C.

- Raad, L., Minassian, G., and Gartin, S. (1992). ''Characterization of saturated granular bases under repeated loads.'' Transp. Res. Rec. 1369, Transportation Research Board, Washington, D.C., 73–82.

- Raad, L., Weichert, D. and Haidar, A. (1989a). “Analysis of full-depth asphalt concrete pavements using shakedown theory.” Transportation Research Record, No. 1227, pp. 53-65.

- Raad, L., Weichert, D. and Haidar, A. (1989b). “Shakedown and fatigue of pavements with granular bases.” Transportation Research Record, No. 1227, pp. 159-172.

- Raad, L., Weichert, D. and Najm, W. (1988). “Stability of multilayer systems under repeated loads.” Transportation Research Record, No. 1207, pp. 181-186.

- Raymond, G.P. & Williams, D.R. (1978). Repeated Load Triaxial tests on a dolomite ballast. Journal of Geotechnical Engineering Division, ASCE, 104(7), 1013-1029.

- Robinson, R. G. (1974). ‘‘Measurement of the elastic properties of granular materials using a resonance method.’’ TRRL Supplementary Rep. No. 111UC, TRRL.

- Rodriguez, A. R., Castillo, H.D., Sowers , G. F. (1988). *Soil Mechanics in Highway Engineering*.

- Roscoe, K. H., and Burland, J. B. On the generalized stress-strain behavior of “wet” clay. In Engineering Plasticity. Cambridge University Press, Cambridge, U.K., 1968, pp. 535—609.

- Roscoe, K. H., Schofield, A. N., and Thurairajah, A. Yielding of clays in states wetter than critical. In Engineering Plasticity. Cambridge University Press, Cambridge, U.K., 1968, pp. 535—609.

- Roscoe, K., Schofield, A. N., and Wroth, C. On the yielding of soils. Geotechnique 8 (1958), 22—53

- Rowe, P. W. The stress-dilatancy relation for static equilibrium of an assembly of particles in contact. Proceedings, Royal Society 269 (1962), 500—527.

- Saad, B., Mitri, H., and Poorooshasb, H. (2005). “ 3D FE Analysis of Flexible Pavement with Geosynthetic Reinforcement” J. Transp. Engrg., Volume 132, Issue 5, pp. 402-415

- SAS Institute Inc. SAS OnlineDoc® 9.1.2**.** Cary, NC, SAS Institute Inc., 2004.

- Sellmeijer, J.B., (1990). “Design of Geotextile Reinforced Paved Roads and Parking Areas,” Proceedings of the Fourth International Conference on Geotextiles, Geomembranes and Related Products, The Hague, The Netherlands

- Balkema, Vol. 1, pp. 177-182.

- Sharp R and Booker J. (1984). Shakedown of pavements under moving surface loads, pp. 1-14, ASCE Journal of Transportation Engineering, No 1, 1984.

- Sharp, R. W. (1983). ‘‘Shakedown analysis and the design of pavements,’’ PhD thesis, University of Sydney, Sydney, Australia. Sharp, R. W., and Booker, J. R. (1984). ‘‘Shakedown of pavements under moving surface loads.’’ J. Transp. Engrg., ASCE, 110(1), 1–14.

- Shaw, P. S. (1980). ‘‘Stress-strain relationships for granular materials under repeated loading,’’ PhD thesis, Dept. of Civ. Engrg., University of Nottingham, Nottingham, England.

- Schofield, A., and Wroth, C.P. (1968). Critical state soil mechanics, McGraw–Hill, N.Y.

- Simo, J.C., Taylor, R.L (1985), "Consistent tangent operators for rate-independent elasto-plasticity", Computer Methods in Applied Mechanics and Engineering, Vol. 48 pp.101-18.

- Sloan, S.W (1987), "Substepping schemes for the numerical integration of elastoplastic stress-strain relations", International Journal for Numerical Methods in Engineering, Vol. 24 pp.893-911.

- Sloan, S.W, Abbo, AJ, and Sheng D. (2001)“Refined explicit integration of elastoplastic models with automatic error control.” Engineering Computations, Vol. 18, pp.121–154.

- Smith, W. S., and Nair, K. (1973). “Development of Procedures for Characterization of Untreated Granular Base Coarse and Asphalt Treated Base Course Materials.” Report No. FhWA-RD-74-61, Federal Highway Administration, Washington, D.C., 1973.

- Sowers, G. F. Robb, A.D. Mullis, C.H. & Glenn, A.J. (1957). The residual lateral pressures produced by compacting soils. Proceedings 4th International Conference 322 on Soil Mechanics and Foundation Engineering, London, UK. Vol. 2, pp. 243-247.

- Stewart, H. E., Selig, E. T. & Norman-Gregory, G. M. (1985). Failure criteria and lateral stresses in track foundations, Transp. Res. Record No. 1027, Transportation Research Board, Washington, DC, 59-64.

- Sweere, G. T. H. (1990). ‘‘Unbound granular bases for roads,’’ PhD thesis, University of Delft, Delft, The Netherlands. Thom, N. H. (1988). ‘‘Design of road foundations,’’ PhD thesis, Dept. of Civ. Engrg., University of Nottingham, Nottingham, England.

- *Tensar Geogrid Product Specification* (2004). Tensar Earth Technologies, Atlanta, Georgia. *www.tensarcorp.com/uploadedFiles/SPECTRA_MPDS_BX_8.05.pdf*

- Theyse, H. L. (2002). Stiffness, Strength, and Performance of Unbound Aggregate Material: Application of South African HVS and Laboratory Results to California Flexible Pavements. University of California Pavement Research Center.

- Thom, N. H., and Brown, S. F. (1987). ‘‘Effect of moisture on the structural performance of a crushed-limestone road base.’’ Transp. Res. Rec. 1121, Transportation Research Board, Washington, D.C., 50–56.

- Thom, N. H., and Brown, S. F. (1988). ‘‘The effect of grading and density on the mechanical properties of a crushed dolomitic limestone.’’ Proc., 14th ARRB Conf., Part 7, 94–100.

- Thom, N., Brown, S. (1987). “Effect of Moisture on the Structural Per-formance of a Crushed-Limestone Road Base”. *Transportation Research Record* 1121, Transportation Research Board, Washington, D.C., pp 50-56.

- Thom, N.H. (1988). Design of road foundations. PhD Thesis, University of Nottingham, UK.

- Trollope, E. H., Lee, I. K., and Morris, J. (1962). ‘‘Stresses and deformation in two-layer pavement structures under slow repeated loading.’’ Proc., ARRB, Vol. 1, Part 2, 693–718.

- Tutumluer, E., Kwon, J., and Kim., M. (2005) “Modeling Geogrid Reinforced Aggregate Layers in Flexible Pavements,” *In Proceedings of the 11th International Conference of the Association for Computer Methods and Advances in Geomechanics* (IACMAG), Turin, Italy.

- Uzan, J. (1985). Characterisation of granular material. Transport Research Record No. 1022. Transport Research Board, Washington DC, USA. pp. 52-59.

- Wathugala, G.W., Huang, B., and Pal, S., (1996), “Numerical simulation of geosynthetic reinforced flexible pavement”, *Transportation Research Record 1534*, Transportation Research Board, national Research Council, Washington, DC, USA, pp.58-65.

- Webster, S. L. *Geogrid Reinforced Base Courses For Flexible Pavements For Light Aircraft, Test Section Construction, Behavior Under Traffic, Laboratory Tests, And Design Criteria*. Technical Report GL-93-6. U.S. Army Corps of Engineers t, Waterways Experiment Station, Vicksburg, Mississippi, 1993.

- Webster, S. L. Geogrid Reinforced Base Courses For Flexible Pavements For Light Aircraft, Test Section Construction, Behavior Under Traffic, Laboratory Tests, And Design Criteria. Technical Report GL-93-6. U.S. Army Corps of Engineers t, Waterways Experiment Station, Vicksburg, Mississippi, 1993.

- Webster, S. L., (1993). "*Geogrid reinforced base courses for flexible pavements for light aircraft, test section construction, behavior under traffic, laboratory tests, and design criteria*." Technical Report GL-93-6. U.S. Army Corps of Engineers, Waterways Experiment Station, Vicksburg, Mississippi.

- Werkmeister, S, Dawson, A., and Wellner, F. (2004) . "Pavement Design Model for Unbound Granular Materials", *ASCE Journal of Transportation Engineering*, Vol. 130, No. 5, pp 665-674.

- Werkmeister, S. (2003). Permanent deformation behaviour of unbound granular materials in pavement constructions. PhD Thesis, Technical University of Dresden, Germany.

- Werkmeister, S. Dawson, A. Wellner, F. (2001). Permanent deformation behavior of granular materials and the shakedown concept. Transportation Research Board, 80th Annual Meeting, Washington D.C. January 7-11, 2001.

- Werkmeister, S. Numrich, R. Wellner, F. (2000). Resilient and permanent deformation of unbound granular materials. The Proceedings of the UNBAR5 Symposium, June 21-23, 2000. Department of Civil Engineering, University of Nottingham, UK.

- Wissmann, J.W. and Hauck, C. (1983), "Efficient elastic-plastic finite element analysis with higher order stress point algorithms." Computers and Structures, Vol. 17, pp. 89-95.

- Wrigley, N. E. (1989). "The Durability and Aging of Geogrids." Proc. GRI-2, Durability and Aging of Geosynthetics, Publ. by Elsevier Appl. Sci., London and New York, pp. 110-134.

- Wong, S.K., Kapoor, A. and Williams, J.A. (1997). "Shakedown limits on coated and engineered surfaces." Wear 203-204, pp. 162-170.

- Wood, D.M. 1990. Soil Behaviour and Critical State Soil Mechanics. Cambridge, England: Cambridge University Press.

- Yu, H.S. and Hossain, M.Z. (1998). "Lower bound shakedown analysis of layered pavements using discontinuious stress fields." Computer Methods in Applied

Mechanics and Engin eering, Vol. 167, pp. 209-222.

- Zaghloul, S.M., and White, T.D. (1993). "Use of a three-dimensional, dynamic finite element program for analysis of flexible pavement." Transportation Research Record. 1388, TRB, National Research Council, Washington, D.C., 60–69.

- Zienkiewicz OC, Best B, Dullage C, Stagg K (1970) “ Analysis of nonlinear problems in rock mechanics with particular reference to jointed rock systems.” Proceedings of the Second International Congress on Rock Mechanics, Belgrade

Vita

Munir Nazzal was born on January 19, 1980, in Jerusalem, Palestine, to Dr. Darwish Nazzal and Ibtisam Nazzal. He finished his high school from Friends Schools, Ramallah, Palestine, in June 1997. He received his bachelor degree in civil engineering from Birzeit University, Birzeit, Palestine, in February 2002, and came to United States in the summer of 2002 to pursue his graduate studies in civil engineering at Louisiana State University, Baton Rouge, Louisiana. In December 2003, he received his master's degree from the civil engineering department. Directly after the completion of his master's degree, he joined the doctoral program in civil engineering. Since August of 2006, Munir was working as research associate at the Louisiana Transportation Research Center. He is married and has a beautiful and adorable daughter. Munir Nazzal is anticipated to fulfill the requirements of the degree of Doctor of Philosophy in civil engineering in May, 2007.